HAL
open science

Qubits de spin : de la manipulation et déplacement d'un spin électronique unique à son utilisation comme détecteur ultra sensible

Romain Thalineau

▶ **To cite this version:**

Romain Thalineau. Qubits de spin : de la manipulation et déplacement d'un spin électronique unique à son utilisation comme détecteur ultra sensible. Physique [physics]. Université de Grenoble, 2012. Français. NNT : 2012GRENY106 . tel-00875970

HAL Id: tel-00875970

https://theses.hal.science/tel-00875970v1

Submitted on 23 Oct 2013

HAL is a multi-disciplinary open access archive for the deposit and dissemination of scientific research documents, whether they are published or not. The documents may come from teaching and research institutions in France or abroad, or from public or private research centers.

L'archive ouverte pluridisciplinaire **HAL**, est destinée au dépôt et à la diffusion de documents scientifiques de niveau recherche, publiés ou non, émanant des établissements d'enseignement et de recherche français ou étrangers, des laboratoires publics ou privés.

UNIVERSITÉ DE GRENOBLE

THÈSE

Pour obtenir le grade de

DOCTEUR DE L'UNIVERSITÉ DE GRENOBLE

Spécialité : **Physique**

Arrêté ministériel :

Présentée par

Romain Thalineau

Thèse dirigée par **Tristan Meunier**

préparée au sein **Institut Néel-CNRS**
et de **Physique**

Qubits de spin :

de la manipulation et déplacement d'un spin électronique unique à son utilisation comme détecteur ultra sensible

Thèse soutenue publiquement le **7 décembre 2012**,
devant le jury composé de :

Mr, Thierry Amand
Dr, Laboratoire de Physique et Chimie des Nano-Objets, Toulouse, Rapporteur
Mr, Lieven Vandersypen
Pr, Kavli Institute of NanoScience, TU Delft, Rapporteur
Mr, Henri Mariette
Dr, Institut Néel-CNRS and CEA/INAC/SP2M, Grenoble, Examinateur
Mr, Patrice Roche
Dr, SPEC, CEA Saclay, Examinateur
Mr, Tristan Meunier
Dr, Institut Néel-CNRS, Grenoble, Directeur de thèse

Remerciements

Ces trois années de thèse se sont révélées être une belle aventure, épanouissante autant d'un point de vue scientifique qu'humain. C'est pourquoi je voudrais profiter de ces quelques lignes pour remercier ceux qui de près ou de loin ont pu y participer.
Tout d'abord je tiens à remercier Tristan MEUNIER pour m'avoir guider tout au long de cette thèse. Tu as su à la fois me laisser la liberté dont j'avais besoin, mais aussi me recadrer au moment opportun. Les discussions scientifiques ouvertes, ton enthousiasme et ton dynamisme font de toi un excellent directeur de thèse et je souhaite à tous tes prochains étudiants de partager cela avec toi.
Je voudrais aussi remercier tout particulièrement Christopher BAUERLE. Tu m'as initié aux joies (et parfois déboires) de la cryogénie, et tu as aussi su te montrer présent et disponible tout au long de cette thèse. Par ailleurs je te suis très reconnaissant d'avoir accepté de lire et corriger mon manuscrit. Ton esprit critique et pédagogique a grandement contribué à l'élaboration de ce dernier.
Je tiens aussi à remercier Thierry Amand ainsi que Lieven Vandersypen pour avoir accepter de juger ce manuscrit, ainsi que Henri Mariette et Patrice Roche pour leur participation en tant qu'examinateur à la soutenance de thèse.
Ces travaux de thèses ont été effectués au sein de l'institut Néel, et je remercie pour cela le directeur de l'institut et le sous-directeur du département Nano respectivement Alain Fontaine et Joël Cibert, puis à partir de 2011 Alain Schulh et Hervé Courtois. Un grand merci à tous les membres du laboratoire qui contribuent à son bon fonctionnement.
Je voudrais aussi remercier les membres permanents du laboratoire avec qui j'ai pu interagir. Je remercie tout d'abord Laurent SAMINADAYAR pour m'avoir accueilli dans l'équipe pour mon stage de Master 2, Olivier BUISSON pour l'organisation des séminaires d'équipe, Pierre PERRIER pour toute ton aide en cryogénie ainsi que pour ta disponibilité pour dépanner, Christophe GUTTIN et Daniel LEPOITTEVIN pour le développement de l'électronique bas bruit utilisée sur les manips, Christophe HOARAU pour ton aide sur tout ce qui concerne l'électronique RF, la team NANOFAB pour leur aide en salle blanche, et l'équipe du liquéfacteur pour la dose d'helium liquide presque quotidienne.
Bien sûr cette thèse n'aurait pas été la même sans la présence des non permanents, partenaires de galères mais aussi et surtout de festivités. Parmi eux j'aimerais remercier en particulier Yannick "Blabla" BAINES résident permanent du Vieux Manoir pour avoir partagé le bureau et pour les délires "babunda, petites filles aux yeux de pierres", Sylvain HERMELIN pour tous ce que tu m'as appris en électronique et en info ainsi que pour les discussions passionnées, Alejandro "l'espingouin" GOMEZ PEREZ et Anna VIANELLI les latinos, pour votre joie de vivre et pour ces bons moments partagés, Soument MANDAL pour ta gentilesse et ta disponibilité, Romain "Sergent" VINCENT l'homme aux milles distributions linux, Marc GANZHORN capitaine de l'équipe de Foot, Sven ROHR

parce que tes talents de "street dater" m'impressionneront toujours, Tobias BAUTZE pour ta bonne humeur et tous ces festivals en Combi VW, et tous les autres thésards ou post-docs côtoyés : Nicolas ROCH, Florent "Poul" LECOCQ, Oana BUNAU, Aurelien "Poual" TRICHET, Pinpin HERON, Benoît BERTRAND, Gregoire ROUSSELLY, Hanno FLENTJE, Guillaume FORESTIER.
Pour finir je voudrais remercier mes amis, rencontrer avant le début de cette thèse, mais avec qui j'ai pu partagé de sacré moments pendant ces trois années. Je tiens donc à remercier Nicolas "Cerz" WARTENBERG, mon colocataire, pour ces super années partagées ainsi que pour avoir supporté nos traits d'humour sur la chimie, Matias "Boomz" URDAMPILLETA parce que avec toi on peut parler et rire de tout, Antoine "Jon la Pipz" Guille pour ta pipzerie et tes coups de sang aussi drôle qu'irréel, Christophe "Petit Corps Malade" BLANC pour avoir accepté de me suivre dans des soirées électro toutes moisies, Valery "Serviette" OZENNE pour ta motivation sans faille, Oriane MOLLET pour la transformation de ta voie vers les hautes fréquences au contact d'éthanol, Caroline REINE pour ta bonne humeur permanente. Enfin un grand merci à mes potes de Lyon, Paris et d'ailleurs pour les bons moments passées ensemble. Je tiens donc à remercier Gallo, Xim, Ben, Mathilde, Breunz, Binouz, Fils, Jul, Matthias, Mahatar and co.
Finalement je tiens à remercier ma famille, et plus particulièrement mes parents pour m'avoir donné tout leur soutien et les moyens de m'épanouir dans ce que je fais aujourd'hui, ainsi que mes deux soeurs pour leur intérêt pour mon travail. Un grand merci aussi à Geta pour avoir accepter mon rythme de travail durant les derniers mois de thèses, notamment les réveils en pleine nuit pour relancer une manip. Tu as été une vrai source de motivation, et je t'en suis très reconnaissant.
Bref, un grand merci à tous.

Contents

Remerciements i

Introduction **i**

Bibliography iii

1 General concepts **1**

Résumé 1

1.1 Laterally defined quantum dots 2

1.2 Charge states in a single quantum dot 4

1.2.1 Constant Interaction model 5

1.2.2 Quantum effects in quantum dot systems 9

1.2.3 Transport measurements 10

1.2.4 Charge detection 13

1.3 Spins in quantum dots 15

1.3.1 Spin states 16

1.3.2 Relaxation and decoherence of a spin 22

1.4 Hyperfine interaction 24

1.5 Spin-orbit interaction 27

Bibliography 29

2 Device fabrication and experimental set-up **33**

Résumé 33

2.1 Device fabrication 34

2.1.1 Lithography process 35

2.1.2 Etching 36

2.1.3 Nanofabrication steps 36

2.2 Cryogenics 38

2.3 DC electronics 40

2.3.1 Voltage sources 40

2.3.2 Amplifiers 42

2.4 RF electronics 42

2.4.1 Coaxial lines 43

2.4.2 RF signal generator 43

2.5 Software 43

Bibliography 46

3 A few-electron quadruple quantum dot in a closed loop **47**
Résumé . . . 47
3.1 Motivations . . . 48
3.2 Geometry . . . 50
3.3 Charge states : From a single to a quadruple quantum dot . . . 52
3.3.1 Charge state of a single quantum dot . . . 53
3.3.2 Charge state of a double quantum dot . . . 54
3.3.3 Charge states of a triple quantum dot . . . 57
3.3.4 Charge states of a quadruple quantum dot . . . 60
3.4 Experimental stability diagram . . . 61
3.5 Electron transport along a closed path . . . 68
3.6 Perspectives . . . 70
Bibliography . . . 72

4 From SWAP to C-phase gate regime in single spin qubits **75**
Résumé . . . 75
4.1 Motivations . . . 76
4.2 Two single spin qubits in a tunnel coupled double quantum dot . . . 79
4.2.1 Spin states in a double quantum dot . . . 80
4.2.2 Measure of the spin state . . . 84
4.3 Characterization and tuning of the system . . . 90
4.3.1 Tunnel coupling between the two quantum dots . . . 90
4.3.2 Tunnel barriers between the quantum dots and the reservoirs . . . 96
4.4 C-phase gate with single spin qubtis . . . 98
4.5 Dynamical polarization of the nuclear spins . . . 99
4.5.1 Polarization pulse . . . 101
4.5.2 $S - T_0$ coherent oscillations induced by ΔB_z . . . 104
4.6 From a SWAP to C-phase gate . . . 108
4.6.1 SWAP gate with single spin qubits . . . 109
4.6.2 Exchange oscillations with a finite gradient ΔB_z . . . 113
4.7 Conclusion and perspectives . . . 119
Bibliography . . . 121

5 Toward the detection of a single electron transported in an edge-state **123**
Résumé . . . 123
5.1 Motivations . . . 124
5.1.1 Quantum Hall Effect (QHE) . . . 124
5.1.2 The electronic Mach-Zehnder interferometer. . . . 127
5.2 A double quantum dot as a single electron detector . . . 129
5.3 Quantum hall regime . . . 131
5.4 Quantification of the detector device . . . 134

5.4.1 Detection of the electron density of the edge-states 134
5.4.2 Detection of stochastic events 138
5.4.3 Evolution of the detector visibility with respect to the QPC transmission 139
5.5 Perspectives : Toward the single electron detection 143
Bibliography 149

Conclusion and perspectives **151**
Bibliography 157

Appendices **159**

Nanofabrication recipes **161**
.1 Optical lithography (thin plating) 161
.2 Optical lithography (thick plating) 162
.3 Electronic lithography 162
.4 Alignment marks 163
.5 Mesa etching 163
.6 Ohmic contacts 163
.7 Thin gates 164
.8 Large gates 164

CI model **165**
.9 Electrostatics of a N conductors system 165
.10 Single quantum dot 166
.11 Double quantum dot 166
.12 Triple quantum dot 168
.13 Quadruple quantum dot 170
Bibliography 172

Introduction

In the early 1950s, the transistor effect was discovered by Brattain, Bardeen, and Shockley. This invention led to the amazing growth of the micro-electronic industry based on the race for components miniaturisation. To give an order of magnitude, today's microprocessors hold billions of transistors whose typical size range 50nm. But this industry will have to face new issues. First the commuting energy (the energy needed to change the state of a transistor) scales with the transistor size. At a certain point, this energy will be dominated by the thermal energy, and the device stability will not be ensured any more. In addition, when the transistor size becomes the same order of magnitude of the electron wavelength, the physics is governed by the quantum mechanics laws. The interest of physicists combined with the necessity for the micro-electronic industry to overcome theses issues gave rises to a new field of research called quantum nanoelectronics. One of the "hot topic" of this field concerns electronics with a single electron.
The first requirement toward electronics with a single electron relies on the ability to isolate this electron. For two or three decades, a particular attention has been given to quantum dots. This is a region in space where the motion of the electrons is confined all along the three dimensions. In this thesis we will focus on laterally confined quantum dots made in AlGaAs heterostructure. Such a semiconducting structure contains a two-dimensional electron gas (2DEG) which allows for electron confinement in a plane. Inside this plane, the electrons are confined by an electrostatic potential which can be controlled by means of macroscopic voltages applied on metallic gates deposited at the surface of the sample. In the 1990s the ability to isolate a single electron in lateral quantum dots has been demonstrated [1], and gave rise to prolific studies. Indeed, since this electron is isolated, we can therefore imagine to control its degrees of freedom, as its charge or its magnetic momentum (spin).
When faced with these new objects, physicists began to think about the possibility to use this electron (meaning its degrees of freedom) in order to encode information, building what is commonly called a qubit (quantum bit). A qubit is the quantum equivalent of the classical bit. It is a two-levels system, but contrary to its classical counterpart, a qubit can exist in a superposition of states. Such a property is at the center of a quantum computer. This quantum machine could take advantage of the quantum parallelism in order to solve complex problems. For instance one of the most cited example is the decomposition of an input number into prime factors . Considering a classical computer, this process is exponential in the number of digits of the input number, and today any public-key cryptographic system relies on this exponential behaviour : to go from the public key to the private one, one needs to factorise it, and for a key of a few hundred of bits, no one is supposed to be able to perform it in a short time. In the case of a quantum

computer, an algorithm (Shor's algorithm) using the features of this machine should be able to break this limitation, because of the polynomial dependence (in the number of digit of the input) of the prime factor decomposition. The resolution of mathematical problems should not be the only capacity of a quantum computer. Indeed when Feynman first introduced the idea in 1982, his idea relied more on the ability of such a machine to simulate quantum systems [2].

In order to experimentally realize such a computer, a certain amount of qubits needs to be entangled. In the context of semiconductor quantum dots, several ways have been proposed in order to do so, but one of the most attractive solution relies in the transport of a single electron from a quantum dot to another one. Recently fast and efficient single electron transports have been obtained by assisting the transport through an electrostatically defined 1D-channel with surface acoustic waves in AlGaAs heterostructures [3, 4]. Nevertheless, such a technique is restricted to displacements along a straight line. To perform more complex displacements, engineering the path of the electron with series of quantum dots is a promising alternative. In this context, we developed a system of a quadruple quantum dot where a single electron can be transported from one quantum dot to another one. In addition interesting topological features arise from the transport of an electron along a closed path. Indeed it has been theoretically predicted that topological spin manipulations could be obtained if an electron is transported adiabatically along a closed path [5, 6], and the system that we designed opens the way toward such manipulations.

Like a classical computer, a quantum computer needs some elementary operations entering in algorithm. In semiconductor quantum dots, all theses operations (known as gates) required for quantum computation with single spins, like the single-shot readout [7] or the single-qubit rotations [8], have been demonstrated recently. In addition the two-qubit gate $\sqrt{SWAP}$ has also been realized experimentally [9]. Although this two-qubit gate combined with the single qubit rotations forms a universal set of gates, meaning that any quantum operations could be implemented via these gates, they are not the natural building block for quantum algorithms. For instance the two-qubit gate entering in the Shor's algorithm are the controlled gates (C-NOT or C-phase), and the implementation of a C-not gate with a combination of the $\sqrt{SWAP}$ and single qubit rotations requires 5 steps. Considering two tunnel coupled quantum dots, each occupied with a single electron spin, it has been demonstrated theoretically [10] that a difference in the local Zeeman splitting ΔB_z between the two quantum dots can be exploited to realize a controlled phase gate (C-phase). Especially the natural two-qubit gate for single spin qubits evolves from the SWAP gate at $\Delta B_z = 0$ to the C-phase gate at larger ΔB_z. Here we propose to study experimentally the effect of a finite gradient ΔB_z on the SWAP operation. By using dynamical nuclear polarization [11], we are able to generate a gradient ΔB_z up to 20mT. This study allows us to study experimentally the feasibility of a C-phase gate with single spin qubits, and to give a value of a controlled $\pi-$phase gate duration.

Finally instead of using a spin qubit as an information carrier, we tried to use it as a very

sensitive electrostatic detector. A Singlet-Triplet qubit is a quantum system where the two quantum levels can be tuned on fast timescales from a charge-like to spin-like qubit. Whereas the qubit is highly sensitive to the electrostatic environment and characterized by timescales as fast as few hundreds of picoseconds in the charge regime, the information stored in the qubit in the spin regime can be preserved for a time longer than few hundreds of microseconds [12]. This gives seven orders of magnitude between the two important quantities of a quantum detector: time of interaction and time to keep the information. It allows for interacting strongly for a very short time with a single electron, storing the resulting effect on the population of the two-level system for a time sufficiently long [13] and reading-out single shot the state of the qubit with fast charge detection [14]. Therefore we will study the use of such a qubit in order to detect the passage of electrons transported in edge-states next to the qubit detector. We will see that this device should be able to detect the passage of a single electron next to the quantum dot, opening the way toward single electron detector for quantum optics experiments with electrons.
Before entering in the details of these results, we will introduce general concepts related to quantum dot systems. We tried to give all the "ingredients" needed to understand the further discussions. Finally we will conclude about the perspectives following these results.

Bibliography

[1] Kouwenhoven, L. P., Austing, D. G., and Tarucha, S. *Reports On Progress In Physics* **64**(6), 701–736 June (2001). i

[2] Feynman, R. P. *International Journal of Theoretical Physics* **21**(6-7), 467–488 (1982). ii

[3] Hermelin, S., Takada, S., Yamamoto, M., Tarucha, S., Wieck, A. D., Saminadayar, L., Baeuerle, C., and Meunier, T. *NATURE* **477**(7365), 435–438 SEP 22 (2011). ii, 49

[4] McNeil, R. P. G., Kataoka, M., Ford, C. J. B., Barnes, C. H. W., Anderson, D., Jones, G. A. C., Farrer, I., and Ritchie, D. A. *NATURE* **477**(7365), 439–442 SEP 22 (2011). ii, 49

[5] Golovach, V. N., Borhani, M., and Loss, D. *Physical Review A* **81**(2), 022315 February (2010). ii, 29, 49

[6] San-Jose, P., Scharfenberger, B., Schoen, G., Shnirman, A., and Zarand, G. *Physical Review B* **77**(4), 045305 January (2008). ii, 29, 49

[7] Elzerman, J. M., Hanson, R., van Beveren, L. H. W., Witkamp, B., Vandersypen, L. M. K., and Kouwenhoven, L. P. *Nature* **430**(6998), 431–435 July (2004). ii, 4, 17, 119, 154

[8] Koppens, F. H. L., Buizert, C., Tielrooij, K. J., Vink, I. T., Nowack, K. C., Meunier, T., Kouwenhoven, L. P., and Vandersypen, L. M. K. *Nature* **442**(7104), 766–771 August (2006). ii, 19

[9] Petta, J. R., Johnson, A. C., Taylor, J. M., Laird, E. A., Yacoby, A., Lukin, M. D., Marcus, C. M., Hanson, M. P., and Gossard, A. C. *Science* **309**(5744), 2180–2184 September (2005). ii, 101, 102

[10] Meunier, T., Calado, V. E., and Vandersypen, L. M. K. *Phys. Rev. B* **83**, 121403 Mar (2011). ii, 12, 23, 79, 98, 99, 108, 114, 119

[11] Foletti, S., Bluhm, H., Mahalu, D., Umansky, V., and Yacoby, A. *Nature Physics* **5**(12), 903–908 December (2009). ii, 26, 89, 101, 102, 104, 106, 108

[12] Bluhm, H., Foletti, S., Neder, I., Rudner, M., Mahalu, D., Umansky, V., and Yacoby, A. *Nature Physics* **7**(2), 109–113 February (2011). iii, 26, 27, 69, 89, 101

[13] Shulman, M. D., Dial, O. E., Harvey, S. P., Bluhm, H., Umansky, V., and Yacoby, A. *SCIENCE* **336**(6078), 202–205 APR 13 (2012). iii, 129, 131

[14] Barthel, C., Reilly, D. J., Marcus, C. M., Hanson, M. P., and Gossard, A. C. *Phys. Rev. Lett.* **103**, 160503 Oct (2009). iii, 131

Chapter 1

General concepts

Résumé

Dans ce chapitre nous présentons quelques concepts généraux relatifs aux boîtes quantiques latérales basées sur des hétérostructures d'arséniure de gallium. Ces hétérostructures semiconductrices présentent la particularité de posséder un gaz d'électrons bidimensionnel à environ 100nm de la surface. Un puits de potentiel électrostatique peut être généré au sein de ce gaz à l'aide de tensions appliquées à des grilles métalliques disposées à la surface de l'échantillon. Des électrons du gaz se retrouvent piégés dans ce puit de potentiel, leur mouvement étant alors confiné dans les trois dimensions. Un tel dispositif est communément appelé une boîte quantique. Nous profitons de ce chapitre pour décrire les propriétés générales de tels objets.
Dans un premier temps, nous étudierons les propriétés liées à la charge des électrons. Par un développement classique (électrostatique) on peut démontrer que les états de charge d'une boîte quantique sont une collection de potentiels électrochimiques, séparés en énergie par l'énergie de charge. Cette énergie est relative à un concept purement classique et correspond à l'énergie qu'il faut fournir pour ajouter un électron à la boîte quantique. Par la suite nous introduirons les notions quantiques de couplage tunnel et d'énergie orbitale. Par ailleurs nous accorderons une grande importance sur la mesure expérimentale de ces états de charge, en étudiant les mesures de transport électronique ainsi que les mesures de détection de charge.
Après avoir abordé le degré de liberté de charge de l'électron, nous nous intéresserons plus en détail à son spin. Nous étudierons les états de spin à 1 et 2 électrons. Dans les systèmes de boîtes quantiques latérales, la mesure directe d'un spin électronique étant difficile, la notion de conversion spin-charge, qui permet la mesure d'un spin électronique unique en mesurant son état de charge, sera introduite. Nous profiterons de cette partie pour détailler un peu plus en détail les notions de relaxation et de décohérence relatives à tout état quantique.
Pour finir, afin de rappeler que la boîte quantique n'est pas un objet isolé du reste du monde, nous introduirons deux interactions qui relient les électrons piégés dans des boîtes quantiques à leur environnement. L'interaction hyperfine entre les spins électroniques et les spins nucléaires ainsi que le couplage spin-orbite reliant le degré de liberté de charge à celui de spin seront détaillés.

Introduction

For the last few decades, the technologies related to semiconductors gave physicists access to new kind of systems, that have been intensely used to study the theoretical predictions of modern physics. For instance high electron mobility transistors (HEMTs) embedded in a two dimensional electron gas (2DEG), and the use of such devices led to the discovery of the quantum hall effect by von Klitzing and co-workers in 1980 [1].
In addition such semiconducting devices can be used to make a lateral quantum dot. It consists of isolating few electrons, and even a single one, in an electrostatic trap. Such a system allows for studying the physic of a single electron, and its degrees of freedom, like its charge or its spin. Physicists took this reasoning further by thinking about the possibility to use a single electron spin to encode information, and to build what is called a quantum bit (spin qubit) [2]. This qubit would be the elementary block of a quantum computer, which should allow to solve mathematical problems like the factorization of an integer into prime numbers or the travelling salesman problem, and to simulate a quantum system [3].
Before discussing about the manipulation of an electron spin in quantum dots, some general concepts related to the physic of such devices will be presented. The way to isolate a single electron in an electrostatic potential, the resulting charge and spin states have to be introduced in order to go further in the understanding of these systems. Nonetheless when a single electron spin is trapped in a quantum dot, it is not totally isolated from the rest of the "world". Two main interactions (hyperfine and spin-orbit interactions) will retain our attention and we will discuss about those at the end of this chapter.

1.1 Laterally defined quantum dots

In quantum dot systems, the motion of an electron is confined along the three dimension. It can be seen as a small island of electrons, isolated from the other electrons (the reservoir) through tunnel barriers. There are several ways to achieve it. Self-assembled quantum dots or carbon nanotubes (CNT) can be used. In these cases, the confinement is intrinsic to these objects. But if they effectively present the expected behaviour of a quantum dot, they may not be tuned as desired. For instance, the tunnel barrier separating the CNT quantum dot and the reservoirs is usually defined by the contact electrode between the substrate and the CNT. As we will see in the following, these tunnel barriers are crucial concerning the electron spin dynamic. For example, take the process of spin relaxation, which allows for an excited spin state to return back in the ground state. This process can be seen as a loss of information, which is not desired. And it is largely dependent on the coupling between the quantum dot and its reservoir(see chapter 4). Indeed the electron spin in the excited state can be exchanged with one from the reservoir in

order to relax in the ground state.
In contrast to these not very tunable systems, a heterostructure containing a 2DEG (Figure 1.1 (a)) can be used. In this way the motion of the electron is first intrinsically confined in a plane. To ensure the confinement in the others two dimensions, a trapping potential can be generated thanks to voltages applied on metallic gates. If the gate geometry has been designed cleverly, the tunability of such quantum dot is generally important, meaning that by changing the gate voltages, the quantum dot characteristics can be tuned. For instance the tunnel rate between a lateral quantum dot and its reservoir can be tuned from more than $1s^{-1}$ to less than $1ns^{-1}$. In addition, it allows to create multiple quantum dot devices, where several quantum dots are coupled to each other through tunnel barriers.
All the quantum dot devices measured in this thesis are fabricated from silicon(Si) doped GaAs/AlGaAs heterostructures. These heterostructures are made of different semiconducting layers stacked in a specific way. These layers are grown on top of each other by molecular beam epitaxy (MBE). A specific sequence of stacking leads to a particular band structure (Figure 1.1 (b)) which gives rise to the formation of a 2DEG. Indeed, around 100nm below the surface, the conduction band goes below the Fermi energy, which results in the confinement of the electrons in a plane, the 2DEG. The 2DEG is usually separated about 20 nm from the AlGaAs donor region by an undoped spacer layer. This separation allows for extremely high mobility of the electrons in the 2DEG, because scattering with the Si donors is strongly reduced. At liquid helium temperature, i.e 4.2 K, the typical electron mobility and electron density are $10^5 - 10^6 cm^2.V^{-1}.s^{-1}$ and $10^{11} cm^{-2}$ respectively. The relatively low electron density results in a large Fermi wavelength, $\lambda_F \sim 50nm$, and a large screening length, which allows to locally deplete the 2DEG with an electric field (orange part in figure 1.2). The Fermi wavelength gives the relevant scale at which the potential landscape seen by the electrons will have to be modelled in order to see quantum effects appear.

Electric fields can be generated by applying a negative voltage on the metal gates electrodes deposited on the surface of the heterostructure (yellow parts in figure 1.2). The Schottky barrier formed at the metal-semiconductor junction ensures that no charges leak into the heterostructure. The coupling between the gate and the electron gas is then purely capacitive. By designing a proper geometry of gates, a confinement potential can be engineered, and consequently a small "island" of electrons (dark blue part in figure 1.2) is isolated from the rest of the gas (light blue part in figure 1.2) by tunnel barriers. Ohmic contacts enable to make electrical contact with the 2DEG and to measure the devices. These contacts are made of an alloy of metallic components (Ni, Ge, Au) which can diffuse from the surface to the 2DEG during an annealing process. In addition the gate geometry can be made more complex in order to form several coupled quantum dots. Moreover changing one of the gate voltages leads to a modification of the electrostatic energy of the system. For instance making these voltages more negative tends to reduce the typical size of the potential. Therefore it increases the electrostatic energy of the system and as

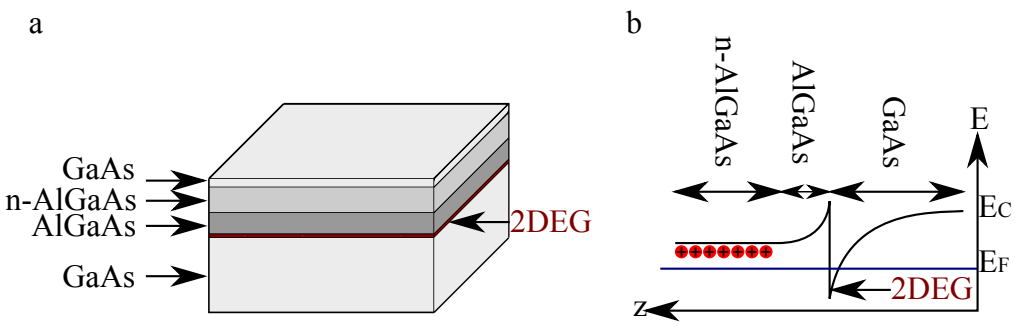

Figure 1.1: **GaAs/AlGaAs heterostructure and 2DEG (Two dimensional electron gas). (a)** Scheme of the stack of semiconductor layers used for the heterostructure. **(b)**Band structures of the heterostructure. 100nm below the surface, the conduction band goes below the Fermi Energy, giving rise to the 2DEG.

a consequence the number of electrons populating it decreases. The control of the charge degree of freedom of a quantum dot is therefore crucial in order to be able to let just a single electron inside, and it implies to go through the understanding of the charge states in quantum dot systems.

All along this chapter, the different physical concepts will be introduced by considering only a single quantum dot. The case of multiple quantum dots will be introduced later, and by using the same approach which will be develop in the following.

1.2 Charge states in a single quantum dot

From an experimental point of view, the only information that we can extract from a GaAs/AlGaAs quantum dot is its charge state. In certain configurations, it allows to know its spin state by using the spin-to-charge conversion technique [4]. The understanding of the charge states is therefore of importance. As it will be detailed in the following, the confinement of the electrons gives rise to a particular energy spectrum. Indeed the Coulomb repulsion between the electrons implies that an energy has to be paid in order to add an electron into the quantum dot. Due to this requirement the charge states of a quantum dot become discrete and we generally deal with electrochemical potential states. In addition the typical size of the trapping potential is of the same order of magnitude as the Fermi wavelength of the electrons. It gives rise to quantum effects, like the concept of single particle states, representing the notion of orbital states in an atom. Although these quantum effects have to be taken into account to get a full picture of the quantum dot physics [5], a simpler classical model (Constant Interaction (CI) model) is generally sufficient to describe its behaviour.

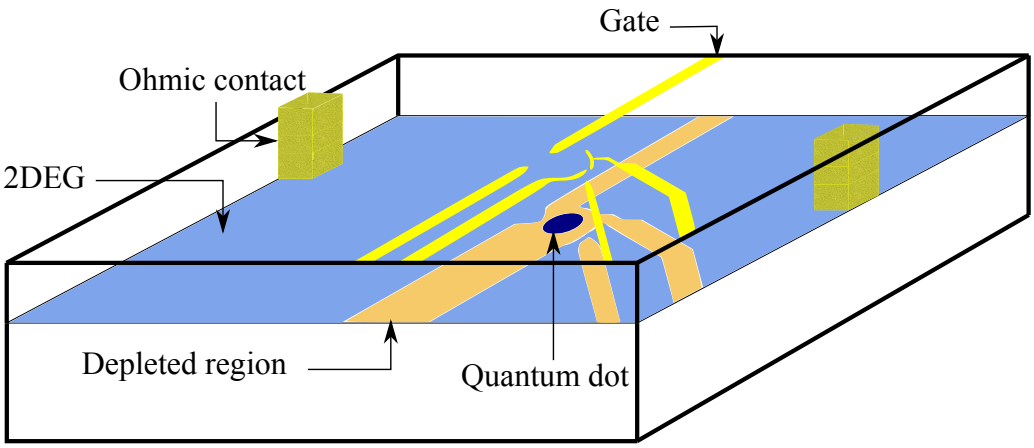

Figure 1.2: **Schematic view of a quantum dot device.** Negative voltages applied to the metal gates (yellow) lead to depleted regions (orange). With a proper gate geometry, a confinement potential can be engineered. A small island of electron (dark blue) is then isolated from the rest of the gas (light blue) via tunnel barriers. Ohmic contacts enable to make electrical contact with the 2DEG.

1.2.1 Constant Interaction model

The use of a "simple" electrostatic model to describe a system made of quantum dots turns out to be quite powerful especially in the case of several quantum dots interacting together (see chapter 3). In addition it allows for the introduction of important concepts like the charging energy or the electrochemical potential. Here we consider a single quantum dot. Its electrostatic energy is controlled thanks to a gate voltage (V_{g1}). Moreover it is coupled to a Fermi sea (a reservoir) (figure 1.3 (a)). In the CI model, this coupling is purely capacitive (classical physics). In reality a tunnel barrier couples the reservoir with the quantum dot, allowing an exchange of electrons between them. We notice that we chose to study the easiest system : a single quantum dot coupled to a single reservoir. But as we will see, in order to probe this quantum dot by transport measurement, we need to couple two reservoirs to the quantum dot. It doesn't change anything to the following discussion, and this is why we chose in a first time to simplify as much as we can the system.

The constant interaction (CI) model (Figure 1.3 (b)) relies on two major assumptions[6]:

- The Coulomb interaction between the electrons in the quantum dot and the ones in the reservoirs and the gates are modelled by a single capacitance C_1. This capacitance is therefore the sum $C_1 = C_g + C_R$ where $C_g = \sum_i C_{gi}$ is the sum of the electrostatic capacitances between the quantum dot and each gates i. C_R is the

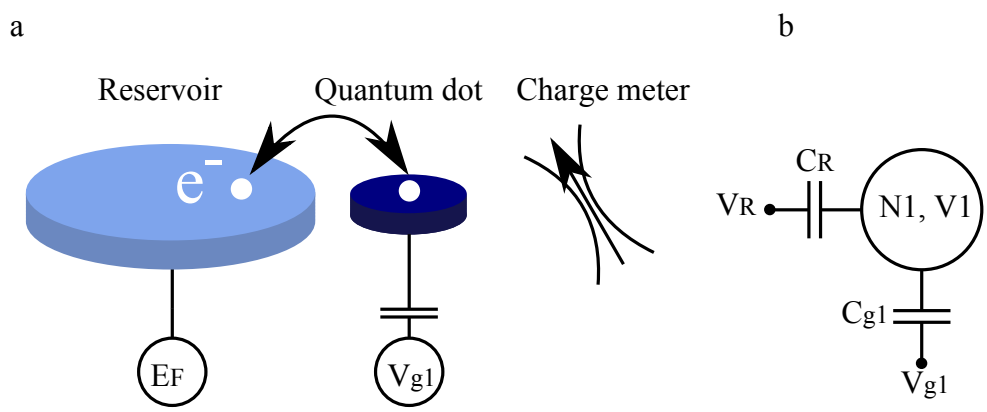

Figure 1.3: **Single quantum dot.** **(a)**Schematic view of a single quantum dot. It is coupled to a Fermi sea at energy E_F. Its energy can be controlled thanks to a gate voltage V_{g1}, and therefore it can exchange electrons with the reservoir. Moreover a charge meter can be capacitively coupled to the quantum dot. **(b)** CI model of a single quantum dot device.

capacitance between the quantum dot and the rest of the gas (the reservoir).

- The discrete energy spectrum is independent on the number of the electrons present in the quantum dot.

The electrostatic energy of the quantum dot can be written as

$$U = -\frac{1}{2}C_1V_1^2 \tag{1.1}$$

where $C_1 = C_{g1} + C_R$ (we intentionally omitted the capacitance of all the gates by considering only one of them) is the total capacitance coupled to the quantum dot, and V_1 is the electrostatic potential of the quantum dot. The number of charges N_1 on the quantum dot can be written as the sum of the charges on all the capacitors connected to:

$$\begin{aligned} -N_1e &= C_{g1}(V_1 - V_{g1}) + C_R(V_1 - V_R) \\ C_1V_1 &= -N_1e + C_{g1}V_{g1} + C_RV_R \end{aligned} \tag{1.2}$$

By substituting V_1 (Equation 1.2) into the equation 1.1, we get :

$$U(N,V_{g1}) = \frac{[-N_1e + C_RV_R + C_{g1}V_{g1}]^2}{2C_1} \tag{1.3}$$

For N_1 fixed, the electrostatic energy U is a parabola with respect to the gate voltage V_{g1} (Figure 1.4). Starting from the very negative gave voltage region ($V_{g1} \to -\infty$),

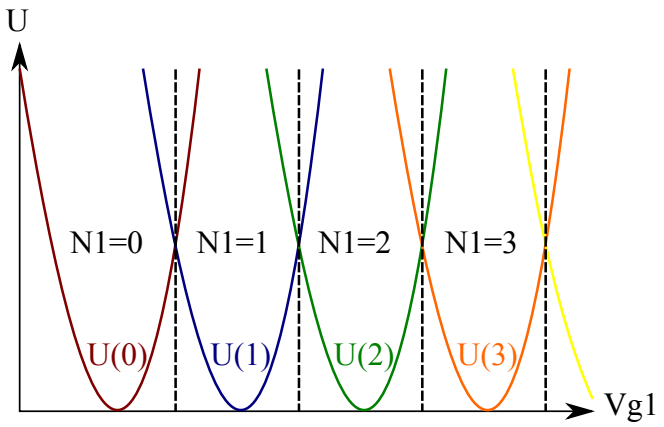

Figure 1.4: **Electrostatic energy of a single quantum dot** with respect to the gate voltage V_{g1} for different values of the number of charges in the quantum dot N_1

the value of N_1 minimizing U is 0, and therefore the quantum dot is empty. Now by increasing V_{g1}, $U(N_1 = 0, V_{g1})$ can be made equal to $U(N_1 = 1, V_{g1})$. The two "charge states" $N_1 = 0$ and $N_1 = 1$ are then degenerate. At this value of V_{g1}, an electron is exchanged between the reservoir and the quantum dot through the tunnel barrier separating them. For larger V_{g1}, the charge state $N_1 = 1$ becomes the ground state until $U(N_1 = 1, V_{g1}) = U(N_1 = 2, V_{g1})$, etc... It defines, in the gate voltage parameter space, regions where the number of electrons in the quantum dot is fixed (in figure 1.4 these regions are separated by dashed lines), that is to say, the charge ground state for each value of V_{g1}.

To describe these charge states, the use of the electrochemical potential is of direct relevance. The electrochemical potential $\mu(N1, V_{g1})$ is defined as the energy needed to add the N_1^{th} electron to the quantum dot and it comes as (we assume $V_R = 0$) :

$$\begin{aligned} \mu(N_1, V_{g1}) &= U(N_1) - U(N_1 - 1) \\ &= (N_1 - \frac{1}{2})E_C - \frac{C_{g1}}{C_1} eV_{g1} \end{aligned} \tag{1.4}$$

We introduced here $E_C = \frac{e^2}{C_1}$, the so-called charging energy. The number of electrons populating the quantum dot for a fixed value of gate voltage V_{g1} corresponds to the largest N_1 leaving $\mu(N_1) < 0$. In addition the electrochemical potential changes linearly with respect to the gate voltage V_{g1} with a proportional factor $\alpha = \frac{C_{g1}}{C_1}$. This factor called the α-factor or gate lever arm is related to the conversion of the gate voltage into the energy ($V \longleftrightarrow \alpha eV$). Furthermore the addition energy $\Delta\mu(N_1)$ can also be introduced. It corresponds to the energy separating two charge states :

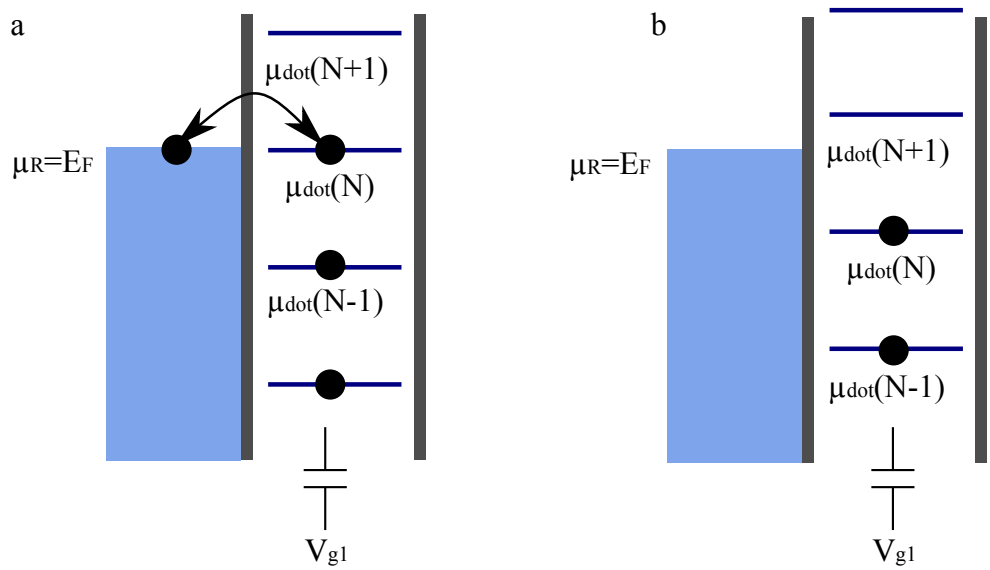

Figure 1.5: **Electrochemical potential of a single quantum dot.(a)**By changing the gate voltage V_{g1} the electrostatic energy of the system can be changed in order to set an electrochemical potential state in resonance with the one of the reservoir set at E_F. An electron is then exchanged between the quantum dot and the reservoir. **(b)** When no level is in resonance, the number of electrons in the quantum dot is fixed.

$$\begin{aligned} \Delta\mu(N_1) &= \mu(N_1+1) - \mu(N_1) \\ &= E_C = \frac{e^2}{C_1} \end{aligned} \tag{1.5}$$

We remind that this model is a purely classical one, which does not take into account any quantum effects. Consequently the origin of the addition energy is hence electrostatic, classical. As we will see afterwards, the quantum effects give rise to a slightly different addition energy.

The electrostatic energy of the quantum dot, i.e its electronic population, can be controlled by changing the gate voltage V_{g1}. In particular one level of electrochemical potential can be set in resonance with the one of the reservoir. An electron is then exchanged between the quantum dot and the reservoir via a tunnel barrier (Figure 1.5 (a)). The number of electrons into the quantum dot is fluctuating between N and $N-1$. If no level is in resonance, the number of electrons is fixed, protected by the charging energy (Figure 1.5 (b)). This is the so-called Coulomb blockade.

In conclusion the charge state spectrum of a single quantum dot is a collection of electrochemical potential level separated by the charging energy E_C. This energy depends

linearly on the capacitance $C_1 = C_{g1} + C_R$, and scales with $\frac{1}{d}$, where d is the size of the quantum dot. A typical size of a quantum dot is 40nm giving a charging energy $E_C \sim 1meV$. This energy is equivalent in the temperature scale to 10K. It fixes some experimental constraints on the working temperature to avoid any thermal excitations, and the techniques used to work at low temperature will be introduced in the next chapter.

1.2.2 Quantum effects in quantum dot systems

Until now, only classical physics has been used to describe the charge state of a quantum dot. Due to Coulomb repulsion and confinement, the charge states of a quantum dot become discrete and separated by the charging energy E_C. The confinement gives also rise to particular quantum effects. The typical quantum dot size (the size of the electrostatic potential, $d \sim 40nm$) is in the same order of magnitude than the Fermi wavelength of the electron ($\lambda_F \sim 50nm$). Then the electrons cannot be considered only as particles, but their wave-like behaviour has to be taken into account. It gives rise to the concept of single particle states, the equivalent of the orbitals in an atom. Consequently electrons occupy orbital states describing their wave-like behaviour and due to Pauli principle, each of these orbital state has to be filled with at maximum one electron (two if we take into account the spin degree of freedom). Then the addition energy is now written as :

$$\Delta\mu(N_1) = E_C + E_{N+1} - E_N = \frac{e^2}{C} + \Delta E \tag{1.6}$$

where E_N is the topmost filled single particle state for an N electron quantum dot. ΔE is called the orbital energy, and scales with $\frac{1}{d^2}$. Indeed the single particle states can be considered as being the ones of an harmonic oscillator $E_n = \hbar\omega(n + \frac{1}{2})$, where $n \in \mathbb{N}$. The frequency ω of this oscillator is related to the typical size of the potential by the formula $d = \sqrt{\frac{\hbar}{m\omega}}$ (m being the electron mass), and therefore $E_n \propto \frac{\hbar^2}{m\,d^2}$. For $d \sim 40nm$ it is roughly equal to $\sim 500\mu eV$. As it will be shown later, we take advantage of this orbital energy to measure spin states in a double quantum dot system.
Another quantum effect already briefly mentioned is the tunnel effect. Indeed a quantum dot can be seen as an island of electrons isolated from the rest of the 2DEG (reservoirs) through tunnel barriers. The transmission of these barriers determines the rate at which an electron occupying the quantum dot can be exchanged with one from the reservoir. In the context of quantum information, if there is such exchange, the information encoded into the spin (or the charge) of this electron will be obviously lost. Consequently we need to be able to perform spin manipulations faster than this exchange process. This process is obviously limited by the tunnel coupling between the quantum dot and the reservoir, a thin (thick) barrier giving rise to fast (slow) relaxation. The purpose of this thesis being the use of a quantum dot as a spin qubit, it involves sufficiently thick tunnel barriers. On the other hand, as it will be explained in the fourth chapter, this process is also used

in order to initialize the spin state of the system. Then a compromise has to be found between a thick barrier which protects in a better way the spin information, and a thin one, allowing faster initialization.

We will now introduce two ways to probe the charge state of quantum dot system :

- Transport measurements which consists of studying the current flowing through a quantum dot
- QPC measurements by using a charge detector capacitively coupled to a quantum dot

1.2.3 Transport measurements

One of the experimental methods to probe these charge states involves studying the current through a quantum dot in response to a bias voltage excitation across it. We consider a single quantum dot (dark blue in figure 1.6 (a)) coupled to two Fermi seas (reservoirs) pinned at two different energies, resulting from the bias excitation. The gate geometry of the sample will be described in details later (chapter 4). Here we just assume the possibility to engineer a confinement potential coupled to two reservoirs. They are called the source and the drain and $-eV_{SD} = \mu_S - \mu_D$, where μ_S (μ_D) corresponds to the electrochemical potential of the source (drain). Contrary to what we have seen before, here in order to perform transport across the quantum dot, it is coupled to two reservoirs. We assume that $|eV_{SD}|$ is relatively small ($\sim 100\mu eV$) in comparison with the energy scales of the system (the charging and orbital energies E_C, ΔE). This assumption ensures that the transport through the quantum dot is always made through the charge ground state (linear transport). The electrostatic energy of the quantum dot can be controlled by using the gate voltage V_{g1}, allowing to change the charge state of the system. This charge state is probed by measuring the current passing through the quantum dot as a response to the voltage bias excitation.

As it has been seen, the energy spectrum of a quantum dot is a collection of discrete electrochemical potential states. Then two distinct cases are possible (Figure 1.6 (b)) :

- One level of the electrochemical potential, for instance $\mu_{dot}(N)$, is aligned to the bias window. Then an electron can tunnel from the source to the drain through the quantum dot by two sequential tunnelling processes. The experimental signature is a non vanishing current across the quantum dot. In this situation, the number of electrons on the quantum dot is not fixed. It fluctuates between N and $N-1$.
- Now, starting from the previous situation, let us imagine that we change the gate voltage V_{g1} in order to set $\mu_{dot}(N) < \mu_D$ and $\mu_{dot}(N+1) > \mu_S$. In this case, no state are aligned in the bias window, and no current can flow through the quantum

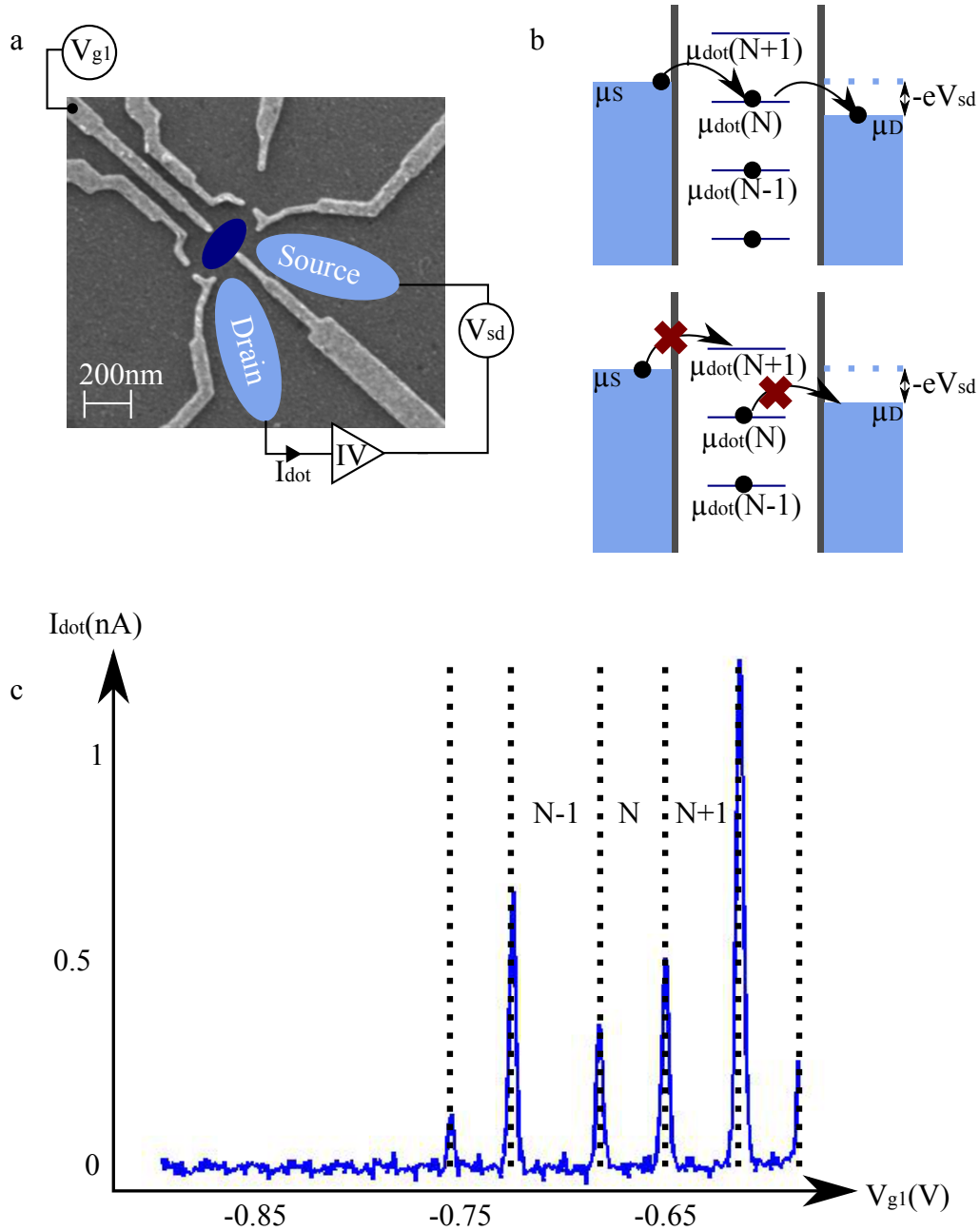

Figure 1.6: **Transport measurement of a single quantum dot.(a)**SEM (scanning electron microscopy) picture of the quantum dot device. The quantum dot (dark blue) is coupled to two Fermi seas (reservoirs), the source and the drain, and a bias voltage V_{SD} is applied between them. The current flowing through the quantum dot is collected and amplified by an IV-converter (see chapter 2). **(b)**Top : if one level of chemical potential is aligned into the bias window, electrons can flow from the source to drain by tunnelling through the quantum dot. A current is then measured. Bottom : if no level is included in this bias windows, the electron are Coulomb blockaded, and no current flows through the device. **(c)** Experimental realization of a transport measurements. The bias voltage has been set to $V_{SD} = 100\mu eV$, and a series of Coulomb peaks is clearly observed.

dot (at least to the first order). This is the so-called Coulomb blockade, and the number of electrons is fixed to N.

By studying the current across the quantum dot as a function of the gate voltage V_{g1}, a collection of current peaks (Coulomb peaks), is obtained (Figure 1.6 (c)). Between two peaks no current flows through the system, the number of electrons is well defined, and the charge state corresponds to the electrochemical potential $\mu_{dot}(N)$ with the greatest N leaving $\mu_{dot}(N) < \mu_D$. On a Coulomb peak, one electrochemical potential of the quantum dot is aligned in the bias windows. In this case, the number of electrons fluctuates between N and $N+1$, and the ground charge state of the system is not well defined, fluctuating between $\mu_{dot}(N)$ and $\mu_{dot}(N+1)$.
We can distinguish two main regimes of tunnelling between the quantum dot and its reservoirs, the weak and strong tunnelling. In order to use a quantum dot as a qubit, we want to preserve it from the environment, therefore the tunnel barrier between the quantum dot and the reservoirs are generally used in the weak tunnelling regime. In this case, the amplitude and the shape of these peaks depend on the parameters of the system, such as the tunnel barriers or the temperature. For instance the amplitude depends on the two tunnel barriers separating the quantum dot with the drain and the source. The passage of a single electron is a sequence of two tunnel processes. So the current flowing through the quantum dot is limited by the smallest tunnel rate. Moreover the shape of the peaks depends on the electron temperature. A finite temperature tends to broaden the Coulomb peaks due to the Fermi distribution of the electrons in the reservoir. But this technique has however some limitations, as we will see below, and has not been used intensively in this thesis.
Indeed the limitations of the transport measurement are due to its very nature : the signal corresponds to a current flowing through the quantum dot system. For instance let us consider the measurement of the spin relaxation of one electron spin in a single quantum dot (we remind that the relaxation is a process leading to the decay of an excited state into the ground state). The typical relaxation time in a single quantum dot is of the range of $T_1 \sim 1ms$ [7]. We will detail later the principle of spin measurement in quantum dot systems, and here we just assume that the electron is allowed to leave the quantum dot if its spin state is the ground state. Therefore we see directly with this example that the current generated by such a measurement is quite small ($I \sim 0.1fA$). In addition in order to perform spin manipulations in quantum dots, we need to be able to reach the few electron regime, where only one electron remains trapped in the quantum dot. And in this regime, the tunnelling rate Γ is relatively small, or approximatively $\Gamma \sim 10^4 s^{-1}$. As we have briefly said, the current flowing through the quantum dot depends on the tunnel barriers. With a tunnel rate equal to $\Gamma \sim 10^4 s^{-1}$, the expected current is $I_{dot} \sim 1fA$ (in the linear regime, only one electron can flow trough the quantum dot). In comparison to the noise in the output of the amplifier ($\sim 10fA/\sqrt{Hz}$, see chapter 2), it implies that the bandwidth of the measurement chain should be lowered. For instance, to get a signal to

noise ratio equal to 10, we need to reduce the bandwidth at 10^{-4}Hz in order to observe a signal equal to 1fA. In other words, although technically feasible, the use of such a measurement technique to probe the charge state of a few electron quantum dot is not really appropriate. For these limitations, we mainly employed the charge detection and we will now describe this technique.

1.2.4 Charge detection

The commonly used technique to detect the last electron leaving the quantum dot relies on the high sensitivity of QPCs (Quantum Point Contact) with regard to their electrostatic environment [8]. A QPC is a short one dimensional channel for the electrons (Figure 1.7 (a)). This small channel can be engineered by using two gates, and by applying a negative voltage V_g^{QPC} on it. When the width of this channel becomes comparable to the Fermi wavelength of the electron, the latter have to flow through the laterally quantized modes of the QPC potential. The QPC exhibits then plateaux of conductance, which are an integer multiple of $\frac{2e^2}{h}$. These plateaux correspond to an integer number of open conducting quantum channels through the QPC (we notice that $\frac{2e^2}{h} = (12.9k\Omega)^{-1}$). Since the QPC conductance varies fast with respect to the gate voltage V_g^{QPC} between these plateaux, the QPC is therefore highly sensitive to the electrostatic environment, and in particular to the number of charges present in the quantum dot. To be able to detect these charges, we tune the V_g^{QPC} to set the QPC where the sensitivity is the highest, generally between the last plateau and the "0" conductance (inset Figure 1.7 (b)). The QPC is biased with a voltage around $V_{QPC} \sim 500\mu V$, and the current flowing through it is collected and amplified by an IV-converter (Figure 1.7 (a)). The larger is the bias voltage V_{QPC}, the larger will be the signal. But the QPC back-action on the system has to be taken into account. Indeed it has been demonstrated [9, 10] that the QPC noise can influence the state of the quantum dot. Indeed the QPC can emit photons with energy up to the bias voltage. Consequently V_{QPC} has to be kept below the charging energy $E_C \sim 1meV$ and the orbital energy $\Delta E \sim 500\mu eV$.
In comparison with the previous measurement, here the reservoirs coupled to the quantum dot are all biased with the same voltage V_R. Consequently the quantum dot can be considered as being coupled to a single reservoir with the Fermi energy defining by the voltage V_R. The typical response of the QPC to a change of V_{g1} can be seen in figure 1.7 (c). Two effects are observed on the conductance of the QPC. First by changing V_{g1} the electrostatic environment of the QPC is directly changed, and this effect is the so-called cross talk between the gate and the QPC. It results in a mean slope of the current I_{QPC} with respect to V_{g1}. On the other hand, by making V_{g1} more and more negative, electrons are pushed outside the quantum dot. Each time the electronic population of the quantum dot decreases (increases) by one, the conductance of the QPC increases (decreases). This results in steps in the QPC current clearly observed in figure 1.7 (c). In order to emphasize the signal, the QPC current I_{QPC} can also be derived with respect

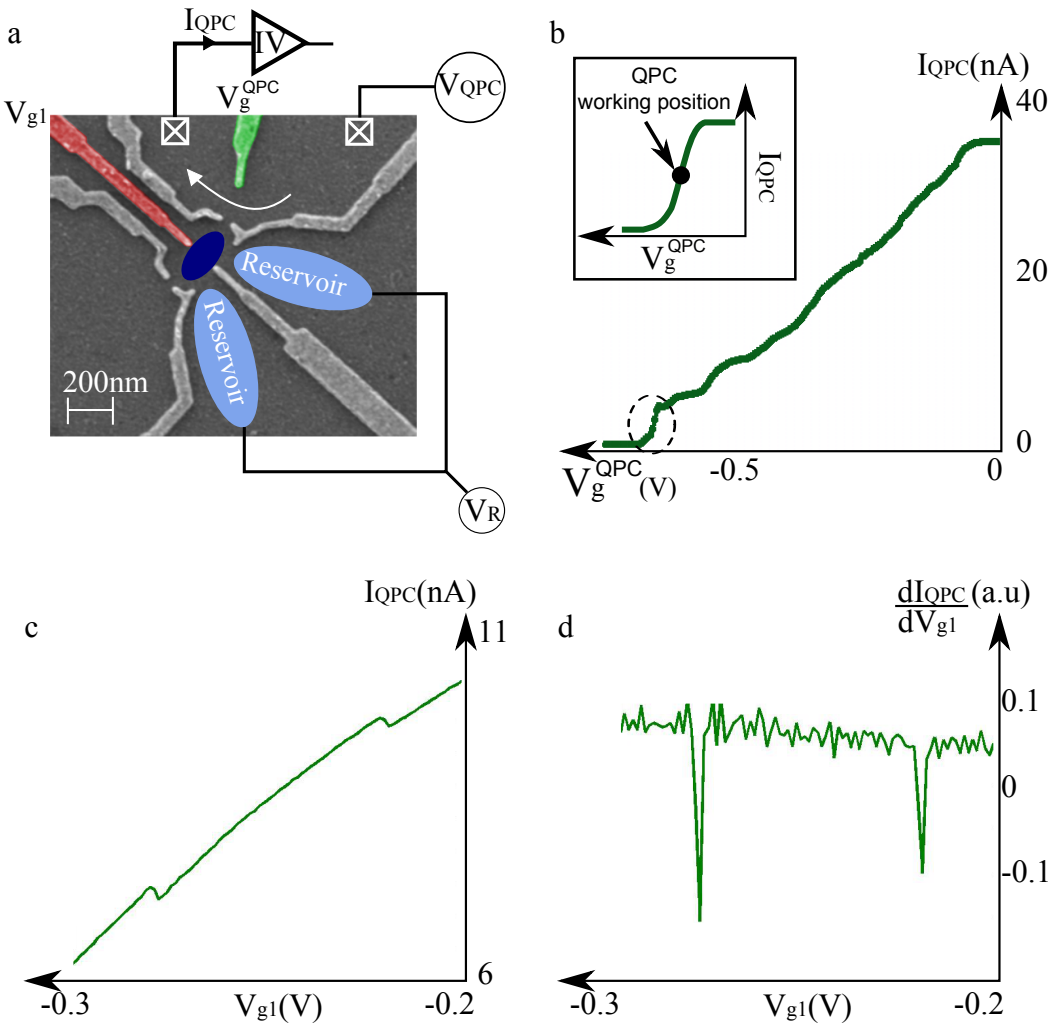

Figure 1.7: **Charge detection.(a)**SEM (scanning electron microscopy) picture of the quantum dot device. The quantum dot (dark blue) is coupled to a reservoir (actually the quantum dot is coupled to two reservoirs, but they are both voltage biased at V_R, and they can therefore be considered as a single reservoir). By using an additional gate in close vicinity of the quantum dot, a channel can be designed and be capacitively coupled to the quantum dot. Its conductance is directly linked to the electrostatic environment, and hence to the number of electrons in the system. **(b)** The conductance of the QPC can be measured by measuring the current flowing through the QPC I_{QPC} in response to a voltage bias excitation V_{QPC} (here the voltage bias has been set at $V_{QPC} = 500\mu eV$. The region where the QPC is the most sensitive is just after the last conductance plateau. In this configuration, the channel is generally more coupled to the quantum dot and its sensitivity is maximum. Inset : The working position of the QPC between the last plateau and the zero conductance. **(c)** Signal of the QPC when the gate voltage V_{g1} is swept. Some steps indicating exchange of electrons with the reservoir are clearly seen. **(d)** Derivative of I_{QPC} with respect to V_{g1}.

to the gate voltage V_{g1}. In this case a change of the electronic population is represented by a peak (Figure 1.7 (d)). These current steps depend obviously on the parameters of the system, and especially on the tunnel barriers with the reservoirs. For a weak (strong) tunnel coupling, these current steps will be quite sharp (smooth), resulting from the tunnel coupling between the quantum dot and the reservoir.
In addition, as it will be shown in the following, a single QPC can probe the electronic population of multiple coupled quantum dots [11, 12, 13]. Indeed the capacitive coupling between the QPC and a quantum dot depends on their distance. For a multiple quantum dot system, the distance between each quantum dot and the QPC is different giving a different signal when the electronic population of the quantum dots changes. In addition, in comparison with the transport measurement scheme, the charge detection allows to probe the last electron leaving the quantum dot, and this will turn out to be crucial in order to perform spin manipulations. But before considering such manipulations, we will discuss a little about the physics of spins in quantum dot systems.

1.3 Spins in quantum dots

Until now we mainly discussed about the charge of an electron in a quantum dot. We can therefore imagine to use this degree of freedom to build a quantum bit (qubit). For instance, this qubit can be made of two coupled quantum dots containing a single electron. The two states of the qubit would be $|R\rangle$ ($|L\rangle$), the electron being in the right (left) quantum dot. The main problem with such qubits is the short coherence time (it corresponds to the time during which the phase information of a superposition of state can be conserved and it will be explained in the following) [14, 15, 16]. The rather-short coherence time ($\sim 1ns$) is mostly due to the charge noise in the system. The answer to this issue can be found in the other degree of freedom of the electron : its spin. At a first glance, the dynamic of the electron spin is totally decoupled from the one of the charge. In other words, these two degrees of freedom belong to two distinct subspaces, and as a results the spin is not coupled to the electrical fluctuations. Consequently the charge noise should not affect the spin, and therefore its coherence time should be much larger than the one of the charge. During this thesis, all spin manipulations have been done with two electron spins, and we will mainly discuss about this case. However to introduce the issue of spin in quantum dots, we will start by considering the simplest case of one electron spin in a single quantum dot. The way to measure it will be briefly explained, and will be more detailed in the fourth chapter. In addition the concept of relaxation and decoherence will be introduced. These two processes lead to a loss of information, and are important issues in the context of quantum information manipulations.

1.3.1 Spin states

The spin is an intrinsic property of a particle like its mass or its charge. The charge is coupled to electric fields, while the spin is coupled to magnetic fields. Electrons exhibit a spin 1/2. The spin operator $\mathbf{S} = (S_x, S_y, S_z)$ is an angular momentum. It means that its 3 components are observable and verify the commutation relations $[S_i, S_j] = i\hbar\varepsilon_{ijk}S_k$, where ε_{ijk} is the Levi-Civita symbol :

$$\varepsilon_{ijk} = \begin{cases} 1 & \text{if } (i,j,k) = (x,y,z) \text{ or } (z,x,y) \text{ or } (y,z,x) \\ -1 & \text{if } (i,j,k) = (x,z,y) \text{ or } (y,x,z) \text{ or } (z,y,x) \\ 0 & \text{if } i = j \text{ or } i = k \text{ or } j = k \end{cases} \tag{1.7}$$

ε_{ijk} is 1 if (i,j,k) is an even permutation of (x,y,z), -1 for an odd permutation, and 0 if any index is repeated. It implies that the uncertainty principle concerns the measure of a spin in the three spatial directions. In addition, as we have briefly mentioned, the spin operators acts on a new space, the spin space ξ_S, where $\mathbf{S}^2$ and S_z constitute a complete set of commuting observables. The space ξ_S is thus spanned by the set of eigenstates common to $\mathbf{S}^2$ and S_z :

$$\begin{aligned} \mathbf{S}^2|{}^{+}_{-}\frac{1}{2}\rangle &= \frac{3}{4}\hbar^2|{}^{+}_{-}\frac{1}{2}\rangle \\ S_z|{}^{+}_{-}\frac{1}{2}\rangle &= {}^{+}_{-}\frac{1}{2}\hbar|{}^{+}_{-}\frac{1}{2}\rangle \end{aligned} \tag{1.8}$$

For the eletron (spin $\frac{1}{2}$) the space ξ_S is therefore a two-dimensional space, with two eigenstates $|{}^{+}_{-}\frac{1}{2}\rangle$. In the following the notation used for these two states will be $|\uparrow\rangle$ ($|\downarrow\rangle$), specifying if the spin state is aligned (opposite) with the external magnetic field. Now we will consider the two cases often used to deal with spin qubits, a single electron spin, and two electron spins.

Single electron spin states

We first consider a system composed of a single electron spin trapped in a single quantum dot. There are two spin states, $|\uparrow\rangle$ and $|\downarrow\rangle$, the Zeeman doublet. They are degenerated at zero magnetic field, and their energy difference, the Zeeman energy E_Z scales linearly with the magnetic field (Figure 1.8) [17]. This energy is written as $E_Z = g^*\mu_B B$ where $g^* = -0.44$ is the Landé factor for the electrons in GaAs, μ_B is the Bohr magneton, and B the magnetic field. We consider in the following that $|\uparrow\rangle$ ($|\downarrow\rangle$) is the ground (excited) state.

The first step towards using the spin as a qubit is to be able to measure it. The readout of spin states has been achieved by using optical methods [18, 19, 20] or by

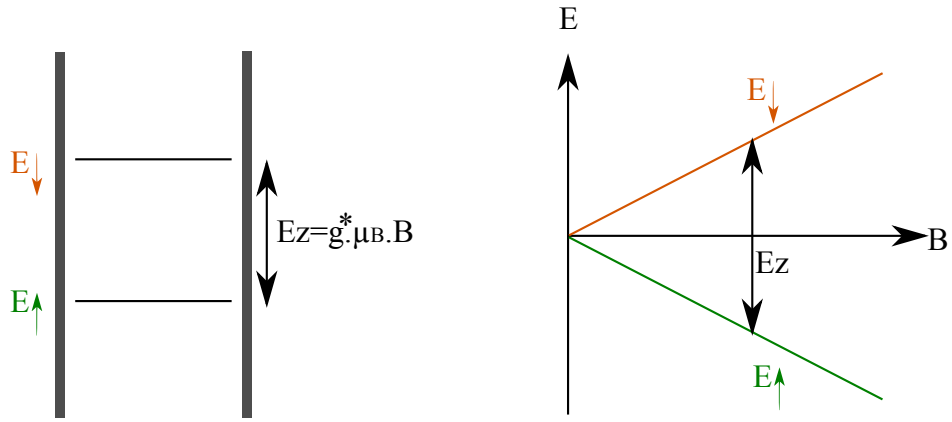

Figure 1.8: **Single spin states.** The two single spin states are $|\uparrow\rangle$ and $|\downarrow\rangle$ and their energy difference E_Z scales linearly with the magnetic field.

using magnetic resonance force microscopy [21]. On the other hand electrical read out of a single electron spin states is difficult. Indeed the only information that we can get electrically from a quantum dot system is its charge state. But as it will be explained, the spin state can be read-out by measuring its charge state. This technique of spin-to-charge conversion has first been experimentally realized by Elzerman and co-workers in 2004 [4] where they performed single shot destructive measurements of a single electron spin in a quantum dot. The principle of this measurement is illustrated in figure 1.9. The idea is to initialize an unknown spin state by setting the two spin state ($|\uparrow\rangle$ and $|\downarrow\rangle$) lower than the Fermi energy of the reservoir. Then with a gate voltage pulse, the energy of $|\downarrow\rangle$ can be set higher than the Fermi energy, while the one of $|\uparrow\rangle$ is still below. Therefore if the spin state was $|\downarrow\rangle$, the electron can tunnel out from the quantum dot, and be replaced by one from the reservoir going into $|\uparrow\rangle$. Otherwise, if the system has been initialized in the ground state $|\uparrow\rangle$, it will remains in the same state all along the measurement scheme. Consequently if the spin state is $|\downarrow\rangle$, we detect with the QPC an electron tunnelling out from the quantum dot to the reservoir, and another one tunnelling in, otherwise we do not detect anything. Here we see that probing the charge state of the system gives information about its spin state. This is a spin to charge conversion.

Few remarks can be done about the measurement of the single electron spin state :

- To perform such measurements, the temperature has to be much smaller than the Zeeman energy, $T \ll E_Z = g^* \mu_B B$. Otherwise there are some non occupied states in the reservoir at the energy of the ground state $|\uparrow\rangle$, and the electron can tunnel out even if it is in the ground state. In a magnetic field scale, a temperature equal to 100mK is equivalent to 300mT. In the work of Elzerman, the magnetic was fixed at 10T.

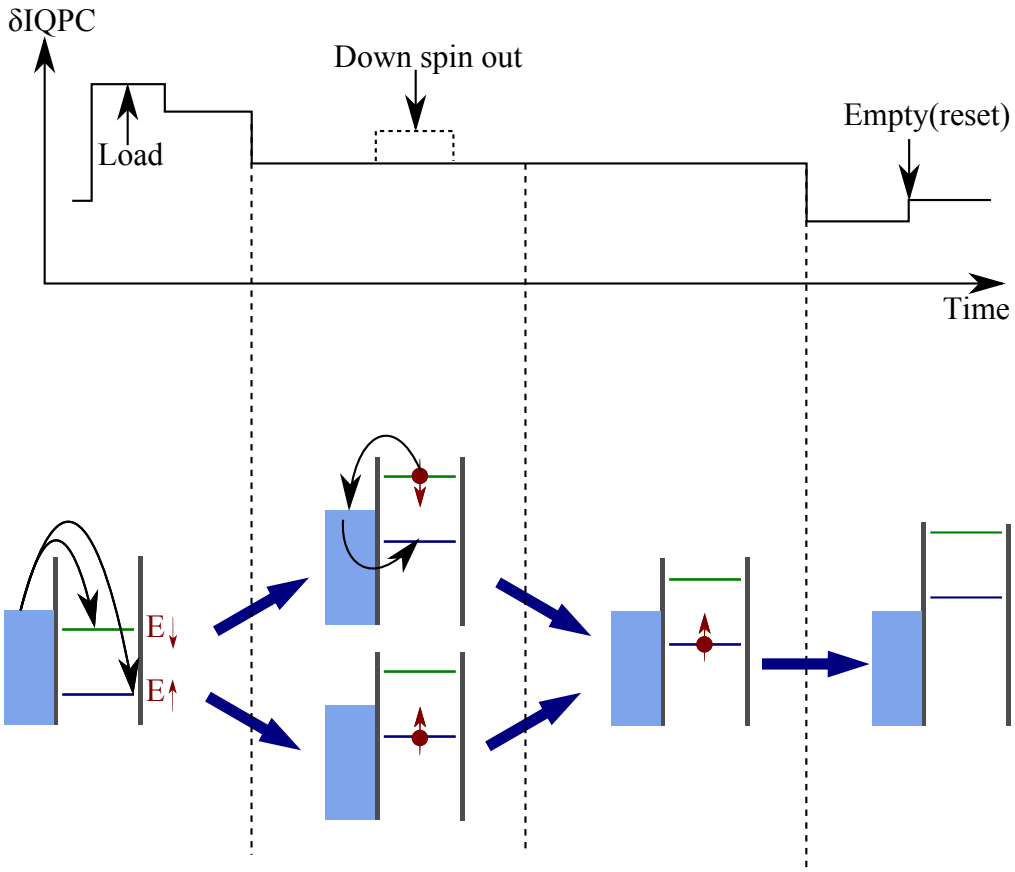

Figure 1.9: **Single spin measurements** The idea of this measurement scheme is to set one of the spin state above the Fermi energy of the reservoir. Then if the electron spin lies in this state, the electron will tunnel out from the quantum dot to the reservoir. This is the so-called spin-to-charge conversion.

- This measurement scheme has to be done faster than the relaxation time. This concept will be described in the next section, and we just mention here that the relaxation is a process that "transform" the excited state ($\downarrow$) into the ground state ($\uparrow$). Consequently such measurements have to be done before relaxation processes might happen. The readout using the tunnelling of an electron from the quantum dot to the reservoir, the tunnel coupling has to be tuned in order to let the electron tunnel out before the relaxation happens (in the work of Elzerman, the tunnelling rate Γ has been set to $\Gamma \sim (0.05ms)^{-1}$).

To be able to use a single electron spin as a qubit, we need to be able to manipulate its state. In other words, we need to be able to prepare any state

$$|\Psi\rangle = cos(\frac{\theta}{2})|\downarrow\rangle + sin(\frac{\theta}{2})e^{i\phi}|\uparrow\rangle \tag{1.9}$$

where $\theta \in [0, \pi]$ and $\phi \in [0, 2\pi]$. To realize it, we need to couple the states $|\uparrow\rangle$ and $|\downarrow\rangle$. This can be achieved by using an oscillating magnetic field $\mathbf{B}_{osc}$ that is resonant with the spin precession frequency in an external magnetic field $\mathbf{B}_{ext}$ oriented perpendicularly to $\mathbf{B}_{osc}$. This technique is called ESR (Electron Spin Resonance) and allows to change the angle θ of the state $|\Psi\rangle$ (equation 1.9). In the work of Koppens and co-workers [22], they obtained a $\theta = \pi$ rotation of the spin on the order of 100ns. The use of the oscillating magnetic field can be replaced by an oscillating electric field. An electric field is supposed to act only on the electron charge, but thanks to spin-orbit interaction, it enables to perform the same kind of manipulation (EDSR : Electron Dipole Spin Resonance) [23, 24]. We will describe later the spin-orbit interaction, and for the moment we just mention that it allows to couple the spin and the charge degrees of freedom, allowing for spin manipulation thanks to electric fields. The control of the angle ϕ (equation 1.9) is achieved by letting the system evolves according to time in a non zero magnetic field.
Due to the readout condition of a single spin qubit, and the relatively slow single qubit rotations ($\sim 100ns$ [22, 23]), physicists have been trying to find a new "basis" to build a qubit in GaAs quantum dot, allowing to overcome these difficulties. Over the last years, a particular attention has been devoted to the $S-T_0$ qubit made of two electron spins in a double quantum dot, and we will now introduce the spin states of two electron spins.

Two electrons spin states

In this part we consider two electrons trapped in a single quantum dot. In this thesis, all the spin manipulation have been done with two electron spins in a double quantum dot. Even if the system is different, the discussion about the spin states is still relevant. The key point to establish the spin states of an electron pair is to remind that electrons are fermions, so the wavefunction describing them has to be antisymmetric. As mentioned previously, the spin and the charge degrees of freedom "live" in two different subspaces.

Therefore the wavefunction $|\Psi\rangle$ can be decomposed into two parts, one for the spin degree of freedom $|\chi_s\rangle$ and one for the orbital degree of freedom $|\Phi_o\rangle$.

$$|\Psi\rangle = |\Phi_o\rangle \otimes |\chi_s\rangle \tag{1.10}$$

The mathematical operator $\otimes$ denotes that $|\Psi\rangle$ is a product state. Consider at first the spin degree of freedom of these two electrons. Each of them can be either in the state $|\uparrow\rangle$, or $|\downarrow\rangle$. So for two electrons, their spin are either aligned, or opposite giving the states $\{|\uparrow,\uparrow\rangle, |\downarrow,\downarrow\rangle, |\uparrow,\downarrow\rangle, |\downarrow,\uparrow\rangle\}$. For the orbital degree of freedom, we will just consider the first two orbital levels, that we called the ground and excited state ($|g\rangle$ and $|e\rangle$). Considering first the two aligned spin states $\{|\uparrow,\uparrow\rangle$ and $|\downarrow,\downarrow\rangle$, it is clearly seen that they are symmetric, meaning that by changing the spin state of the first electron with the one of the second the final state is equal to the intial one. Consequently the orbital part of the wavefunction has to be antisymmetric and we get the first two triplet states $|T_+\rangle$ and $|T_-\rangle$:

$$\begin{aligned} |T_+\rangle &= (|e,g\rangle - |g,e\rangle) \otimes |\uparrow,\uparrow\rangle \\ |T_-\rangle &= (|e,g\rangle - |g,e\rangle) \otimes |\downarrow,\downarrow\rangle \end{aligned} \tag{1.11}$$

In the following, we will intentionally forget the orbital part of the wavefunction, and we will just write $|T_+\rangle = |\uparrow,\uparrow\rangle$ and $|T_-\rangle = |\downarrow,\downarrow\rangle$.

Now we consider the two opposite spin states. The two electrons are undistinguishable. So the spin part of the wavefunction has to be either $|\uparrow,\downarrow\rangle - |\downarrow,\uparrow\rangle$, or $|\uparrow,\downarrow\rangle + |\downarrow,\uparrow\rangle$. In the first (second) case, the spin part of the wavefunction is antisymmetric (symmetric), and therefore the orbital part has to be symmetric (antisymmetric), giving the singlet $|S\rangle$ and the triplet $|T_0\rangle$:

$$\begin{aligned} |T_0\rangle &= (|e,g\rangle - |g,e\rangle) \otimes (|\uparrow,\downarrow\rangle + |\downarrow,\uparrow\rangle \\ |S\rangle &= (|g,g\rangle) \otimes (|\uparrow,\downarrow\rangle - |\downarrow,\uparrow\rangle) \end{aligned} \tag{1.12}$$

Finally we get four spin states, one singlet $|S\rangle$ and three triplets $\{|T_0\rangle, |T_+\rangle, |T_-\rangle\}$. The energy of the two triplets $|T_+\rangle = |\uparrow,\uparrow\rangle$ and $|T_-\rangle = |\downarrow,\downarrow\rangle$ is linearly dependent on the magnetic field via the Zeeman Energy (Figure 1.10). In addition the three triplet $\{|T_+\rangle = |\uparrow,\uparrow\rangle$, $|T_-\rangle = |\downarrow,\downarrow\rangle$, $|T_0\rangle = |\uparrow,\downarrow\rangle + |\downarrow,\uparrow\rangle\}$ are higher in energy compared to the singlet $|S\rangle = |\uparrow,\downarrow\rangle - |\downarrow,\uparrow\rangle$ due to the charge part of the wavefunction. Indeed the orbital energy ΔE has to be paid. The discussions about the manipulation and the readout of such spin states will be detailed in the fourth chapter. Two more concepts related to spins have to be introduced : the relaxation and the decoherence. We have already mentioned these two processes, and we will now developed them through the example of a fluctuating environment.

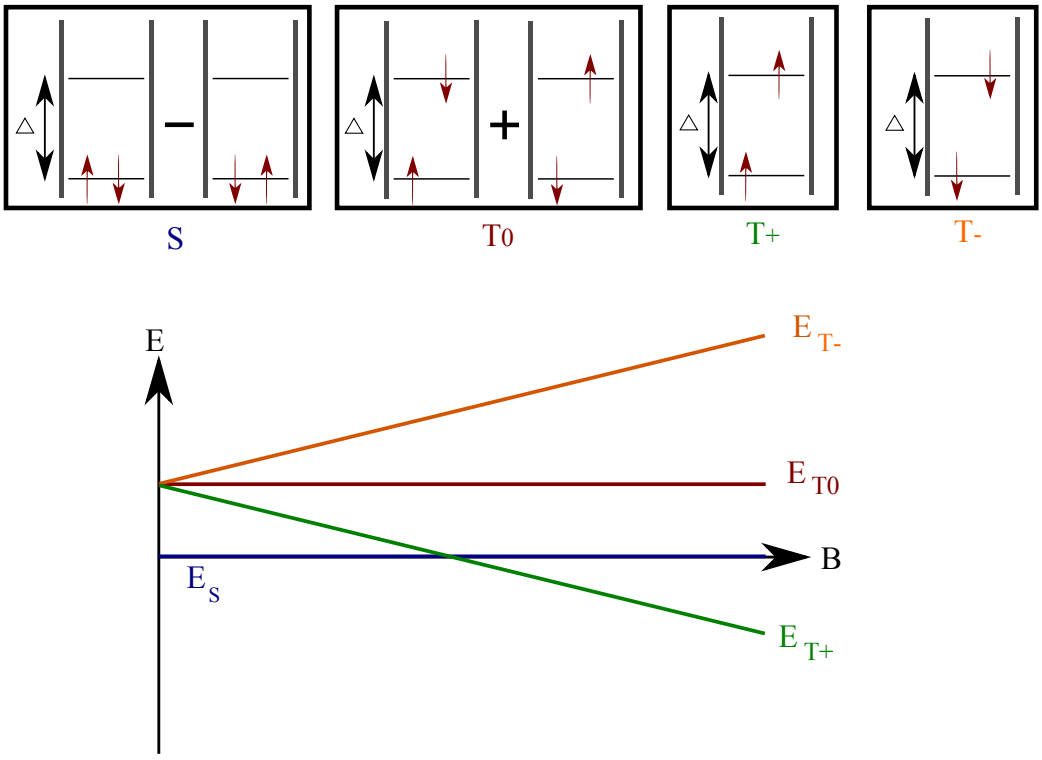

Figure 1.10: **Two electrons spin states in a single quantum dot** The above schemes gives the four spin states of an electron pair. They are antisymmetric : for the singlet (triplets), the orbital part of the wavefunction is symmetric (antisymmetric) while the spin part is antisymmetric (symmetric).

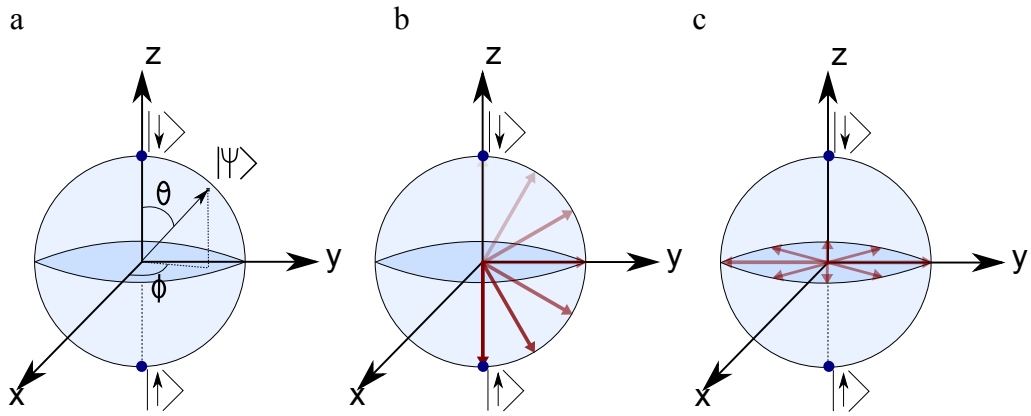

Figure 1.11: **Relaxation and decoherence of two-level system.** **(a)** The Bloch sphere representation of the qubit state (equation 1.14). **(b)** Relaxation and **(c)** dephasing of the quantum system corresponding to a loss of information.

1.3.2 Relaxation and decoherence of a spin

Until now we have considered a quantum system, an electron or two electron spins, without taking into account of the interaction of this system with its environment. The environment will disturb the quantum system, and since the interaction between them is uncontrolled, it can be seen as a loss of information stored in the quantum state of the system. The dominant interactions of the electron spin of a GaAs quantum dot with its environment are the hyperfine interaction with the host nuclei and the spin orbit. Before we describe more precisely these two interactions, we will consider a simple model where a two-level quantum system (TLS), a qubit, interacts with a fluctuating environment [25, 26]. This model has the advantage to be quite easy to understand and to describe the concept of relaxation and decoherence.
The state of the qubit can be written, up to a global phase, as :

$$|\Psi\rangle = cos(\frac{\theta}{2})|\uparrow\rangle + sin(\frac{\theta}{2})e^{i\phi}|\downarrow\rangle \tag{1.13}$$

To get a picture of such a state for a TLS, the so called Bloch sphere can be introduced. Its poles correspond to the qubit ground state $|\uparrow\rangle$ and excited state $|\downarrow\rangle$ (figure 1.11 (a)). Any superposition of states $|\downarrow\rangle$ and $|\uparrow\rangle$ is represented by a point on the Bloch sphere, defining the two angles θ and ϕ (equation 1.13).

The coupling of the qubit with its environment leads to two processes :

- If the qubit is coupled to a dissipative environment, it relaxes after some time from the excited to the ground state. In this case there is an energy transfer from the

quantum system to the environment and it can be seen as a loss of information about the angle θ (figure 1.11 (b)). The time scale describing such a decay is referred to as T_1. Relaxation can be viewed as the decay of the initial longitudinal (parallel to the quantification axis) polarization $\langle\hat{\sigma}_z\rangle$ to its equilibrium state. $\hat{\sigma}_{x,y,z}$ represent the Pauli matrices.

- On the other hand decoherence refers to the decay of the transverse polarisation $\langle\hat{\sigma}_\perp\rangle$ ($\hat{\sigma}_\perp$ includes both $\hat{\sigma}_{x,y}$). The timescale associated to such a process is generally defined as T_2. It corresponds to a loss of information about the angle ϕ (figure 1.11 (c)). In contrast to the relaxation, decoherence does not imply any energy transfer.

To illustrate these two processes, we consider the qubit interacting with a fluctuating environment. The system is then described by the hamiltonian :

$$H = \frac{\hbar}{2}[\omega_z\hat{\sigma_z} + \delta\omega_z(t)\hat{\sigma_z} + \delta\omega_x(t)\hat{\sigma_x} + \delta\omega_y(t)\hat{\sigma_y}] \tag{1.14}$$

Here $\hbar\omega_z$ is the energy splitting of the qubit. For instance in the case of a single electron spin trapped in a quantum dot, it corresponds to the Zeeman energy defined by the external magnetic field $E_Z = E_\downarrow - E_\uparrow = g^*\mu_B B$. In addition the qubit is coupled to a fluctuating environment and this appears through $\hbar\delta\omega_{x,y,z}(t)$, that are the fluctuations along the x,y,z directions. For example in the case of a single spin qubit made of GaAs quantum dots, these fluctuations can arise from the fluctuations of the nuclear spins as we will see later.
The relaxation is a process that allows an excited state to exchange energy with the environment in order to "relax" in the ground state. Therefore to induce relaxation, the ground and the excited states need to be coupled. This is done by the transverse fluctuations along the x and y axis ($\delta\omega_{x,y}(t)$). Fluctuations along the longitudinal axis z do not allow relaxation since they do not couple $|\uparrow\rangle$ and $|\downarrow\rangle$. In addition as we said, the relaxation is accompanied by an energy transfer from the qubit to the environment. Due to the energy conservation, it means that the environment has to exhibit a non-zero density of state at the energy splitting of the qubit. This can be seen in GaAs quantum dots by studying the relaxation time as a function of the magnetic field giving rise to the energy splitting $\hbar\omega_z$. For a single electron spin trapped in a quantum dot, the main relaxation process is due to the spin-orbit interaction. In this case the system can exchange energy with the phonons. They have a larger density of states at high energies, and it has been demonstrated [7] that the relaxation of a single spin is faster for higher magnetic fields (leading to larger qubit energy splitting).
The fluctuations along the z axis $\delta\omega_z(t)$ leads to dephasing or decoherence. Indeed a qubit in a superposition of state $\alpha|\uparrow\rangle + \beta|\downarrow\rangle$ ($\alpha^2 + \beta^2 = 1$) undergoes due to ω_z a Larmor precession in the (x, y) plane. The Larmor precession is changed by the fluctuations $\delta\omega_z(t)$, and this results in the accumulation of an extra unknown phase $\delta_\phi(\tau) = \int_0^\tau \delta\omega_z(t)dt$. In

contrast with relaxation, in this case all the noise spectrum of the fluctuations along the z axis contributes to the decoherence. The way to measure this two processes experimentally will be described in more detail in the chapter 4. For now on we will have a look at the two particular interactions with the environment in the case of GaAs quantum dot systems : the hyperfine interaction with the host nuclei and the spin-orbit interaction which links the orbital subspace of an electron to its spin subspace.

1.4 Hyperfine interaction

The hyperfine interaction between the electron spin trapped in a GaAs quantum dot and the host nuclear spins present in all III-V semiconductors leads to the strongest decoherence effect [27, 28, 29, 30, 31]. As we will see, the interaction with the nuclear spins can be seen as a slowly fluctuating magnetic field along the z-direction. It induces an extra unknown phase leading to decoherence as explained previously. We will introduce here the hyperfine interaction by considering one electron spin $\mathbf{S}$ in a single quantum dot interacting with the surrounding nuclear spins $\mathbf{I}_k$. Then a semi classical approach will be used to describe the effect on the spin dynamic [32, 33].
The hamiltonian of the hyperfine interaction between a localized electron in a quantum dot and the host nuclear spins can be written as :

$$H_{hf} = \hbar\gamma_e \mathbf{S}.\sum_k A_k \mathbf{I}_k \tag{1.15}$$

where A_k is the hyperfine coupling constant between the nuclear spin k $\mathbf{I}_k$ and the electron spin$\mathbf{S}$, and $\gamma_e = \frac{g^*\mu_B}{\hbar}$ is the gyromagnetic ratio for electron spin $\mathbf{S}$. A_k can be written $A_k = A\nu_0|\Psi(r_k)|^2$, where A is the average hyperfine coupling constant, ν_0 is the volume of a crystal unit containing one nuclear spin, and $|\Psi(r_k)|^2$ is the value of the electronic wavefunction $\Psi(r)$ at the position of the nucleus k (figure 1.12 (a)). In GaAs $A \sim 90\mu eV$ [34].

The precession frequency of the electron is much greater than the precession frequency of the nuclei, because the g^* factor of the nucleus is 1000 times smaller than the one of the electrons. Consequently we can consider, in a first approach, that the electron sees the nuclear spins as frozen. Therefore the quantum operator $\sum_k A_k \mathbf{I}_k$ can be substituted by an effective nuclear hyperfine magnetic field $\mathbf{B}_{nuc}$, the so-called Overhauser field. The field $\mathbf{B}_{nuc}$ corresponds to the magnetic field felt by the electron spin trapped in the quantum dot. If the nuclear spins are fully polarized, $|\mathbf{B}_{nuc}| \sim 5T$ [34], independent of N, the number of nuclei, because A, the average hyperfine constant does not depend on N. However in thermal equilibrium with typical temperature ($T > 10mK$), the thermal energy k_BT ($\sim 10\mu eV$ at 100mK) dominates the Zeeman energy of the nucleus ($\sim 2.5neV$ at $B_{ext} = 100mT$), and also the hyperfine energy ($\sim 0.1 - 1\mu eV$). Consequently the average

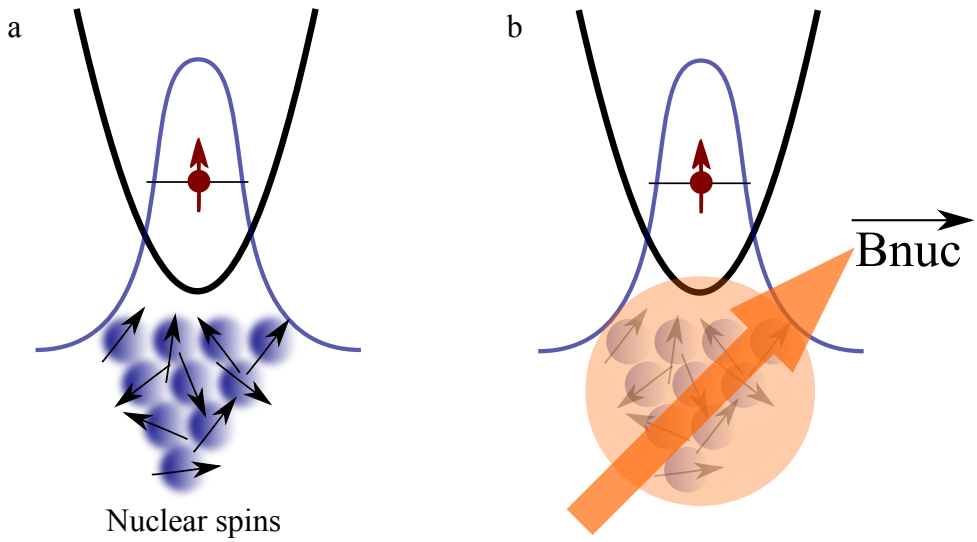

Figure 1.12: **Hyperfine interaction between an electron spin in a quantum dot and the host nuclear spins of the semiconductor (a)** A single electron spin interacts with many nuclear spins. The coupling depends on the value of the electronic wavefunction at the position of the nucleus. **(b)** The interaction with all the nucleis can be replaced by a classical magnetic field $\vec{B}_{nuc}$.

effective nuclear magnetic field is zero, but its distribution along the three directions is gaussian with spread $\Delta_B \propto \frac{1}{\sqrt{N}}$. For $N = 10^6$, which is the typical number of nuclei overlapping with the wavefunction of an electron spin trapped in a quantum dot, $\Delta_B \sim 5mT$. Then the effect of nuclear spins is often seen as a statistical nuclear field which fluctuates around 0 with spread Δ_B . The timescale of these fluctuations is $\sim 1s$ [35], which is consistent with dipole-dipole mediated nuclear diffusion [36]. The statistical distribution of the nuclear field has been measured in different kind of systems (optical and electrical dots) and it varies from 1 to few tens of mT [37, 38, 39, 40].
To conclude the electron spin feels an effective magnetic field $\mathbf{B} = \mathbf{B}_{ext} + \mathbf{B}_{nuc}$, where $\mathbf{B}_{ext}$ is the external magnetic field applied to the sample. The nuclear spin dynamics being much slower than the electron spin dynamic, we can consider this effective magnetic field as being fixed during the electron spin manipulation. However between the repetition of the electron spin manipulation, the effective magnetic field can be different. This is the quasi-static approximation. This allows us to write the Hamiltonian as an electron spin interacting with an effective magnetic field $H_{eff} = \hbar\gamma_e \mathbf{B}.\mathbf{S} = \hbar\gamma_e(\mathbf{B}_{ext} + \mathbf{B}_{nuc}).\mathbf{S}$. The equation of motion of the spin $\mathbf{S}$ in a fixed magnetic field $\mathbf{B}$ is given by [33]

$$\mathbf{S}(t) = (\mathbf{S}_0.\mathbf{n})\mathbf{n} + [\mathbf{S}_0 - (\mathbf{S}_0.\mathbf{n})\mathbf{n}]cos(\omega t) + [(\mathbf{S}_0 - (\mathbf{S}_0.\mathbf{n})\mathbf{n}) \times \mathbf{n}]cos(\omega t) \tag{1.16}$$

with $\mathbf{S}_0$ the initial spin, $\mathbf{n} = \frac{\mathbf{B}}{B}$ and $\omega = \gamma_e B$ the Larmor frequency. The first term is the projection of the spin along the quantification axis. The two others give the precession in the plane (x,y) induced by the magnetic field. Although the electron spin precession frequency allows to consider the nuclear spins as frozen, the effective magnetic field fluctuate from one measurement to the others. Consequently equation 1.16 as to be averaged over the nuclear magnetic field distribution. Then the time dependence of the electron spin over a large number of measurements is given by [33] :

$$< \mathbf{S}(t) >= \frac{\mathbf{S}_0}{3}\{1 + 2(1 - 2(\frac{t}{2T_2^*})^2)exp[-(\frac{t}{2T_2^*})^2]\} \tag{1.17}$$

where $T_2^* = \frac{\hbar}{\mu_B g_e \Delta_B}$ is the time ensemble average decoherence time, Δ_B being the amplitude of the magnetic field fluctuations. As it has been seen, the order of magnitude of these fluctuations is $\Delta_B \sim 5mT$. It gives a time ensemble average decoherence time T_2^* equal to $\sim 10ns$ which has been measured in [27]. To reduce these fluctuations, some techniques of spin echo [27, 41, 42, 43], well known in the NMR (Nuclear Magnetic Resonance) community, can be used. The idea is to take advantage of the slowly evolving nuclear magnetic field to cancel the unknown phase acquired by the electron spin. Another way could be the use of dynamical nuclear spin polarisation (DNP) [44, 45]. Recently it has been demonstrated that the coherence of a spin qubit can be enhanced by operating it as a feedback loop that controls the nuclear spins with which the electron spins interacts

[41]. To conclude we see that the nuclear spin fluctuations along the $\hat{z}$ axis leads to dephasing (decoherence). Previously we mentioned that these fluctuations exist in the three dimensions (x,y,z). The fluctuations along the $\hat{x}$ and $\hat{y}$ axis could induce relaxation. For the electron spin, the nuclear spins can be seen as a bath with which it can exchanges energy and momentum. But the density of states of this bath is finite only at the Zeeman energy of the nuclear spins. The g^* factor of the nuclear being 1000 times smaller than the one of the electron, the fluctuations of the nuclear spins along the $\hat{x}$ and $\hat{y}$ axis can induce relaxation of the electron spin only at low magnetic fields [39]. We will come back to this point in the chapter 4, and for now on we will have a look at another interaction, known as the spin-orbit interaction.

1.5 Spin-orbit interaction

In an atom, the electron is orbiting with velocity $\frac{\mathbf{p}}{m}$ (m being the electron mass) in the electric field $\mathbf{E}$ of the proton. In the frame of the electron, the motion in the electric field gives rise to an effective magnetic field $\mathbf{B}_{int} = -\frac{1}{mc^2}\mathbf{p} \times \mathbf{E}$ with c the light velocity. This effective or internal magnetic field interacts with the spin of the electron resulting in the spin-orbit coupling $H_{SO} = -\boldsymbol{\mu}_S \mathbf{B}_{int}$ with $\boldsymbol{\mu}_S$ the magnetic moment of the electron spin. In other words the spin-orbit interaction couples the spin degree of freedom with the charge degree of freedom, and their relative subspace are therefore no more independent. The spin states are then no more an eigenstate of the system and the wavefunction does not factorize in a pure spin and orbital component. In the literature, the expression "pseudo-spin" is commonly used. In a potential ($\mathbf{E} = -\boldsymbol{\nabla} V$) the electron experiences the spin-orbit interaction :

$$H_{SO} = -\frac{\hbar}{4m_0^2c^2}\boldsymbol{\sigma}.(\mathbf{p} \times (\boldsymbol{\nabla} V)) \tag{1.18}$$

m_0 being the mass of the free electron and $\boldsymbol{\sigma} = (\sigma_x, \sigma_y, \sigma_z)$ the Pauli matrices. Concerning an electron in a crystal lattice, the spin-orbit interaction arises for the same reasons, since the electron feels the electric fields generated by the charged atoms in the lattice. The hamiltonian 1.18 can be viewed as an effective magnetic field $\mathbf{B}_{eff} \propto \mathbf{p} \times (\nabla V)$. This results in a splitting of the spin states even at zero magnetic field. The strength of the spin orbit coupling in bulk structure depends above all on two things :

- The symmetry of the crystal is of direct relevance. In a crystal with inversion symmetry, all electronic states are at least doubly degenerated. This is the consequence of the requirements imposed by the time reversal symmetry and inversion symmetry. Indeed the time reversal symmetry implies that $E_\uparrow(\mathbf{k}) = E_\downarrow(\text{-}\mathbf{k})$, where $E_{\{\uparrow,\downarrow\}}(\mathbf{k})$ is the energy dispersion of the lowest conduction band and $(\uparrow, \downarrow)$ the two possible pseudo-spins. In addition the inversion symmetry implies that $E_\uparrow(\mathbf{k}) = E_\uparrow(\text{-}\mathbf{k})$. Put

together, these two requirements gives $E_{\uparrow}(\mathbf{k}) = E_{\downarrow}(\mathbf{k})$, and then the spin states are degenerated. On the other hand, in a crystal lacking the inversion symmetry (called bulk inversion asymmetry), the condition $E_{\uparrow}(\mathbf{k}) = E_{\uparrow}(\mathbf{-k})$ is not necessary, and a splitting can occur even at zero magnetic field. This is the case of the zinc-blende structure of GaAs, which exhibits a bulk inversion asymmetry. This contribution to the spin-orbit interaction is known as the Dresselhauss term [46]. Due to confinement and by using symmetry consideration, the Dresselhauss contribution to spin-orbit interaction in 2D can be written $H_D = \beta(-p_x\sigma_x + p_y\sigma_y)$, with β the Dresselhauss coupling constant.

- Moreover another contribution to the spin-orbit interaction arises from the asymmetry of the confinement potential. Indeed the potential trapping the electron in a 2DEG is triangular shaped. This contribution is known as the Rashba spin orbit term. To understand it in an intuitive way, we consider the potential oriented along the growth direction z, $\mathbf{E} = (0, 0, E_z)$. Substituting this potential in the equation 1.18 yields to the following form, $H_R = \alpha(-p_y\sigma_x + p_x\sigma_y)$, with $\alpha \sim |E_z|$, the Rashba coupling constant.

A convenient way to describe the magnitude of the spin-orbit interaction is the spin orbit length l_{SO}, defined as the length after which a spin has undergone a π-rotation when moving under influence of the spin-orbit effective magnetic field. In GaAs, this length has been measured and is of order of 1-10μm [47].
The size of a lateral quantum dot ($\sim 40nm$) is then typically much smaller than the spin orbit length l_{SO}. Therefore we can reasonably expect that the spin orbit interaction weakly affects the electron spin states in a quantum dot. Indeed since the electron is bound in a quantum dot, it does not have a momentum $< p_{x,y} >= 0$. Consequently the spin orbit does not couple directly the Zeeman doublet because $< n, \uparrow |H_{SO}|n, \downarrow > \sim < n|p_{x,y}|n > < \uparrow |\sigma_{x,y}| \downarrow >= 0$, where n labels the orbital levels in the quantum dot. But the spin orbit can couple levels with different orbital and spin $< n', \uparrow |H_{SO}|n, \downarrow > \neq 0$, with $n \neq n'$. Then we can write down the two "new" spin eigenstates $|\uparrow\rangle^{SO}$ and $|\downarrow\rangle^{SO}$inside a quantum dot under spin orbit interaction (at first order) :

$$\begin{aligned} |g\uparrow\rangle^{SO} &= |g\uparrow\rangle + \varepsilon_{g\uparrow}|e\downarrow\rangle \\ |g\downarrow\rangle^{SO} &= |g\downarrow\rangle + \varepsilon_{g\downarrow}|e\uparrow\rangle \end{aligned} \tag{1.19}$$

where $|g\uparrow\rangle$ ($|g\downarrow\rangle$) corresponds to a spin up (down) in the ground state of the trapping potential, and $|e\uparrow\rangle$ ($|e\downarrow\rangle$) to a spin up (down) in the first excited state of the trapping potential. $\varepsilon_{g\uparrow}$ and $\varepsilon_{g\downarrow}$ are related to the strength of the spin-orbit coupling.
Finally we see that an electric field which couples to the oribtal degree of freedom of an electron, can also acts on its spin. This lead to relaxation [48, 49, 50], but can also serve to drive coherent spin manipulations [23]. In addition it has been demonstrated

[51, 52] that topological spin manipulations (see chapter 3) can be obtained if the electron is transported adiabatically along a closed path under spin-orbit interaction. It will be developed in the third chapter.

Bibliography

[1] Klitzing, K. v., Dorda, G., and Pepper, M. *Phys. Rev. Lett.* **45**, 494–497 Aug (1980). 2, 124

[2] Loss, D. and DiVincenzo, D. P. *Phys. Rev. A* **57**, 120–126 Jan (1998). 2

[3] Feynman, R. P. *International Journal of Theoretical Physics* **21**(6-7), 467–488 (1982). 2

[4] Elzerman, J. M., Hanson, R., van Beveren, L. H. W., Witkamp, B., Vandersypen, L. M. K., and Kouwenhoven, L. P. *Nature* **430**(6998), 431–435 July (2004). ii, 4, 17, 119, 154

[5] Stopa, M. *Phys. Rev. B* **54**, 13767–13783 Nov (1996). 4

[6] Kouwenhoven, L. P., Austing, D. G., and Tarucha, S. *Reports On Progress In Physics* **64**(6), 701–736 June (2001). 5

[7] Meunier, T., Vink, I. T., van Beveren, L. H. W., Tielrooij, K. . J., Hanson, R., Koppens, F. H. L., Tranitz, H. P., Wegscheider, W., Kouwenhoven, L. P., and Vandersypen, L. M. K. *Physical Review Letters* **98**(12), 126601 March (2007). ii, 12, 23, 79, 98, 99, 108, 114, 119

[8] Field, M., Smith, C. G., Pepper, M., Ritchie, D. A., Frost, J. E. F., Jones, G. A. C., and Hasko, D. G. *Physical Review Letters* **70**(9), 1311–1314 March (1993). 13

[9] Aguado, R. and Kouwenhoven, L. P. *Phys. Rev. Lett.* **84**, 1986–1989 Feb (2000). 13

[10] Onac, E., Balestro, F., van Beveren, L. H. W., Hartmann, U., Nazarov, Y. V., and Kouwenhoven, L. P. *Phys. Rev. Lett.* **96**, 176601 May (2006). 13

[11] DiCarlo, L., Lynch, H. J., Johnson, A. C., Childress, L. I., Crockett, K., Marcus, C. M., Hanson, M. P., and Gossard, A. C. *Physical Review Letters* **92**(22), 226801 June (2004). 15

[12] Elzerman, J. M., Hanson, R., Greidanus, J. S., Willems van Beveren, L. H., De Franceschi, S., Vandersypen, L. M. K., Tarucha, S., and Kouwenhoven, L. P. *Phys. Rev. B* **67**, 161308 Apr (2003). 15

[13] Thalineau, R., Hermelin, S., Wieck, A. D., Bauerle, C., Saminadayar, L., and Meunier, T. *Applied Physics Letters* **101**(10), 103102 (2012). 15

[14] Hayashi, T., Fujisawa, T., Cheong, H. D., Jeong, Y. H., and Hirayama, Y. *Phys. Rev. Lett.* **91**, 226804 Nov (2003). 15

[15] Petersson, K. D., Petta, J. R., Lu, H., and Gossard, A. C. *Phys. Rev. Lett.* **105**, 246804 Dec (2010). 15

[16] Petta, J. R., Johnson, A. C., Marcus, C. M., Hanson, M. P., and Gossard, A. C. *Physical Review Letters* **93**(18), 186802 October (2004). 15

[17] Hanson, R., Witkamp, B., Vandersypen, L. M. K., van Beveren, L. H. W., Elzerman, J. M., and Kouwenhoven, L. P. *Phys. Rev. Lett.* **91**, 196802 Nov (2003). 16

[18] Kohler, J., Disselhorst, J., Donckers, M., Groenen, E., Schmidt, J., and Moerner, W. *NATURE* **363**(6426), 242–244 MAY 20 (1993). 16

[19] Wrachtrup, J., Vonborcyskowski, C., Bernard, J., Orrit, M., and Brown, R. *NATURE* **363**(6426), 244–245 MAY 20 (1993). 16

[20] Gruber, A., Drabenstedt, A., Tietz, C., Fleury, L., Wrachtrup, J., and vonBorczyskowski, C. *SCIENCE* **276**(5321), 2012–2014 JUN 27 (1997). 16

[21] Rugar, D., Budakian, R., Mamin, H., and Chui, B. *NATURE* **430**(6997), 329–332 JUL 15 (2004). 17

[22] Koppens, F. H. L., Buizert, C., Tielrooij, K. J., Vink, I. T., Nowack, K. C., Meunier, T., Kouwenhoven, L. P., and Vandersypen, L. M. K. *Nature* **442**(7104), 766–771 August (2006). ii, 19

[23] Nowack, K. C., Koppens, F. H. L., Nazarov, Y. V., and Vandersypen, L. M. K. *Science* **318**(5855), 1430–1433 November (2007). 19, 28, 49

[24] Laird, E. A., Barthel, C., Rashba, E. I., Marcus, C. M., Hanson, M. P., and Gossard, A. C. *Physical Review Letters* **99**(24), 246601 December (2007). 19, 101

[25] Martinis, J. M., Nam, S., Aumentado, J., Lang, K. M., and Urbina, C. *Phys. Rev. B* **67**, 094510 Mar (2003). 22

[26] Ithier, G., Collin, E., Joyez, P., Meeson, P. J., Vion, D., Esteve, D., Chiarello, F., Shnirman, A., Makhlin, Y., Schriefl, J., and Schön, G. *Phys. Rev. B* **72**, 134519 Oct (2005). 22

[27] Petta, J. R., Johnson, A. C., Taylor, J. M., Laird, E. A., Yacoby, A., Lukin, M. D., Marcus, C. M., Hanson, M. P., and Gossard, A. C. *Science* **309**(5744), 2180–2184 September (2005). 24, 26, 69, 77, 85, 89, 92, 94, 110

[28] Burkard, G., Loss, D., and DiVincenzo, D. P. *Physical Review B* **59**(3), 2070–2078 January (1999). 24

[29] Erlingsson, S. I. and Nazarov, Y. V. *Physical Review B* **70**(20), 205327 November (2004). 24

[30] Khaetskii, A. V., Loss, D., and Glazman, L. *Physical Review Letters* **88**(18), 186802 May (2002). 24

[31] Coish, W. A. and Loss, D. *Physical Review B* **72**(12), 125337 September (2005). 24

[32] Taylor, J. M., Petta, J. R., Johnson, A. C., Yacoby, A., Marcus, C. M., and Lukin, M. D. *Physical Review B* **76**(3), 035315 July (2007). 24, 84, 93

[33] Merkulov, I. A., Efros, A. L., and Rosen, M. *Physical Review B* **65**(20), 205309 May (2002). 24, 26

[34] Paget, D., Lampel, G., Sapoval, B., and Safarov, V. I. *Phys. Rev. B* **15**, 5780–5796 Jun (1977). 24

[35] Barthel, C., Reilly, D. J., Marcus, C. M., Hanson, M. P., and Gossard, A. C. *Phys. Rev. Lett.* **103**, 160503 Oct (2009). 26, 107

[36] Reilly, D. J., Taylor, J. M., Petta, J. R., Marcus, C. M., Hanson, M. P., and Gossard, A. C. *Physical Review Letters* **104**(23), 236802 June (2010). 26

[37] Braun, P.-F., Marie, X., Lombez, L., Urbaszek, B., Amand, T., Renucci, P., Kalevich, V. K., Kavokin, K. V., Krebs, O., Voisin, P., and Masumoto, Y. *Phys. Rev. Lett.* **94**, 116601 Mar (2005). 26

[38] Dutt, M. V. G., Cheng, J., Li, B., Xu, X., Li, X., Berman, P. R., Steel, D. G., Bracker, A. S., Gammon, D., Economou, S. E., Liu, R.-B., and Sham, L. J. *Phys. Rev. Lett.* **94**, 227403 Jun (2005). 26

[39] Johnson, A. C., Petta, J. R., Taylor, J. M., Yacoby, A., Lukin, M. D., Marcus, C. M., Hanson, M. P., and Gossard, A. C. *Nature* **435**(7044), 925–928 June (2005). 26, 27

[40] Koppens, F. H. L., Folk, J. A., Elzerman, J. M., Hanson, R., van Beveren, L. H. W., Vink, I. T., Tranitz, H. P., Wegscheider, W., Kouwenhoven, L. P., and Vandersypen, L. M. K. *Science* **309**(5739), 1346–1350 August (2005). 26

[41] Bluhm, H., Foletti, S., Mahalu, D., Umansky, V., and Yacoby, A. *Physical Review Letters* **105**(21), 216803 November (2010). iii, 26, 27, 69, 89, 101

[42] Medford, J., Cywiński, L., Barthel, C., Marcus, C. M., Hanson, M. P., and Gossard, A. C. *Phys. Rev. Lett.* **108**, 086802 Feb (2012). 26

[43] Barthel, C., Medford, J., Marcus, C. M., Hanson, M. P., and Gossard, A. C. *Phys. Rev. Lett.* **105**, 266808 Dec (2010). 26

[44] Petta, J. R., Taylor, J. M., Johnson, A. C., Yacoby, A., Lukin, M. D., Marcus, C. M., Hanson, M. P., and Gossard, A. C. *Physical Review Letters* **100**(6), 067601 February (2008). 26

[45] Foletti, S., Bluhm, H., Mahalu, D., Umansky, V., and Yacoby, A. *Nature Physics* **5**(12), 903–908 December (2009). ii, 26, 89, 101, 102, 104, 106, 108

[46] Dresselhaus, G. *Phys. Rev.* **100**, 580–586 Oct (1955). 28

[47] Zumbühl, D. M., Miller, J. B., Marcus, C. M., Campman, K., and Gossard, A. C. *Phys. Rev. Lett.* **89**, 276803 Dec (2002). 28

[48] Khaetskii, A. V. and Nazarov, Y. V. *Phys. Rev. B* **61**, 12639–12642 May (2000). 28

[49] Khaetskii, A. V. and Nazarov, Y. V. *Phys. Rev. B* **64**, 125316 Sep (2001). 28

[50] Golovach, V. N., Khaetskii, A., and Loss, D. *Phys. Rev. Lett.* **93**, 016601 Jun (2004). 28

[51] Golovach, V. N., Borhani, M., and Loss, D. *Physical Review A* **81**(2), 022315 February (2010). ii, 29, 49

[52] San-Jose, P., Scharfenberger, B., Schoen, G., Shnirman, A., and Zarand, G. *Physical Review B* **77**(4), 045305 January (2008). ii, 29, 49

Chapter 2

Device fabrication and experimental set-up

Résumé

Dans ce chapitre, nous présentons brièvement le dispositif expérimental utilisé tout au long de cette thèse ainsi que la fabrication des échantillons. Dans un premier temps, nous décrirons les techniques de nanofabrications permettant de réaliser les échantillons de boîtes quantiques latérales, comme la lithographie ou la gravure. Une description succincte de chaque étape de fabrication sera donnée. Par la suite, une brève description du réfrigérateur à dilution permettant de refroidir un échantillon à des températures proche du mK sera exposée. Enfin, l'"électronique" utilisée durant cette thèse, comme par exemple les sources de tensions ou encore les amplificateurs, sera décrite.

Introduction

To manipulate electron spins trapped in quantum dot systems, some experimental constraints have to be overcome. They can be divided into three parts :

- In the context of lateral quantum dot systems, the confining potential is defined by voltages applied on metallic gates. These gates have to be fabricated by using nanofabrication techniques. In addition, the 2DEG, where the quantum dot system is located, is embedded 100nm below the surface. In order to measure the device, it has to be contacted.

- Due to the typical energy scale of a quantum dot (the charging energy E_C and the orbital energy are on the same order $1meV \sim 10K$), the devices have to be measured at low temperature. This is achieved by cooling down the sample thanks to a dilution refrigerator.

- All the electronics used in the experiment has to be low noise due one more time to the energy scale of such systems. By considering a gate lever arm (converting a gate voltage into energy) equal to 0.1 (being the typical order of magnitude of the gate lever arm α), it means that the voltages sources have to be very stable in front of 10mV in order to minimize the potential fluctuations. In addition all the spin manipulations that we perform in this thesis are done by manipulating electric fields with gate voltages. For instance the exchange coherent oscillations that we will present in chapter four are controlled by defining the energy splitting of two spin states thanks to gate voltages (see chapter 4). It necessitates sufficiently low noise on the voltage sources used. Moreover the typical signal extracted from a GaAs quantum dot systems is relatively small ($I_{QPC} \sim 100pA$). Therefore all the acquisition chain has to be engineered in order to be able to detect such small signals.

2.1 Device fabrication

Before manipulating and measuring an electron spin, we have to be able to define the confining potential. Starting from a bare wafer of GaAs/AlGaAs with a 2DEG, the electron confinement in a plane is already ensured. In order to ensure the confinement in the two other dimensions, it has been explained in the first chapter that an electrostatic potential could be engineered by applying negative voltages on metallic gates deposited at the surface of the wafer. The set of gates allowing for such potential has to be fabricated. Although the nanofabrication techniques employed during this thesis are somehow standard and do not present any particularity, we will give the main requirements in order to get a measurable sample. For instance we mentioned the necessity to get a system with energy scale much smaller than the temperature. We have seen that the charging

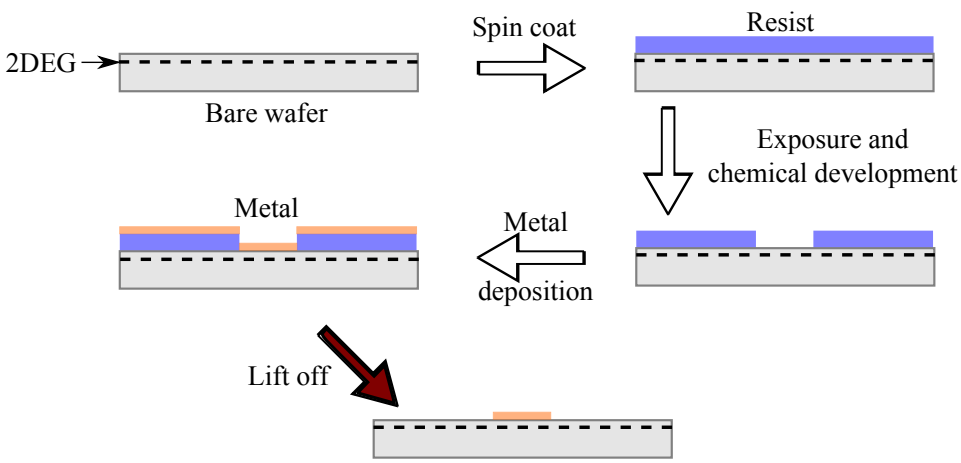

Figure 2.1: **Description of a lithography step.** The first step consists of spin coating a photo or electro sensitive resist. Then this resists is exposed through a mask designing a pattern and developed. Afterwards a metal is deposited on the surface of the sample. Finally the metal deposited on the top of resist is removed, and only the one deposited directly on the top of the sample remains. This is the so-called lift-off step.

energy, the energy needed to add an electron into a quantum dot, and the orbital energy, defining the single particle level spacing, depends on the quantum dot size. For instance a size close to $\sim 50nm$ gives a charging energy and an orbital energy equal to $\sim 1meV$, equivalent to $\sim 10K$. These energy scales set a temperature limit beyond which thermal excitations do not permit any manipulations. Then the first requirement is to be able to fabricate a set of gates allowing for creating a potential whose size is sufficiently small in order to get an energy scale of the quantum dot much smaller than the thermal energy. In addition the 2DEG where the quantum dot system is located, is embedded 100nm below the surface of the sample. In order to probe the system we need to contact it. In addition to avoid any short between these contact, one step of etching is required. Therefore several steps of nanofabrication are required. As we will see, all these steps can be done by using standard photo or electron lithography.

2.1.1 Lithography process

To design devices at nano or micro scales, the use of lithography is of direct relevance. The principle is the same, whether photo or electron lithography are used (Figure 2.1):

- A layer of photo (or electron) sensitive resist is spin coated on the heterostructure surface. This results in a uniform thin layer. The choice of the resist depends

obviously on the technique used (photo or electron lithography). In addition the thickness of the resist layer can vary from $\sim 100nm$ to $\sim 1\mu m$, depending on the resist used and on the spin coating duration.

- The resist is exposed with a beam of light (or electrons). The wavelength of the light (electrons) defines the smallest size of the objects which can be patterned. The photo lithography is done with photons in the UV range ($\lambda_{UV} \sim 200nm$), and consequently we are not able to use it in order to define nanometer size patterns, which is generally done with electron lithography. For a positive resist, the exposed part becomes soluble in the chemical developer, and can be consequently removed. For a negative resist, the inverse happens.

- Afterwards a layer of metal is deposited uniformly on the surface of the sample by using a metal evaporator. The desired metal thickness imposes the use of a resist whose thickness is much larger than the metal. Otherwise some problem can be encountered during the removal of the resist, called "bridging". We generally try to use a resist layer at least three times thicker than the metal layer.

- The last step is the removal of the resist by using solvents like acetone. Afterwards all the metal which was sitting on the top of resist is removed, and only the desired pattern remains. This is the so-called "lift-off".

2.1.2 Etching

As we will see, a step of etching is required. Indeed we want to remove some part of the 2DEG in order to avoid any shorts between the ohmic contacts(see after). Several etching techniques can be employed. The one used during this thesis is IBE(Ion Beam Etching). It consists of attacking the surface of the sample with ions (Argon) that have been accelerated. In order to protect the part of the sample which don't have to be etched, a metal mask (Aluminium) is deposited on the surface, as explained in the previous section. By using an IBE machine, the heterostructure can be etched, except for the part covered by the aluminium mask. Indeed the GaAs is etched much faster than the aluminium (for 100nm of etched GaAs, only few nm of Al are generally etched). Then the aluminium layer is removed with NaOH (Figure 2.2).

2.1.3 Nanofabrication steps

Thereby all the nanofabrication steps can be done by using these techniques sequentially in five steps. All these steps have been achieved in the clean room of the laboratory and we describe here the goal of each of these steps (Figure 2.3). The complete recipe can be found in annexe.

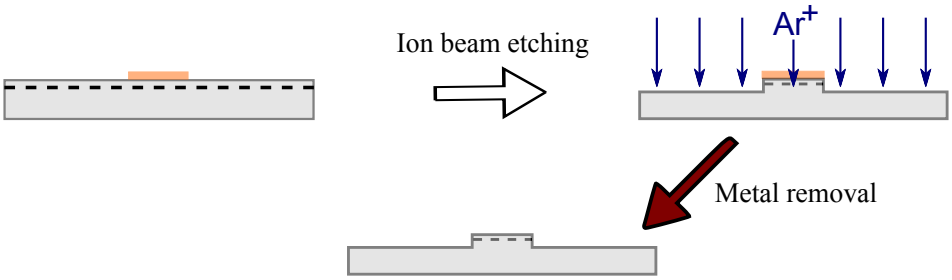

Figure 2.2: **Description of an etching step.** After deposition of a metal layer (Aluminium), the sample is etched using IBE (Ion Beam Etching). The metal acts as a mask and only the part of the surface not covered by the metal is etched. Afterwards the metal is removed.

- **Alignment marks :** Starting from the bare wafer of GaAs/AlGaAs, metallic crosses (Ti-Au) are deposited on the surface of the sample in order to align the following steps together (yellow parts in figure 2.3 (a)). This is done by using photo lithography. The alignment requirement in our case is of the order of $\sim 1\mu m$.

- **Mesa etching :** As we will see, the 2DEG is contacted by the ohmic contacts. Without etching the 2DEG all these contacts would be shorted via the gas. The electrical isolation is guaranteed when all the Si donors in the AlGaAs layer are removed during the etching process, since they provide the electrons to form the 2DEG. The remaining unaffected regions by the etching form a conducting area called the "mesa"(blue parts in figure 2.3 (b)). An aluminium mask is designed with a photo lithography machine, and then the heterostructure is etched with an IBE machine. Although the electrical isolation is ensured when all the Si donors in the AlGaAs layer are removed, we have etched away around 100nm of heterostructure in order to do not take any risks. The aluminium layer is then removed by using a highly concentrated NaOH chemical solution.

- **Ohmic contacts :**The 2DEG is embedded 100nm below the surface of the sample. So first we have to contact it, in order to perform measurements. The idea is to diffuse a metal alloy to define an electrical contact with the gas. This is done by rapid thermal annealing (RTA) of surface electrodes (orange parts in figure 2.3 (c)) made out of a sandwich of nickel and gold-germanium. During the RTA process, the electrode metal melts, diffuses into the heterostructure and forms an ohmic contact with the 2DEG. The incorporation of germanium plays two roles. First of all, with gold it forms an eutectic with a melting point around $360^{\circ}C$. It allows us to avoid to anneal the sample at the gold melting point ($1064^{\circ}C$). At this temperature Ga atom of the heterostructure would sublimate, and then the wafer would be damaged

(Sublimation point $490^{\circ}C$). On the other hand germanium atoms provide dopants in the GaAs region near the metal interface reducing thereby the heterostructure diffusion barrier formed between the metals and the semiconductor. The nickel plays an important role to improve the uniformity of the contacts, and to enhance the adhesion of the electrode to the substrate. This will be really appreciated when we will have to wire bond the sample. One more time this step is done with a photo lithography machine. The typical resistance of 200 μm^2 contact between the surface and the 2DEG is equal to $\sim 1k\Omega$ at low temperature ($T \leq 4K$).

- **Thin gates :** In order to define the actual device geometry, a set of thin gates has to be made. Due to the typical size of the potential that has to be reached ($\sim 50nm$), it induces some constraints on the gate sizes. That is the reason why a step of electron lithography has first to be made in order to define the thin gate patterns (middle of the sample in figure 2.3 (d)). Therefore the desired geometry of gates $\sim 25nm$ thick (5nm of Ti and 20nm of Au) is deposited on the central part of the wafer (mesa, blue in figure 2.3 (d)). It allows for defining a typical potential size equal to $\sim 50nm$. By considering a parabolic quantum dot, its size d is related to the orbital energy Δ by the formula $d = \sqrt{\frac{\hbar^2}{m\Delta}}$. Then with $d \sim 50nm$, we get $\Delta \sim 1meV$.

- **Large gates :** Finally large gates (yellow part in figure 2.3 (e)) are patterned to contact the bonding pad (ohmic contacts) with the thin gates. There are two main reasons to separate this step from the previous one. First due to the etching of the heterostructure, there is a stair $\sim 100nm$ high between the mesa and the rest of the wafer. Then the gate thickness ($\sim 20nm$)deposited in the previous step could be a problem. In addition the time needed to "write" a pattern with the electron lithography process is much longer than the photonic one.

Finally when all these steps have been realized, the sample is glued on a chip carrier. Then the sample bonding pads are wire bonded to chip carrier. The sample is finally ready to be measured.

2.2 Cryogenics

As our experiments required to work at temperature $T \ll 10K$ we briefly review the functioning of a dilution refrigerator which allows for temperature $T \sim 10mK$ and for specific details we let the reader refer to [1]. The main idea proposed originally by London, Clarke and Mendoza [2] stands on the thermodynamic properties of ^3He and ^4He mixtures. If the temperature of any solution $^3He/^4He$ of more than 6% ^3He is sufficiently lowered, the mixture will separate into two phases. One of these phases will (at $T < 0.8K$) be almost pure ^3He. The other one will be mostly pure ^4He, but even

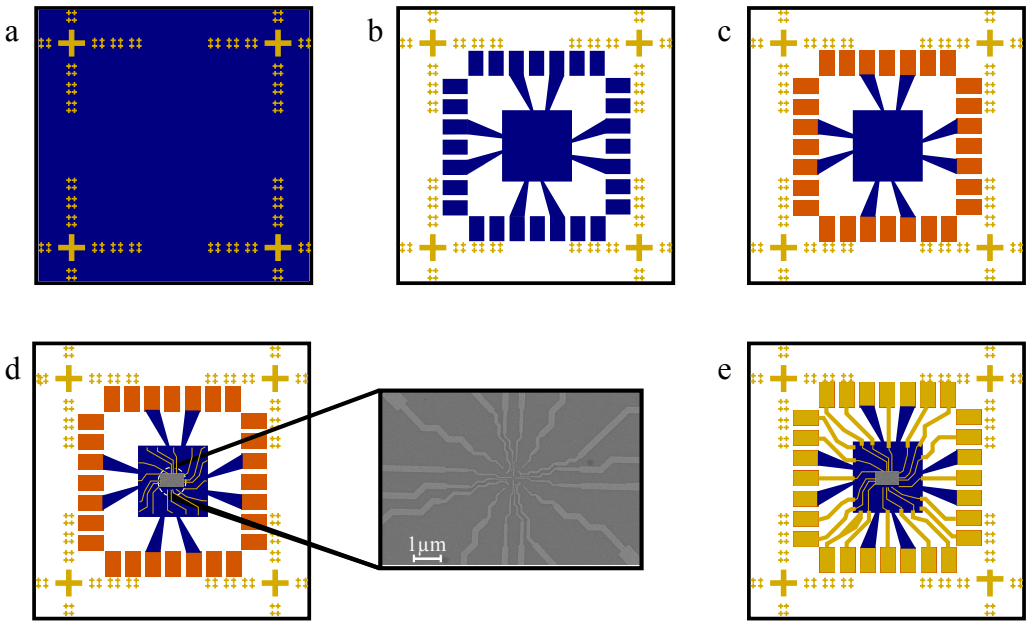

Figure 2.3: **Description of the nanofabrication steps.** **(a)** Alignement crosses. **(b)** Mesa etching. **(c)** Ohmic contacts. **(d)** Fine gates. **(e)** Large gates.

at $T = 0$, will contain a fraction of $\sim 6\%$ ^3He impurity. This property is the key of the operation of dilution refrigerator. If we consider a mixing chamber (Figure 2.4, mixing chamber) holding a solution of $^3He - ^4He$, at low temperature the light phase rich in ^3He atoms will float on top of the heavy phase poor in ^3He atoms. At the boundary of the the two phases, an effective liquid-vapor interface of ^3He develops below 0.7K. By pumping on the poor ^3He phase, the equilibrium is broken. In order to re-establish the equilibrium, ^3He atoms from the rich ^3He phase will migrate towards the poor one. This process is an endothermic process, and the energy will be taken from the environment, being in our situation the mixing chamber and the sample thermally anchored to it. By injecting back the ^3He into the mixing chamber, it can be reproduced continuously and enables in principle to cool down samples below 10mK. During this thesis, two different dilution refrigerators have been used. The one used for the third chapter allows for base temperature equal to $\sim 10mK$. The one used for the fourth and fifth chapter should allow for the same base temperature, but due to contact between a RF coaxial line and a 4K part, the working temperature was equal to $\sim 150mK$. Figure 2.4 shows a schematic representation of the dilution stage of a refrigerator.

2.3 DC electronics

To measure lateral quantum dot systems, the electronic set-up is very important. Indeed the confining potential is defined by applying negative voltages on metallic gates. As mentioned in the introduction, the typical energy scale of such a potential is of the order of $\sim 1meV$. The first requirement is then to get a low noise and stable voltage source. Moreover to probe the system we measure currents which are quite small (100pA). Therefore the acquisition chain has to be low noise too.

2.3.1 Voltage sources

The voltages sources used in our experiment is based on a commercial digital-to-analog converter (DAC) chip : Linear Technology LTC2604. The main interests of this chip is its 16 bits, the operating range -5V to 5V, its low output noise and its "high" speed. The resolution of a single voltage source is $150\mu V$ with 30 $nV\sqrt{Hz}$ noise. The output voltage is stable with respect to time and temperature. The sources has a thermal drift of $0.25ppm/^{\circ}C$, and they exhibit a drift smaller than $10\mu V$ in 10 hours. In addition the power supply part of the voltage sources has been optically isolated in order to reduce problems related to ground loop (50Hz). The present set-up allows to change one of the sources every microsecond, with a rate limited to 300 mV μs^{-1}. This point will be very crucial to explore the parameter space of the system, that is to say to tune the device. Indeed the number of gates for quantum dot systems can be large. For instance the quadruple quantum dot device presented in the next chapter holds 16 gates. The ability

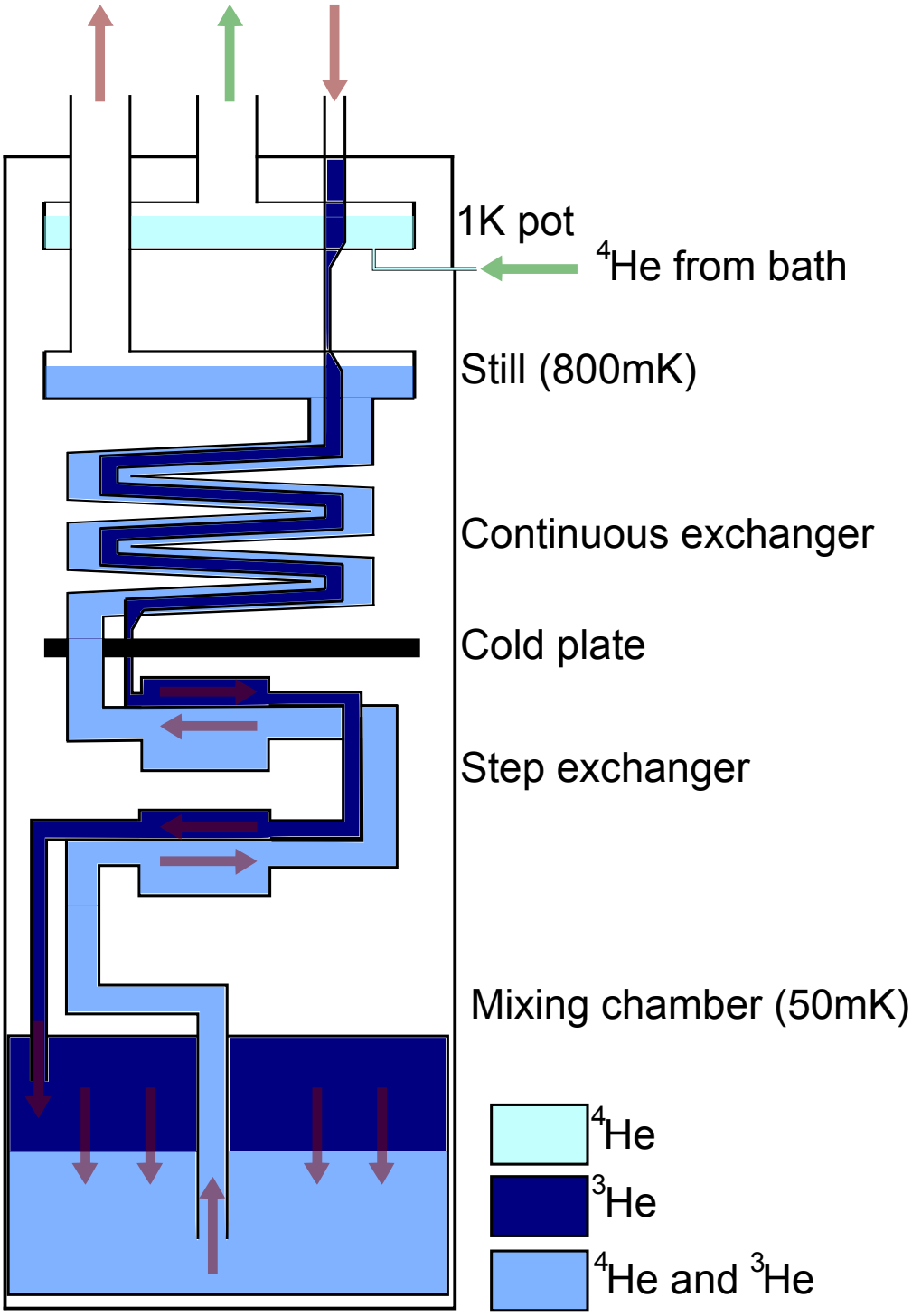

Figure 2.4: **Scheme of a dilution refrigerator.**

to explore this gate voltage parameter space on a fast time-scale is appreciable.
The DACs are controlled by a National Instruments Single Board RIO 9602. This board hosts a FPGA (Field Programmable Gate Array), a chip hosting logic gates that can be rewired during a programming stage. This is an ideal tool for digital electronics prototyping. In addition an embedded microcomputer takes care of the communication between the board and a computer.
As we have mentioned, the gate voltages defining the potential has to be as stable as possible, and also low noise. This is first achieved by using the voltage sources described previously but also by filtering the output voltage of these sources. The idea is to filter as much as possible the high frequency part of the noise spectrum. For this reason the dilution refrigerator had been wired with "Thermocoax" [3] cables exhibiting a low pass cut-off frequency at $\sim 100MHz$. Filtering the signal at low temperature gives rise effectively to a reduction of the noise spectrum. Three low pass filters (with cut off frequency at 80MHz, 1MHz, and 1kHz) have been put at the output of the voltage sources. By considering the present bandwidth ($\Delta f \sim 1kHz$) we get a voltage noise applied to the device smaller than $\sim 1\mu V$ (30 $nV\sqrt{Hz}$ noise time $\Delta f = 1kHz$).

2.3.2 Amplifiers

The current coming out of the system in response to a voltage excitation is collected by an home made current-to-voltage converter (IV converter), based on a Texas Instruments TLC2201 operational amplifier. Since the currents we want to deal with span in a range of a few hundreds of pA to a few nA, the noise of this amplifier has to be as small as possible. The progress in electronics is such that the IV converters are only limited by the Johnson-Nyquist noise of the feedback resistance giving the gain of the amplifier. Most of the measurement performed during this thesis have been done with a gain of 10^8, that is to say a $100M\Omega$ feedback resistance. This leads to an input current noise of $\sim 10fA/\sqrt{Hz}$. Considering the bandwith of the amplifier $1kHz$, it leads to $300fA$ noise. Finally the output voltage is directly measured by two Keithley K2000, transferring the data to a computer.

2.4 RF electronics

To manipulate a single spin electrically the gate voltage operations have to be made faster than the relaxation time of the spin, that is to say a few μs. The voltage sources described earlier do not allow to perform faster than $1\mu s$ operations. Then a RF (Radio frequency) generators has been used. To bring down to the sample the high frequency signal, four coaxial lines (with proper high frequency transmission) have been added into the dilution fridge.

2.4.1 Coaxial lines

The addition of these coaxial lines gives rise to two main issues. The first role of these lines is to guide down to the sample excitations in the GHz range. So the use of filters, or "Thermocoax" coaxial lines is not relevant (the cut-off frequency of these coaxial lines is equal to $\sim 100MHz$). But we still need to attenuate the electromagnetic noise transported by the lines in order to not cancel all the filtering which has been discussed previously. Therefore an attenuator (-20dB) is placed at 4K in order to reduce the electromagnetic excitations from 300K. The same operation is done to attenuate the excitations from 4K by placing another attenuator (-10dB) at the mixing chamber (Figure 2.6). In addition this attenuation allows for reducing of the noise coming from the RF generator. To decouple thermally speaking the 4K stage and the low temperature one (mixing chamber), superconducting CuNi coaxial lines have been used between these two stages.
On the other hand, these lines has to be connected to the gates. The idea is to superpose on some gates the DC voltages generating by the DACs and the high frequency signal. For this purpose home-made bias tees have been used. A bias tee is a device with two inputs, one for the DC and one for the RF voltages (figure 2.5). Its output gives the sum of these two voltages. In order to avoid any "leakage" of the RF signal into the DC input, a low pass filter is added (R and C_{DC} in figure 2.5). Similarly a capacitance protects the RF input for the DC signal (C_{RF} in figure 2.5, high-pass filter with the 50 Ω impedance of the coaxial line). The typical value of these components is $R = 1k\Omega$, $C_{DC} = C_{RF} = 1nF - 10\mu F$. It gives the lowest frequency that can pass trough the RF input equal to $20kHz - 20MHz$ and the highest in the DC input equal to $1kHz - 1MHz$.

2.4.2 RF signal generator

During the thesis we have used an arbitrary waveform generator AWG 5014B from Tektronix. This generator has a sampling rate of $1.2GHz$ and a resolution of 14 bits on the range $\pm 4.5V$. It allows to generate complex waveforms on 4 different synchronized channels. The generator was connected to a computer, from where the waveform were designed. In addition the generator can be triggered by the FPGA.

2.5 Software

All the instruments used for the measurements were connected to a computer, and can be controlled directly from it via a home made software. The main purpose of this software is to be able to change every parameters of the experiments, like the gate voltages, the magnetic field, the RF waveforms, etc. The computer hosting this software recovers the data points and store it into a file. Figure 2.7 shows a schematic view of the acquisition chain used during this thesis.

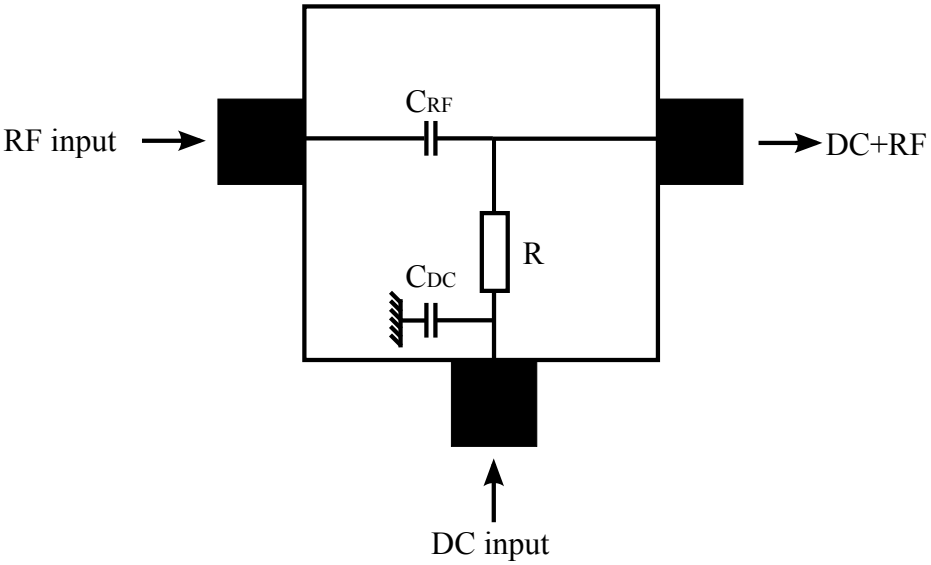

Figure 2.5: **Scheme of a bias tee.** The device is made of two inputs (RF and DC) and one output ($RF + DC$).

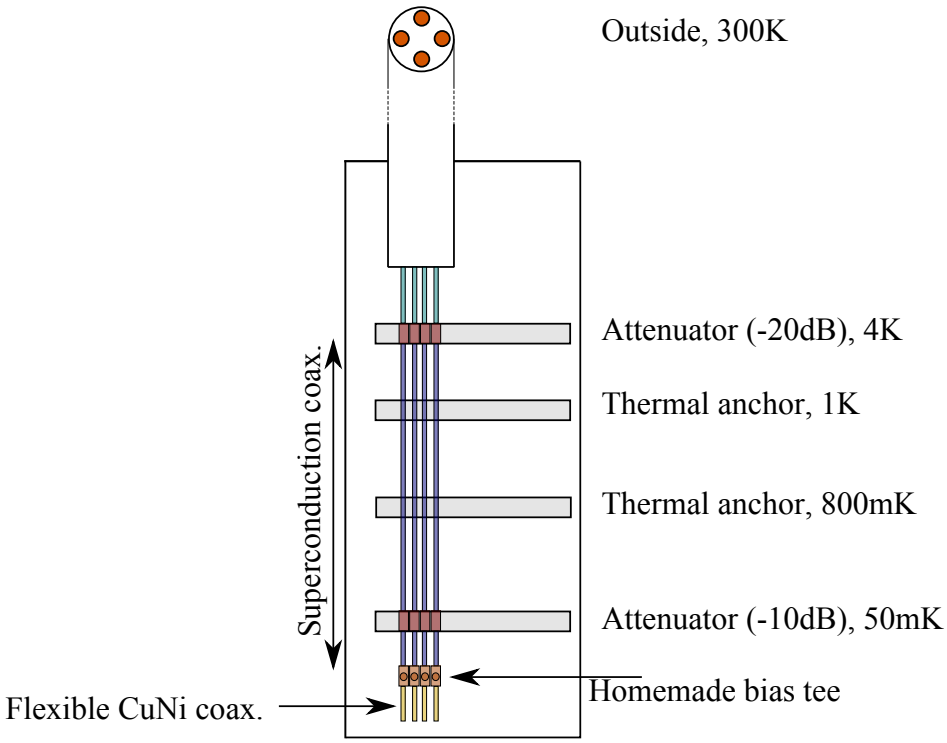

Figure 2.6: **Scheme of the RF coaxial lines, and their thermal anchoring.**

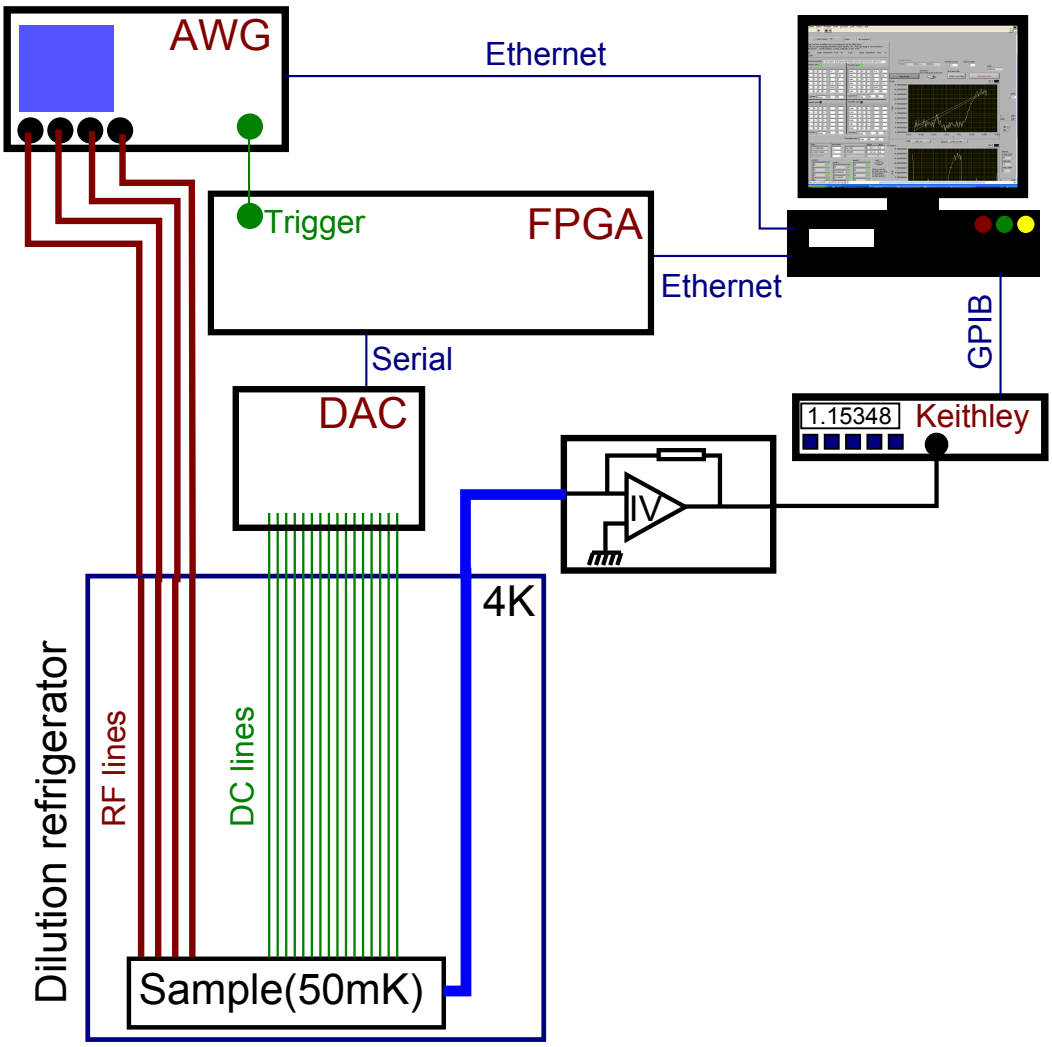

Figure 2.7: **Schematic view of the acquisition chain used to measure lateral quantum dot, and to do spin manipulation.**

Bibliography

[1] Lounasmaa, O. *Experimental Principles and Methods Below 1K*. Academic Press Inc, (1974). 38

[2] London, H., Clarke, G. R., and Mendoza, E. *Phys. Rev.* **128**, 1992–2005 Dec (1962). 38

[3] Zorin, A. B. *Review of Scientific Instruments* **66**(8), 4296–4300 (1995). 42

Chapter 3

A few-electron quadruple quantum dot in a closed loop

Résumé

Dans ce chapitre nous discutons la réalisation d'un dispositif de quatre boîtes quantiques couplées. Nous démontrerons que ce dispositif nous permet de contrôler le transport d'un électron unique le long d'un circuit fermé. Dans le contexte des qubits de spin, ce résultat ouvre la voie à des manipulations topologiques utilisant l'interaction spin-orbite.
Après avoir exposé les motivations qui nous ont amené à étudier un tel système, nous décrirons en détail les états de charge de différents systèmes de boîtes quantiques couplées. En commençant par un système composé d'une boîte quantique unique, nous aborderons le cas de boîtes quantiques multiples en les ajoutant les unes après les autres. Les diagrammes de stabilité de tels systèmes seront étudiés théoriquement en détail, nous permettant ainsi d'expliquer les réalisations expérimentales de ces diagrammes pour une quadruple boîte quantique. Nous verrons alors que les résultats expérimentaux démontrent que la géométrie étudiée permet de vider toutes les boîtes quantiques du système, ainsi que de contrôler la population électronique de chacune d'entre elles.
Nous démontrerons alors qu'il est possible de vider le système de tout électron, de faire entrer dans une des boîtes quantiques un électron unique, et de le transporter d'une boîte quantique à l'autre par des processus tunnel.

3.1 Motivations

In the context of quantum computing, a key challenge is to achieve sufficiently low error probabilities for qubit manipulations [1]. Indeed a quantum computer relies on the manipulation of quantum states stored in qubits. In order to build quantum algorithms, we need to perform some elementary operations on these quibts. These operations rely on physical manipulations of the qubits states, and due to their nature they are generally submitted to errors, meaning that the final state (the qubit state at the end of the manipulation) might not be the desired one. Let me introduce a simple example in order to understand this error concept. Let consider a spin $\frac{1}{2}$ experiences an external magnetic field $\mathbf{B} = B\hat{z}$. We assume the qubit (the spin) being prepared in the following superposition of states $|\Psi(\tau = 0)\rangle = 1/\sqrt{2}(|\uparrow\rangle + |\downarrow\rangle)$. Due to the external magnetic field, this state evolves coherently and the phase difference depends on the magnetic field amplitude (defining the qubit energy splitting E_Z) and on the evolution duration τ :

$$|\Psi(\tau)\rangle = \frac{1}{\sqrt{2}}(|\uparrow\rangle e^{\frac{iE_Z\tau}{2\hbar}} + |\downarrow\rangle e^{-\frac{iE_Z\tau}{2\hbar}}) \tag{3.1}$$

This manipulation can be seen as a qubit rotation around the $\hat{z}$ axis in the Bloch sphere representation of the qubit (see chapter 1). Let consider a quantum algorithm needing a π-rotation around the $\hat{z}$ axis, which can be done by letting the initial state evolves according to time. For $\tau = \tau_1 = \pi\hbar/(2g^*\mu_B B)$, the system is in the state (up to a global phase) $\Psi(\tau = \tau_1)\rangle = 1/\sqrt{2}(|\uparrow\rangle - |\downarrow\rangle)$, and a π-rotation around the $\hat{z}$ axis has been performed. From an experimental point of view, it is almost impossible to get an evolution duration τ exactly equal to τ_1, and this implies an error on the final state scaling with $|\tau - \tau_1|$. This example shows that the concept of errors is something inherent to quantum manipulations.

On the other hand topological features can be used in order to overcome such errors. Indeed Berry demonstrated in 1984 [2] that a quantum system could be manipulated by driving it adiabatically along a closed path in the parameter space. In particular, he demonstrated that the final state of this system differs from the initial one by a phase. This phase includes the dynamical phase (depending on time and on state energies), but also another contribution, known today as the geometric or Berry phase. The particularity of this phase relies on its path dependence instead of energy and time dependences. Therefore if we are able to engineer and control this path in the parameter space, we should be able to manipulate a qubit state in a topological manner, meaning that this manipulation depends only on the path while the time dependence issue has been overcome. To illustrate this concept, a classical picture can be introduced. Considering a tangent vector $\vec{v}$ on the surface of a sphere transported from the north pole around the path C (red in figure 3.1), with $\vec{v}$ pointing south at all time. Even if the initial and final position are the same, the final state $\vec{v}_f$ is rotated compared to the initial one $\vec{v}_i$ by an

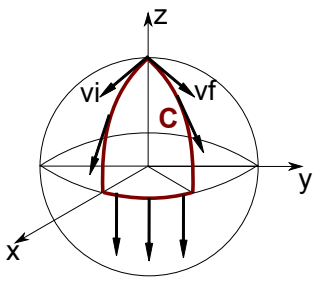

Figure 3.1: **Classical picture of the geometric phase.** The initial vector $\vec{v}_i$ does not point along the same direction than the final one $\vec{v}_f$

angle equal to the solid angle subtended by the path C at the origin. We see clearly that this angle depends only on the geometry of the path C, and not on the rate at which it is traversed. This angle is nothing else than a classical geometric phase.

In the context of semiconductor spin qubits, it has been recently demonstrated that topological manipulations could be obtained if the electron is driven along a closed path in the real space under spin-orbit interaction [3, 4]. The effect of the closed path can be modelled by an effective magnetic field, being path dependent, acting on the electron spin (figure 3.2 (b)). Although manipulations using spin-orbit interaction have been experimentally reported [5, 6, 7], these measurements do not take advantage of the topological features that we described. In this sense, the first step toward topological manipulations consists of being able to engineer and to control the path of a single electron. Two solutions are conceivable :

- This electron can be confined in a single quantum dot. Then the confining potential has to be modified in such a way that the position of the electron is changed according to time. In other words, the quantum dot moves, and consequently the electron trapped inside follows this movement. Recently, fast and efficient single electron transport have been obtained through a 1D channel (a long depleted channel), electrostatically defined, with SAW(surface acoustic waves)[8, 9]. Nevertheless, such a technique is restricted to a displacement on a straight line.

- To perform more complex displacements, engineering the path of a single electron with series of quantum dots is a promising alternative (Figure 3.2 (a)). By building an array of quantum dots (qubits), we can consider to transfer the electron from one quantum dot to another one by sequential tunnelling processes.

The solution chosen was the second one. We decided to use a system of a quadruple quantum dot in a square-like configuration. This geometry should allow to transport a single electron along a closed path, and open the way toward the topological manipulation. In addition, the transport of a single electron into a quantum dot array gives rise to a

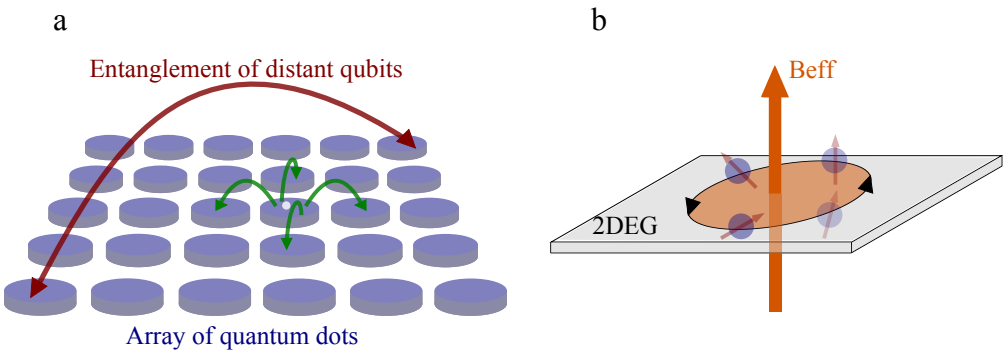

Figure 3.2: **(a) Array of quantum dots.** A single electron can be transported from one dot to any other by sequential tunnelling, allowing for entanglement of distant qubits. **(b) single electron transported along a closed path.** Due to spin orbit interaction, its spin feels an effective magnetic field, opening a new way to manipulate it.

possible way to scale system of spin qubits up. Indeed we can consider to entangle two qubits of this array by transporting a single electron from one of these qubits to another one. Finally, up to now, only triple quantum dot devices have been reported. Thus the experimental realization of a quadruple quantum dot presents an interesting challenge from a technical standpoint.

3.2 Geometry

The design of the geometry of several coupled quantum dots is challenging. In fact in the context of laterally defined quantum dots, the potential which traps the electrons, is engineered with the help of electrostatic gates. The number of these gates scales generally with the expected number of interacting quantum dots. It is therefore important to think about the arrangement of these gates, keeping in mind the role of each gate. A scanning electron microscopy coloured picture of the sample which has been measured can be found on figure 3.3 (a). As we will see, this gate pattern allows us to define a quadruple well potential, which confines the electrons. The red gates are used to create a tunnel barrier between the quantum dots while the yellow ones are used to define tunnel barriers with the leads and to control the electrochemical potential of each quantum dot. By modifying the voltage applied to these gates, the electrochemical potential of each quantum dot can be changed, and consequently the electronic population can be controlled. Finally the blue gates are used to form quantum point contacts that we use as charge detectors to probe changes in the electronic population of the system.

To converge to such a geometry, simulations of the potential generated by these gates have been performed. Because of the size of the well, which is comparable to the wave-

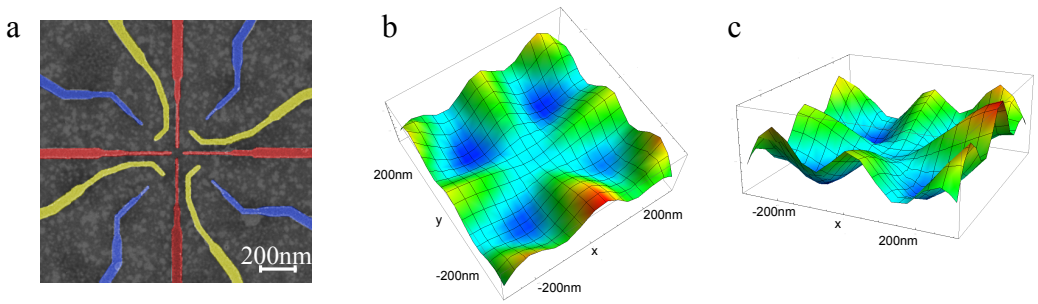

Figure 3.3: **(a) Gate geometry.** SEM (scanning electron microscopy) of sample measured. **(b) and (c)** Simulation of the potential generated by such gate geometry.

length of the electron ($\lambda_f \sim 40nm$), quantum mechanical treatments may be needed. Especially a solution of the Schrödinger equation which is self-consistent with the electrostatic potential should be found [10]. But such a simulation needs some skills, and it's a major numerical task. In contrast with a quantum treatment, a simple resolution of the Laplace equation ($\Delta\Phi = 0$ where Φ is the potential) could already give an idea of the potential [11] as we can see on figure 3.3 (b) and 3.3 (c). This model allows for calculating the electrostatic potential in a plane "d" nm below the surface of the heterostructure covered by a set of gates. We assume that the surface occupies the (x,y) plane and z the growing axis of the heterostructure ((x,y,z=0) corresponds to the surface, while (x,y,z=d) is the 2DEG. The boundary conditions are the following :

- The surface potential $\Phi(x, y, 0)$ is set at 0 always except on the gate, where it is pinned to V_g the gate voltage.
- The potential is also subjected to the boundary condition $\frac{\partial\Phi}{\partial z} = 0$ as $z \to \infty$

Then we have to find a solution $\Phi(\mathbf{R})$ (where $\mathbf{R} = \{x, y, z\}$) to the Laplace equation $\Delta\Phi = 0$ which respects the boundary conditions.
Davies and coworkers [11] demonstrated that the potential in the plane of the 2DEG comes as :

$$\Phi(\mathbf{r}, d) = \int \frac{|d|}{2\pi([\mathbf{r} - \mathbf{r'}|^2 + d^2)^{\frac{3}{2}}} \Phi(\mathbf{r'}, 0) d\mathbf{r'} \tag{3.2}$$

where $\mathbf{r} = (x, y)$. They derived from this formula the potential generated by different gate geometry and for a finite rectangle gate pinned to V_g and defined by $L < x < R$ and $B < y < T$, they obtained :

$$\Phi(x,y,d) = V_g[g(x-L,y-B)+g(x-L,T-y)+g(R-x,y-B)+g(R-x,T-y)]$$
$$where \qquad g(u,v) = \frac{1}{2\pi}arctan(\frac{u.v}{d.R}) \quad ; \quad R=\sqrt{u^2+v^2+d^2} \tag{3.3}$$

By considering the gates as rectangles and by using the superposition principle (the system is linear), we can add the contribution of several gates simply by adding the potential generated by each gate. Such simulations have been performed for the gate geometry presented in figure 3.3 (a). These simulations (figure 3.3 (b) and (c)) show clearly the presence of the four wells separated by potential barriers (tunnel barriers). In addition we observe that the barriers between diagonally opposite quantum dots seem quite wider compared to the one of close-by quantum dots. It allows us to expect a bigger coupling between close-by quantum dots. Before presenting the measurements, we will describe the expected charge states of such a system. We notice that all along this chapter, only the charge degree of freedom of the electrons will be investigated, without paying attention to the spin degree of freedom. Therefore we will develop the charge states of multiple quantum dot systems, and in particular, for the understanding of the stability diagrams of the quadruple quantum dot system, we will give the main "ingredients" in order to understand them.

3.3 Charge states : From a single to a quadruple quantum dot

Until now we have only considered the case of a single quantum dot. We have studied its charge and spin states. The question we want to address concerns the case of several coupled quantum dots. One solution to it can be found in the CI model : the coupling between these quantum dots is then considered as purely capacitive and the electrostatic energy of the overall system has to be minimized. The mathematical development of this model for multiple quantum dots can be found in appendix. We prefer here to work with a "hand waving" approach. Starting with the case of a single quantum dot studied in the first chapter, we will add one after one the other quantum dots, considering them first as independent (uncoupled), and finally we will "branch" the coupling between them.
Along this section, different systems of coupled quantum dots will be introduced. For each of those, we assume that each quantum dot is coupled to a Fermi sea (Reservoir) at the Fermi energy E_F, with which it can exchange electrons. It is worth noticing that this exchange is a tunnelling process, even if this quantum effect is not needed for the electrostatical model. Moreover, quantum dots are coupled to each other, capacitively, but also through a tunnel barrier.

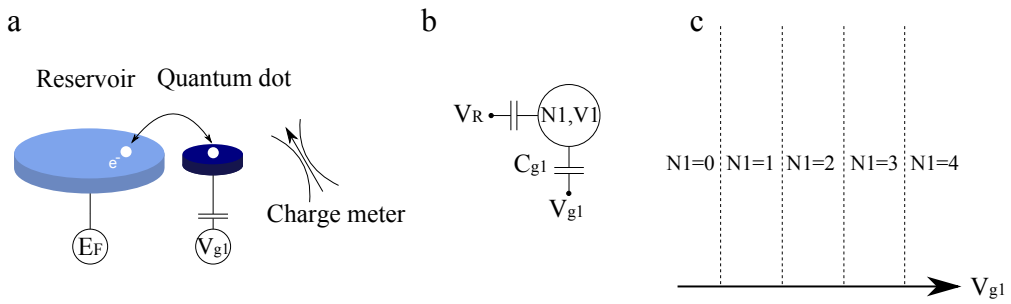

Figure 3.4: **(a) Single quantum dot.** It is coupled to a Fermi Sea at E_F and its energy can be tuned by changing the voltage applied to a gate capacitively coupled to the 2DEG. **(b) CI model for a single quantum dot. (c) Stability diagram of a single quantum dot.** It defines the charge states of a single quantum dot with respect to the gate voltage V_{g1}.

3.3.1 Charge state of a single quantum dot

It has been demonstrated in the first chapter, by using the CI model (Figure 15 (a) and 15 (b)), that the charge states of a single quantum dot are a collection of electrochemical potential levels separated by the charging energy $E_{C1} = \frac{e^2}{2C_1}$. The energies of these levels depend on the gate voltage V_{g1}, and for each value of V_{g1} a ground state can be defined. It corresponds to the largest number of electrons N_1 leaving $\mu(N1) < 0$ (μ being the electrochemical potential, see chapter 1). Therefore the electronic population changes with respect to the gate voltage, and the commonly used picture is the stability diagram.

Such a diagram exhibits regions in the gate voltage space where the number of electrons in the quantum dot system is well defined (15 (c)), defining for each of these regions a ground state. These regions are separated by charge degeneracy lines, and the distance between two charge degeneracy lines is equal to the charging energy E_{C1}. For a single quantum dot, a single gate is sufficient to control its electronic population, and then the stability diagram is 1-dimensional (vertical parallel lines in figure 15 (c)). The passage from one region to another one is related to the exchange of an electron with the reservoir and this process is a tunnelling process. Therefore from an experimental point of view, if the measurement duration (time spent at each value of the gate voltage) is much longer than the tunnelling time, the measurement of the ground state is ensured. To probe the stability diagram of a single quantum dot, we can perform transport through the quantum dot, or we can use a charge meter capacitively coupled to the system. These measurements have already been shown in the first chapter, and in the following we will only use the charge detection technique in order to probe the charge states of multiple coupled quantum dot systems.

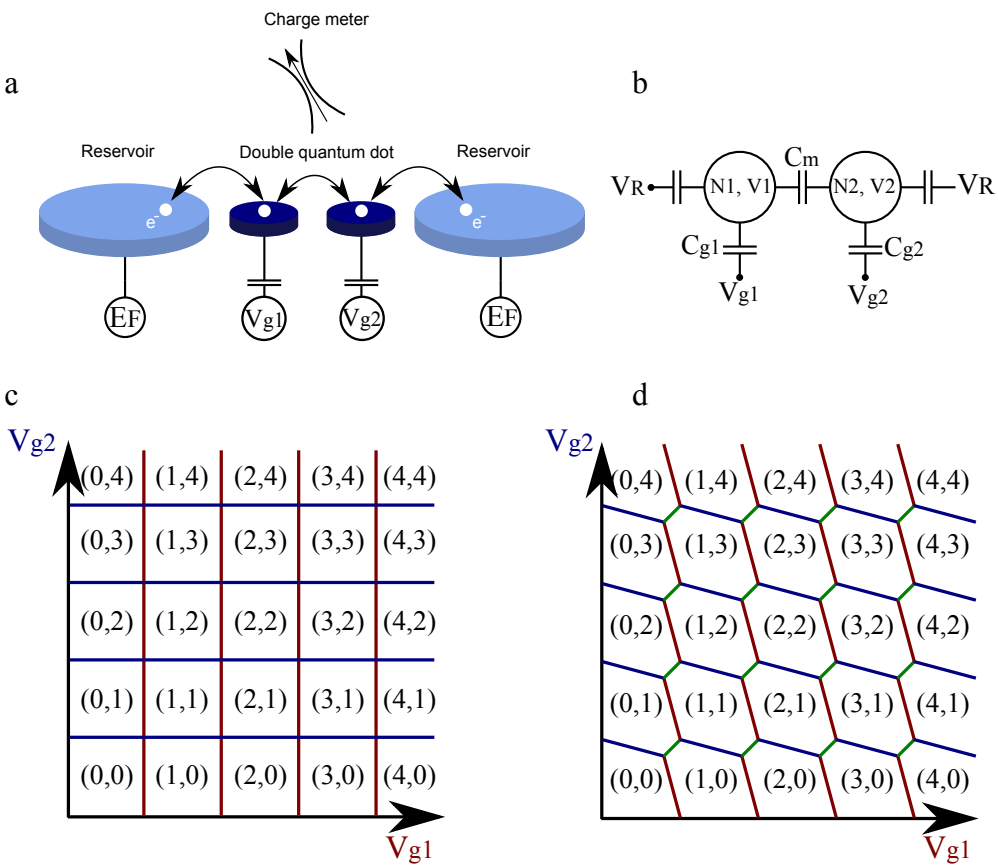

Figure 3.5: **(a) Double quantum dot system.** They are both coupled to a Fermi Sea at E_F, and their energy can be tuned thanks to a gate. **(b) CI model for a double quantum dot.** The coupling between those can be tuned from a low coupling regime $C_m \to 0$, to any higher coupling $C_m \neq 0$. **(c) and (d) Stablity diagram of double quantum dot.** For a vanishing coupling (c), and for finite coupling (d)

3.3.2 Charge state of a double quantum dot

To start the study of a double quantum dot system, we first consider that the two systems are totally independent. Hence we can study each quantum dot as a single one. Each of them is coupled to a reservoir pinned at the Fermi energy E_F, and their potential can be changed independently via the gate voltages V_{g1} and V_{g2} (Figure 16 (a)). The stability diagram of two uncoupled quantum dots is given in figure 16 (c). It is a two dimensional (V_{g1} and V_{g2}) diagram where regions with fixed number of electrons in both quantum dot are delimited by charge degeneracy lines. The size of these regions is related to the charging energies associated to the quantum dots E_{C1} and E_{C2}. In figure 16 (c), we assumed $E_{C1} = E_{C2}$ giving square-like regions.

We consider now that the quantum dots are capacitively coupled (capacitance C_m in

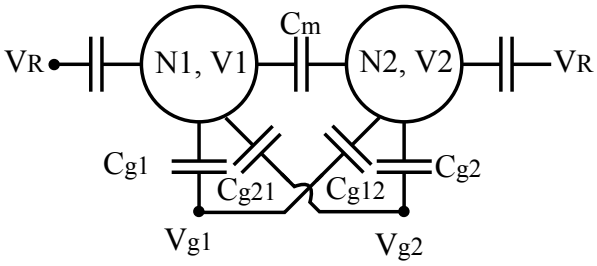

Figure 3.6: **Cross talk.**Modelisation of the cross talk in the CI model.

figure 16 (b)). The coupling introduces two features compared to the uncoupled picture:

- A change of gate voltage V_{g1} (V_{g2}) will also change indirectly the energy of the quantum dot 2 (1). For instance by setting V_{g1} more negative, the potential of the quantum dot 1 will increase. Due to the capacitive coupling between the two quantum dots (capacitance C_m), it will increase the potential of the quantum dot 1. The consequence is that the degeneracy lines get finite slopes (Figure 16 (d)).

- The addition of an electron in the quantum dot 1 (2) will increase the energy of quantum dot 2 (1). This is due to the coulomb repulsion, and it gives rise to a "new" charging energy, called the mutual charging energy E_{cm}. This can be seen by the opening of a "gap" at the crossing of two charge degeneracy lines (green lines, Figure 16 (d)). These green lines correspond to degeneracies between (N,M+1) and (N+1,M) charge states, where (N,M) indicates the electronic population of quantum dot 1 and 2.

In the following this approach will be used to study qualitatively charge states of triple and quadruple quantum dot. But one more ingredient is needed to go further. We have not yet considered what is called the "cross talk". A gate is not coupled only to a single dot, and a small capacitive coupling between this gate and the adjacent quantum dot has to be taken into account. It means that a voltage change of V_{g1} (V_{g2}) influences mainly the energy of quantum dot 1 (2), but also to a lesser extent directly the energy of quantum dot 2 (1). We use the term "directly" in order to distinguish it from the "indirect" effect via the mutual capacitance discussed previously. In the CI model, it adds two capacitances C_{g12} and C_{g21}, with $C_{g12} \ll C_{g2}$ ($C_{g21} \ll C_{g1}$) (Figure 3.6). We will mainly use this effect in the case of triple and quadruple quantum dots. Thanks to this effect we should be able to control the electronic populations of more than two quantum dots with only two gate voltages.

Experimental stability diagrams of a double quantum dot, whose gate pattern is depicted in figure 3.7 (a), are reported in figure 3.7 (b) and (c). The expected positions of the two quantum dots are represented by the white dots in figure 3.7 (a) and the gate

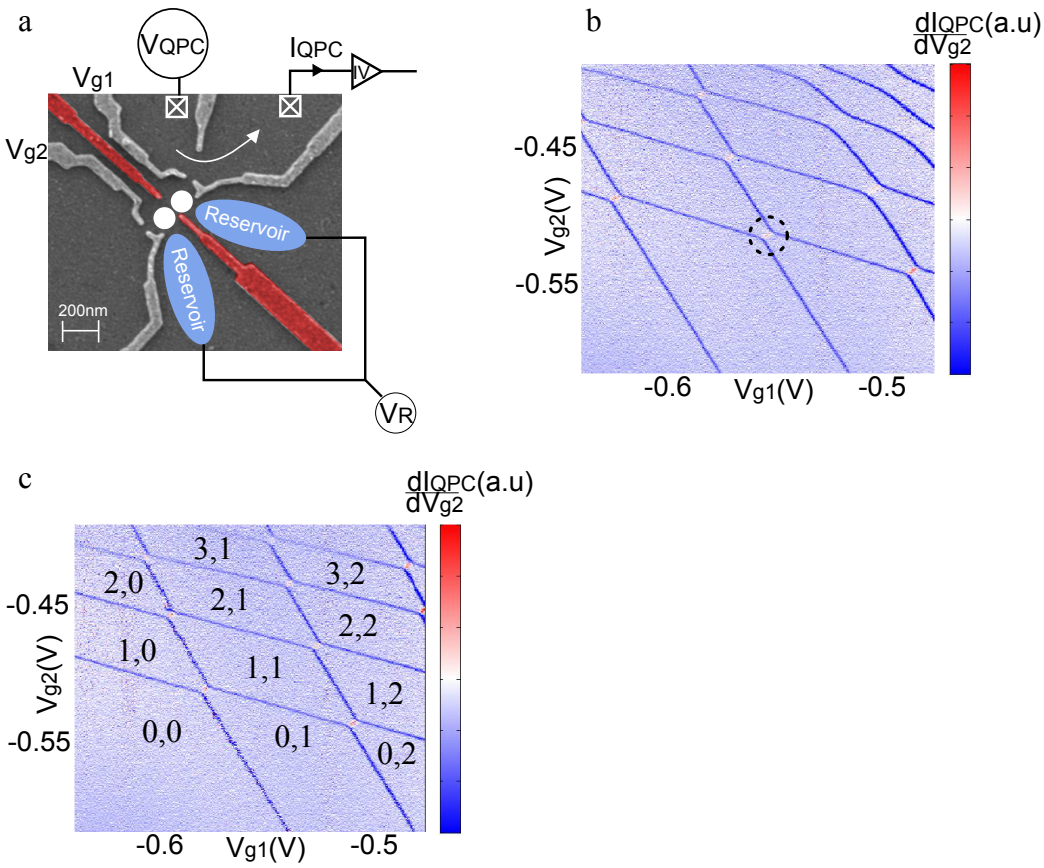

Figure 3.7: **(a) Double quantum dot device.** SEM picture of the double quantum dot measured. By monitoring the current flowing through the QPC I_{QPC}, electronic populations can be probed as a function of the gate voltages V_{g1} and V_{g2}. **(b) and (c) Stability diagrams.** Double quantum dot stability diagram obtained for two different couplings between the two quantum dots (smaller coupling in (c)).

geometry of this device will be discussed in more detail in the next chapter. Charge states are probed by monitoring the conductance of the QPC. Gates V_{g1} and V_{g2} are used to control the energy of each quantum dot, and consequently the numbers of electrons of quantum dot 1 (N_1) and 2 (N_2). As seen in the first chapter, a change in the electrostatic environment modifies the QPC conductance. When an electron enters (leaves) one of the quantum dots, the QPC conductance decreases (increases). The QPC conductance is probed by measuring the current through the QPC in response to a voltage bias ($\sim 500\mu eV$). In order to highlight the degeneracy lines (the positions in the gate voltage space where several charge states are degenerated), we plot the numerical derivative of the QPC current with respect to V_{g2}. In figure 3.7 (b) and (c), two sets of parallel degeneracy lines are clearly observed, delimiting regions where the electronic populations are well defined. The influence of the capacitive coupling between the two quantum dots is clearly observed, especially at the intersection between two charge degeneracy lines, where a small "gap" opens (dotted circle in figure 3.7 (b)). By studying the diagram of figure 3.7 (b), we observe that the size of Coulomb blockaded regions is approximatively equal to $\sim 30mV$. In order to obtain the charging energy we have to take into account the gate lever arm (α factor, see chapter 1). This α factor have been extracted from previous transport measurement at finite voltage bias and we get the conversion factor $0.1eV/V$. This gate level arm conversion factor has to be taken with caution because these transport measurements have been done for the system tuned as a single quantum dot. Therefore it only gives an rough estimation of its value in a double quantum dot configuration. In this sense we can estimate the charging energy of the quantum dot as being roughly equal to $\sim 3meV$. In addition we can also extracted the mutual charging energy by looking at the size of the gap in the stability diagram [12]. We obtained $E_{cm} \sim 500\mu eV$. By the way, this coupling can be tuned by changing the gate voltages applied on the red gates. Two stability diagrams are shown, corresponding to two different values of the coupling : the coupling is higher (the voltage applied on the red gates is less negative) in figure 3.7 (b) than in figure 3.7 (c). In figure 3.7 (c) the mutual charging energy is approximatively twice smaller than the one in the configuration of figure 3.7 (b).

3.3.3 Charge states of a triple quantum dot

In this section charge states of a triple quantum dot (Figure 17 (a)) will be addressed with the same principle than before. The exact resolution of the CI model (Figure 17 (b)) is given in annexe. First let us mention that the stability diagram of a triple quantum dot is a three dimensional entity. For simplicity we fix the gate voltage V_{g3}, and deal with a 2-dimensional stability diagram with respect to V_{g1} and V_{g2}. These two gates control the energy of quantum dot 1 and 2, but also to a lesser extent the one of quantum dot 3, due to the cross talk ((Figure 17 (b)). Consequently we should be able to probe the charge states of a triple quantum dot thanks to only two gate voltages.

Let us consider the uncoupled system. In the CI model (figure 17 (b)), it corresponds

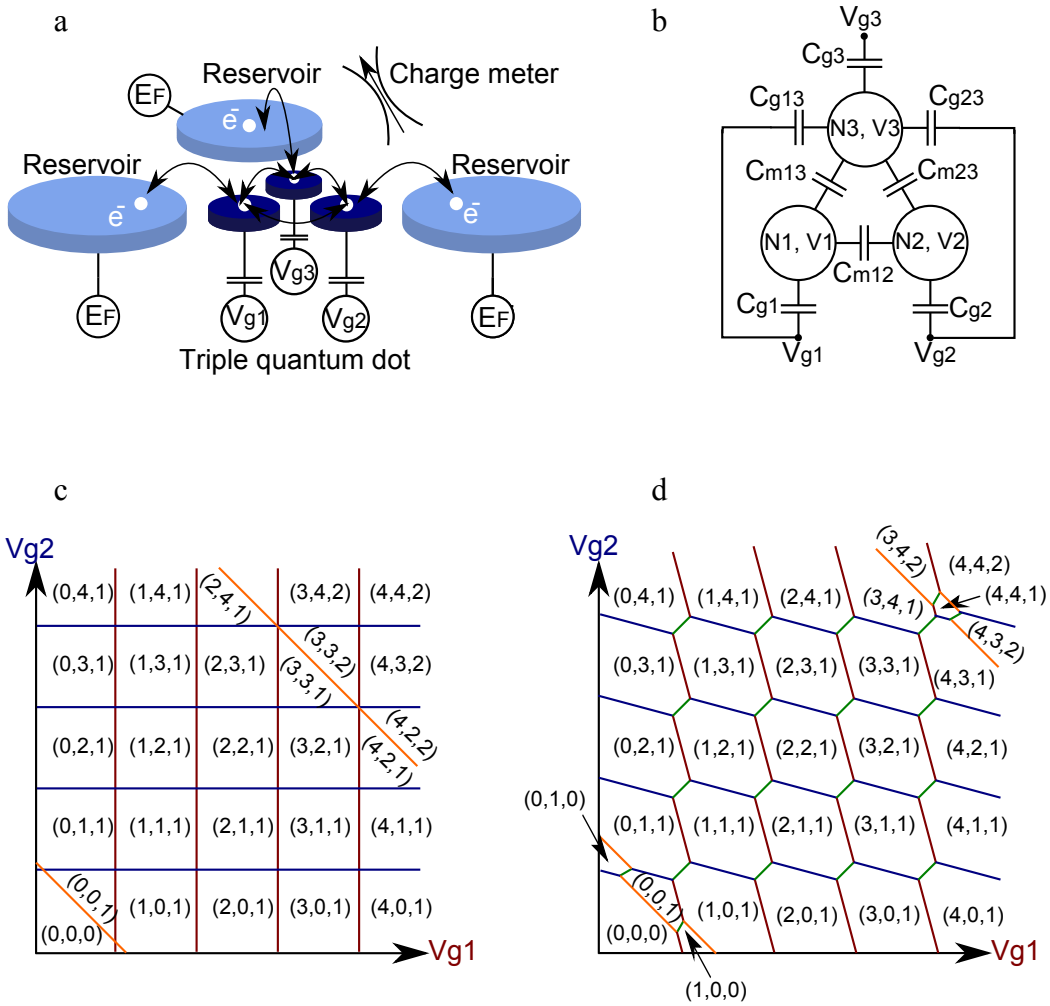

Figure 3.8: **(a) Triple quantum dot system.** Each quantum dot is coupled to a Fermi sea at E_F, and their energy can be tuned thanks to a gate V_{gi}. **(b) CI model of a triple quantum dot.** For simplicity reservoirs have been omitted. Coupling can be tuned by changing the value of C_{m12}, C_{m13}, and C_{m23}. The cross talk of gate 1 and 2 on quantum dot 3 is taken into account to be able to get a two dimensional diagram. **(c) and (d) Stability diagrams.** For an uncoupled system (c) and for a finite coupling (d).

to $C_{m12} = C_{m13} = C_{m23} = 0$. As mentioned, we want to deal with stability diagrams as a function of V_{g1} and V_{g2}, while V_{g3} is fixed. Due to the presence of a third quantum dot, we expect to get the same diagram than the one in figure 3.7 (c), with another set of parallel degeneracy lines. This diagram is given in figure 17 (c). We assume that the cross talk of the gates 1 and 2 on the quantum dot 3 are the same ($C_{g13} = C_{g23}$). This leads to charge degeneracy lines related to the quantum dot 3 (orange lines in figure 17 (c)) with a slope with respect to V_{g1} and V_{g2} equals to -1. The quantum dot 3 being less coupled to gate 1 and 2 than the quantum dot 1 and 2 ($C_{g13}, C_{g23} < C_{g1}, C_{g2}, C_{g3}$), less charge degeneracy lines related to the quantum dot 3 are observed. This diagram will change if the fixed value of V_{g3} is modified. For instance if V_{g3} is set less negative, the electrostatic energy of the quantum dot 3 will decrease. It implies that the charge degeneracy lines related to the quantum dot 3 will be shifted toward a region with more negative value for V_{g1} and V_{g2}.
The effect of the capacitive coupling between the quantum dots has the same effect as previously explained for a double quantum dot. The charge degeneracy lines get an additional slope, and a gap is opened each time two of these lines are crossing (green line, figure 17 (d)). The size of the green lines depends on the different coupling (C_{m12},C_{m13}, and C_{m23}). Different regimes of coupling can be reached as a function of these capacitances. For instance the quantum dot 1 can be coupled either to 2 and 3 ($C_{m12} \neq 0$ and $C_{m13} \neq 0$), but the quantum dots 2 and 3 are not directly coupled ($C_{m23} = 0$).
During this thesis, we have not studied triple quantum dot devices. However we can still use the geometry designed originally for a quadruple quantum dot in order to engineer a triple well potential. Figure 3.9 (a) shows again the SEM picture of the sample where we have intentionally "hidden" the unused gates. The three gate voltages (V_{g1}, V_{g2} and V_{g3}) allow for controlling of the electronic population of each quantum dot (white dots in figure 3.9 (a)). In addition, each quantum dot is coupled to a Fermi sea (reservoir), and all these reservoirs have been biased with the same voltage ($V_{QPC} = 500\mu eV$). A QPC located next to the quantum dot 2 is used to probe the charge states of the system. Then by monitoring the current flowing through the QPC with respect to gate voltages V_{g1} and V_{g3} (V_{g2} has been fixed), we obtain the stability diagram given in figure 3.9 (b). Three sets of charge degeneracy lines with different slopes (in the (V_{g1}, V_{g3}) space) are clearly observed. One set is almost vertical (horizontal), and we can relate these degeneracy lines to the quantum dot 1 (3). Indeed due to the sample geometry we expect that the gate 1 (3) is weakly coupled to the quantum dot 3 (1) explaining the slope of these lines. Another line is clearly seen, and it is related to quantum dot 2. The slope of this line shows that the quantum dot 2 is more coupled to the gate 1 than to the gate 3, which is consistent with the gate geometry. Indeed the yellow gates are the only gates breaking the symmetry of the sample. For instance from the sample geometry (figure 3.9 (a)), we can expect that quantum dot 2 is more capacitively coupled to the gate voltage V_{g1} than to V_{g3}. Therefore the degeneracy line related to quantum dot 2 is almost vertical. Moreover, as it can be observed in figure 3.9 (b), we do not see any degeneracy lines in the

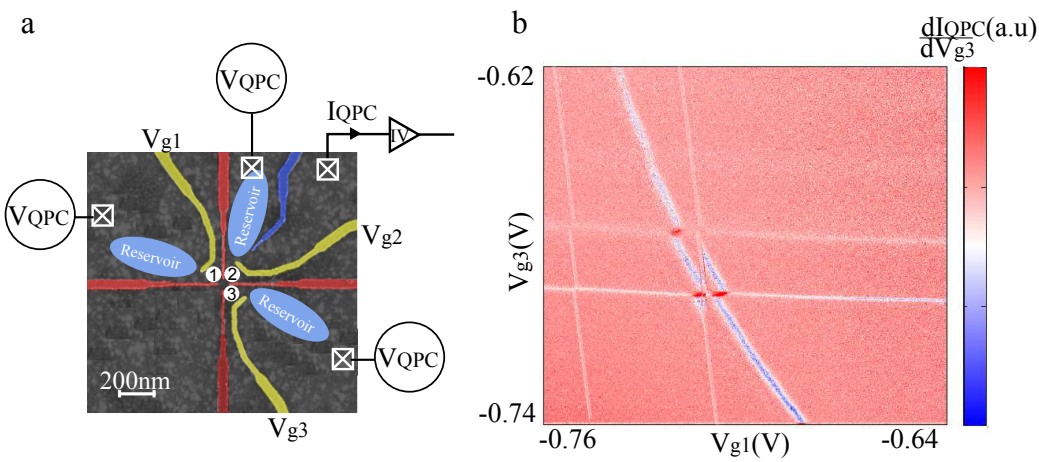

Figure 3.9: **(a) Triple quantum dot device.** SEM (Scanning Electron Microscopy) picture of the sample. The energies of the device are controlled with gate voltages V_{g1}, V_{g2} and V_{g3}. The electronic population of the system is probed by using a QPC located next to the quantum dot 2. **(b)Experimental stability diagram of a triple quantum dot.** Three sets of charge degeneracy lines with different slopes can be seen.

right part of the diagram. This can be explained by the lack of tunability of the sample, an especially explained by the relatively large tunnel coupling between quantum dot 2 and its reservoirs. We will come back to this point later. Experimental realizations of triple quantum dot have been previously reported. We let the reader refer to [13, 14, 15] for complete set of measurement of triple quantum dot stability diagrams.

Up to now, only three dots in series have been demonstrated to be tunable [14, 13] in the few electron regime. A triple quantum dot geometry in a star-like configuration has been demonstrated, but the geometry did not allow tunnelling between all close-by dots and the few electron regime was not reached [15]. As we will see, the geometry which has been designed for the quadruple quantum dot, tends to answer to these issues. But first let's have a look to the charge states and especially to the stability diagram expected for such devices.

3.3.4 Charge states of a quadruple quantum dot

So far we have studied the charge states of a single quantum dot and derived from it the case of an uncoupled double quantum dot. The addition of a capacitive coupling between them has been related to the addition of a mutual charging energy. Finally we have seen that the charge states of a triple quantum dot can be visualized on a two-dimensional stability diagram due to the cross-talk. The case of a quadruple quantum dot is identical to a triple quantum dot (Figure 18 (a)). Each quantum dot is coupled

to a Fermi sea(reservoir) at E_F, the gate voltages V_{gi} (with $i \in (1,2,3,4)$) allow for control of the electronic population of each quantum dot (Figure 18 (b)). In order to be able to control all these electronic populations, we have taken into account the cross talk between the gates (1,3) and the quantum dots (2,4). Therefore we will plot the stability diagram with respect to the gate voltages V_{g1} and V_{g3}, while V_{g2} and V_{g4} will be fixed. The decision to use V_{g1} and V_{g3} to drive all the system, and keep V_{g2} and V_{g4} fixed, comes from experimental considerations. Indeed, due to the screening of the gates, the coupling of each QPC to its diagonally opposite dot was too small to observe any change in its electronic population. Nevertheless, combining the signal from two QPCs was sufficient to see any charge change in the whole four-dot system. Therefore the measurements have been done using two QPC's, the ones in the upper right part and in the lower left part (figure 3.3 (a)). In addition all the quantum dots are capacitively coupled to each others via the mutual capacitance C_{ij} ($(i,j) \in (1,2,3,4)$).

Figure 18 (c) shows the uncoupled stability diagram of the system ($C_{mij} = 0$). As expected, four sets of degeneracy lines with different slopes (in the gate voltage space (V_{g1}, V_{g3})) are obtained. To be able to distinguish lines related to quantum dots 2 and 4, their capacitive coupling to gate 1 and 3 have been voluntary disymmetrized. For instance, the coupling between gate 1(3) and quantum dot 2(4) have been made stronger than the one between gate 1(3) and quantum dot 4(2) ($C_{g12} > C_{g14}$ and $C_{g34} > C_{g32}$). When the coupling is non zero (Figure 18 (d)), the diagram evolves in the same way than the one of triple quantum dot. Due to mutual charging energies, new degeneracy lines appears (green lines). They correspond to the degeneracy charge states with an equal total number of electrons, for instance (K,L,M,N+1) and (K,L,M+1,N) (where K,L,M, and N represents the number of electrons in quantum dot 1,2,3 and 4). The coupling between diagonally opposite quantum dots is wilfully chosen smaller than the one between close-by quantum dots, considering that their distance is greater. We will now describe the experimental stability diagrams obtained for a quadruple quantum dot.

3.4 Experimental stability diagram

Here we present measurements done on a sample allowing to form four quantum dots in a closed loop geometry (square-like configuration) (Figure 3.11 (a)). The geometry of the sample is the one previously described and we recall it in figure 3.11 (a). Figure 3.11(b) shows a zoom image of the white dotted circle of the figure 3.11 (a), and in particular the expected position (white dots) of the four quantum dots and their labels. Each quantum dot of the quadruple well potential is most strongly capacitively coupled to the closest yellow gate and is labelled accordingly. The four gate voltages V_{gi} ($i \in (1,2,3,4)$) allow for controlling the electronic population of each quantum dot. The measurement of the charge states of the system is done thanks to QPC located next to each quantum dot. As previously explained, two of them have been used during this experiment, the ones in the

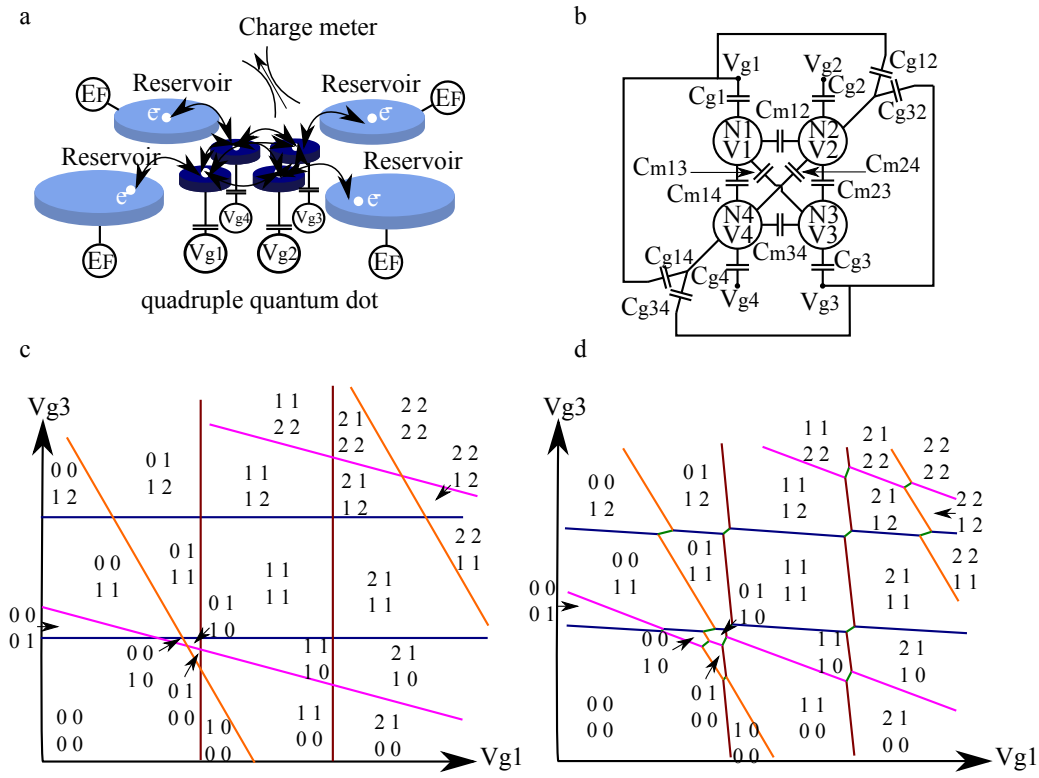

Figure 3.10: **(a) Quadruple quantum dot system.** Each quantum dot is coupled to a Fermi sea at E_F, and their energy can be tuned thanks to a gate V_{gi}. **(b) CI model of a quadruple quantum dot.** For simplicity reservoirs have been omitted. Coupling can be tuned by changing the value of C_{mij}. The cross talk of gate 1 and 3 on quantum dot 2 and 4 is taken into account to be able to get a two dimensional diagram. **(c) and (d) Stability diagrams.** For an uncoupled system (c) and for a finite coupling (d).

upper right (I_{QPC2}) and in the lower left (I_{QPC4}). They were DC-biased with a voltage $V_R = 500\mu$eV, defining also the bias of the four reservoirs. All measurements have been done in a dilution refrigerator with a base temperature around 20mK corresponding to an electronic temperature calibrated to 40mK from weak localization measurement realized in earlier experiments [16].

Similarly to the case of the triple quantum dot, we decided to work with two dimensional stability diagrams for convenience. We chose to fix the gate voltages V_{g2} and V_{g4} due to their proximity with the used QPC. We expect to be able to control the electronic population of the quantum dot 2 and 4 thanks to cross talk of the gates 1 and 3 on these quantum dots. The QPC currents are monitored with respect to the gate voltages V_{g1} and V_{g3}. We have chosen to plot $\frac{dI_{QPC}}{dV} = (\frac{dI_{qpc2}}{dV_{g1}} + \frac{dI_{qpc2}}{dV_{g3}}) + (\frac{dI_{qpc4}}{dV_{g1}} + \frac{dI_{qpc4}}{dV_{g3}})$ to emphasize any change of all electronic populations. Indeed as previously mentioned, by combining the signal from the two QPCs, we were able to see any charge change in the whole quadruple quantum dot system. In addition we summed the derivative of the two QPCs currents with respect to the two gate voltages in order to emphasize each degeneracy line. The charge stability diagram with respect to gate voltages V_{g1} and V_{g3} (for V_{g2} and V_{g4} fixed) obtained from analysing the QPCs current is presented in figure3.12 (c). As expected from the sample geometry, we observe four different types of charge degeneracy lines that we can identify with their slopes with respect to V_{g1} and V_{g3}. They delimit Coulomb blockaded regions where the number of electrons in each quantum dot is fixed. Each of these lines correspond to the exchange of exactly one electron between one of the quantum dots and its closest reservoir and their slopes depend on their relative capacitive coupling to the two gates V_{g1} and V_{g3}. The almost vertical (horizontal) degeneracy lines are related to the quantum dot 1 (3). One more time, their slopes can be explained by the expected low coupling between the gate voltage 1(3) and the quantum dot 3 (1). The two remaining degeneracy lines correspond to the quantum dot 2 and 4. As expected from the sample geometry, these two quantum dots are coupled almost symmetrically to gates V_{g1} and V_{g3}. The slope differences of the corresponding degeneracy lines observed in figure 3.12 (c) are explained by the geometry of the yellow gates. These gates break the symmetry of the sample. For instance, V_{g1} is more capacitively coupled to quantum dot 2 than to 4. Consequently, the degeneracy line of quantum dot 2 has to exhibit a larger slope than the one of quantum dot 4.
Thanks to our identification of the four-dot positions and their corresponding charge degeneracy lines, we can infer the charge configuration of each Coulomb blockade region. The charge label used is defined from the sample geometry (see figure 3.11(b)). To understand the indexing, it is convenient to start from the emptied region (lower left part of figure 3.11(c)). By increasing voltages V_{g1} or V_{g3}, we can add electrons to the four-dot system by crossing one of these charge degeneracy lines. Depending on which charge degeneracy line is crossed, the added electron is labeled accordingly.

In the previous discussion, we have taken into account of the gate geometry to relate any set of charge degeneracy lines to a quantum dot. Although the relation between the

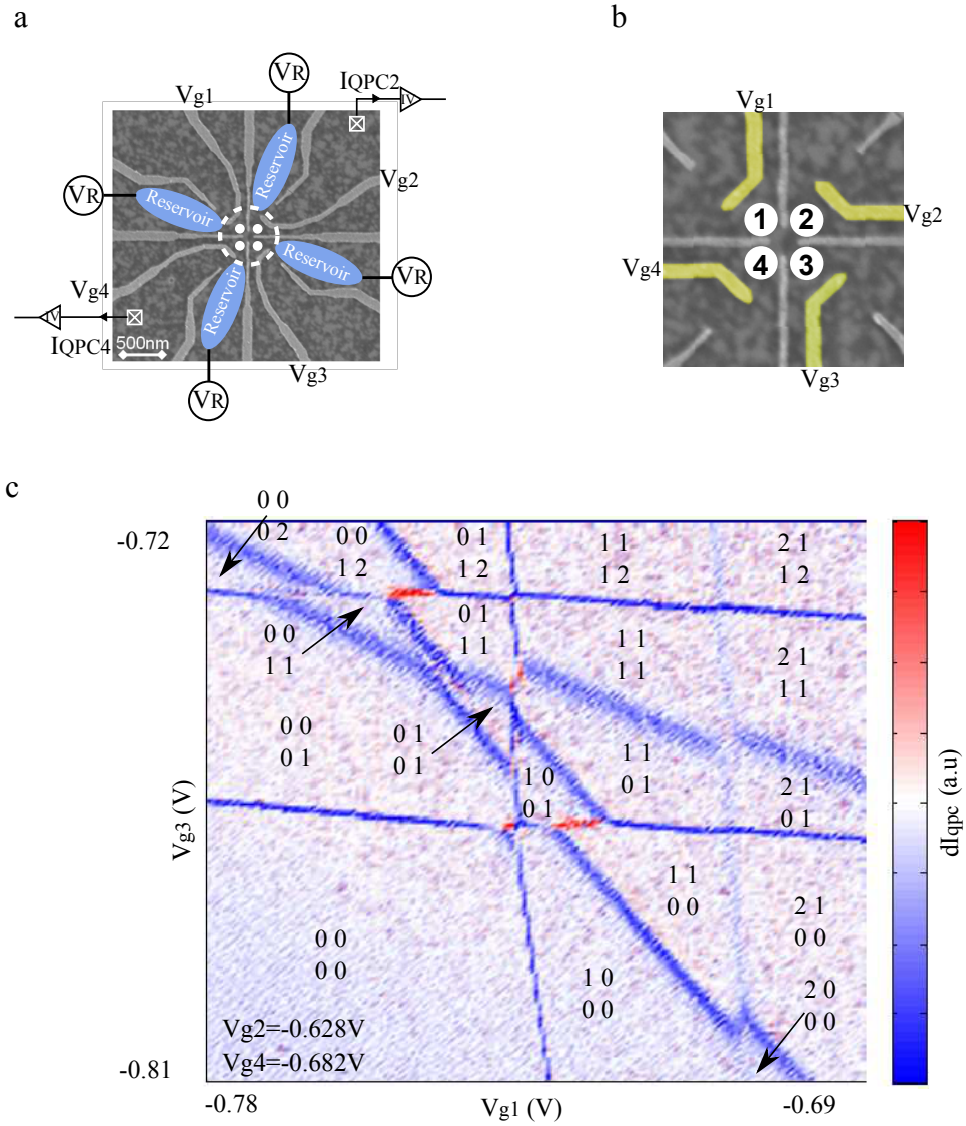

Figure 3.11: **(a) Quadruple quantum dot device.** They are located at the corner of a square. To probe charge states of the system, just two QPCs have been used during this experiment. **(b) Zoom Image.** It shows the expected position (white dots) of the four quantum dots and their labels. **(c) Stability diagram.** Plot of $\frac{dI_{QPC}}{dV} = (\frac{dI_{QPC1}}{dV_{g1}} + \frac{dI_{QPC1}}{dV_{g3}}) + (\frac{dI_{QPC2}}{dV_{g1}} + \frac{dI_{QPC2}}{dV_{g3}})$ as a function of V_{g1} and V_{g3}, for V_{g2} and V_{g4} fixed.

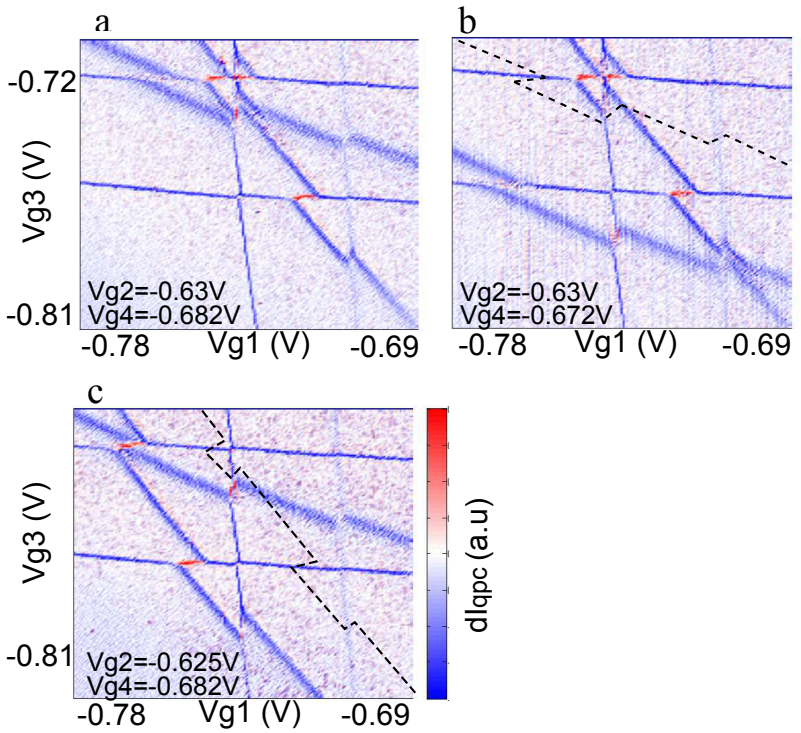

Figure 3.12: **(a, b, and c) Stability diagram of quadruple quantum dot as a function of V_{g1} and V_{g3} for different values of V_{g2} and V_{g4}. The dashed lines corresponds to the previous positions of the degeneracy lines**

almost vertical (horizontal) degeneracy lines and the quantum dot 1(3) is obvious, the case of the quantum dots 2 and 4 is less evident. In order to give another proof of it, we can change one of the two fixed gate voltages (V_{g2} or V_{g4})) and observe how the diagram evolves. Figures 3.12 (a), 3.12 (b), and 3.12 (c) show three stability diagrams for different values of V_{g2} and V_{g4}. As earlier $\frac{dI_{QPC}}{dV}$ is plotted with respect to V_{g1} and V_{g3}. Between figures 3.12 (a) and 3.12 (b), V_{g2} remains the same while V_{g4} is increased. It decreases the potential of quantum dot 4, and as expected the charge degeneracy line related to these quantum dots is shifted to the lower left part of the diagram. We highlighted the previous position of the degeneracy line by a dotted line. Similarly the figure 3.12 (c) shows the same stability diagram than the one in figure 3.12 (a), but V_{g2} has been increased while V_{g4} remains fixed. The charge degeneracy line related to quantum dot 2 is then also shifted in the lower left part of the diagram.
Until now, it has been assumed that the lower left part of figure 3.12 (c) corresponds to the emptied Coulomb blockade region. The charge detection can demonstrate that the proposed labels correspond to an absolute number of charge present in the four-dot system. In figure 3.12(c), no degeneracy line is observed for $V_{g1} < -0.74V$ and $V_{g3} < -0.77V$. Due to the strong capacitive coupling between these two gates and the two quantum dots 1 and 3, one would have expected to observe degeneracy lines in this gate voltage region if they were not emptied. This demonstrates that the quantum dots 1 and 3 have been emptied. On the contrary, we cannot conclude from figure 3.12(c) on the population of quantum dots 2 and 4 due to the small capacitive coupling with gates V_{g1} and V_{g3}. Indeed we only observe a single degeneracy line for each of these quantum dots, and we cannot conclude whether they are related to the first electron or not. To check whether the few electron regime was reached for the quantum dots 2 and 4, stability diagrams varying gate voltages V_{g2} and V_{g4} were recorded. Figures 3.13(a) and (b) show $\frac{dI_{QPC}}{dV}$ plotted with respect to V_{g3} and V_{g4} (figure 3.13(a)), V_{g2} and V_{g3} (figure 3.13(b)). For both cases, the quantum dot chemical potentials have been set such that the quantum dot 1 is empty ($V_{g1} = -0.785V$). Such a large negative voltage is also applied to $V_{g2}(V_{g4})$ in figure 3.13 (a) (Figure 3.13 (b)) in order to empty quantum dots 2 (4). In both figures, we demonstrate that no degeneracy line corresponding to quantum dots 2 and 4 are observed, confirming that no electron are in the four dot system in the bottom left Coulomb blockade region of figure 3.12(c). In figure 3.13 (b) the line which have been circled corresponds to an experimental switch and is therefore not related to any physics.

From this set of data, we can therefore demonstrate that by changing the gate voltages V_{gi} ($i \in (1, 2, 3, 4)$), we are able to remove all the electrons from the quantum dot system, control the injection of a single electron within the four-dot structure as well as its transfer from one dot to the other. Before realizing such a single electron transport let us get a more quantitative analysis of this novel system. The first observation concerns the charging energy of each quantum dot. From figure 3.11, 3.12 and 3.13 we can clearly see that they are almost identical since the typical distance between two parallel degeneracy

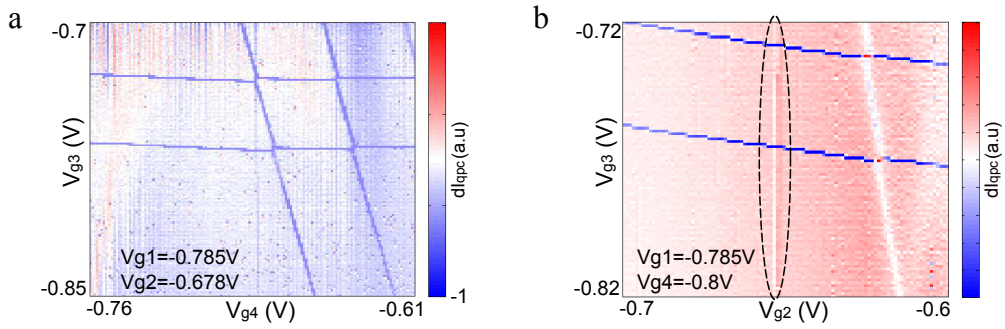

Figure 3.13: **Stability diagram of double quantum dots where the two others have been set to unreachable energies. It gives the proof of the few electrons regimes for all the system. (a) Stability diagram with respect of gate V_{g3} and V_{g4}. (b) Stability diagram with respect of gate V_{g2} and V_{g3}.**

lines is equal to $\sim 50mV$. In order to get the charging energy, we have to take into account the gate lever arm (α factor). This factor is related to the effect of the gate on the quantum dot potential, and in order to get an estimation of it we performed transport measurement across a big quantum dot made with only the yellow gates (figure 3.11 (b)). We notice it was not possible to perform this transport measurement across the quadruple quantum dot system because of the tunnel rates between the quantum dots and their reservoirs. These rate were relatively small and the current flowing through the system too weak to be easily detected. By studying the transport across the quantum dot with respect to the gate voltage and the bias voltage, we obtain a Coulomb diamond. This allows for estimating the gate lever arm conversion factor as $0.6eV/V$. If we consider the same α factor in the case of a quadruple quantum dot, we get a charging energy E_C equal to $\sim 3meV$. In addition in this square-like geometry, we expect that the distance between quantum dots to be larger if they are sitting on opposite corners rather than on adjacent corners. The closer the dots are, the larger the inter-dot capacitive coupling is. In the charge stability diagram, this coupling opens a Coulomb gap at the crossings between charge degeneracy lines. Figure 3.12(c) clearly shows that the gaps opened at the crossing between the lines of dot 1(2) and 3(4) are much smaller than the other ones confirming the square-like distribution of the four quantum dots expected from the sample geometry. We can estimate the mutual charging energy by looking at the size of the opened gap [12]. Therefore we obtain that the mutual charging energy for close-by quantum dots is roughly $100\mu eV$ while it is $50\mu eV$ for diagonally opposite quantum dots. Concerning the tunnel coupling, few remarks can be done. First let us have a look at the tunnel coupling between each quantum dot and its closest reservoir. By studying the width of the degeneracy lines, we can get information about the tunnel coupling with the reservoirs. As we can clearly observe the degeneracy lines related to the quantum dot 2

and 4 (the two being close to the QPC) are clearly larger than the ones related to the quantum dot 1 and 3. With the present geometry we were not able to tune the system in order to get smaller tunnel coupling between the quantum dots 2 and 4 and their reservoirs. This can be understood by considering the role of the yellow gates, which are used in order to change the potential of the quantum dot, but they are also used to define tunnel barriers between the quantum dots and their reservoirs. Concerning the tunnel coupling between the quantum dots, although we could not estimate it easily, we noticed that we were not able to increase it as much as we could have liked. Indeed by decreasing the voltages applied on the red gates (figure 3.3 (a)), we observed the apparition of a new set of lines, which can be related to the presence of a fifth quantum dot in the middle of the geometry. To conclude, the present geometry allows for reaching the few-electron regime, but the tunability of the sample is presently too small. We will come back on this issue at the end of this chapter.

3.5 Electron transport along a closed path

The control of the four quantum dots system opens the route towards single electron transport on a closed path. In this section, we want to give a strategy to perform such an electron displacement. The idea is to keep in close vicinity the chemical potential of quantum dots 1 and 3 and to bring sequentially in this vicinity the chemical potential of quantum dots 2 and 4. By modifying V_{g2} and V_{g4} at the same time, such chemical potential movements can be engineered as demonstrated in the two stability diagrams presented in figures 3.14(a) and (b). They represent the two gate voltage configurations used in the transport sequence. On figure 3.14(a), the Coulomb blockaded regions (0,0,0,0)/(1,0,0,0)/(0,0,1,0)/(0,0,0,1), where the (i,j,k,l) correspond to the number of electrons in the quantum dots (1,2,3,4), have been set in close vicinity. Starting from the empty region (0,0,0,0) (label 1 in figure 3.14(a)), an electron can be loaded into the quantum dot 3 by increasing V_{g3} (label 2 in figure 3.14(a)). By changing voltages on the two gates V_{g1} and V_{g3} , the electron can then be transferred from quantum dot 3 to 1 via two tunnel processes (label 3 and 4 in figure 3.14(a)). To complete the closed path, we need to transfer this electron into the quantum dot 2. Consequently the region (0,1,0,0) has to be set in vicinity with (1,0,0,0) and (0,0,1,0). This can be achieved by increasing V_{g2} and decreasing V_{g4} as demonstrated in figure 3.14(b). In a similar way, we can then transfer the electron from dot 1 (label 4 in figure 3.14(b)) to dot 3 (label 6 in figure 3.14(b)) through dot 4 (label 5 in figure 3.14(b)). A strategy to repeatedly displace a single electron on a closed loop is therefore possible. The position of the electron (with respect to the corresponding labels) and the response of the QPC during the repeated transfer are shown in figure 3.14(c) and (d). Each QPC response step corresponds to a wait time in a stable charge configuration and fast transitions between steps appear when the electron transfer takes place. Movement of the gates are faster than the bandwidth of

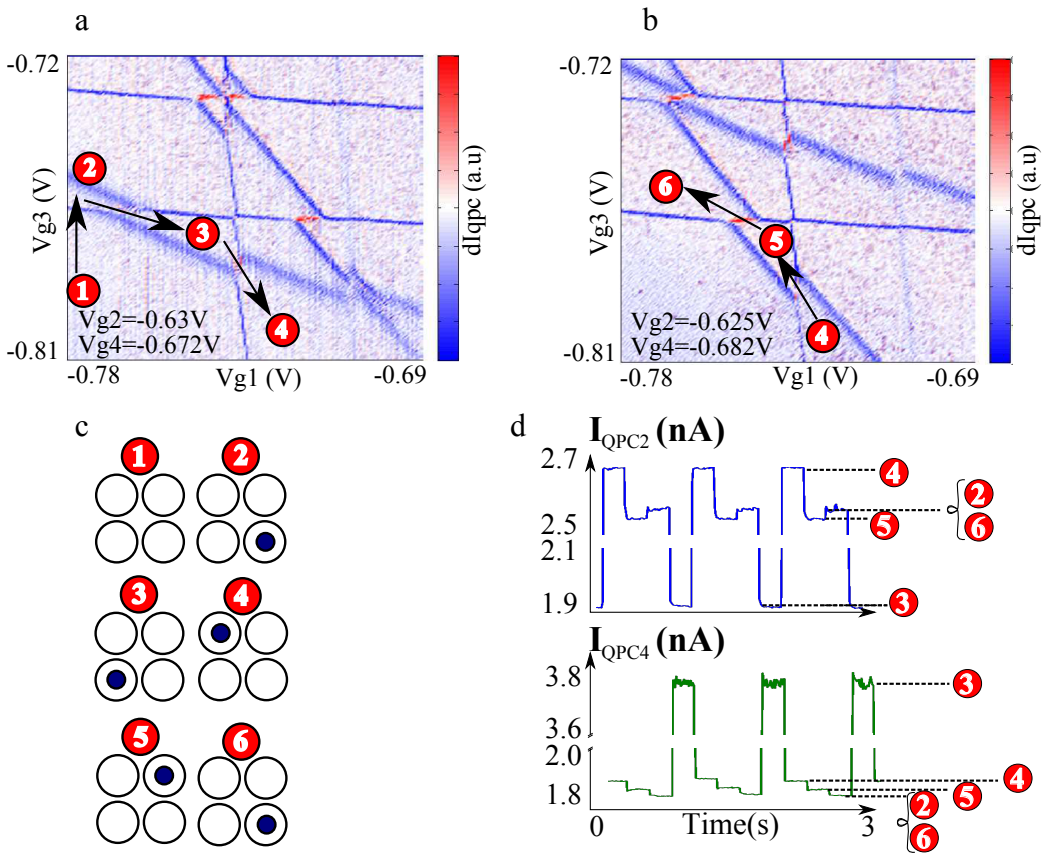

Figure 3.14: **(a) and (b) Strategy for the electron transport.** These two stability diagrams corresponding to the gate voltage configuration used for the transport sequence. **(c) Position of the electron** with respect to the corresponding labels and **(d) the response of the QPC's** during the repeated transfer

the detector (set to 800Hz). Possible exchange of the electron between quantum dot and the leads are too fast to be observable with our current set-up. As expected we observe four steps corresponding to the four possible positions of the electron.

To be able to use such a transfer to manipulate the spin of the electron, one needs to realize the transfer on time scales faster than the spin decoherence time which is of the order of 10-100 ns [17, 18]. Tunneling between the close-by quantum dots needs then to be strong enough. Indeed two competing mechanisms can explain a change of charge configuration when the electron is transferred between two tunnel-coupled dots. First, the electron can tunnel directly between the two dots and second it can be replaced in the dot system by an electron coming from the leads. The second scenario requires two energetically allowed tunnel processes, each of them is an electron transfer between one

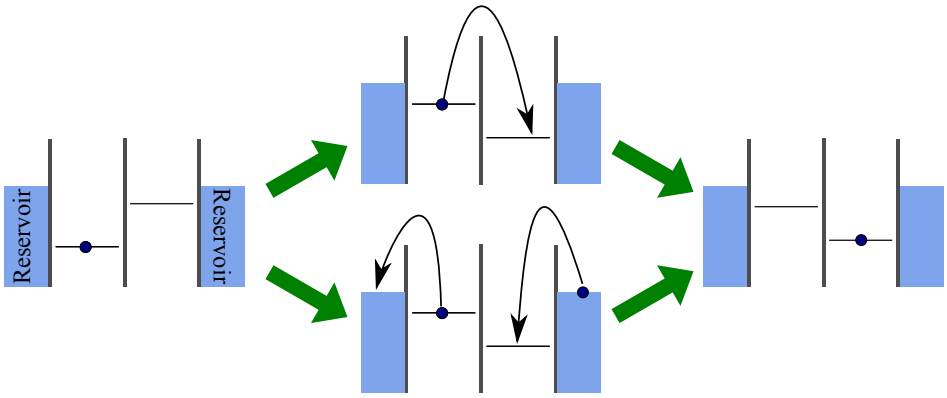

Figure 3.15: **Two possible processes** to go from one charge configuration to another one. In the upper one, the electron is transferred thanks to the tunnel barrier separating the two quantum dots. In the lower one, the electron is exchanged with one from the reservoirs via two allowed direct tunnelling processes.

dot and its closest reservoir: the electron in the quantum dot tunnels out and an electron from the reservoir tunnels into the emptied dot. The timescale of the second scenario is set by the coupling of the dots with their adjacent reservoirs. The results of the slow QPC measurement presented in figure 3.14 (d) do not permit to discriminate between these two mechanisms. Moreover, due to the restricted number of gates used to define the dots, we were not able to tune all the tunnel couplings of this system in the regime of a few tens of μeV. This coupling corresponds to a tunnel timescale inferior to 1 ns, which would be at least three orders of magnitude faster than the one between the dots and the leads. Consequently, with such tunnel coupling, we would be able to transfer the electron along this closed path for several turns with a small probability of an exchange with one electron from the reservoirs. A more complete study of the tunneling in this dot configuration is needed to reach the nanosecond transfer of a single electron in a closed loop.

3.6 Perspectives

The lack of tunability of the device was mainly due to the small number of gates. Especially the gate which was used to change potential of a quantum dot was also the ones to make a tunnel barrier with its reservoir. We expect that the addition of some gates may increase the tunability of the sample. From the geometry used here, an improved version has been already designed and fabricated, which should solve the raised issues. Several gates have been added as shown on figure 3.16. More precisely, the green gates should allow us to change the energy of each quantum dot while the yellow ones would be used

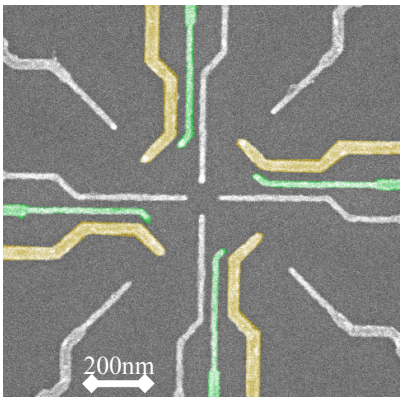

Figure 3.16: **SEM (scanning electron microscopy) of a sample with the improved geometry.**

to tune their tunnel coupling to the reservoir. But this new geometry have not yet been measured.

Bibliography

[1] Knill, E. *NATURE* **434**(7029), 39–44 MAR 3 (2005). 48

[2] BERRY, M. *PROCEEDINGS OF THE ROYAL SOCIETY OF LONDON SERIES A-MATHEMATICAL PHYSICAL AND ENGINEERING SCIENCES* **392**(1802), 45–57 (1984). 48

[3] San-Jose, P., Scharfenberger, B., Schoen, G., Shnirman, A., and Zarand, G. *Physical Review B* **77**(4), 045305 January (2008). ii, 29, 49

[4] Golovach, V. N., Borhani, M., and Loss, D. *Physical Review A* **81**(2), 022315 February (2010). ii, 29, 49

[5] Nowack, K. C., Koppens, F. H. L., Nazarov, Y. V., and Vandersypen, L. M. K. *Science* **318**(5855), 1430–1433 November (2007). 19, 28, 49

[6] Salis, G., Kato, Y., Ensslin, K., Driscoll, D., Gossard, A., and Awschalom, D. *NATURE* **414**(6864), 619–622 DEC 6 (2001). 49

[7] Nadj-Perge, S., Frolov, S. M., Bakkers, E. P. A. M., and Kouwenhoven, L. P. *NATURE* **468**(7327), 1084–1087 DEC 23 (2010). 49, 101, 119

[8] Hermelin, S., Takada, S., Yamamoto, M., Tarucha, S., Wieck, A. D., Saminadayar, L., Baeuerle, C., and Meunier, T. *NATURE* **477**(7365), 435–438 SEP 22 (2011). ii, 49

[9] McNeil, R. P. G., Kataoka, M., Ford, C. J. B., Barnes, C. H. W., Anderson, D., Jones, G. A. C., Farrer, I., and Ritchie, D. A. *NATURE* **477**(7365), 439–442 SEP 22 (2011). ii, 49

[10] Reimann, S. M. and Manninen, M. *Rev. Mod. Phys.* **74**, 1283–1342 Nov (2002). 51

[11] DAVIES, J., LARKIN, I., and SUKHORUKOV, E. *JOURNAL OF APPLIED PHYSICS* **77**(9), 4504–4512 MAY 1 (1995). 51

[12] van der Wiel, W. G., De Franceschi, S., Elzerman, J. M., Fujisawa, T., Tarucha, S., and Kouwenhoven, L. P. *Rev. Mod. Phys.* **75**, 1–22 Dec (2002). 57, 67, 165

[13] Laird, E. A., Taylor, J. M., DiVincenzo, D. P., Marcus, C. M., Hanson, M. P., and Gossard, A. C. *Physical Review B* **82**(7), 075403 August (2010). 60

[14] Gaudreau, L., Kam, A., Granger, G., Studenikin, S. A., Zawadzki, P., and Sachrajda, A. S. *Applied Physics Letters* **95**(19), 193101 November (2009). 60

[15] Rogge, M. C. and Haug, R. J. *New Journal of Physics* **11**(11), 113037 (2009). 60

[16] Niimi, Y., Baines, Y., Capron, T., Mailly, D., Lo, F.-Y., Wieck, A. D., Meunier, T., Saminadayar, L., and Bäuerle, C. *Phys. Rev. Lett.* **102**, 226801 Jun (2009). 63

[17] Petta, J. R., Johnson, A. C., Taylor, J. M., Laird, E. A., Yacoby, A., Lukin, M. D., Marcus, C. M., Hanson, M. P., and Gossard, A. C. *Science* **309**(5744), 2180–2184 September (2005). 24, 26, 69, 77, 85, 89, 92, 94, 110

[18] Bluhm, H., Foletti, S., Mahalu, D., Umansky, V., and Yacoby, A. *Physical Review Letters* **105**(21), 216803 November (2010). iii, 26, 27, 69, 89, 101

Chapter 4

From SWAP to C-phase gate regime in single spin qubits

Résumé

Dans ce chapitre nous étudions les portes logiques à deux qubits dans le contexte des qubits à spin unique. Nous démontrons que la porte logique à deux qubits naturelle évolue de la porte SWAP à faible gradient de champ magnétique nucléaire ΔB_z à la porte C-phase pour de plus grandes valeurs de ΔB_z. Cette étude prouve la faisabilité de cette porte C-phase, et nous permet d'estimer la durée d'une telle opération dans notre configuration.
Nous commencerons ce chapitre par un exposé des motivations relatives à la réalisation d'une porte C-phase, en replaçant cette étude dans le cadre plus général de l'ordinateur quantique. Dans le cadre de cette étude, nous utilisons une double boîte quantique, où chacune des boîtes contient un unique spin électronique. Nous verrons qu'un tel système est adapté à l'étude des portes logiques à deux qubits dans le contexte des qubits à spin unique. Nous introduirons alors les états de spin à deux électrons dans un système composé de deux boîtes quantiques couplées par effet tunnel. Le principe de la mesure de ces états sera détaillé, et nous verrons comment ces mesures nous permettent de caractériser et de régler les différents paramètres du système.
Après avoir rappelé les conditions théoriques préalables à la réalisation d'une porte C-phase, nous développerons le concept de polarisation dynamique des spins nucléaires, permettant d'augmenter le gradient de champ magnétique ΔB_z entre les deux boîtes quantiques. Afin de quantifier le gradient induit par la polarisation, nous étudierons les oscillations cohérentes entre le singlet S et le triplet T_0.
Nous introduirons alors la porte logique à deux qubits SWAP dans le cadre des qubits à spin unique. Nous étudierons le comportement de cette porte en fonction du gradient ΔB_z et montrerons qu'elle n'est plus réalisable à fort gradient, la porte à deux qubits naturelle devenant alors la porte C-phase.

4.1 Motivations

In the context of quantum computing, the elementary block, where the information is encoded, is the qubit. Several systems have been proposed like atoms, photons, or ions. Although it has been demonstrated that these quantum systems can form suitable qubits, they miss a key point : the scalability, meaning that it appears complicated to increase the number of these qubits interacting together. On the other hand, superconducting or semiconductor qubits are attractive for scalability considerations, assisted by decades of technological development from micro-electronic industries. In particular, as we have already mentioned, a single electron spin trapped in a quantum dot can form a qubit, and the information is encoded in the spin degree of freedom.
In order to realize a quantum computer, we need to be able to perform some crucial manipulations on these qubits, the so-called gates. Nielsen and Chuang [1] demonstrated that only few particular gates are needed to perform any quantum operation. Among them the single qubit rotations, allowing for preparing the state of a single qubit on any point of the Bloch sphere. For a single spin qubit, the two states are ($|\uparrow\rangle$,$|\downarrow\rangle$), representing the orientation of the electron spin along the quantification axis. In the Bloch sphere representation, these two eigenstates occupy the poles of the sphere. The single qubit rotations should allow to prepare any state :

$$|\Psi\rangle = cos(\frac{\theta}{2})|\uparrow\rangle + sin(\frac{\theta}{2})e^{i\phi}|\downarrow\rangle \tag{4.1}$$

where $\theta \in [0, \pi]$ and $\phi \in [0, 2\pi]$. In order to perform this operation, we need to be able to rotate any state $|\Psi\rangle$ around two distinct axis. Figure 4.1 shows two $\pi-$rotations around the $\hat{x}$ axis (figure 4.1 (a)) and the $\hat{z}$ axis (figure 4.1 (b)). These unitary transformations can be expressed in matrix form written in the $\{|\uparrow\rangle,|\downarrow\rangle\}$ basis :

$$X = \begin{pmatrix} 0 & 1 \\ 1 & 0 \end{pmatrix} \tag{4.2}$$

$$Z = \begin{pmatrix} 1 & 0 \\ 0 & -1 \end{pmatrix} \tag{4.3}$$

The π-rotation around the $\hat{x}$ axis represented by the matrix 4.2 is the quantum equivalent of the classical NOT gate. More generally a rotation of an angle θ can be written as :

$$R_X(\theta) = e^{-i\frac{\theta}{2}X} = cos(\frac{\theta}{2}).I - i.sin(\frac{\theta}{2}).X \tag{4.4}$$

$$R_Z(\theta) = e^{-i\frac{\theta}{2}Z} = cos(\frac{\theta}{2}).I - i.sin(\frac{\theta}{2}).Z \tag{4.5}$$

where I is the identity matrix. Previously we claimed that only two rotations around two distinct axis were needed to perform any rotation in the Bloch sphere. Indeed it can be demonstrated that for any arbitrary unitary matrix U acting on a single qubit, we can find $\{\alpha, \beta, \gamma, \delta\} \in \Re^4$ and write U as [1] :

$$U = e^{i\alpha} R_Z(\beta) R_X(\gamma) R_Z(\delta) \tag{4.6}$$

Concerning single spin qubits, the single qubit rotations have already been demonstrated experimentally. As mentioned in the first chapter, the rotation around the $\hat{x}$ axis can be achieved by using an oscillating magnetic field $\mathbf{B}_{osc}$ aligned along the $\hat{x}$ axis and resonant with the spin precession frequency in an external magnetic field $\mathbf{B}_{ext}$ oriented along the $\hat{z}$ axis. This technique of electron spin resonance (ESR) allows for rotation around the $\hat{x}$ axis and has been experimentally demonstrated by Koppens and coworker [2]. This can also be achieved by use of an oscillating electric fields (EDSR :electron dipole spin resonance) as first demonstrated by Nowack and coworkers [3]. The rotations around the $\hat{z}$ axis can be achieved by letting the system evolve according to time in a non zero magnetic field.

In order to allow for parallel computation, the qubits have to be entangled and it requires two-qubit gates. For single spin qubits, the natural two-qubit gate is the SWAP gate, first experimentally demonstrated by Petta and coworker [4]. The effect of this gate is to "exchange" the states of the two qubits. It can be represented by the unitary matrix written in the $\{(|\uparrow,\uparrow\rangle), (|\uparrow,\downarrow\rangle), (|\downarrow,\uparrow\rangle), (|\downarrow,\downarrow\rangle)\}$ basis (where $|S_1, S_2\rangle$, $S_1, S_2 \in \{\uparrow,\downarrow\}$ denoted the states of the qubit 1 (S_1) and the qubit 2 (S_2)) :

$$SWAP = \begin{pmatrix} 1 & 0 & 0 & 0 \\ 0 & 0 & 1 & 0 \\ 0 & 1 & 0 & 0 \\ 0 & 0 & 0 & 1 \end{pmatrix} \tag{4.7}$$

But in the context of quantum computing, it is interesting to look for a set of gates which are universal, meaning that any arbitrary unitary transformation (matrix) acting on N qubits can be implemented by this set of gates. The SWAP gate does not allow for entanglement, and therefore it is not universal with single qubit rotations. The experimental way to perform the SWAP gate with single spin qubits can be used (as it will be seen later) in order to design a $\sqrt{SWAP}$ gate which can be represented by the unitary transformation :

$$\sqrt{SWAP} = \begin{pmatrix} 1 & 0 & 0 & 0 \\ 0 & \frac{1}{\sqrt{2}} & \frac{i}{\sqrt{2}} & 0 \\ 0 & \frac{i}{\sqrt{2}} & \frac{1}{\sqrt{2}} & 0 \\ 0 & 0 & 0 & 1 \end{pmatrix} \tag{4.8}$$

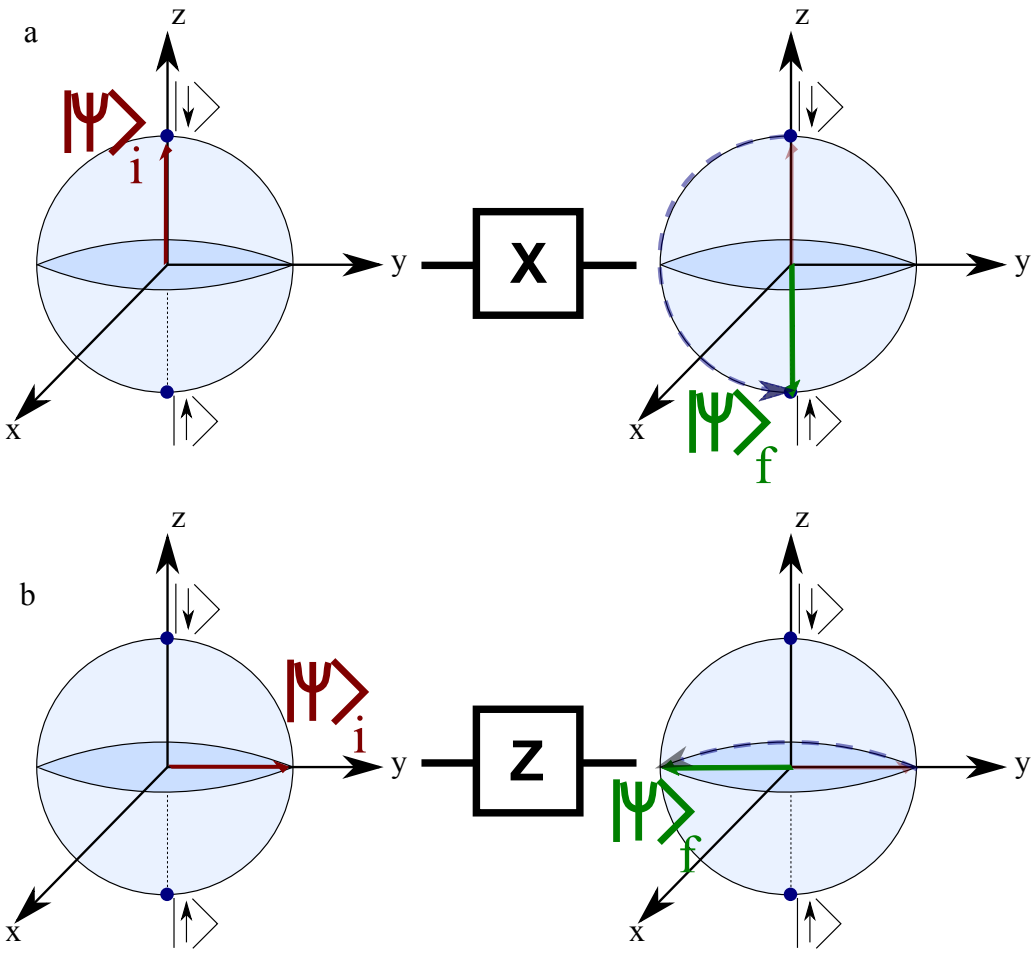

Figure 4.1: **Single qubit rotations.** **(a)** Bloch sphere representation of a single qubit π-rotation around the $\hat{x}$ axis. **(b)** Bloch sphere representation of a single qubit π-rotation around the $\hat{z}$ axis

Although this gate allows for qubit entanglement, it is not the one entering the Shor algorithm, one of the first quantum algorithm allowing for factorizing an input number in prime factors. Indeed, this algorithm uses the two-qubit controlled gate like the C-NOT or the C-phase that we will describe in the following. in order to perform a C-NOT gate with the $\sqrt{SWAP}$ gate (combined with the single qubit rotations), it needs 5 operations. Therefore it turns out to be useful to find an experimental way to perform directly one of the controlled gate. Concerning these gates, one qubit acts as a control qubit, while one is the target qubit. As a function of the state of the control qubit, a single qubit gate is applied to the target. For instance the controlled NOT gate corresponds to apply a NOT gate (X) to the target qubit if the state of the control is $|\downarrow\rangle$. The unitary matrix related to such transformation can be written (in the basis $\{(|\uparrow,\uparrow\rangle),(|\uparrow,\downarrow\rangle),(|\downarrow,\uparrow\rangle),(|\downarrow,\downarrow\rangle)\}$) :

$$C-NOT=\begin{pmatrix}1&0&0&0\\0&1&0&0\\0&0&0&1\\0&0&1&0\end{pmatrix} \tag{4.9}$$

Another well known controlled gate is the C-phase, which consists to apply a $\pi-$rotation around the $\hat{z}$ axis to the target qubit :

$$C-Phase=\begin{pmatrix}1&0&0&0\\0&1&0&0\\0&0&1&0\\0&0&0&-1\end{pmatrix} \tag{4.10}$$

The single qubit rotations and one of the two-qubit controlled gates constitute an universal set of gates. This demonstration can be found in [1], and we let the reader refer to it. The realization of a C-phase gate with single spin qubits has been first theoretically proposed by Loss and di Vincenzo [5], and it has been recently demonstrated theoretically that an efficient controlled phase gate could be achieved with single spin qubits in realistic conditions [6]. Before entering the details of this operation, we will now study the system used in order to realize such a gate.

4.2 Two single spin qubits in a tunnel coupled double quantum dot

As we already mentioned, a single spin qubit consists in a single electron spin trapped in a quantum dot. Therefore we can consider a double quantum dot system, where one electron spin lies in each quantum dot, as two single spin qubits. We will study the spin states of this system. Then the experimental measurements and control of these spin states will be detailed. Finally we will describe how the system can be characterized and then tuned in order to allow for such manipulations.

4.2.1 Spin states in a double quantum dot

We consider a system made of two tunnel coupled quantum dots. Figure 4.2 (a) shows the scanning electron microscopy picture of the measured sample. The gate pattern allows to define a double quantum dot. The gate voltages V_{g1} (blue gate) and V_{g2} (red gate) are used to control the electrochemical potential of each quantum dot. These gates are connected to home made bias tees allowing for adding DC and RF voltages. In addition a quantum point contact (QPC) located next to the quantum dot 1 acts as a charge detector in order to probe the charge state of both quantum dots. The current flowing through this QPC (I_{QCP}) in response to a bias voltage excitation V_{QOC} is collected and amplified (IV converter). As we will see later, the system has to be tuned into a proper configuration in order to perform spin manipulations and measurements. There are three main parameters limiting it : the tunnel coupling between the two quantum dots, and the tunnel coupling between the quantum dots and their reservoirs. These parameters can be tuned by changing the gate votlages (V_t, V_b) for the interdot tunnel coupling, and (V_r, V_l) for the tunnel coupling to the reservoirs. This set of measurements have been performed in a dilution fridge with a base temperature equal to 150mK. For now on we will focus on the spin states where two electrons occupying the system.

Let us start with the charge states. Figure 4.2 (b) shows the stability diagram of the double quantum dot system around the region (1,1) and (2,0), where (m,n) corresponds to the number of the electron in quantum dot 1 (m) and dot 2 (n). Until now we mainly took the derivative of the QPC current with respect to the gate voltages in order to emphasize the charge degeneracy lines. Here we want to emphasize the charge ground states, and this is why we chose to plot I_{QPC} with respect to V_{g1} and V_{g2}. In order to obtain the diagram of figure 4.2 (b), we remove the mean slope of the QPC current related to the cross talk leading to a flat QPC current in the Coulomb blockaded region. As we can see, four charge states are accessible in the gate voltage range used here: (1,0), (1,1), (2,0), (2,1). Each of these charge states gives a particular value of QPC current I_{QPC}. In the following we will only consider the two charge states (1,1) and (2,0), where the total number of electrons into the system is fixed (equal to 2). We define the detuning parameter ε (black arrow in figure 4.2 (b)) as the difference of energy between these two charge states (figure 4.2 (b)) : $\varepsilon = E_{2,0} - E_{1,1}$. For $\varepsilon < 0$, the charge ground state is (1,1), while for $\varepsilon > 0$ it is (2,0). This parameter can be controlled by changing the gate voltages V_{g1} and V_{g2}. For $\varepsilon = 0$ the two charge states (2,0) and (1,1) are degenerated. In order to get fast control of it, these two gates have been connected to home made bias tees (see chapter 2) allowing to add DC and high frequency (RF) voltages. Before continuing with the spin states description, let us describe a little bit the energy schemes of the charge states in different positions of this stability diagram. Figure 4.2 (c) shows the energy of the four charge states at the position labelled in the diagram 4.2 (b). Obviously the lower energy state depends on the position, but the main feature is the difference between the label 1 and the labels 3,4. Indeed inside the triangular shape (figure 4.2 (b)) the energy

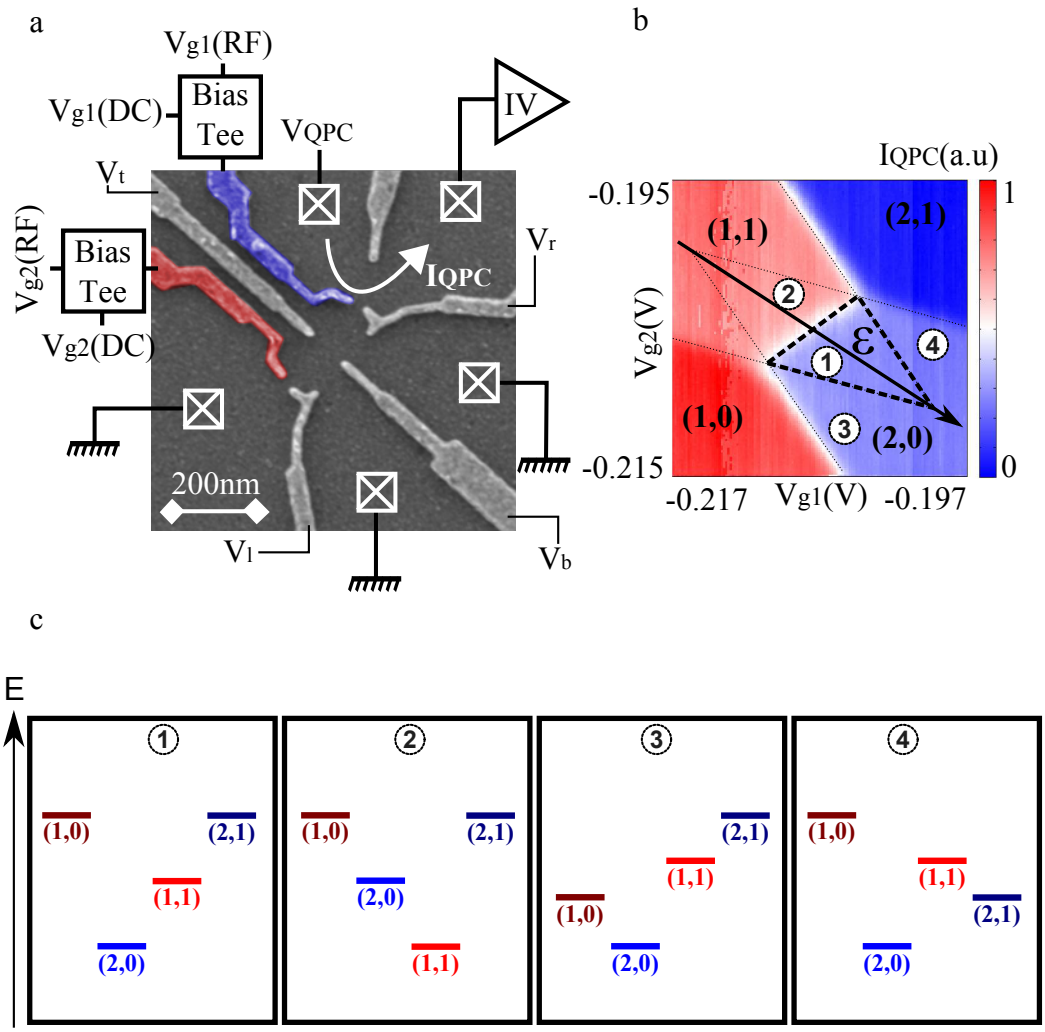

Figure 4.2: **Double quantum dot.** **(a)** Scanning electron microscopy (SEM) picture of the sample measured. The gate pattern allows for definition of two tunnel coupled quantum dots. The electrochemical potential of quantum dot 1 (2) is controlled by the gate voltage V_{g1} (V_{g2}). A quantum point contact located next to the quantum dot 1 allows to probe the charge state of the system. **(b)** Stability diagram of the system. The QPC current (where the mean slope due to the cross talk has been removed) is plotted with respect to V_{g1} and V_{g2} around the region where two electrons are trapped in the system. We define the detuning parameter ε as the difference of energy between the charge states (2,0) and (1,1) (black arrow). **(c)** Energy schemes at the different postions labelled in figure 4.2 (b). In the region (2,0), outside the triangular shape, the energy of the charge state (1,1) is higher than the one of (1,0) (label 3) or (2,1) (label 4).

of the charge state (1,1) is lower in energy than the ones of (1,0) and (2,1). This is no more the case at the position labelled 3 and 4. This feature induces some consequences concerning the spin relaxation, and we will come back to it later.
Now we consider the spin states for this two charge states. The two-electron spin states are the three triplets $|T_+\rangle$, $|T_0\rangle$, $|T_-\rangle$ and the singlet $|S\rangle$ (see chapter 1). But in the (2,0) region ($\varepsilon > 0$), the triplet states are lying $\Delta E \sim 500\mu eV$ (ΔE being the orbital energy, see chapter 1) above the singlet due to the confinement. The wavefunction being antisymmetric (Pauli principle), the orbital part of the triplet states has to be antisymmetric (the spin part being symmetric). Therefore one of the electrons has to occupy the first excited orbital lying $\sim 500\mu eV$ above the lower level. Consequently in the (2,0) region, we assume that the three triplets are energetically not accessible which implies that the only accessible spin state for the electrons in the (2,0) region is the singlet denoted $|S_{2,0}\rangle$. In the (1,1) region ($\varepsilon < 0$), the three triplets and the singlet are accessible and we write them as :

$$\begin{aligned}
|S\rangle &= \frac{1}{\sqrt{2}}(|\uparrow,\downarrow\rangle - |\downarrow,\uparrow\rangle) \\
|T_0\rangle &= \frac{1}{\sqrt{2}}(|\uparrow,\downarrow\rangle + |\downarrow,\uparrow\rangle) \\
|T_+\rangle &= |\uparrow,\uparrow\rangle \\
|T_-\rangle &= |\downarrow,\downarrow\rangle
\end{aligned} \tag{4.11}$$

where the state $|\uparrow,\downarrow\rangle$ means that the electron spin lying in quantum dot 1 (2) is up (down). The energy of these spin states as a function of the detuning parameter ε can be seen in figure 4.3. For $\varepsilon > 0$, the charge ground state is (2,0) and the only accessible spin state is the singlet $|S_{2,0}\rangle$. Due to tunnel coupling, the two singlet states hybridize at $\varepsilon = 0$ (blue lines in figure 4.3). We remind that the tunnelling is a spin conservative process, and therefore the triplets cannot hybridize with the singlet. It gives rise to an exchange energy between the singlet $|S\rangle$ and the triplet $|T_0\rangle$, $J(\varepsilon) = E_{T_0} - E_S \propto \frac{t^2}{|\varepsilon|}$, where t is the tunnel coupling (we will come back to this formula in the following). This energy characterizes the coupling between the two spins : for $J \to 0$, the two spins can be considered as independent which is no more the case when J is finite. In addition the three triplets are split by the Zeeman energy $E_Z = g^*\mu_B B$. Apart when mention, all this set of measurements have been done with the external magnetic field equal to 100mT, which gives a Zeeman energy equal to $2.5\mu eV$.

Another feature has to be seen in the region $\varepsilon \ll 0$, where the exchange energy J vanishes. In this region the two spins can be considered as independent, and the "relevant energy" is no more J but ΔB_z, the gradient of magnetic field between the two quantum dots. Indeed as we mentioned in the first chapter, the electron spins trapped in the quantum dots are surrounded by nuclear spins. The Zeeman energy of these nuclei is dominated by the thermal energy, and consequently they are not polarised with the

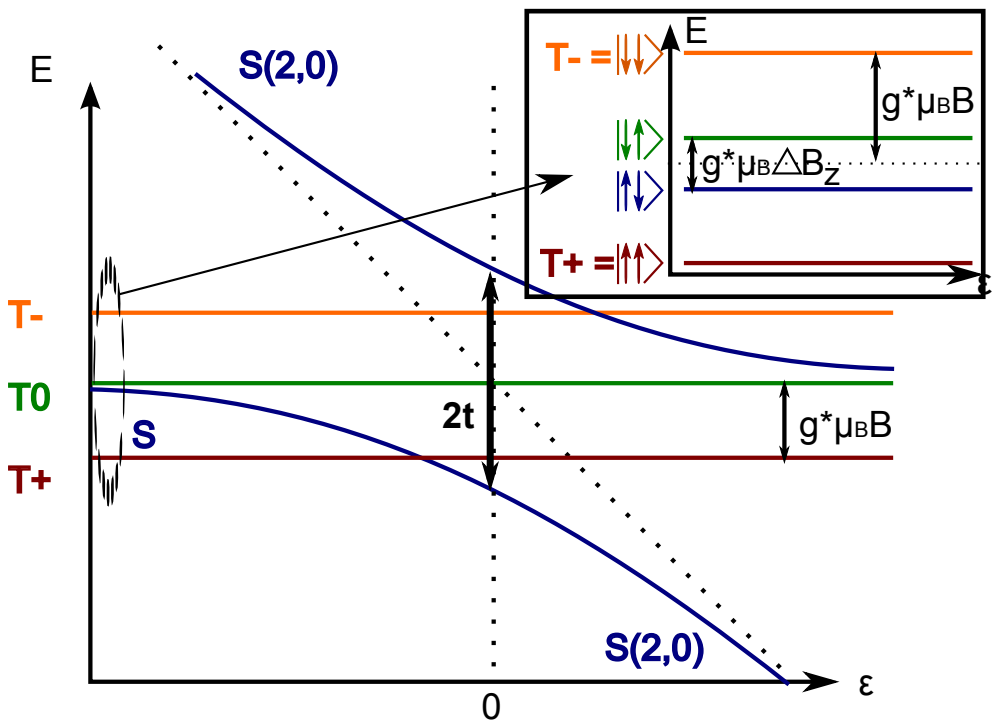

Figure 4.3: **Energy of the spin states with respect to ε.** The three triplets states are split by the Zeeman energy $E_Z = g^* \mu_B B$. The two singlet states hybridize at $\varepsilon = 0$ due to the tunnel coupling and it gives rise to two "new" eigenstates (blue lines). **Inset :** Spin states for $\varepsilon \ll 0$. The relevant spin states are no more $|S\rangle$ and $|T_0\rangle$ but $|\downarrow,\uparrow\rangle$ and $|\uparrow,\downarrow\rangle$.

external magnetic field. In addition each electron spin interacts with the nuclear spins through the hyperfine interaction (see chapter 1). The interaction between the electron spin and a nuclear spin depends on the electron wavefunction value at the position of the nucleus. Then each electron spin "sees" a particular configuration of nuclear spins, which can be modelled by an effective classical field which is different for the two quantum dots. This difference gives rise to a gradient $\Delta B_z = B_z^{n1} - B_z^{n2}$, where B_z^{n1} (B_z^{n2}) is the effective nuclear magnetic field felt by the electron in the quantum dot 1 (2). This gradient is equal to few mT, which is equivalent in energy to $\sim 0.1\mu eV$ ($100mT \leftrightarrow 2.5\mu eV$). We emphasize that the dynamics of the nuclear spins is relatively slow compared to the one of the electron spins (quasi static approximation [7]). Therefore we can assume that the nuclear spin configuration is fixed during a spin manipulation, but evolves from one manipulation to another one. For $\varepsilon \ll 0$, the exchange energy vanishes and becomes smaller than the gradient ΔB_z. Therefore, for $\varepsilon \ll 0$ the singlet $|S\rangle$ and the triplet $|T_0\rangle$ are no more the eigenstates of the system, which are now $|\uparrow,\downarrow\rangle$ and $|\downarrow,\uparrow\rangle$. The four accessible spin states at $\varepsilon \ll 0$ are the ones seen in the inset of figure 4.3, and correspond to the states of two single spin qubits.
In order to manipulate and measure the spin states of this system, we will often refer to this energy diagram. All these manipulations rely on the fast control of the energy detuning ε. We will now introduce the measurement of the spin states by studying the mixing induced by the nuclei.

4.2.2 Measure of the spin state

As we mentioned in the first chapter, it is not possible to measure directly a single spin in our system, and the only information that we can get is its charge state. In the case of a single quantum dot, we have seen in the first chapter a technique of spin-to-charge conversion to measure the spin state of the quantum dot. One more time, we use such a technique in order to read-out the spin states of the system but here we take advantage of the avoided triplet states in the (2,0) regions. Indeed let us consider an unknown spin state in the (1,1) region ($\varepsilon < 0$). The detuning can be set positive where only the singlet $|S_{(2,0)}\rangle$ is accessible. The tunnelling being a spin conservative process, if this unknown spin state is a singlet, the charge state should be (2,0), while if it is a triplet, the charge state should be (1,1) (figure 4.4). This effect is commonly known as a spin-blockade effect. Then by measuring the charge state of the system via the QPC, we should be able to measure its spin state. This is obviously true only if the spin is preserved during the measurement, meaning that the measurement duration has to be shorter than the relaxation time, which is, as we will see, in the range of few tens of μs. Otherwise an initial triplet could relax into the singlet $|S\rangle$, tunnel into the singlet $|S_{(2,0)}\rangle$, giving rise to the measurement of a singlet state. By combining the relaxation time $T_1 \sim 50\mu s$ with the measurement bandwidth $\sim 1kHz$ (related to the bandwidth of the amplifier, see chapter 2) it implies that we are not able to perform a single measurement of the spin states : an

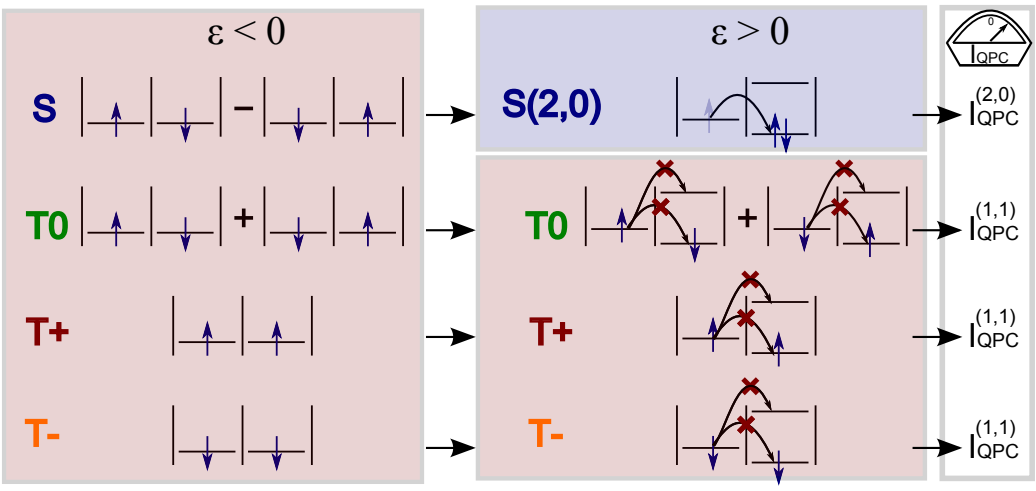

Figure 4.4: **Measurement of the spin states.** Starting with an unknown spin state in the (1,1) region ($\varepsilon < 0$), the detuning parameter ε is set positive ((2,0) region). The tunnelling being a spin conservative process, the electron can tunnel only if its spin state is a singlet. Therefore the measure of the charge state via the QPC gives $I_{QPC}^{(2,0)}$ if the spin state is a singlet, while it gives $I_{QPC}^{(1,1)}$ for any triplets.

experimental point will therefore be the results of the repetition of many manipulation pulses and the only information that we are able to extract is the time averaged QPC signal. This fixes a new constraint in the design of the pulse that we use. Indeed as we will see, the pulse can be decomposed in three main part being the initialization, the manipulation and finally the measurement. The measurement part duration has to be accounted for large percentage of the whole pulse in order that this time averaged QPC signal mainly reflects the charge state during the measurement part. Therefore we generally set the measurement part duration as accounted for 80% of the whole pulse.

This technique of spin to charge conversion has been first introduced by Johnson and coworkers [8]. To illustrate the measurement of the spin states, we will study the example of the mixing between the singlet $|S\rangle$ and the triplet $|T_0\rangle$ induced by the nuclei. Indeed for $\varepsilon \ll 0$, the four spin states are $(|T_+\rangle = |\uparrow,\uparrow\rangle, |\uparrow,\downarrow\rangle, |\downarrow,\uparrow\rangle, |T_-\rangle = |\downarrow,\downarrow\rangle$ due to the vanishing exchange energy and the presence of a nuclear magnetic field gradient ΔB_z. Therefore an initial singlet $|S\rangle = \frac{1}{\sqrt{2}}(|\uparrow,\downarrow\rangle - |\downarrow,\uparrow\rangle)$ should evolve in a superposition of singlet $|S\rangle$ and triplet $|T_0\rangle$ according to the time spent in the region $\varepsilon \ll 0$.
The measurement of singlet-triplet mixing induced by the nuclei can be decomposed in four stages (figure 4.5 (a) and 4.5 (b)) and has been first performed by Petta and coworkers [4] :

- **(1)** Any spin manipulation begins with the initialization of a well-known spin state.

In order to initialize the system, we set it in the (2,0) region where only the singlet $|S_{(2,0)}\rangle$ is accessible. But this is not sufficient to ensure that the initial spin state is the singlet. Indeed if the initialization stage duration is shorter than the relaxation time, the system might not be able to relax. In order to overcome it, we set the system in a particular configuration (label 1 in figure 4.5 (b)). At this position, an electron from the double quantum dot can be exchanged with one from the reservoir, via two sequential tunnelling process which is not possible in the configuration 2 (figure 4.5 (d)) [8]. To understand this principle, let us consider that $\varepsilon < 0$ and the system state is one of the triplets (1,1). In order to reset the system into the singlet state $S_{2,0}$, we change ε and go at the position 1 (region (2,0)) in figure 4.5 (b). Since the state of the system is a triplet, the electron will not be able to tunnel, and the system is first spin-blockaded in the region (1,1). But at the position 1, the charge state (1,1) is higher in energy than the charge state (1,0). Therefore the electron which was lying in quantum dot 2 can tunnel out from quantum dot 2, and be replaced by an electron from the reservoir tunnelling into quantum dot 1. At the end of this process, the system has been reset in the singlet $|S_{(2,0)}\rangle$ (figure 4.5 (d)). We notice here that this initialization process is possible only if the tunnel barriers between the quantum dots and the reservoirs are sufficiently fast compared to the time spent in the stage (1) ($\sim 200ns$), since this relaxation process relies on tunnelling events. We will come back to this point in the following.

- **(2)** The second stage allows for positioning the system along the detuning parameter ε axis. Its duration is equal to $\sim 200ns$. We remind that in this gate voltage configuration (label 2 in figure 4.5 (b)), the relaxation via the reservoir is much longer than the one at the stage 1. Indeed at this position the charge state (1,1) is lower in energy than the two charge states (1,0) and (2,1). Therefore as we will see later the relaxation at the position 2 has to be thermally activated. We will take advantage of this longer relaxation in order to measure the spin state at this position (see stage 4).

- **(3)** During the third stage, the detuning ε is pulsed from $\varepsilon > 0$ to the region where the exchange energy J vanishes ($\varepsilon \ll 0$). The key point here is that the pulse is adiabatic compared to the tunnelling $t \sim 20\mu eV$(our measured estimation will be presented in the next section). Therefore the initial singlet state $|S_{(2,0)}\rangle$ is adiabatically transformed into a singlet (1,1) $|S\rangle$. But this pulse is assumed non-adiabatic compared to the gradient $\Delta B_z \sim 0.1\mu eV$. Experimentally speaking this is achieved by pulsing ε from $\varepsilon > 0$ to $\varepsilon \ll 0$ in one nanosecond. At the end of this pulse, the spin state can be assumed as being the singlet $|S\rangle$. For $\varepsilon \ll 0$, the eigenstates are not $|S\rangle$ and $|T_0\rangle$, but $|\uparrow,\downarrow\rangle$ and $|\downarrow,\uparrow\rangle$ due to the gradient $\Delta B_z > J(\varepsilon \ll 0)$. Then the initial singlet $|S\rangle$ should evolve in a coherent superposition of $|S\rangle$ and $|T_0\rangle$ with a frequency determined by the energy splitting of the states $|\uparrow,\downarrow\rangle$ and $|\downarrow,\uparrow\rangle$:

$$
\begin{aligned}
|\Psi(\tau)\rangle &= \frac{1}{\sqrt{2}}(|\uparrow,\downarrow\rangle e^{i\frac{g^*\mu_B\Delta B_z.\tau}{2\hbar}} - |\downarrow,\uparrow\rangle e^{-i\frac{g^*\mu_B\Delta B_z.\tau}{2\hbar}}) \\
|\Psi(\tau)\rangle &= \frac{1}{2}(|S\rangle(e^{i\frac{g^*\mu_B\Delta B_z.\tau}{2\hbar}} + e^{-i\frac{g^*\mu_B\Delta B_z.\tau}{2\hbar}}) + |T_0\rangle(e^{i\frac{g^*\mu_B\Delta B_z.\tau}{2\hbar}} - e^{-i\frac{g^*\mu_B\Delta B_z.\tau}{2\hbar}})) \\
|\Psi(\tau)\rangle &= cos(\frac{g^*\mu_B\Delta B_z.\tau}{2\hbar})|S\rangle + i.sin(\frac{g^*\mu_B\Delta B_z.\tau}{2\hbar})|T_0\rangle
\end{aligned}
\tag{4.12}
$$

where τ is the time spent in the region $\varepsilon \ll 0$. Therefore the probability of singlet P_S should be equal to :

$$
\begin{aligned}
P_S(\tau) &= |\langle S|\Psi(\tau)\rangle|^2 = |cos(\frac{g^*\mu_B\Delta B_z.\tau}{2\hbar})|^2 \\
P_S(\tau) &= \frac{1 + cos(\frac{g^*\mu_B\Delta B_z.\tau}{\hbar})}{2}
\end{aligned}
\tag{4.13}
$$

The typical value of the gradient being $\Delta B_z \sim 4mT \equiv 0.1\mu eV$, the period of these coherent oscillations should be equal to $\sim 30ns$. But in order to reconstruct the quantum state, we need to perform a large number of measurements, and during each measurement the system feels a different configuration of nuclear spins. As seen in the first chapter the spin state has to be averaged over the distribution of the nuclear fluctuations centered in zero with a typical spread $\sigma_B \sim 5mT$. This causes apparent decoherence, and the time ensemble average decoherence time can be written as $T_2^* = \frac{\hbar}{\mu_B g^* \sigma_B}$. Then the system experiences the decoherence as fast as it oscillates. Finally the singlet probability has to be written as :

$$
P_S(\tau) = \frac{1 + e^{-\frac{\tau}{T_2^*}} cos(\frac{g^*\mu_B\Delta B_z.\tau}{\hbar})}{2} \tag{4.14}
$$

In order to measure experimentally the spin state, one has to project back the system by setting it in the (2,0) region, which is the role of the next stage.

- **(4)** The last stage is the measurement one. The detuning is pulsed back in the region (2,0). One more time this pulse is adiabatic compared to the tunnelling t, but non adiabatic compared to the gradient ΔB_z. Therefore the singlet part of the final state of the stage (3) $|\Psi(\tau)\rangle$ can tunnel and we will measure a (2,0) charge state, while the triplet part is blocked and the charge measurement will give a (1,1) charge state. If the measurement would be perfect we should measure a current $I_{QPC}(\tau)$ (we remind that τ is the time spend in the stage 3) :

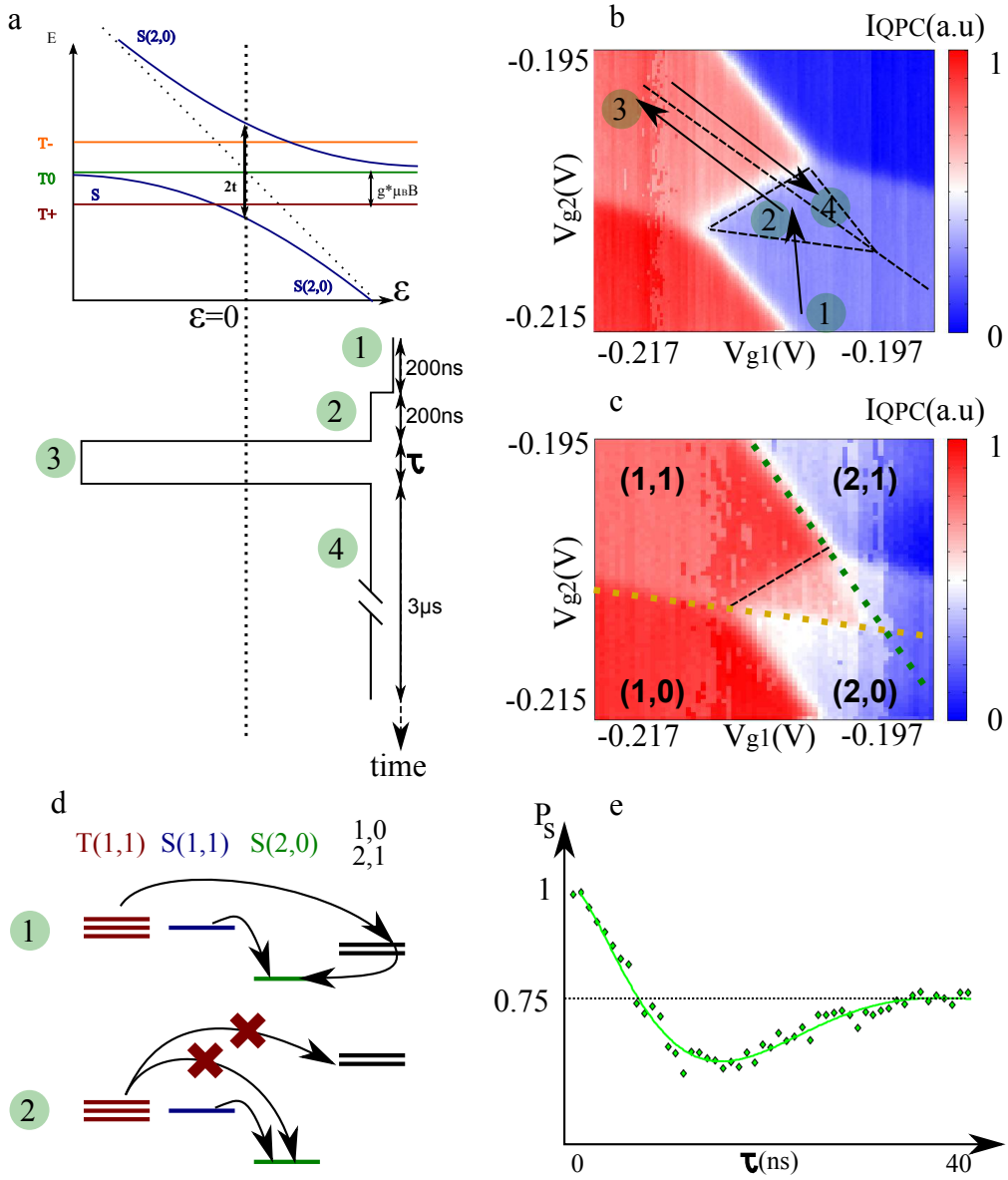

Figure 4.5: **Measurement of the mixing induced by the nuclei.** **(a)** Top : Energy diagram of the two electron spins states in a double quantum dot. Bottom : Applied pulse sequence : the first two stages (1 and 2) allow for initializing a singlet $|S_{2,0)}\rangle$. Then this initial state is pulsed where the exchange energy J is dominated by the gradient ΔB_z (3). Finally the final state is projected back in the (2,0) region where the singlet probability can be known by measuring the charge state (4). **(b)** Pulse positions in the stability diagram. The first stage allows for fast relaxation because it is outside the triangle shape where the relaxation via the reservoirs is energetically allowed. **(c)** Same stability diagram than in (b) with the pulse superposed to the DC voltage V_{g1} and V_{g2}. A triangle shape is clearly observed in the (2,0) region, where the charge state is not (2,0). **(d)** Energetic schemes of the two stages (1) and (2). In the stage (1), the relaxation is enhanced by an exchange of an electron with the reservoir ensured by two sequential tunnelling processes.

$$
\begin{aligned}
I_{QPC}(\tau) &= I_{(2,0)}P_S + I_{(1,1)}P_{T_0} \\
I_{QPC}(\tau) &= I_{(2,0)}[\frac{1+e^{-\frac{\tau}{T_2^*}}cos(\frac{g^*\mu_B\Delta B_z.\tau}{\hbar})}{2}] + I_{(1,1)}[\frac{1-e^{-\frac{\tau}{T_2^*}}cos(\frac{g^*\mu_B\Delta B_z.\tau}{\hbar})}{2}]
\end{aligned}
\tag{4.15}
$$

Finally if $\tau \gg T_2^*$ the measured QPC current should be equal to $I_{QPC} = \frac{I_{(2,0)}+I_{(1,1)}}{2}$, reflecting the mixing of the singlet and the triplet induced by the nuclear spins through the hyperfine interaction. We notice that the measurement stage duration is equal to 3000ns which is accounted as 80% of the whole pulse duration.

Figure 4.5 (d) shows a stability diagram where the RF pulse sequence described previously has been added to the DC gate voltage V_{g1} and V_{g2}. In this figure the time spent in the region $\varepsilon \ll 0$ has been set equal to $\tau = 100ns$. We can clearly see a triangular shape in the (2,0) region where the QPC current is equal to $I_{QPC} \sim 0.75.I_{(2,0)} + 0.3.I_{(1,1)}$. Outside the triangle, the relaxation occurs quickly due to the exchange of an electron with one from the reservoirs (figure 4.5 (c)), explaining why we do not observe any spin blockade in this region. Especially if the gate voltages are set below (above) the yellow (green) dotted line, the charge state (1,0) is lower in energy than (1,1) ((2,1)) (see energy schemes in figure 4.2 (c)). In addition, as mentioned earlier, for $\tau \gg T_2^*$ we expected a probability to measure a singlet $P_S = 0.5$. The measured $P_S = 0.75$ can be associated to a reduction of contrast due to relaxation of the triplet. This measurement has been performed in an external magnetic field $B_{ext} = 100mT$. For $B_{ext} = 0mT$, the expected singlet probability should be $P_S(\tau \gg T_2^*) = 1/4$, because all the three triplets can mix with the singlet. But a semiclassical model assuming independent quasi-static nuclear magnetic fields acting on the two spins, and perfect measurement contrast shows that for $B_{ext} = 0mT$ $P_S(\tau \gg T_2^*) = 1/3$ [4, 9].
To characterize experimentally the mixing induced by the nuclei, the singlet probability can be measured with respect to the time τ spent in the region $\varepsilon \ll 0$ [4]. We fixed the two DC voltages V_{g1} and V_{g2} in order to stand inside the triangular shape (where the relaxation time is the longer), and we measure the QPC current as a function of τ. To convert the measured QPC current into singlet probability, we assume that $P_S = 1$ if $I_{QPC} = I_{(2,0)}$, and $P_S = 0$ if $I_{QPC} = I_{(1,1)}$. The experimental points have been fitted with an exponentially damped cosine, with amplitude, decay time (T_2^*), and period ($T = \frac{g^*\mu_B\Delta B_z}{\hbar}$) as fit parameters. We got $T_2^* = 15ns$ and $\Delta B_z = 4mT$, consistently with previous measurements [4, 10, 11].
This spin state measurement example shows that we could manipulate the spin states of the system, and measure the singlet probability. In order to achieve coherent manipulations of the spin states, more sophisticated manipulations are required, and we will introduce them in the following. We will now detailed how such spin measurements can help in order to tune the system in a proper configuration.

4.3 Characterization and tuning of the system

As we briefly mentioned, three parameters are of direct relevance in order to perform spin manipulations in quantum dot systems : the tunnel barriers between each quantum dot and its reservoir, and the tunnel barrier between the two quantum dots. We remind that the inter-dot tunnelling can be tuned by changing the gate voltages applied to V_t and V_b, while the tunnel coupling with the reservoir is mainly tunable via the gate voltages V_r and V_l (figure 4.2 (a)). In this section we will explain how simple spin manipulations can be used in order to tune the device.

4.3.1 Tunnel coupling between the two quantum dots

In the previous example, we assumed that the pulse was adiabatic compared to the tunnelling between the two quantum dots. It ensures the initialized singlet $|S_{(2,0)}\rangle$ is "transformed" into a singlet $|S\rangle$ when a detuning pulse is applied from $\varepsilon > 0$ to $\varepsilon < 0$. We will detail a little bit this concept of adiabaticity : consider two singlet states $|S_{(2,0)}\rangle$ and $|S\rangle$ coupled by the tunnelling t. The energy of the singlet $|S_{(2,0)}\rangle$ is equal to ε (we remind that ε is the detuning parameter) and the one the singlet $|S\rangle$ is 0. Therefore the Hamiltonian of this system comes as (in the basis $\{|S_{(2,0)}\rangle, |S\rangle\}$):

$$H = \begin{pmatrix} -\varepsilon & t \\ t & 0 \end{pmatrix} \tag{4.16}$$

Due to the tunnel coupling t, the two singlet states hybridize at $\varepsilon = 0$, giving rise to two "new" eigenstates $|\Psi_1\rangle$ and $|\Psi_2\rangle$ with energy $E_1 = \frac{-\varepsilon-\sqrt{\varepsilon^2+4t^2}}{2}$ and $E_2 = \frac{-\varepsilon+\sqrt{\varepsilon^2+4t^2}}{2}$ (figure 4.6) :

$$\begin{aligned} |\Psi_1\rangle &= \frac{1}{2t\sqrt{1+\frac{1}{4}|\frac{\Omega_1(\varepsilon)}{t}|^2}} \begin{pmatrix} -\Omega_1(\varepsilon) \\ 2t \end{pmatrix} \\ |\Psi_2\rangle &= \frac{1}{2t\sqrt{1+\frac{1}{4}|\frac{\Omega_2(\varepsilon)}{t}|^2}} \begin{pmatrix} -\Omega_2(\varepsilon) \\ 2t \end{pmatrix} \end{aligned} \tag{4.17}$$

where $\Omega_{\frac{1}{2}}(\varepsilon) = \varepsilon \pm \sqrt{\varepsilon^2 + 4t^2}$. As we can see for $\varepsilon \gg 0$, $|\Psi_1\rangle \sim |S_{(2,0)}\rangle$ and $|\Psi_2\rangle \sim |S\rangle$. For $\varepsilon \ll 0$, $|\Psi_1\rangle \sim |S\rangle$ and $|\Psi_2\rangle \sim |S_{(2,0)}\rangle$. In addition it allows us to justify the formula of the exchange energy given earlier. By considering $|\varepsilon| \gg t$ (in the (1,1) region), the energy E_1 comes as $E_1 = -t^2/|\varepsilon|$. The energy of the triplet $|T_0\rangle$ being $E_{T_0} = 0$, we get $J(\varepsilon) = t^2/|\varepsilon|$.

Then the question arising is : assuming $\varepsilon \gg 0$ and the system being in the ground state $|\Psi_1\rangle$, what happens to the system if ε is pulsed into the region $\varepsilon \ll 0$? The

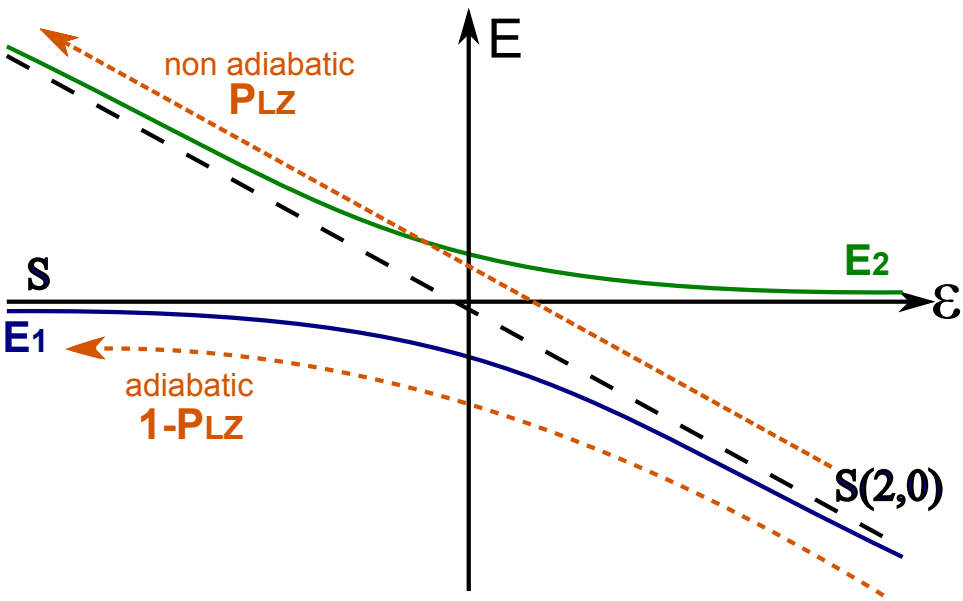

Figure 4.6: **Tunnel coupling between the two singlet states, and adiabatic(non adiabatic) evolution.** When ε is pulsed from positive to negative values, the probability to be in the eigenstate $|\Psi_1\rangle$ at the end of the evolution is given by the Landau-Zener formula.

probability to be in the state $|\Psi_2\rangle$ at the end of the evolution (non-adiabatic evolution) is given by the Landau-Zener formula [12], and depends on the speed at which the pulse is applied :

$$P_{LZ} = e^{-2\pi\Gamma}, \qquad \Gamma = \frac{4t^2}{\hbar\frac{d\varepsilon}{dt}} \tag{4.18}$$

Assuming a pulse speed $\frac{d\varepsilon}{dt} \sim 10^5 eVs^{-1}$ (which is approximatively the range of our pulse generator and it corresponds to an ε-change of $100\mu eV$ in 1ns), for a tunnelling equal to $t = 10\mu eV$, we get $P_{LZ} \sim 0$. But for $t = 0.1\mu eV$, $P_{LZ} \sim 1$. In the pulse sequence described earlier (mixing induced by the nuclei) and generally for all the pulses used during this thesis, we assume the adiabaticity with respect to the tunnelling (between the two quantum dots) in order to transform correctly a singlet $|S_{(2,0)}\rangle$ into a singlet $|S\rangle$, and this is the first reason to correctly tune the tunnel coupling. We will see the second one later when we will study the exchange coherent oscillations, and for the moment we will introduce an experimental way to estimate this tunnelling.
In order to get an order of magnitude of this tunnel coupling, we can perform a measurement of the exchange energy with respect to the detuning parameter ε. Indeed as it has been demonstrated, the exchange energy J depends on the tunnel coupling between the two quantum dots ($J(\varepsilon) = t^2/|\varepsilon|$). One of the way to achieve it consists in the measurement of the position ε^* of the anticrossing between the singlet state $|S\rangle$ and the triplet $|T_+\rangle$ (figure 4.7 (a)) . Indeed at this position, the exchange energy should be equal to the Zeeman energy defined by the external magnetic field. Therefore if we are able to probe this position with respect to the external magnetic field, we should be able to extract a formula of the exchange energy with respect to the detuning ε, and consequently get an order of magnitude of the tunnel coupling. This measurement has been first realized by Petta and coworkers [4]. To measure the position of the anticrossing between the singlet $|S\rangle$ and the triplet $|T_+\rangle$, we can take advantage of the hyperfine interaction between the electron spins and the nuclear spins. Indeed as it will be demonstrated in the following, when the singlet $|S\rangle$ and the triplet $|T_+\rangle$ are degenerated (meaning at the crossing of these two levels), the nuclei can induce a mixing between them. This is quite similar to the mixing induced by nuclei between the singlet $|S\rangle$ and the triplet $|T_0\rangle$ seen in the previous section. But two different features can be distinguished :

- As we will see, in this case the mixing is not induced by the gradient of the nuclear magnetic field along the $\hat{z}$ axis, but by the gradient along the $\hat{x}$ and $\hat{y}$ axis $\Delta B_{x,y}$. The order of magnitude of these gradients is similar to the one along the $\hat{z}$ axis : $\Delta B_{x,y} \sim 4mT$.

- The $S - T_0$ mixing occurs since the energy difference between $|S\rangle$ and $|T_0\rangle$ (the exchange energy $J(\varepsilon)$) is smaller than the gradient ΔB_z. As we have seen, this

condition is verified for relatively large region in ε. The case of the mixing $S - T_+$ occurs also when the energy difference between $|S\rangle$ and $|T_+\rangle$ is smaller than $\Delta B_{x,y}$, but as it is directly observed in the energy diagram 4.7 (a), this condition is verified just around the crossing between the singlet $|S\rangle$ and the triplet $|T_+\rangle$. In other words, the position (in ε) where the mixing $S - T_+$ occurs is well localized, and it corresponds to the value of ε making the exchange energy $J(\varepsilon)$ equal to the Zeeman energy $E_Z = g^* \mu_B B$.

Let us develop how the hyperfine interaction between the nuclei and the electrons spins allows for such a mixing. This interaction can be modelled by the Hamiltonian [7]:

$$H_{hf} = g^* \mu_B \vec{\Delta B}(\vec{S}^l - \vec{S}^r) \tag{4.19}$$

where $\vec{\Delta B} = (\Delta B_x, \Delta B_y, \Delta B_z)$ is the nuclear magnetic field gradient vector and $\vec{S}^{l(r)} = (S_x^{l(r)}, S_y^{l(r)}, S_z^{l(r)})$ is the spin operator of the electron spin in the left (right) quantum dot. We can rewrite this hamiltonian by using the spin creation/annihilation operator $S_{\pm} = S_x \pm i S_y$ as :

$$H_{hf} = g^* \mu_B [\Delta B_z (S_z^l - S_z^r) + \frac{(S_+^l - S_+^r)}{2}(\Delta B_x - i\Delta B_y) + \frac{(S_-^l - S_-^r)}{2}(\Delta B_x + i\Delta B_y)] \tag{4.20}$$

Then we get the matrix element between the singlet $|S\rangle$ and the triplet $|T_+\rangle$:

$$\langle S|H_{hf}|T_+\rangle = g^* \mu_B \frac{\Delta B_x - i\Delta B_y}{\sqrt{2}} \tag{4.21}$$

The singlet $|S_{(2,0)}\rangle$ being not coupled to the triplet $|T_+\rangle$, the matrix element between $|\Psi_1\rangle$ (the eigenstate resulting from the tunnel coupling between the two singlet, equation 4.17) and the triplet $|T_+\rangle$ is :

$$\langle \Psi_1|H_{hf}|T_+\rangle = \langle \Psi_1|S\rangle\langle S|H_{hf}|T_+\rangle = \frac{-g^* \mu_B}{\sqrt{1 + \frac{1}{4}|\frac{\Omega_1(\varepsilon)}{t}|^2}} \frac{\Delta B_x - i\Delta B_y}{\sqrt{2}} \tag{4.22}$$

We remind that the anticrossing between, $|S\rangle$ and $|T_+\rangle$ occurs when the exchange energy $J(\varepsilon)$ is equal to the Zeeman energy $E_z = g^* \mu_B B z$. For low values of the Zeeman energy, the anticrossing occurs in the region $\varepsilon < 0$, while it occurs in the $\varepsilon > 0$ region for large value of the Zeeman energy. In addition as we can see from equation 4.22, the strength of the coupling depends on the detuning parameter ε. For instance if the anticrossing happens for $\varepsilon \gg 0$ (where $|\Psi_1\rangle \sim |S_{(2,0)}\rangle$), $\frac{\Omega_1(\varepsilon)}{t} \gg 0$ and then $\langle \Psi_1|H_{hf}|T_+\rangle \sim 0$.

For $\varepsilon \ll 0$ (where $|\Psi_1\rangle \sim |S\rangle$), $\frac{\Omega_1(\varepsilon)}{t} = 0$ and then $\langle\Psi_1|H_{hf}|T_+\rangle \sim -g^*\mu_B\frac{\Delta B_x - i\Delta B_y}{\sqrt{2}}$.

In order to probe this mixing, a pulse sequence similar to the previous one can be designed(figure 4.7 (a)). The first two stages allow for initializing the spin state into $|S_{(2,0)}\rangle$. During the third stage, the detuning is pulsed at the position of the anticrossing $S - T_+$ (ε^* in figure 4.7 (a)). At this position the nuclei will induce a mixing between the initial singlet $|S\rangle$ and the triplet $|T_+\rangle$, and as a result we expect to detect a lower singlet probability. The last stage corresponds to the measurement of the spin state as seen earlier.

Figure 4.7 (b) shows the stability diagram where the pulse sequence has been superimposed to the DC voltages. We can clearly observed a small line in the region (2,0) where the current is not equal to $I_{QPC}^{(2,0)}$ indicating a singlet probability smaller than one. We remind that contrary the $S - T_0$ mixing, the position where the $S - T_+$ mixing occurs is localized at $\varepsilon = \varepsilon^*$. This explain why only a small line is observed. In addition, as we mentioned in the begining, this anticrossing appears when the exchange energy $J(\varepsilon) = E_{T_0} - E_S = \frac{t^2}{\varepsilon}$ equal the Zeeman energy $E_Z = g^*\mu_B B$. Then by measuring the position of this anticrossing with respect to the magnetic field, we should be able to extract a formula for $J(\varepsilon)$, and get the value of the tunnelling t. Figure 4.7 (c) shows the singlet probability with respect to the detuning and the magnetic field, the so-called spin funnel first demonstrated by Petta and coworkers [4]. We notice that the value of ε takes into account the α factor, which is related to the gate lever arm on the quantum dot potential. This α factor has been extracted from previous transport measurements at finite voltage bias and we obtained a conversion factor of $0.1eV/V$. This gate lever arm conversion factor has to be taken with caution because these transport measurements have been done for the system tuned as a single quantum dot. Therefore it only gives a rough estimation of its value in a double quantum dot configuration. Concerning the figure 4.7 (c), we clearly observe the expected dependence of the anticrossing $S - T_+$ position with respect to the magnetic field. The inset of figure 4.7 (c) shows the QPC signal obtained along the dotted line, and we observe a clear peak related to the studied mixing.

By fitting the position ε^* of the anticrossing $S - T_+$ with respect to the magnetic field, we can extract a formula for the exchange energy J. Indeed as we have seen, at this position the Zeeman Energy is equal to the exchange energy. We fitted it by a power law we obtain a formula for the exchange energy :

$$J(\varepsilon) = \frac{5.11 * 10^{-10}}{\varepsilon^{1.2}} \qquad (eV) \tag{4.23}$$

The ε power $\beta = 1.2$ rather than the expected $\beta = 1$ is not understood, but this behaviour has been reported in other set of experiments [4]. This measurement allows us to give an order of magnitude of the tunnelling, by comparing to the formula $J(\varepsilon) =$

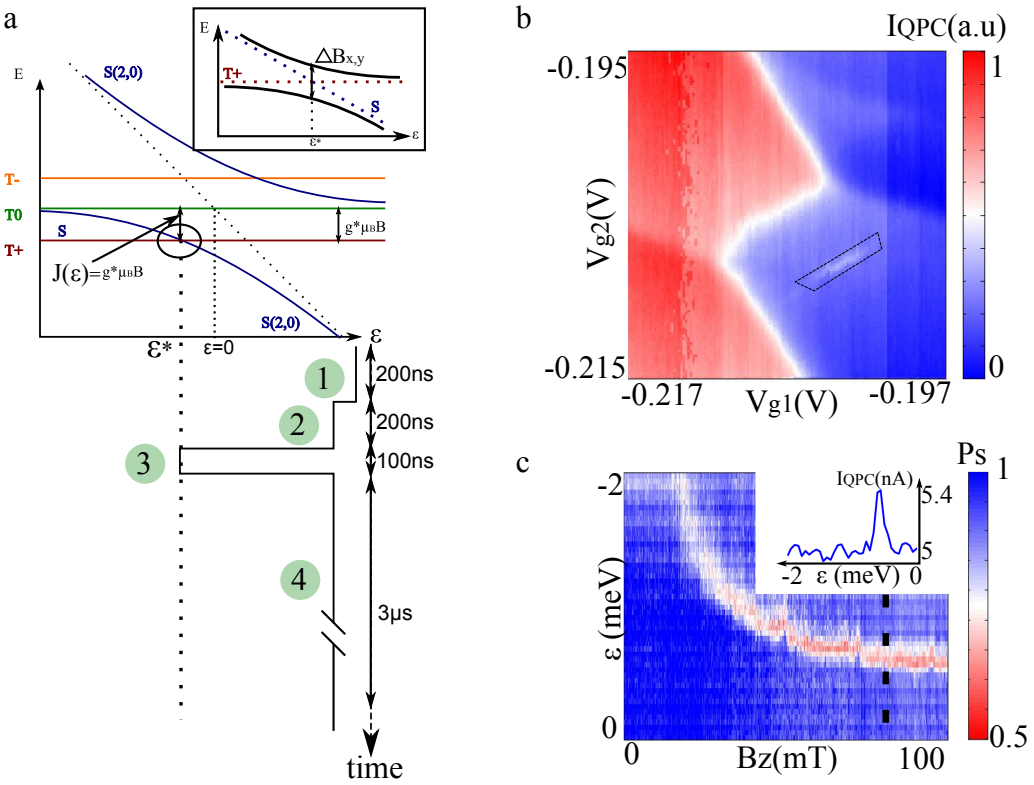

Figure 4.7: **Measurement of the mixing between the singlet state $|S\rangle$ and the triplet $|T_+\rangle$ induced by the nuclei through the hyperfine interaction. (a)** Applied pulse sequence : the first two stages allow for initializing a singlet $|S_{2,0)}\rangle$. Then this initial state is pulsed to the anticrossing between $|S\rangle$ and $|T_+\rangle$ (third stage). Finally the final state is projected back into the (2,0) region where the singlet probability can be obtained by measuring the charge state (fourth stage). Inset : zoom around the anticrossing between the singlet $|S\rangle$ and the triplet $|T_+\rangle$.**(b)** Stability diagram measured with the pulse sequence described in (a). We observe a small line in the (2,0) region indicating a singlet probability smaller than one. **(c)** Measurement of the position of the $S - T_+$ anticrossing with respect to the magnetic field. Inset : QPC signal of the mixing between $|S\rangle$ and $|T_+\rangle$.

$\frac{t^2}{|\varepsilon|}$. We can therefore estimate the tunnel coupling as $t \sim 20\mu eV$ in this gate voltage configuration. We remind that this is only a rough estimation due to the low confidence of the α factor estimation. But it gives a good order of magnitude and it demonstrates that the adiabaticity condition is fulfilled.
In order to increase (decrease) this tunnel coupling, the gate voltages V_t and V_b (figure 4.2 (a) have to be decreased (increased). We will now discuss about the others parameters which can alter spin measurements : the tunnel barriers between the quantum dots and the reservoirs.

4.3.2 Tunnel barriers between the quantum dots and the reservoirs

Previously we specified the requirement to get a sufficiently long relaxation time compared to the duration of the spin manipulations. This process can induce the decay of a triplet into a singlet and hence induces a measurement "error". Indeed if the relaxation occurs, a triplet relaxes into the singlet and lead to the measure of a singlet, meaning a measurement error. It appears therefore important to understand what is the origin of this phenomenon. As mentioned in the first chapter, the relaxation process is an energy exchange between the system and the environment. Due to the energy conservation principle, the environment has to exhibit a finite density of states at the energy splitting of the excited and ground states. For instance it has been demonstrated that at low external magnetic field, the relaxation in a double quantum dot system was dominated by the interaction with the nuclear spins [8]. Indeed, at $B = 0mT$, all the triplets mix with the singlet $|S\rangle$ due to nuclear spins fluctuations. This mixing induced by nuclei is followed by inelastic decays of the singlet $|S\rangle$ into the singlet $S_{(2,0)}$. But for $B = 100mT$, the nuclear spins do not present a finite density of states, because the g^* factor of the nuclei is 1000 time smaller than the one of the electrons. In other words the Zeeman energy of the nuclei is 1000 time smaller than the one of the electron, and consequently the system cannot exchange energy with the nuclei. Therefore, in this configuration, the relaxation is dominated by the exchange of one electron with the reservoirs via two sequential tunnelling processes (figure 4.5 (d)) : $(1,1) \longrightarrow^{(2,1)}_{(1,0)} \longrightarrow (2,0)$. Such a process depends obviously on the energy difference between the charge state (1,1) and (2,1) (or (1,0)). Outside the triangular shape of figure 4.5 (c), the charge state (1,1) is higher in energy than (2,1) or (1,0) (see figure 4.2 (c)). It explains the fast relaxation outside this triangle. But inside the energy of the charge state (1,1) is lower than the ones of (2,1) or (1,0). In this case the relaxation is a thermally activated process and we can model its rate by $\Gamma_T \propto exp(-E_T/k_BT)$, where E_T is the energy difference between the charge states (1,1) and (2,1) (or (1,0)).
In addition, due to the nature of this relaxation process, implying exchange of electrons between the system and the reservoir, the relaxation rate depends strongly on the tunnel barriers separating the quantum dots and the reservoirs. Consequently in order to per-

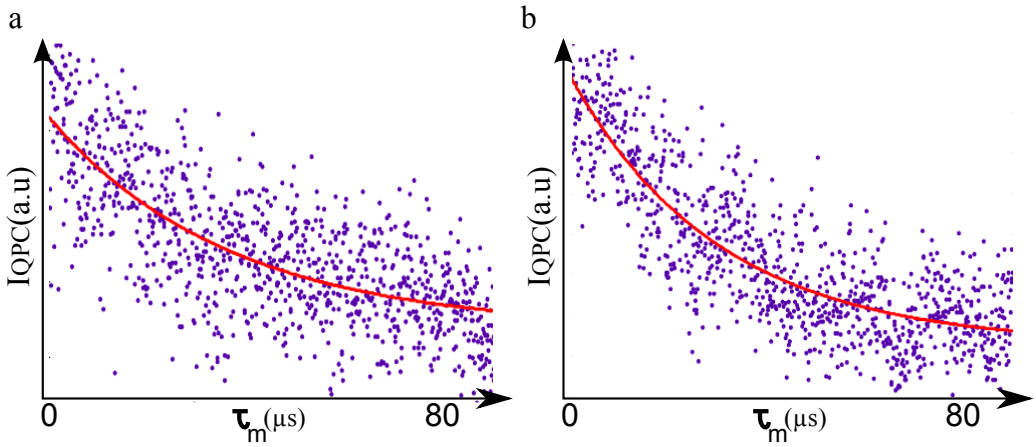

Figure 4.8: **Relaxation of the triplet states.** **(a)** Relaxation of the triplet $|T_0\rangle$. The QPC current is measured with respect to the time spent in the measurement stage. The relaxation time of $|T_0\rangle$ can be estimated to $T_1(T_0) = 32\mu s$. **(b)** Relaxation of the triplet $|T_+\rangle$. The QPC current is measured with respect to the time spent in the measurement stage. The relaxation time of $|T_+\rangle$ can be estimated to $T_1(T_+) = 27\mu s$

form spin manipulations, it is of direct relevance to tune correctly these tunnel barriers. The first naive assumption could be to close these barriers as much as we can, in order to decrease the rate Γ_T. But as we have seen previously, we take advantage of the fast relaxation outside the triangular shape (figure 4.5 (d)) to initialize the spin state before every manipulations. Then a compromise has to be found between sufficiently long relaxation time inside the triangle, and a relatively slow one outside.
In order to tune the two barriers with the reservoir, we simply perform a spin measurement (for instance the mixing $S - T_0$ or $S - T_+$), and we observe the QPC current as a function of the measurement stage duration that we denote τ_M. Indeed if the measurement stage duration becomes longer, a triplet can relax into a singlet, and consequently the electron tunnels into the (2,0) region and we finally measure a QPC current equal to $I_{QPC} = I_{QPC}^{(2,0)}$.

Figure 4.8 (a) and 4.8 (b) shows the decay of the triplets $|T_0\rangle$ (a) and $|T_+\rangle$ (b) inside the triangular shape ((figure 4.5 (c)), meaning that the DC voltages V_{g1} and V_{g2} have been fixed during the measurement. The QPC current is measured with respect to the measurement stage duration τ_M for the two pulse sequences described earlier. By fitting it to an exponential decay, we can estimate the relaxation time T_1. For the two measurements we find a similar $T_1 \sim 30\mu s$ ($T_1(T_0) = 32\mu s$ and $T_1(T_+) = 27\mu s$). In this configuration, the tuning of the tunnel barriers with the reservoirs allows for sufficiently long relaxation time, but also for fast initialization of the spin states. This relaxation

rate can be decreased (increased) by increasing (lowering) the gate voltages V_r and V_l (figure 4.2 (a)).
For all the measurements being described in the following, the system has been tuned with a tunnelling coupling between the two quantum dots $t \sim 20\mu eV$, and a relaxation time $T_1 > 30\mu s$. We remind that the purpose of this work is to study a way to realize an efficient C-phase gate with single spin qubits by following the theoretical proposal [6]. The authors demonstrated that the two-qubit gate for single spin qubits evolves from the SWAP gate at zero gradient ΔB_z to the C-phase gate for larger gradient. We will now develop this theoretical proposal.

4.4 C-phase gate with single spin qubtis

As seen at the beginning of the chapter, a C-phase gate consists in operating a conditional rotation around the $\hat{z}$ axis on a target qubit. The condition is related to the state of a control qubit. A π-controlled phase gate can be expressed in matrixform as :

$$C - Phase = \begin{pmatrix} 1 & 0 & 0 & 0 \\ 0 & 1 & 0 & 0 \\ 0 & 0 & 1 & 0 \\ 0 & 0 & 0 & -1 \end{pmatrix} \tag{4.24}$$

We can easily demonstrate that :

$$\begin{aligned} C - Phase &= \begin{pmatrix} 1 & 0 & 0 & 0 \\ 0 & 1 & 0 & 0 \\ 0 & 0 & 1 & 0 \\ 0 & 0 & 0 & -1 \end{pmatrix} = R_Z(\phi_1).R_Z(\phi_2).U \\ where \quad U &= \begin{pmatrix} 1 & 0 & 0 & 0 \\ 0 & e^{i\phi_1} & 0 & 0 \\ 0 & 0 & e^{i\phi_2} & 0 \\ 0 & 0 & 0 & 1 \end{pmatrix} \end{aligned} \tag{4.25}$$

for $\phi_1 + \phi_2 = \pi$, and $R_Z(\phi)$ is the single qubit ϕ rotation around the $\hat{z}$ axis. Then if we are able to engineer the two qubits gate related to the unitary transformation U, we should be able to perform a C-phase gate. The unitary transformation U corresponds to a phase shift of the antiparallel spin states. Therefore we can distinguish two main requirements for the C-phase gate experimental realization :

- First the eigenbasis of the system has to be $\{|\uparrow,\uparrow\rangle, |\uparrow,\downarrow\rangle, |\downarrow,\uparrow\rangle, |\downarrow,\downarrow\rangle\}$.
- In this eigenbasis, we need to design a pulse sequence changing the energies of the two antiparallel spin states while the ones of the parallel spin states remain the same.

For the mathematical development, we let the reader refer to [6], and here we will try to give an "hand waving" demonstration.

In the previous section, we demonstrated that the "good" eigenbasis was related to the strength of the exchange energy $J(\varepsilon)$ and the one of the gradient ΔB_z. Indeed if $J(\varepsilon) > \Delta B_z$, we can assume that the eigenstates are the singlet $|S\rangle$, the triplet $|T_0\rangle$, and the two parallel spin states $|T_+\rangle = |\uparrow,\uparrow\rangle$, $|T_-\rangle = |\downarrow,\downarrow\rangle$. In opposite, if $J(\varepsilon) < \Delta B_z$ the eigenstates are now the two antiparallel spin states $|\uparrow,\downarrow\rangle$, $|\downarrow,\uparrow\rangle$, and the two parallel ones $|T_+\rangle = |\uparrow,\uparrow\rangle$, $|T_-\rangle = |\downarrow,\downarrow\rangle$. In the following we will compare the two regimes described in figure 4.9 :

- First we consider the gradient ΔB_z as weak, let says $\Delta B_z \sim 4mT$ (figure 4.9 (a)). In this case the region (in ε) where the gradient ΔB_z dominates the exchange energy corresponds to the region $\varepsilon \ll 0$ (dotted circle in figure 4.9 (a)). In this region, the two electron spins can be considered as independent ($J(\varepsilon) \to 0$). This results in the flat energy scheme as seen in the bottom picture of figure 4.9 (a). Consequently it is not possible to design a pulse sequence which induces an energy shift to the antiparallel spins states.

- On the other hand, if the gradient ΔB_z is made larger (figure 4.9 (b)), the condition $\Delta B_z > J(\varepsilon)$ is still verified for the lower values of ε (right part of figure 4.9 (b)). For these lower values of ε, the two electron spins are no more independent (although $\Delta B_z > J(\varepsilon)$, the exchange energy J is no more negligible). Since the antiparallel spin states contain a singlet $|S\rangle$ component, and this singlet $|S\rangle$ couples to the singlet $|S_{(2,0)}\rangle$ via the tunnel coupling t, the energies of the antiparallel spin states decrease when ε decreases. The parallel spin states do not contain any singlet $|S\rangle$ component and consequently their energies remains the same all along the detuning ε axis (bottom picture of figure 4.9 (b)). To conclude, by increasing the gradient ΔB_z, we should be able to find a region where the eigenbasis is $\{|\uparrow,\uparrow\rangle, |\uparrow,\downarrow\rangle, |\downarrow,\uparrow\rangle, |\downarrow,\downarrow\rangle\}$, and where an energy shift of the antiparallel spin states is possible.

The authors of [6] demonstrated that this energy shift scales with the gradient ΔB_z : the bigger is the gradient ΔB_z, the bigger will be the energy shift. The duration of the controlled π-phase gate operation depends obviously on this energy shift. In the following we will study the cross-over between the two regimes described above by increasing progressively the gradient ΔB_z. We will now study the way used during this thesis in order to increase this gradient.

4.5 Dynamical polarization of the nuclear spins

Although we want to use an engineered magnetic field gradient to build an efficient C-phase gate, the first interest of this gradient relies in the possibility to perform spin

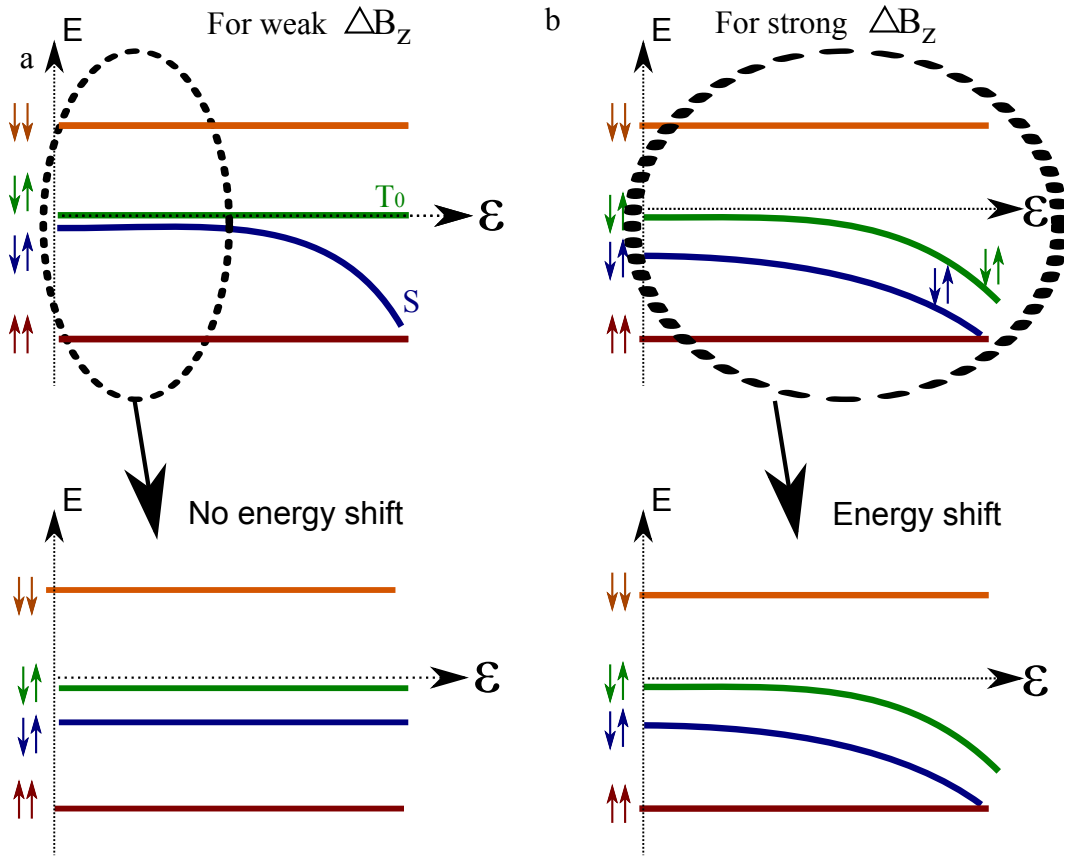

Figure 4.9: **a** Energy scheme for weak gradient ΔB_z. The dotted circle corresponds to the region where the gradient ΔB_z dominates the exchange energy J. As a consequence in this region, the eigenstates are $\{|\uparrow,\uparrow\rangle, |\uparrow,\downarrow\rangle, |\downarrow,\uparrow\rangle, |\downarrow,\downarrow\rangle\}$. In addition inthis region ($\varepsilon \ll 0$), the energies of the four states $\{|\uparrow,\uparrow\rangle, |\uparrow,\downarrow\rangle, |\downarrow,\uparrow\rangle, |\downarrow,\downarrow\rangle\}$ are constant. **(b)** Energy scheme for stronger gradient ΔB_z. The condition $J(\varepsilon) < \Delta B_z$ is fulfilled for lower value of the detuning parameter ε (dotted circle). Due to tunnel coupling, the energies of the two antiparallel states decreases while the one of the parallel spin states remains constant with respect to ε.

selective manipulations. Indeed due to the gradient, the Zeeman energy of the electron spins is different between the two quantum dots. Therefore it allows for manipulating independently each electron spin present in the tunnel coupled quantum dots by performing electron spin resonance [13]. It exists different ways to engineer a nuclear gradient. Using for instance a micro-magnet located close to the quantum dot allows for a gradient up to 30 mT [13, 14, 15]. Also a difference in the g-factor between neighbouring quantum dots offers similar possibilities and has been used in order to address independently electrons spins lying in a double quantum dot nanowire [16]. Although these methods are efficient to built a finite gradient, they need technological developments. On the other hand, it has been recently demonstrated that this gradient can be engineered by taking advantage of the hyperfine interaction between the electrons and nuclear spins [17, 10, 11]. Indeed we can use fast control of the electron spin states in a double quantum dot to induce this gradient, and we will now described this process.

4.5.1 Polarization pulse

In order to polarize the nuclear spins, we take advantage of the coupling between the singlet $|S\rangle$ and the triplet $|T_+\rangle$ induced by the nuclear spins gradient along the $\hat{x}$ and $\hat{y}$ axis (see previous section). As already seen, this coupling is also the results of the hyperfine interaction between the electrons and nuclear spins. Contrary to the coupling between $|S\rangle$ and $|T_0\rangle$, it involves an exchange of spins between the electrons and the nuclei and opens the route toward nuclear polarization. The idea, first introduced by Petta and coworkers [17] is to prepare a singlet $|S\rangle$ and to ramp adiabatically (with respect to $\Delta B_{x,y}$) the detuning ε across the anticrossing between $|S\rangle$ and $|T_+\rangle$ (figure 4.10 (a) and 4.10 (b)). If the evolution is perfectly adiabatic, the initial singlet should be transformed into a triplet $|T_+\rangle$. This process ideally transfers one unit of angular momentum into the nuclear system. Then the detuning is quickly (non-adiabatically) pulsed back across this anticrossing, and the electron spin can relax via an exchange of electron with the reservoirs. During this second step, the nuclear spins are not affected, because the relaxation of the triplet state is ensured by the exchange of an electron via the reservoir. By repeating this pulse during a time T_{pump}, one can build up a polarization of the nuclear spins.

The first issue relies on the value of $\Delta B_{x,y} \sim 0.1\mu eV$ which gives rise to the anticrossing between the singlet $|S\rangle$ and the triplet $|T_+\rangle$. This value being quite small, the adiabaticity criterion is not easy to achieve. The first naive assumption should be to use a long adiabatic ramp across this anticrossing. But we have also to take into account the interactions between the nuclei. Indeed a polarized nucleus can interact with the others close-by nuclei, and exchange with them its polarization. The timescale related to such a process is of the range of a second [18]. Therefore we have to find a compromise between the adiabaticity and the diffusion of the induced polarization. During this thesis the duration of the adiabatic ramp has been fixed at 200ns. The polarization pulse sequence

is described in figure 4.10 (b). The first two stages correpond to the standard singlet initialization. The third one is the adiabatic ramp detailed above, and the last one corresponds to the return in the region (2,0).
In addition, as it has been demonstrated in the first chapter, the hyperfine interaction depends on the value of the wavefunction of the electron at the nuclei positions. Therefore if the quantum dot sizes are not identical, the wavefunction of the electrons should be different, giving rise to two distinct hyperfine couplings. Then the induced polarization could be different in both quantum dots. This is confirmed by the presence of a nuclear magnetic field gradient ΔB_z between the two quantum dots, as it has been first demonstrated by Foletti and coworkers [10]. But first let us study the effect of the dynamical nuclear polarization by looking at the total induced polarization. In order to verify this process, we can probe the position (ε^* in figure 4.10 (b)) of the anticrossing $S-T_+$, using the pulse described earlier [17]. Indeed this position being magnetic field dependent, we should be able to detect a shift of this anticrossing due to the induced polarization. Such a measurement can be decomposed in two parts :

- First the polarization pulse sequence runs continuously during a time T_{pump}, and leads to the polarization of the nuclear spins.
- Secondly in order to probe this induced polarization, the $S-T_+$ pulse sequence described in the previous section runs for 1s. We remind that the purpose of this pulse sequence is to probe the mixing between the singlet $|S\rangle$ and the triplet $|T_+\rangle$. The QPC current is then averaged during this second of $S-T_+$ pulse sequence.

By following this measurement principle, we expect to get a steady state of the induced polarization. We measure the singlet probability during the $S-T_+$ pulse sequence for different value of the detuning ε and for different polarization duration T_{pump}. Figure 4.10 shows this measurement. We remind that each measurement point is the succession of a polarization pulse sequence running for a time T_{pump}, and of the $S-T_+$ pulse sequence running for 1s, and during which the QPC current is averaged. We notice that in order to get a higher sensitivity of the induced polarization, we set the external magnetic field at a low value ($\sim 10mT$). Indeed, as we can see in figure 4.7 (c), at low magnetic field, the position of this anticrossing is highly sensitive to the magnetic field felt by the electron spins. As it is clearly observed in figure 4.10 (c), the effect of an increase of T_{pump} is the same than an increase of the external magnetic field, confirming the polarization of the nuclear spins. By comparing figure 4.7 (c) and figure 4.10 (c), we can estimate that the induded polarization reaches 100mT for a polarization time $T_{pump} \sim 100ms$ (in figure 4.7 the position of the $S-T_+$ anticrossing becomes approximatively constant with respect to the external magnetic field for $B \sim 100mT$; in figure 4.10 (c), this position becomes approximatively constant with respect to the polarization time for $T_{pump} \sim 100ms$). In addition, it has been demonstrated that this polarization can stand for few seconds after the end of the polarization pulse [19].

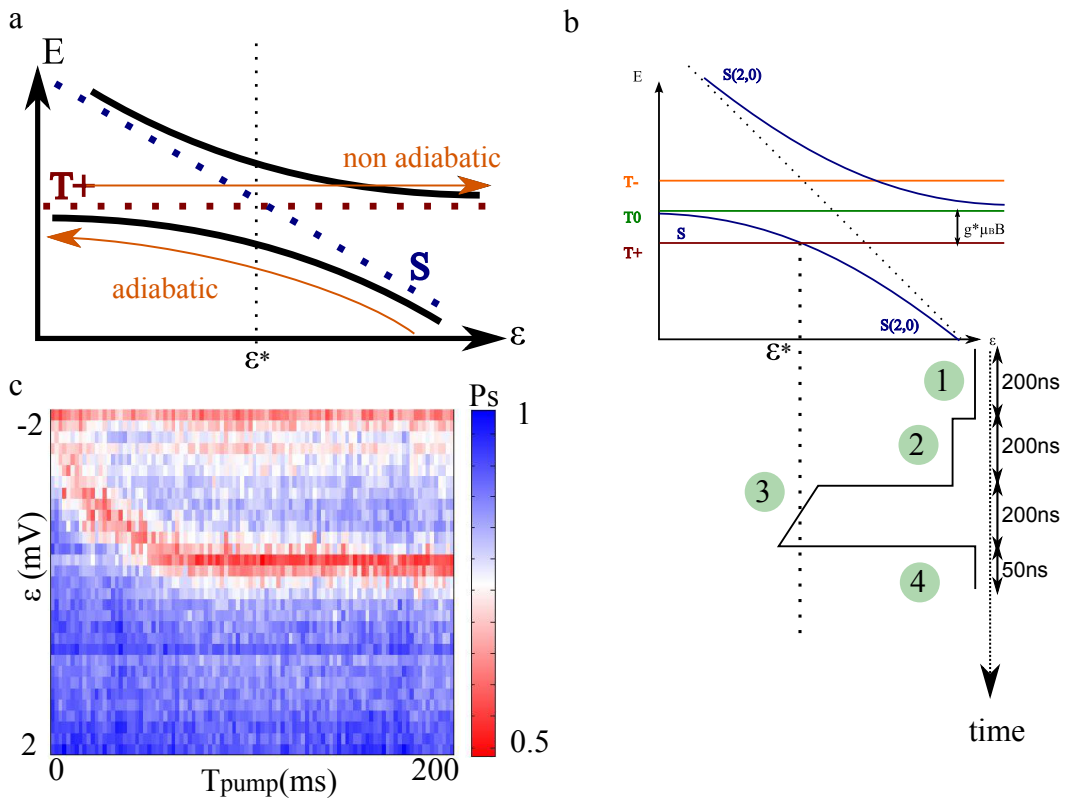

Figure 4.10: **Polarization of the nuclear spins.** **(a)** Principle of the dynamical polarization pulse : an initial singlet S is ramped adiabatically across the anticrossing between $|S\rangle$ and $|T_+\rangle$, followed by a non adiabatic return. This process ideally transfers one unit of angular momentum into the nuclear system **(b)** Polarization pulse. The first two stages allow for initialization of a singlet $S_{(2,0)}$. Then the detuning is adiabatically ramped across the anticrossing $S-T_+$. **(c)** Measurement of the effect of the polarization pulse. The external magnetic field has been set at 16mT, and we measure the position of anticrossing $S-T_+$ by using the pulse described in figure 4.7 (a). The singlet probability P_S is measured with respect to the detuning and the polarization time T_{pump}.

4.5.2 $S - T_0$ coherent oscillations induced by ΔB_z

Although this polarization pulse induces a finite nuclear magnetic field, for the moment it does not demonstrate that a gradient ΔB_z is created. At the beginning of this chapter, we studied the mixing of the singlet $|S\rangle$ and the triplet $|T_0\rangle$ induced by the gradient ΔB_z. We demonstrated (equation 4.15) that the gradient ΔB_z could induces coherent oscillations between these two states ($|S\rangle$ and $|T_0\rangle$). Especially we have seen that the frequency of these oscillations depends on the amplitude of the gradient ΔB_z. Therefore in order to verify if the gradient increases with respect to the polarization time T_{pump}, we can measure these oscillations. The first experimental realization of such manipulations has been done by Foletti and coworkers [10]. The principle of this measurement is quite similar to the previous one and it is depicted in figure 4.11 (a) :

- First the polarization pulse sequence runs continuously during a time T_{pump}, and leads to the polarization of the nuclear spins. As explained above, the induced polarization could be different in both quantum dots, leading to the creation of the gradient ΔB_z.

- The $S - T_0$ pulse sequence described in figure 4.5 is then applied during 1s. We want to reconstruct the coherent oscillations between the singlet $|S\rangle$ and the triplet $|T_0\rangle$, consequently we need to change the time during which these two states can mix. As seen previously we denoted this time τ, and we remind that it corresponds to the time spent in the $\varepsilon \ll 0$ region. Therefore τ is first set to 0, and we averaged the QPC current during 1s. Afterwards the polarization pulse sequence runs again during T_{pump}, before applying again the $S - T_0$ pulse sequence where τ has been increased. This measurement principle is repeated until $\tau = 41.6ns$.

To conclude, for each measurement point (τ from 0ns to $\sim 41.6ns$ in 50 points), the polarization pulse (figure 4.10 (b)) is applied during a time T_{pump} and followed by 1s of the $S - T_0$ pulse (figure 4.5 (a)) during which the QPC current is averaged. In addition, this measurement (where τ is varying from 0ns to $\sim 41.6ns$ in 50 points) is repeated fifty times. This averaging technique is related to the nuclear spin dynamic. Indeed this dynamic is relatively slow compared to the measurement time (1s). Therefore in order to probe the greatest number of nuclear spin configurations it is better to repeat the whole cycle (τ from 0ns to $\sim 41.6ns$ in 50 points) fifty times than to repeat fifty times the measurement for each value of τ (figure 4.11 (a)).

Figure 4.11 (b) shows the oscillations between the two states $|S\rangle$ and $|T_0\rangle$ induced by the gradient ΔB_z for different pumping time T_{pump}. The singlet probability is plotted with respect to τ, the time spent in the $\varepsilon \ll 0$ region. We notice that the curve at $T_{pump} = 0$ is the same one already shown at the beginning of this chapter (figure 4.5 (e)). The experimental data could have been fitted to an exponentially damped cosine (equation 4.14) but in the following all the fits will be done by numerically solving the Schrödinger equation for the time-dependent Hamiltonian (in the basis $\{|S\rangle, |T_0\rangle\}$:

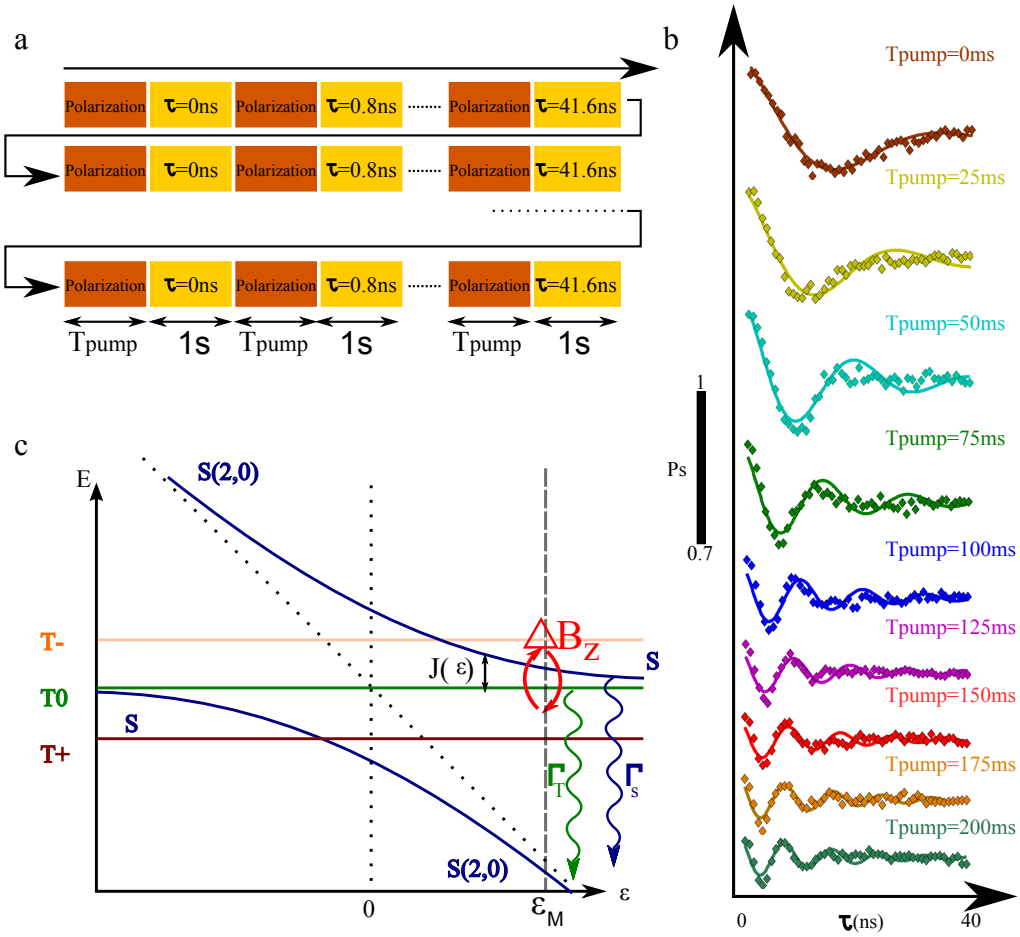

Figure 4.11: **S-T_0 oscillations induced by a nuclear magnetic field gradient ΔB_z.** **(a)** Measurement scheme : Each measurement point of figure 4.11 (b) is an average over 1s, and it is preceded by a polarization pulse running for T_{pump}. In addition, in order to average the signal, this is repeated 50 times for a fixed value of T_{pump}. **(b)** S-T_0 coherent oscillations for different polarization times T_{pump}. The singlet probability is plotted with respect to τ, the time spent in the $\varepsilon \ll 0$ region. **(c)** Relaxation at the measurement point induced by a finite gradient ΔB_z. At the measurement point, the exchange energy can become smaller than the gradient ΔB_z under polarization. This induces a mixing between the blockaded triplet $|T_0\rangle$ and the singlet $|S\rangle$. Then the relaxation is possible via a spin conserving phonon emission. This relaxation is quite faster compared to the thermal relaxation through the reservoir.

$$H(t) = \frac{J(t)}{2}\sigma_z + \frac{\Delta B_z}{2}\sigma_x \tag{4.26}$$

In this case the fit parameters are the gradient ΔB_z, the amplitude of the oscillations reflecting a non perfect contrast, the time ensemble average decoherence time T_2^*, and the rise time of the pulse (due to the finite bandwidth of the present experimental setup, mainly limited by the bias tees). In addition the time dependence of the exchange energy $J(\varepsilon)$ is related to the time dependence of ε during the pulse sequence. Instead of using the formula of equation 4.23 (extracted from the funnel diagram 4.7 (c)), we chose J as exponentially dependent on ε and we will see in the next section how we have extracted this formula. By choosing J as exponentially dependent on ε, it appears to fit quite well with experiments. In addition such a dependence is commonly used in literature [10, 20]. The principle of the S-T0 oscillations fit is the following :

- **(1)** The initial state is a singlet. We initialized the system in the lowest energy eigenstate (ground state) of the Hamiltonian (equation 4.26) for $\varepsilon_i = -0.2\mu eV$ where the exchange energy J is $J(\varepsilon_i) \sim 5\mu eV$ (see next section). For such a large exchange energy, the eigenstates of the Hamiltonian are the singlet $|S\rangle$ and the triplet $|T_0\rangle$, the lower energy eigenstate being the singlet $|S\rangle$. We can therefore estimate that the initial state is $|\Psi_i\rangle = |S\rangle$.

- **(2)** Afterwards the detuning parameter ε is pulsed in 0.83ns (corresponding to the sampling rate of our pulse generator) from $\varepsilon_i = -0.2\mu eV$ to $\varepsilon_f = -2meV$, where the exchange vanishes to $\sim 50neV$ (see next section). We took into account the finite rise time of the pulse that we denote T_R by adding an exponential increase of the detuning $(1 - exp(-\frac{t}{T_R}))$.

- **(3)** Then we let the system evolve in this configuration during a time τ. For a vanishing exchange J, an initial singlet should evolves under a nuclear gradient accordingly to equation 4.14.

- **(4)** At the end of the evolution, the system is brought back into the position ε_i in 0.83ns, where the eigenstates are the singlet $|S\rangle$ and the triplet $|T_0\rangle$. We project the state of the system on the initial state $|\Psi_i\rangle = |S\rangle$, in order to get the singlet probability.

- **(5)** The decoherence is introduced by an exponential damping of these oscillations.

- **(6)** Finally these oscillations are renormalized accordingly to the amplitude parameter in order to take into account the finite contrast experimentally observed.

A numerical routine finds the minimum of the square difference between the experiment and the calculated point ("least squares" method). The fit for $T_{pump} = 0$ allows for

T_{pump}(ms)	0	25	50	75	100	125	150	175	200
amplitude	0.30	0.28	0.28	0.22	0.16	0.12	0.11	0.12	0.11
ΔB_z(mT)	3.8	5.2	7.5	10.8	14.9	16.6	16.8	18.9	19.3

Table 4.1: Fit parameters of the S-T_0 oscillations (amplitude and gradient).

determining the value of the decoherence time T_2^* and the rise time of the pulse T_R. We found $T_2^* = 16ns$ and $T_R = 1.1ns$, and we assumed them as independent of the polarization time T_{pump}. For each polarization time a fit routine with the gradient ΔB_z and the amplitude as fit parameters has been performed. The fits and the experimental points have been superimposed in figure 4.11, while the fit parameters are presented in table 4.1.

The first observation is the expected increase of the gradient ΔB_z with T_{pump} (figure 4.12 (a)). In addition to the induced nuclear magnetic field (figure 4.10 (c)), the polarization pulse gives rise to a gradient between the two quantum dots. As we mentioned already an increase of the gradient gives rise to higher frequency of the $S - T_0$ coherent oscillations, and this feature can easily be seen in figure 4.11 (b). This is accompanied by a decrease of the oscillation amplitude (figure 4.12 (a)). This loss of contrast is also due to the gradient ΔB_z. Indeed it has been demonstrated [21] that a gradient can enhance the relaxation of the triplet $|T_0\rangle$ at the measurement point ε_M. The exchange energy is generally small at ε_M, and hence a gradient ΔB_z can induce a mixing of the triplet $|T_0\rangle$ and the singlet $|S\rangle$ (figure 4.11 (c)). The relaxation of the singlet $|S\rangle$ into the singlet $|S_{(2,0)}\rangle$ is possible via a spin conserving phonon emission (relaxation rate Γ_S, figure 4.11 (c)). The relaxation rate of such a process is quite fast compared to the thermal relaxation, where an electron is exchanged with one from the reservoir (relaxation rate Γ_T, figure 4.11 (c)). In order to obtain an expression for the relaxation time taking into account these two relaxation processes we follow the development of Barthel and coworkers [21]. The populations of the eigenstates $|\Phi_1\rangle$ and $|\Phi_2\rangle$ of the Hamiltonian (equation 4.26) decays as :

$$\Gamma_{\frac{1}{2}} = \Gamma_S(\varepsilon_M)|\langle S|\Phi_{\frac{1}{2}}\rangle|^2 + \Gamma_T|\langle T_0|\Phi_{\frac{1}{2}}\rangle|^2 \tag{4.27}$$

These eigenstates can be written as :

$$\begin{aligned} |\Phi_1\rangle &= \frac{1}{g^*\mu_B\Delta B_z\sqrt{1+|\frac{\Omega_1}{g^*\mu_B\Delta B_z}|^2}}\begin{pmatrix}\Omega_1\\ g^*\mu_B\Delta B_z\end{pmatrix} \\ |\Phi_2\rangle &= \frac{1}{g^*\mu_B\Delta B_z\sqrt{1+|\frac{\Omega_2}{g^*\mu_B\Delta B_z}|^2}}\begin{pmatrix}\Omega_2\\ g^*\mu_B\Delta B_z\end{pmatrix} \end{aligned} \tag{4.28}$$

where $\Omega_{\frac{1}{2}} = J(\varepsilon_M)^{+}_{-}\sqrt{J(\varepsilon_M)^2 + (g^*\mu_B\Delta B_z)^2}$. The triplet $|T_0\rangle$ probability decays as :

$$P_{T_0}(t) = P_{T_0}(0)[|\langle T_0|\Phi_1\rangle|^2 e^{-\Gamma_1 t} + |\langle T_0|\Phi_2\rangle|^2 e^{-\Gamma_2 t}] \tag{4.29}$$

But for $J(\varepsilon_M) \gg g^*\mu_B\Delta B_z$, we get $\Omega_1 \sim 2J(\varepsilon_M)$ and $\Omega_2 \sim 0$ implying that $|\Phi_1\rangle \sim |S\rangle$ and $|\Phi_2\rangle \sim |T_0\rangle$. Therefore $|\langle T_0|\Phi_1\rangle|^2$ is relatively small, while $\Gamma_1 \gg \Gamma_2$. The bi-exponential decay of the triplet probability can consequently be reduced to a single exponential decay $P_{T_0}(t) = P_{T_0}(0)e^{-\frac{t}{T_1}}$ with :

$$T_1 = [\Gamma_S(1 - \frac{J(\varepsilon_M)}{(\sqrt{g^*\mu_B\Delta B_z)^2 + J(\varepsilon_M)^2}}) + \Gamma_T(1 + \frac{J(\varepsilon_M)}{\sqrt{(g^*\mu_B\Delta B_z)^2 + J(\varepsilon_M)^2}})]^{-1} \tag{4.30}$$

Through this formula we can clearly expect an increasing relaxation rate for higher ΔB_z which could decrease the amplitude of the $S - T_0$. By considering the duration of a single spin measurement T_M, the amplitude should evolve as $amplitude \propto e^{-\frac{T_M}{T_1(\Delta B_z)}}$. Figure 4.12 (b) shows the dependence of the amplitude with respect to the nuclear magnetic field gradient ΔB_z. The data have been fitted by considering the amplitude as exponentially damped ($amplitude \propto e^{-\frac{T_M}{T_1}}$, where $T_M = 12\mu s$ is the total measurement time), reflecting that the contrast is reduced due to the relaxation of the triplet states. By considering the rates Γ_S, Γ_T and the exchange energy at the measurement point $J(\varepsilon_M)$ as fit parameters we obtain $\Gamma_S = 5\,10^6 s^{-1}$, $\Gamma_T = 3\,10^4 s^{-1}$ and $J(\varepsilon_M) = 5\,10^{-7} eV$. The value of Γ_T is consistent with the relaxation time ($T_1 \sim 30\mu s$) measured for low gradient ΔB_z (figure 4.8), where the relaxation is dominated by the exchange of an electron with one from the reservoir. However it should be possible to overcome this relaxation at the measurement point by increasing the tunnel coupling between the two quantum dots. Indeed, it should give rise to a higher exchange energy $J(\varepsilon_M)$, and therefore avoid the mixing between the triplet and the singlet at the measurement point. It is worth noticing that this increasing relaxation at the measurement point does not change the relaxation time in the (1,1) region.

This set of data demonstrates that we are able to induce a nuclear magnetic gradient between the two quantum dot with the above mentioned polarization procedure. We expect that the induced gradient could be increased significantly by properly tuning the polarization pulse, and especially the adiabatic part of this pulse. Gradients higher than 100mT have been reported in [10]. In addition running the polarization pulse for longer time T_{pump} should also increase the induced gradient ΔB_z.

4.6 From a SWAP to C-phase gate

As we mentioned earlier, it has been demonstrated theoretically [6] that the natural two qubit gate in single spin qubits evolves from the SWAP gate at vanishing gradient ΔB_z

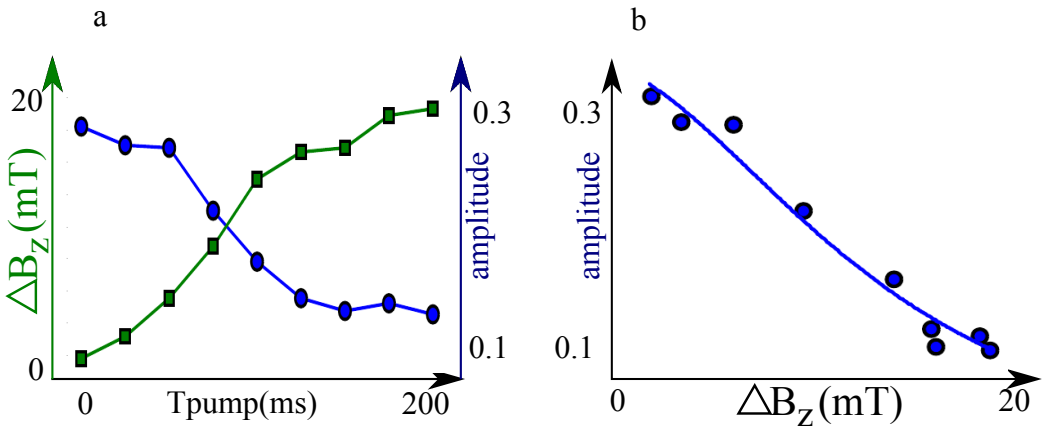

Figure 4.12: **Amplitude and gradient ΔB_z extracted from the $S - T_0$ oscillation fits. (a)** Gradient ΔB_z and amplitude with respect to T_{pump}. When T_{pump} increases, ΔB_z increases while the amplitude decreases.**(b)** Amplitude of the oscillations with respect to the induced gradient ΔB_z. We observe a decrease of the amplitude for increasing gradient. This feature can be explained by enhanced relaxation at the measurement point induced by the gradient (figure 4.11 (c))

to a controlled phase gate at larger ΔB_z. We will now explain it by starting to study the SWAP gate in single spin qubits.

4.6.1 SWAP gate with single spin qubits

At the beginning of this chapter we saw that the SWAP gate exchanges the state of the two qubits. It can be represented by the unitary transformation given by the matrix (equation 4.7). Such a gate relies on a coherent spin exchange between the two electron spins, and we can take advantage of the control of the exchange energy $J(\varepsilon)$ to realize this gate. In order to achieve such manipulations, we need to find a pulse that couples the two states $|\uparrow,\downarrow\rangle$ and $|\downarrow,\uparrow\rangle$ and let unchanged $|\uparrow,\uparrow\rangle$ and $|\downarrow,\downarrow\rangle$. Let us start in the $\varepsilon \ll 0$ region where the four spin eigenstates are $\{|\uparrow,\uparrow\rangle, |\uparrow,\downarrow\rangle, |\downarrow,\uparrow\rangle, |\downarrow,\downarrow\rangle\}$, and let us consider a superposition of these states :

$$|\Psi(\tau = 0)\rangle = \alpha|\uparrow,\uparrow\rangle + \beta|\uparrow,\downarrow\rangle + \gamma|\downarrow,\uparrow\rangle + \delta|\downarrow,\downarrow\rangle \tag{4.31}$$

where $\alpha^2 + \beta^2 + \gamma^2 + \delta^2 = 1$. Now a pulse can be applied in order to set ε where $J(\varepsilon)$ becomes finite, and greater than the gradient ΔB_z. In this region, the four "new" eigenstates are now $\{|\uparrow,\uparrow\rangle, |S\rangle, |T_0\rangle, |\downarrow,\downarrow\rangle\}$. We assumed this pulse to be non adiabatic with respect to the gradient ΔB_z, then the state of the system becomes :

$$
\begin{aligned}
|\Psi(\tau)\rangle &= \alpha|\uparrow,\uparrow\rangle + \frac{\beta}{\sqrt{2}}(|S\rangle e^{-\frac{i.J(\varepsilon).\tau}{2\hbar}} + |T_0\rangle e^{\frac{i.J(\varepsilon).\tau}{2\hbar}}) + \frac{\gamma}{\sqrt{2}}(-|S\rangle e^{-\frac{i.J(\varepsilon).\tau}{2\hbar}} + |T_0\rangle e^{\frac{i.J(\varepsilon).\tau}{2\hbar}}) + \delta|\downarrow,\downarrow\rangle \\
&= \alpha|\uparrow,\uparrow\rangle + \frac{\beta-\gamma}{\sqrt{2}} e^{-\frac{i.J(\varepsilon).\tau}{2\hbar}}|S\rangle + \frac{\beta+\gamma}{\sqrt{2}} e^{\frac{i.J(\varepsilon).\tau}{2\hbar}}|T_0\rangle + \delta|\downarrow,\downarrow\rangle \\
&= \alpha|\uparrow,\uparrow\rangle + \frac{\beta-\gamma}{2} e^{-\frac{i.J(\varepsilon).\tau}{2\hbar}}(|\uparrow,\downarrow\rangle - |\downarrow,\uparrow\rangle) + \frac{\beta+\gamma}{2} e^{\frac{i.J(\varepsilon).\tau}{2\hbar}}(|\uparrow,\downarrow\rangle + |\downarrow,\uparrow\rangle) + \delta|\downarrow,\downarrow\rangle
\end{aligned}
\tag{4.32}
$$

$$
\begin{aligned}
|\Psi(\tau)\rangle = \alpha|\uparrow,\uparrow\rangle &+ (\beta cos(\frac{J(\varepsilon).\tau}{2\hbar}) + i\gamma sin(\frac{J(\varepsilon).\tau}{2\hbar}))|\uparrow,\downarrow\rangle \\
&+ (\gamma cos(\frac{J(\varepsilon).\tau}{2\hbar}) + i\beta sin(\frac{J(\varepsilon).\tau}{2\hbar}))|\downarrow,\uparrow\rangle + \delta|\downarrow,\downarrow\rangle
\end{aligned}
\tag{4.33}
$$

Here the non-adiabatic assumption is crucial. Indeed, if this criterion is not respected, the pulse will just tranform the initial state $|\uparrow,\downarrow\rangle$ into a singlet $|S\rangle$ and $|\downarrow,\uparrow\rangle$ into the triplet $|T_0\rangle$. From equation 4.33 we can see that $\frac{J(\varepsilon).\tau}{2\hbar} = \frac{\pi}{2}$ gives the SWAP operation, meaning that the states of the two qubits have been "exchanged" :

$$
|\Psi(\tau)\rangle = \alpha|\uparrow,\uparrow\rangle + i\gamma|\uparrow,\downarrow\rangle + i\beta|\downarrow,\uparrow\rangle + \delta|\downarrow,\downarrow\rangle \tag{4.34}
$$

while it gives the $\sqrt{SWAP}$ operation (matrix 4.8) for $\frac{J(\varepsilon).\tau}{2\hbar} = \frac{\pi}{4}$.
Therefore we see that a SWAP gate with single spin qubits can be achieved by simply pulsing the system in order to get a finite exchange energy J. Figure 4.13 (a) shows the experimental gate voltage pulse sequence used to perform such a SWAP gate [4].

- **(1) and (2)** are the usual initialization steps, where a singlet is prepared.
- **(3)** In order to prepare one of the states $\{|\uparrow,\downarrow\rangle, |\downarrow,\uparrow\rangle\}$, the detuning can be ramped adiabatically (compared to ΔB_z) from $\varepsilon > 0$ to $\varepsilon \ll 0$. In addition to avoid the anticrossing $S - T_+$, the detuning is first pulsed non-adiabatically across it (but adiabatically compared to the tunnelling). Then the initial singlet is adiabatically transformed into one of the two states $\{|\uparrow,\downarrow\rangle, |\downarrow,\uparrow\rangle\}$ according to the gradient ΔB_z
- **(4)** The fourth stage consists in the exchange manipulation. The state prepared after stage 3, for instance $|\uparrow,\downarrow\rangle$, is transformed into a superposition of singlet $|S\rangle$ and triplet $|T_0\rangle$ by pulsing the detuning ε in order to get a finite value of the exchange energy J(ε). As mentioned previously, this pulse has to be non-adiabatic compared to the gradient ΔB_z. All along the duration of the exchange pulse, the initial superposition of states dynamically evolves in time according to the exchange energy $J(\varepsilon)$ at the ε value of the pulse (equation 4.32).

- **(5)** The exchange pulse is set off (in a non adiabatic manner) and we come back to the position 3. At the end of the exchange pulse, the state of the system can be described by equation 4.33.

- **(6)** To readout this state, we need to project back the system into the (2,0) region. Therefore we follow the same steps in reverse: ε is ramped slowly in the large detuning region, in order to get a singlet $|S\rangle$ from $|\uparrow,\downarrow\rangle$ and a triplet $|T_0\rangle$ from $|\downarrow,\uparrow\rangle$. Then ε is quickly pulsed back into the (2,0) region across the $S-T_+$ anticrossing. By measuring the charge state of the system, we obtain the singlet probability P_S.

As the exchange energy depends on ε, the time needed to perform a SWAP operation can be tuned by changing the ε value of the stage 4. Figure 4.13 (b) shows the exchange oscillations induced by the pulse described previously. The singlet probability P_S is plotted with respect to the exchange pulse detuning ε and the exchange pulse duration τ. We can clearly observe oscillations whose frequencies depends on ε. Figure 4.13 (c) shows a cut along the dotted line of figure 4.13 (b). In order to get a better signal, this oscillations have been averaged over 50 repetitions. In addition to the oscillation feature, we observed a decoherence effect inducing a decay of these oscillations. In this case it is not induced by the nuclear spin fluctuations, but by ε fluctuations. For a non zero $\frac{dJ}{d\varepsilon}$ a fluctuation of ε implies a fluctuation of $J(\varepsilon)$. These ε fluctuations exist and are mainly due to the gate voltage noise. As expected, we can see in figure 4.13 (b) that the decoherence rate is faster for ε close to 0 where $\frac{dJ}{d\varepsilon}$ is greater.
In the previous section we mentioned that the exchange energy J exhibits an exponential dependence on the detuning ε. By fitting the figure 4.13 (b) we are able to obtain an expression of $J(\varepsilon)$. Compared to the previous formula of the exchange energy (obtained by measuring the mixing $S-T_+$, equation 5.4), this new expression of $J(\varepsilon)$ (given in equation 4.35) presents the interest to be performed at a fixed value of the external magnetic field ($B_{ext} = 100mT$), while the previous one used the magnetic field dependence of the anticrossing $S-T_+$ position. Therefore we fitted the data of figure 4.13 (b) by numerically solving the Schrodinger equation for the Hamiltonian (equation 4.26). The principle of this fit is :

- The system is initialized in the lowest energy eigenstate of the Hamiltonian (equation 4.26) for $\varepsilon_i = -2meV$ ((3) in figure 4.13 (a)). For this value of ε, we assume an almost vanishing exchange energy $J(\varepsilon) \sim 50neV$ and the gradient $\Delta B_z = 4mT = 100neV > J(\varepsilon_i) = 50neV$. We can therefore consider for instance an initial state as being $|\uparrow,\downarrow\rangle$.

- The detuning ε is pulsed in 0.83ns from $\varepsilon_i = -2meV$ to ε_f, where the energy $J(\varepsilon_f)$ acts as a fit parameter. The finite rise time of the pulse is taken into account.

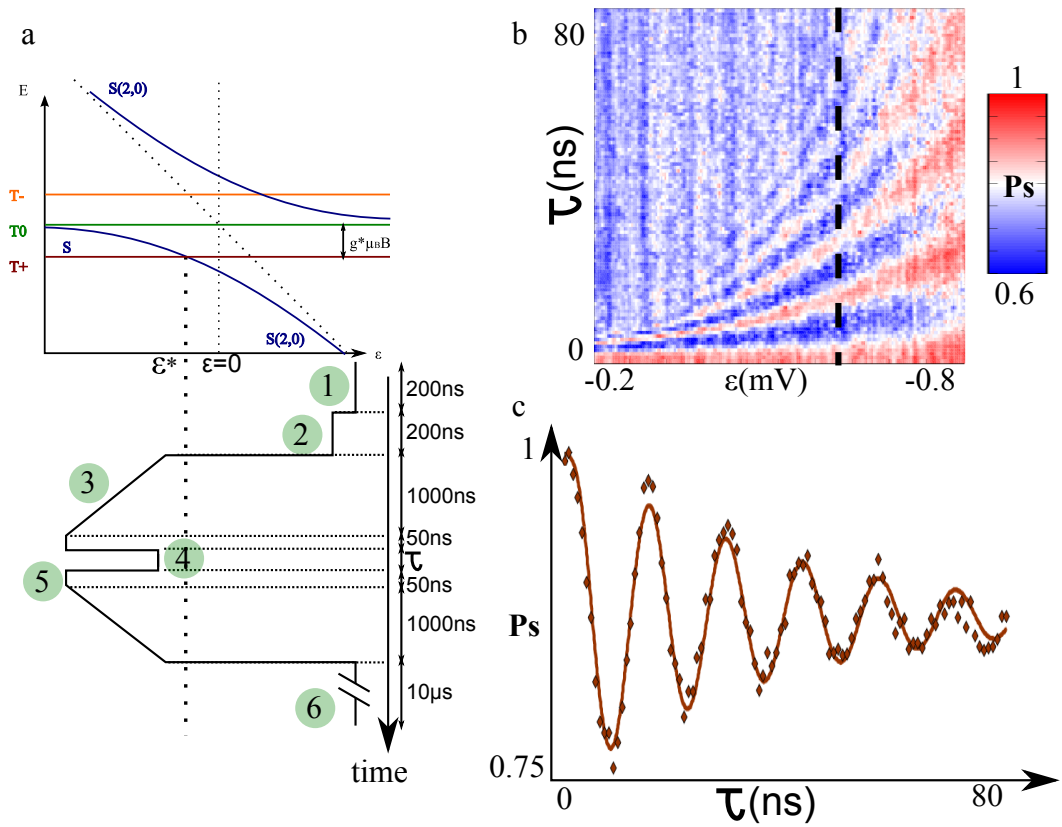

Figure 4.13: **A SWAP gate with single spin qubits.** **(a)** SWAP pulse. After an adiabatic initialization of one of the antiparallel states ($|\uparrow,\downarrow\rangle, |\downarrow,\uparrow\rangle$) (3), the detuning ε is change in order to get a finite exchange energy J(ε) during a time τ (4). The measurement is done by adiabatically transforming the resulting state into the singlet $|S\rangle$ and the triplet $|T_0\rangle$ (6). The singlet probability is obtained by measuring the charge state of the system. **(b)** Exchange oscillations. The singlet probability is plotted with respect to the exchange pulse detuning ε and the exchange pulse duration τ. Inset : Exchange oscillations fit by numerically solving the Schrödinger equation for the Hamiltonian (equation 4.26). **(c)** Exchange oscillations along the dotted line in figure 4.13 (b). For this value of ε, the SWAP gate is achieved in $\sim 7ns$. By increasing ε this gate duration can be lowered.

- The system evolves during a time τ , before pulsing back the detuning to $\varepsilon_i = -2meV$ in 1ns ((4) in figure 4.13 (a)).
- The singlet probability is then related to the probability to be in the state $|\uparrow,\downarrow\rangle$.
- Finally the probability is renormalized by an amplitude factor, being a fit parameter. The decoherence is also taken into account as a fit parameter.

The fit obtained is shown in the inset of the figure 4.13. The ε dependence of the exchange energy J has been fitted to $J(\varepsilon) = J_0 + J_1 exp(-\frac{\varepsilon}{\varepsilon_0})$. This expression seems to fit better the data than the one found earlier (see equation 5.4). We obtain :

$$J(\varepsilon) = 50.10^{-9} + 6.10^{-6} exp(-\frac{\varepsilon}{-0.2\,10^{-3}})(eV) \tag{4.35}$$

For $\varepsilon \ll -0.2meV$, the exchange energy J is equal to 50 neV. The reason why it does not vanish to zero is related to the tunnel coupling. Indeed the singlet $|S\rangle$ is tunnel coupled to the singlet $|S_{(2,0)}\rangle$ (around $\varepsilon = 0$) but also to the singlet $|S_{(0,2)}\rangle$ (around $\varepsilon = -E_c$, where E_c is the charging energy of the system). In addition the value of the exchange energy at $\varepsilon = 0$ can be related to the tunnel coupling t by the formula $J(\varepsilon = 0) = t = 6\mu eV$. We note that this value differs from the one obtain earlier, and we attribute this difference to the low level of confidence of the gate level arm α.
Concerning the decoherence time, we assume it as inversely proportional to $\frac{dJ}{d\varepsilon}$. This is justified by the recent work of Dial and coworkers [20].
We will now focus on the behaviour of these oscillations under a finite gradient.

4.6.2 Exchange oscillations with a finite gradient ΔB_z

Until now we have considered that the exchange pulse (step 4, figure 4.13) was non-adiabatic with respect to the gradient ΔB_z. Indeed this stage is assumed to pulse the system from the region $\varepsilon \ll 0$ where the eigenstates are $\{|T_+\rangle = |\uparrow,\uparrow\rangle, |\uparrow,\downarrow\rangle, |\downarrow,\uparrow\rangle, |T_-\rangle = |\downarrow,\downarrow\rangle\}$ (because $J(\varepsilon) < g^*\mu_B\Delta B_z$) to the region where the exchange energy dominates the gradient, and consequently the eigenstates are the singlet $|S\rangle$ and the three triplets $|T_0\rangle$, $|T_+\rangle$, $|T_-\rangle$). If the pulse is non-adiabatic with respect to the gradient ΔB_z, an initial state for instance $|\uparrow,\downarrow\rangle$ should be transformed into a superposition of singlet and triplet $\frac{|S\rangle+|T_0\rangle}{\sqrt{2}}$. All along the duration of the exchange pulse τ, this superposition will acquire a phase related to the exchange energy, and as a function of this duration we expect to observe exchange oscillations. Let us now consider the opposite case, where the pulse is adiabatic. The initial state $|\uparrow,\downarrow\rangle$ will be transformed adiabatically by the pulse into the singlet $|S\rangle$. In this case there is no superposition of states, and therefore we do not expect to observe any exchange oscillations. This point is at the heart of the C-phase gate that we want to realize. In order to illustrate it, let us come back to the development done in the case of the SWAP gate.

As an initial state, we assumed a superposition of the four eigenstates ($\{|\uparrow,\uparrow\rangle, |\uparrow,\downarrow\rangle, |\downarrow,\uparrow\rangle, |\downarrow,\downarrow\rangle\}$) in the region $\varepsilon \ll 0$ (equation 4.31) :

$$|\Psi(\tau=0)\rangle = \alpha|\uparrow,\uparrow\rangle + \beta|\uparrow,\downarrow\rangle + \gamma|\downarrow,\uparrow\rangle + \delta|\downarrow,\downarrow\rangle \tag{4.36}$$

where $\alpha^2+\beta^2+\gamma^2+\delta^2 = 1$. As we have seen when we introduced the principle of the C-phase gate proposed in [6], a pulse can be designed in order to shift the anti parallel spin states energies while the parallel spin states remain constant in energy. Contrary to the SWAP operation, this pulse has to be adiabatic with respect to the gradient. In the following we denote the energy shifts of the antiparallel spin states as $\Delta E_{|\uparrow,\downarrow\rangle/|\downarrow,\uparrow\rangle}$. In this case the state of the system becomes :

$$|\Psi(\tau)\rangle = \alpha|\uparrow,\uparrow\rangle + \beta|\uparrow,\downarrow\rangle e^{-\frac{i\Delta E_{|\uparrow,\downarrow\rangle}t}{\hbar}} + \gamma|\downarrow,\uparrow\rangle e^{-\frac{i\Delta E_{|\downarrow,\uparrow\rangle}t}{\hbar}} + \delta|\downarrow,\downarrow\rangle \tag{4.37}$$

This evolution corresponds to the unitary operation described by the matrix U (equation 4.25), which combines with two single qubit rotations around the $\hat{z}$ axis gives the C-phase gate (see before). To conclude we see that the only working principle difference between the SWAP gate and the C-phase gate is the adiabaticity of the pulse with respect to the gradient ΔB_z. Let us recall that the energy shifts $\Delta E_{|\uparrow,\downarrow\rangle/|\downarrow,\uparrow\rangle}$ scale with the gradient. We can therefore study the behaviour of the exchange oscillations described previously while the system experiences a higher gradient ΔB_z. We expect to observe a vanishing of these oscillations due to the adiabatic character of the pulse. Before analysing the experimental data, let us detail how the adiabaticity influences the measurements. We first introduced the adiabaticity in the case of the tunnel coupling of the two singlets $|S\rangle$ and $|S_{(2,0)}\rangle$. The Landau-Zener probability 4.18 was related to the ratio between the tunnel coupling t and the derivative with respect to time of the energy splitting between the two singlets :

$$P_{LZ} = e^{-2\pi\Gamma}, \qquad \Gamma = \frac{4t^2}{\hbar\frac{d\varepsilon}{dt}} \tag{4.38}$$

In the present case the coupling is described by the gradient ΔB_z, and the energy splitting is no more ε but the exchange energy $J(\varepsilon)$. Therefore in this case the Landau-Zener probability comes as :

$$P_{LZ} = e^{-2\pi\Gamma}, \qquad \Gamma = \frac{4(g^*\mu_B\delta B_z)^2}{\hbar\frac{dJ(\varepsilon)}{dt}} \tag{4.39}$$

The derivative $\frac{dJ(\varepsilon)}{dt}$ can be rewritten as $\frac{dJ(\varepsilon)}{d\varepsilon}\frac{d\varepsilon}{dt}$. Let us assume $\frac{d\varepsilon}{dt}$ as constant and approximatively equal to $10^5 eV.s^{-1}$. Therefore the adiabaticity of the exchange pulse

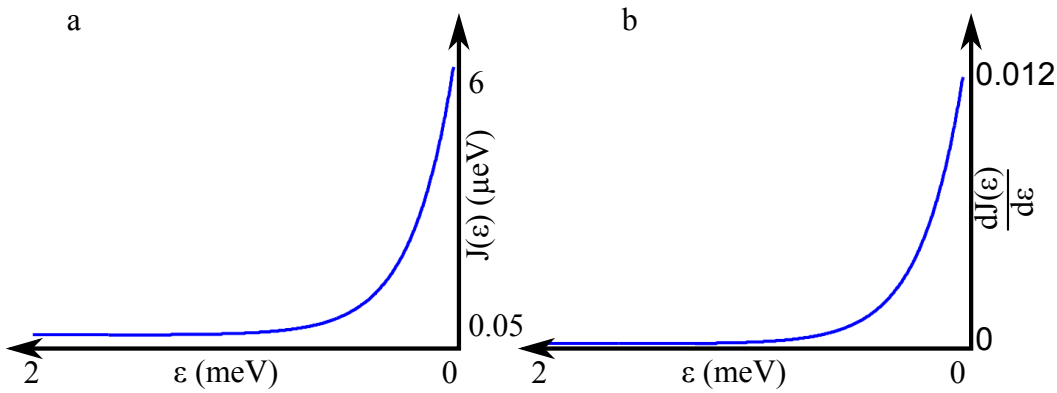

Figure 4.14: **(a)** Exchange energy $J(\varepsilon)$ with respect to the detuning ε **(b)** Derivative of the exchange energy $\frac{dJ}{d\varepsilon}$ with respect to the detuning ε

depends mainly on the ratio between the gradient ΔB_z and the derivative of the exchange energy with respect to the detuning $\frac{dJ(\varepsilon)}{d\varepsilon}$. In the previous part we extracted an expression of the exchange energy (equation 4.35). In figure 4.14, we plotted the exchange energy $J(\varepsilon)$ and its derivative $dJ/d\varepsilon$ with respect to the detuning ε. For $\varepsilon \ll 0$ $dJ/d\varepsilon$ is almost zero and it exponentially increases with respect to ε. By looking at this behaviour we can expect that the adiabaticity should be first ensured for the lower exchange pulse detuning values (stage (4) in figure 4.13 (a)). This feature can already be observed in the figure 4.15 (a) with $T_{pump} = 0$. Indeed lower values of the exchange pulse detuning (right part of figure 4.15 (a)) we can observe that the oscillations seem to vanish. If the gradient ΔB_z is increased by adding a pumping time before each measurement point, this behaviour occurs even for the larger exchange pulse detuning ε (figure 4.15 (a) with $T_{pump} = 100ms$). For $T_{pump} = 200ms$ the exchange oscillations vanished completely. This feature is the result of the adiabatic behaviour of the exchange pulse.

In order to perform a more quantitative analysis of the experimental data, we studied the behaviour of the oscillations at fixed ε with respect to the pumping time (along the dotted line in figure 4.15 (a)). As already explained in figure 4.11 (a), the data have been averaged over 50 repetitions. The data and their fits have been superimposed in figure 4.15 (b), and the fit follows the same procedure than as explained in the previous part : we numerically solved the Schrodinger equation for the time dependent Hamiltonian 4.26. In this case the fit parameters are the gradient ΔB_z and the oscillations amplitude. We notice that for this value of ε, the exchange energy has been measured equal to $0.27\mu eV$. The fit parameters have been regrouped in the table 4.2.

Figure 4.16 (a) shows the oscillation amplitude and the magnetic gradient ΔB_z with respect to the polarization time T_{pump}. As expected an increasing polarization time results in an increase of the induced gradient ΔB_z and a decrease of the amplitude, which is

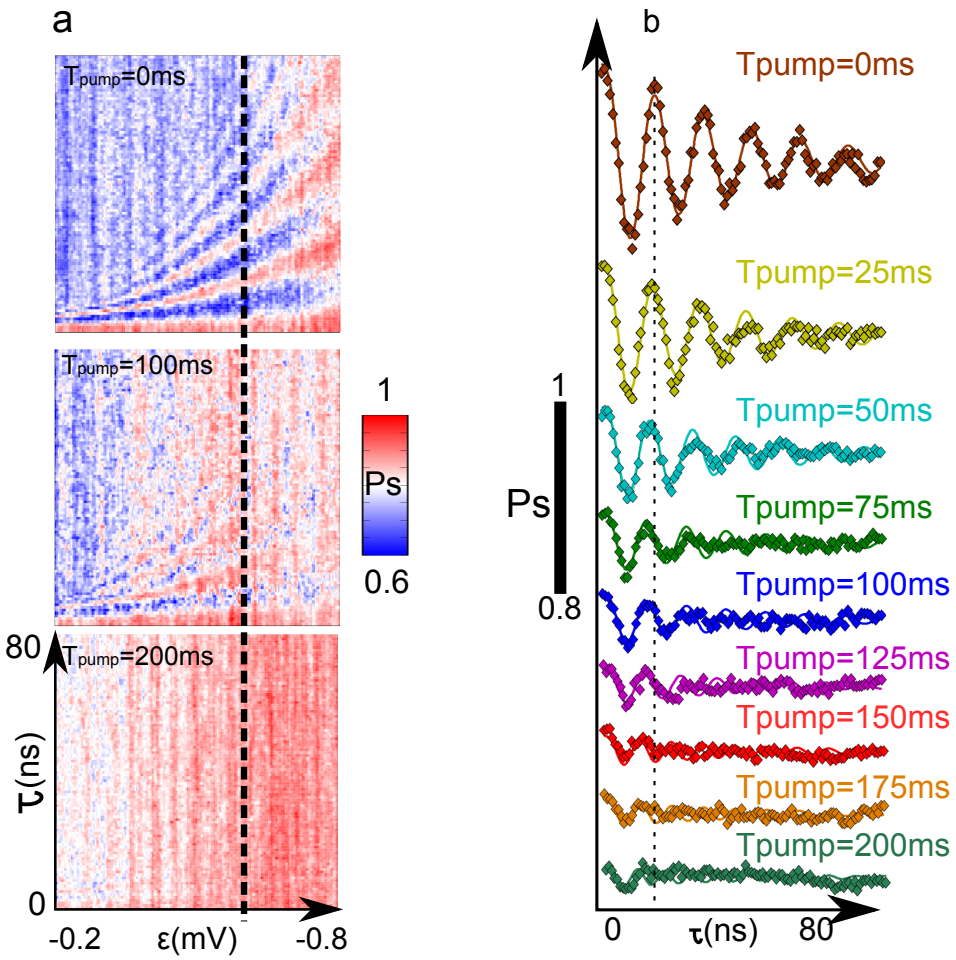

Figure 4.15: **Gradient ΔB_z dependence of the exchange oscillations.** **(a)** Singlet probability with respect to the exchange pulse detuning ε and duration τ. We observed a net vanishing of the oscillations while the polarization time T_{pump} is increased. This is related to the adiabaticity of the exchange pulse. **(b)** Exchange oscillations taken along the dotted line in figure 4.15. For each value of T_{pump}, the singlet probability is averaged over 50 repetitions. Experimental data and fit have been superimposed. We observe a clear decrease of the amplitude of the oscillations for increasing T_{pump}. In addition the oscillation frequency increases.

T_{pump}(ms)	0	25	50	75	100	125	150	175	200
amplitude	0.20	0.14	0.10	0.066	0.054	0.037	0.032	0.027	0.020
ΔB_z(mT)	4.1	5.3	7.2	8.9	9.0	10.8	14.1	13.8	20.2

Table 4.2: Fit parameters of the exchange oscillations (amplitude and gradient)

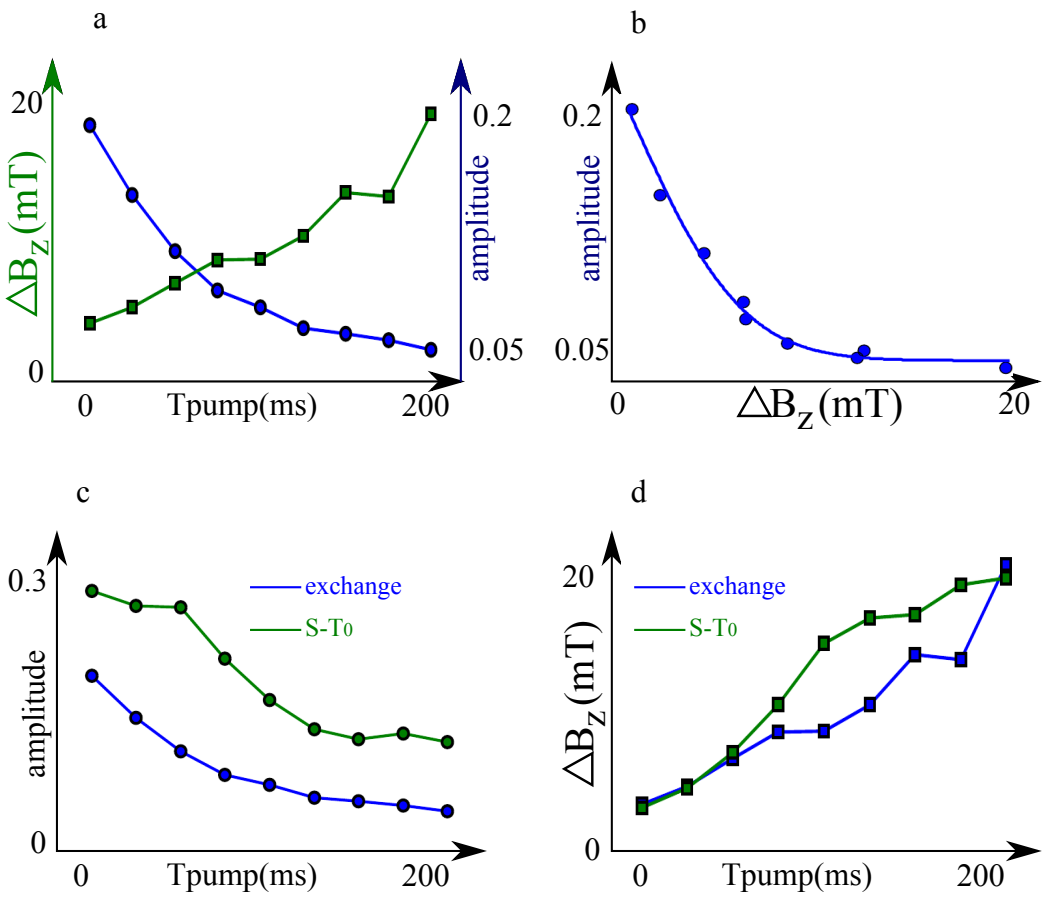

Figure 4.16: **Gradient ΔB_z and oscillations amplitude extracted from the exchange oscillation fits.** **(a)** Gradient ΔB_z and oscillations amplitude with respect to the polarization time T_{pump}. Similarly to what we obtained in the case of the $S - T_0$ oscillations, the gradient increases for increasing T_{pump}, while the amplitudes decreases. **(b)** Oscillation amplitude with respect to the induced gradient ΔB_z. The data have been fit to $Amplitude = a.e^{-\frac{\Delta B_z^2}{b}} + c$ in order to mimic the criterion of adiabaticity (4.18). **(c)** and **(d)** Amplitude (c) and gradient (d) of the exchange (blue) and $S - T_0$ (green, data from figure 4.12) oscillations with respect to the polarization time T_{pump}.

consistent with the study of the $S - T_0$ oscillations (figure 4.12). The values of ΔB_z are similar to the ones found previously(figure 4.16 (d)). In this figure we plot the fitted values of the gradient ΔB_z in the case of the $S - T_0$ oscillations (green curve), and in the case of the exchange oscillations (blue curve). By looking at the evolution of the amplitude with respect to the gradient ΔB_z (figure 4.16 (b)), we get a different feature than the one obtained in the $S - T_0$ case. Indeed, as already mentioned, we expect the exchange pulse being more and more adiabatic for increasing gradient. Therefore the decrease of the exchange oscillations amplitude is related to the increasing relaxation rate at the measurement point (as seen previously), but also related to the pulse adiabaticity. In order to confirm this, we fitted the amplitude by the following expression :

$$amplitude = a.e^{-\frac{\Delta B_z^2}{b}} e^{-\frac{T_M}{T_1}} \tag{4.40}$$

The second exponential is exactly the same than the one seen earlier in the study of the $S - T_0$ oscillations. The first one reflects the adiabaticity of the exchange pulse and we assume that the amplitudes are proportional to the Landau-Zener probability (equation 4.39). We obtained $a = 0.39$, $b = 4.6\,10^{-5}(T^2)$. Knowing $b = \frac{\hbar \frac{dJ}{d\varepsilon}\frac{d\varepsilon}{dt}}{8\pi(g^*\mu_B)^2}$ we get $\frac{dJ(\varepsilon)}{dt} \sim 0.01$. This value of $dJ/d\varepsilon$ is very similar to the one extracted previously, and we can conclude that the behaviour of the exchange oscillation amplitude is well related to the adiabaticity of the exchange pulse with respect to the gradient ΔB_z.
Another feature which is interesting to point out is the fact that the exchange oscillation frequency increases with increasing polarisation time T_{pump} (figure 4.15 (b)). This frequency seems to increase while the polarization time T_{pump} increases. This is due to the gradient dependence of the singlet and triplet energy (E_S and E_{T_0}) :

$$\begin{aligned} E_S &= -\frac{1}{2}\sqrt{(g^*\mu_B\Delta B_z)^2 + J(\varepsilon)^2} \\ E_{T_0} &= +\frac{1}{2}\sqrt{(g^*\mu_B\Delta B_z)^2 + J(\varepsilon)^2} \end{aligned} \tag{4.41}$$

The frequency being proportional to $E_{T_0} - E_S$, we expect to observe an increase of the exchange oscillations frequency for increasing gradient. This is clearly observed in figure 4.15 (b). The dotted line corresponds to exactly one period of the exchange oscillations for $T_{pump} = 0$. For $T_{pump} = 125ms$ the oscillation frequency is approximatively 1.5 faster than the one at $T_{pump} = 0ms$, while for $T_{pump} = 200ms$ it is twice faster. Indeed for a gradient equal to 20mT, we get $E_{T_0} - E_S = 0.57\mu eV$, which is roughly twice bigger than $E_{T_0} - E_S \sim J = 0.27\mu eV$ for $\Delta B_z = 4mT$.
To conclude, we observed a net gradient ΔB_z dependence of the exchange oscillations. An increasing gradient tends to make the exchange pulse more and more adiabatic, while it also accelerates the exchange oscillations. This allows us to conclude about the feasibility of a C-phase gate. We can estimate the duration of a controlled π-phase gate by evaluating the order of magnitude of the antiparallel spin states energy shifts. By using the formula

obtained in [6] and by taking into acoount the parameters of our configuration ($\Delta B_z = 20mT$, $t \sim 10\mu eV$) we obtain a duration equal to $\sim 80ns$. We expect this duration could be lowered by increasing the tunnel coupling t between the quantum dot and the gradient ΔB_z, giving rise to higher energy shifts.

4.7 Conclusion and perspectives

We demonstrated the vanishing of the exchange oscillations when the double quantum dot system experiences a magnetic field gradient ΔB_z. This vanishing is explained by the adiabaticity of the exchange pulse with respect to the gradient ΔB_z. In addition such a feature constitutes the proof of the C-phase gate feasibility with single spin qubits. In order to demonstrate the entanglement induced by this quantum operation, we need to be able to perform single-shot readout of each qubit independently in order to obtain the correlations between the two qubit states. The single-shot readout of two tunnel coupled spin qubits have been demonstrated recently [22]. Their readout method follows the principle seen in chapter 1 and first demonstrated by Elzerman and coworkers [23] : for the readout of a qubit spin state, the quantum dot potential is increased in order to set the excited state higher than the Fermi energy of the reservoir. Therefore if the electron spins is in the excited state, it can tunnel out from the quantum dot to the reservoir, while if it occupies the ground state the electron will remain in the quantum dot. By measuring the charge state of the qubit (0 or 1 electron), we obtain its spin state. But such a readout method relies on relatively slow tunnelling rate between the quantum dot and the reservoir. Indeed we are one more time limited by the bandwidth of the amplifier (IV convertor) $\Delta f = 1kHz$, and if the electron leaves the dot and be replaced by one of the reservoir faster than $1/\Delta f$, we will not be able to detect it. We could be tempted to lower the tunnel coupling between the quantum dots and their reservoir in order to lower this rate, but we took advantage of a relatively fast tunnelling rate in our polarization scheme. Indeed during each polarization sequence, the electrons spins are allowed to be exchanged with the ones from the reservoir in order to relax. This fix us an additional constraint and it constitutes an interesting challenge from an experimental standpoint.
In addition, another issue arises from the fast qubit adressing (single qubit rotations) needed to perform the C-phase gate. Indeed, for lateral quantum dot systems, up to now a single spin qubit $\pi-$rotation is performed in $\sim 100ns$ [2, 3]. Compared to the expected duration of the C-phase gate ($< 80ns$), the single qubit rotations are too slow. Recently faster single qubit rotations has been obtained in InAs nanowire quantum dots with strong spin-orbit [16].

Bibliography

[1] M.A. Nielsen, I. C. *Quantum Computation and Quantum Information.* Cambridge University Press, (2000). 76, 77, 79

[2] Koppens, F. H. L., Buizert, C., Tielrooij, K. J., Vink, I. T., Nowack, K. C., Meunier, T., Kouwenhoven, L. P., and Vandersypen, L. M. K. *Nature* **442**(7104), 766–771 August (2006). 77, 119, 152

[3] Nowack, K. C., Koppens, F. H. L., Nazarov, Y. V., and Vandersypen, L. M. K. *Science* **318**(5855), 1430–1433 November (2007). 77, 119

[4] Petta, J. R., Johnson, A. C., Taylor, J. M., Laird, E. A., Yacoby, A., Lukin, M. D., Marcus, C. M., Hanson, M. P., and Gossard, A. C. *Science* **309**(5744), 2180–2184 September (2005). 24, 26, 69, 77, 85, 89, 92, 94, 110

[5] Burkard, G., Loss, D., DiVincenzo, D. P., and Smolin, J. A. *Phys. Rev. B* **60**, 11404–11416 Oct (1999). 79

[6] Meunier, T., Calado, V. E., and Vandersypen, L. M. K. *Phys. Rev. B* **83**, 121403 Mar (2011). ii, 12, 23, 79, 98, 99, 108, 114, 119

[7] Taylor, J. M., Petta, J. R., Johnson, A. C., Yacoby, A., Marcus, C. M., and Lukin, M. D. *Physical Review B* **76**(3), 035315 July (2007). 24, 84, 93

[8] Johnson, A. C., Petta, J. R., Taylor, J. M., Yacoby, A., Lukin, M. D., Marcus, C. M., Hanson, M. P., and Gossard, A. C. *Nature* **435**(7044), 925–928 June (2005). 85, 86, 96

[9] Knapp, E.-W. and Schulten, K. *The Journal of Chemical Physics* **71**(4), 1878–1883 (1979). 89

[10] Foletti, S., Bluhm, H., Mahalu, D., Umansky, V., and Yacoby, A. *Nature Physics* **5**(12), 903–908 December (2009). ii, 26, 89, 101, 102, 104, 106, 108

[11] Bluhm, H., Foletti, S., Mahalu, D., Umansky, V., and Yacoby, A. *Physical Review Letters* **105**(21), 216803 November (2010). iii, 26, 27, 69, 89, 101

[12] Zener, C. *Proceedings of the Royal Society of London Series A-containing Papers of A Mathematical and Physical Character* **137**(833), 696–702 September (1932). 92, 125

[13] Pioro-Ladriere, M., Obata, T., Tokura, Y., Shin, Y. . S., Kubo, T., Yoshida, K., Taniyama, T., and Tarucha, S. *Nature Physics* **4**(10), 776–779 October (2008). 101

[14] Laird, E. A., Barthel, C., Rashba, E. I., Marcus, C. M., Hanson, M. P., and Gossard, A. C. *Phys. Rev. Lett.* **99**, 246601 Dec (2007). 19, 101

[15] Obata, T., Pioro-Ladrière, M., Tokura, Y., Shin, Y.-S., Kubo, T., Yoshida, K., Taniyama, T., and Tarucha, S. *Phys. Rev. B* **81**, 085317 Feb (2010). 101

[16] Nadj-Perge, S., Frolov, S. M., Bakkers, E. P. A. M., and Kouwenhoven, L. P. *Nature* **468**(7327), 1084–1087 December (2010). 49, 101, 119

[17] Petta, J. R., Taylor, J. M., Johnson, A. C., Yacoby, A., Lukin, M. D., Marcus, C. M., Hanson, M. P., and Gossard, A. C. *Physical Review Letters* **100**(6), 067601 February (2008). ii, 101, 102

[18] Barthel, C., Reilly, D. J., Marcus, C. M., Hanson, M. P., and Gossard, A. C. *Phys. Rev. Lett.* **103**, 160503 Oct (2009). 101

[19] Reilly, D. J., Taylor, J. M., Petta, J. R., Marcus, C. M., Hanson, M. P., and Gossard, A. C. *Physical Review Letters* **104**(23), 236802 June (2010). 102

[20] O. E. Dial, M. D. Shulman, S. P. H. H. B. V. U. A. Y. *arxiv* **arXiv:1208.2023** (2012). 106, 113, 124, 131

[21] Barthel, C., Medford, J., Bluhm, H., Yacoby, A., Marcus, C. M., Hanson, M. P., and Gossard, A. C. *Physical Review B* **85**(3), 035306 January (2012). 26, 107

[22] Nowack, K. C., Shafiei, M., Laforest, M., Prawiroatmodjo, G. E. D. K., Schreiber, L. R., Reichl, C., Wegscheider, W., and Vandersypen, L. M. K. *Science* **333**(6047), 1269–1272 (2011). 119

[23] Elzerman, J. M., Hanson, R., van Beveren, L. H. W., Witkamp, B., Vandersypen, L. M. K., and Kouwenhoven, L. P. *Nature* **430**(6998), 431–435 July (2004). ii, 4, 17, 119, 154

Chapter 5

Toward the detection of a single electron transported in an edge-state

Résumé

Dans ce chapitre, nous étudions la possibilité d'utiliser les états de spin d'une double boîte quantique à deux électrons afin de détecter le passage d'un électron unique dans un canal de bord relatif à l'effet Hall quantique.
En effet, dans le régime de l'effet Hall quantique, les électrons d'un gaz d'électrons bidimensionnel se déplacent le long de canaux de bords. Une telle propriété a été mise à profit afin de réaliser des expériences d'optiques quantiques avec des électrons. Nous commencerons ce chapitre par un bref descriptif de l'effet Hall quantique, et nous insisterons notamment sur l'existence des canaux de bords. Nous introduirons ensuite l'équivalent électronique de l'interféromètre de Mach-Zehnder afin de mettre en relief la nécessité d'un détecteur d'électrons uniques.
Nous décrirons alors comment les oscillations cohérentes entres deux états de spin d'une double boîte quantique peuvent être utilisées comme outil de détection de l'environnement électrostatique de cette double boîte. Pour ce faire nous caractériserons notre détecteur en introduisant des électrons dans des canaux bords définis aux abords de la double boîte quantique.
Cette étude nous permettra d'envisager la détection d'un électron unique transporté dans des canaux de bord, et nous développerons les contraintes liées à cette détection.

Introduction

Over the last few years, the sensitivity of detectors has been continuously enhanced. As a result, today it is possible to probe a single particle while the past generations had only access to the properties of an assembly of particles. Among these recent progresses, we can mention the nanosquid [1] or the NV centers based magnetometer [2]. In this thesis we are interested in the electron detection. A very common and precise way to measure the electron charge is the radio-frequency single electron transistor(RF-SET) which can reach sensitivities of $\sim 10^{-6} e/\sqrt{Hz}$. Recently Dial and coworkers demonstrated the use of the coherent exchange oscillations in a double quantum dot as an electrometer and reached a sensitivity two orders of magnitude ($\sim 10^{-8} e/\sqrt{Hz}$) better than the one of the RF-SET [3]. In this chapter we will attempt to measure a single electron charge, by using the double quantum dot device as described previously (chapter 4). In particular we will see that such a device could be of direct relevance to detect a single electron transported in an edge-state (in the quantum hall regime).
First we will develop the motivations related to this work, by introducing the Quantum Hall Effect and especially the existence of edge-states where the electrons are transported at sufficiently high magnetic field. We will introduce the use of these edge-states as electron beams for quantum optics experiment with electrons. Afterwards the use of a double quantum dot device (with a single electron spin in each quantum dot) in order to probe the electrostatic environment will be explained. Finally the study of such a new detector will be detailed.

5.1 Motivations

5.1.1 Quantum Hall Effect (QHE)

The Quantum Hall Effect (QHE) is the quantum equivalent of the classical Hall effect. In the classical case, an electrical current flowing through a conductive material subjected to a perpendicular magnetic field, gives rise to an electrical field perpendicular to them (figure 5.1 (a)) . Von Klitzing and coworkers [4] discovered in 1980 that the conductance of a two dimensional electron system (figure 5.1 (b)) becomes quantized at high magnetic fields and exhibits steps with respect to the magnetic field while it is linear in the classical case. This effect can be observed in a 2DEG sample with a Hall bar geometry (figure 5.1 (c)). By measuring the potential V_{xx} and V_{xy} in response to current excitation I and by applying a perpendicular magnetic field, they observed a nearly vanishing dissipation $R_{xx} = V_{xx}/I = 0$ and a quantization of the Hall conductance $R_{xy} = V_{xy}/I = \frac{1}{\nu}\frac{e^2}{h}$ (figure 5.1 (d)). This quantization is universal and independent of the used material or all the other details, the only requirement being a two dimensional electron system. We will not go into the detail of the physic of the QHE which is extremely rich, and we refer the reader to available reviews [5, 6]. In our case we will exploit the existence of edge states

in which the electrons are transported. In order to explain the existence of such states, we will follow the approach given by Landau [7].

Consider a two dimensional electron system, where the electrons are confined in an area $A = L_x L_y$ in the plane xy. An external magnetic field $\mathbf{B}$ is applied perpendicularly to this plane $\mathbf{B} = B_z\mathbf{z}$. The hamiltonian of the system can be written as :

$$H = \frac{1}{2m}(\hat{\mathbf{p}} + \frac{e\hat{\mathbf{A}}}{c})^2 \tag{5.1}$$

where $\hat{\mathbf{p}}$ is the momentum and $\hat{\mathbf{A}}$ the vector potential related to $\mathbf{B}$. The hamiltonian 5.1 being gauge invariant, the physical properties are not dependent on the choice of this gauge. We can therefore choose the Landau gauge without reducing the generality of the following discussion. We therefore define $\hat{\mathbf{A}}$ as:

$$\hat{\mathbf{A}} = \begin{pmatrix} 0 \\ B_z\hat{x} \\ 0 \end{pmatrix} \tag{5.2}$$

where $\hat{x}$ is the x-axis component of the position operator. Therefore the hamiltonian 5.1 can be written as :

$$H = \frac{\hat{p_x}^2}{2m} + \frac{1}{2m}(\hat{p_y} + \frac{eB_z}{c}\hat{x})^2 \tag{5.3}$$

We notice that $\hat{p_y}$ commutes with the hamiltonian then it can be written simply by introducing the cyclotron frequency $\omega_c = eB_z/mc$:

$$H = \frac{\hat{p_x}^2}{2m} + \frac{1}{2}m\omega_c^2(\frac{\hbar k_y}{m\omega_c} + \hat{x})^2 \tag{5.4}$$

We got the hamiltonian of an harmonic oscillator (space shifted by $x_0 = \frac{\hbar k_y}{m\omega_c}$). Consequently the energies of such a system are the one of the quantum harmonic oscillator:

$$E_n = \hbar\omega_c(n + \frac{1}{2}), \quad n \in \mathbb{N} \tag{5.5}$$

In addition, the sample size is finite, and therefore due to the confinement of the electrons inside the sample plane, the energy of the electrons should increase on the edge of the sample. Finally we notice that these energies depend on the external magnetic field through ω_c. We plotted the energy of the Landau levels for two different value of the magnetic field (figure 5.2 (a) and 5.2 (b)). In one case the value of the magnetic field

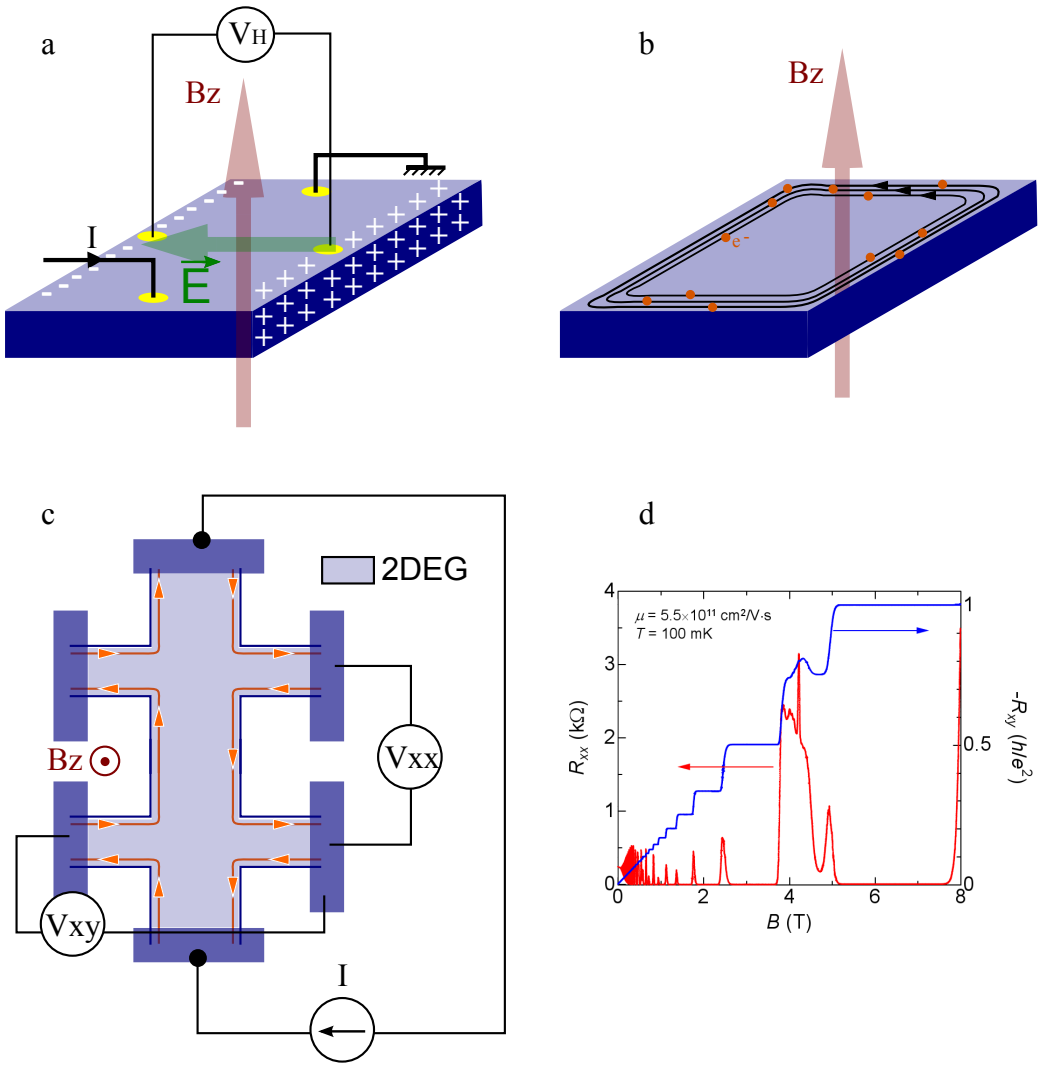

Figure 5.1: **Hall effect.** **(a) Classical Hall Effect :** an electrical current flowing through a conducting material subjected to a perpendicular magnetic field gives rise to an electric field perpendicular to the current and the magnetic field. **(b) Quantum Hall Effect :** In a two dimensional system, for a sufficiently high magnetic field, the motion of the electrons is confined along the edges of the sample. **(c) Hall bar geometry.** Such a geometry allows for measuring the transverse and longitudinal conductances in response to a current bias excitation and with respect to the perpendicular magnetic field B_z. **(d) Measurement of the quantum Hall effect.** This measurement comes from earlier measurement performed in the team. The nearly vanishing dissipation $R_{xx} = 0$ and the quantization of the Hall conductance $R_{xy} = \frac{1}{\nu}\frac{h}{e^2}$ can be observed.

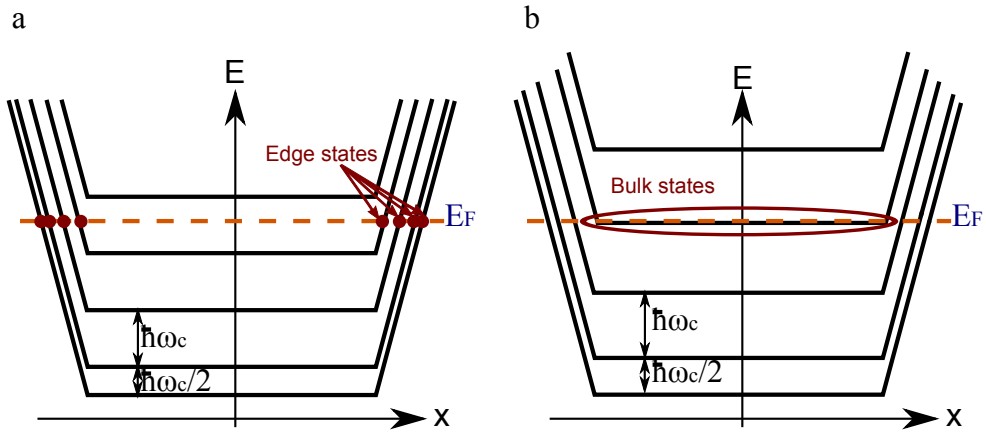

Figure 5.2: **Landau level.** **(a)** The magnetic field is set in order to avoid conduction into the bulk. The conduction electrons are located at the edges of the sample. **(b)**By increasing the magnetic field, we can set $E_3 = E_F$, and the conduction electrons exists therefore also in the bulk.

is set in such a way that there is no $n \in \mathbb{N}$ allowing for $E_n = \hbar\omega_c(n + \frac{1}{2}) = E_F$, where E_F is the Fermi energy. As we can see in figure 5.2 (a), there is no free state in the bulk, and the conduction electrons are on the edge of the sample (where $x \sim L_x$ $(y \sim L_y)$). The number of allowed edge states is generally denoted by ν, where $\nu = 1$ corresponds to a single allowed edge state. In the second case (figure 5.2 (b)), the magnetic field has been increased (which increases the cyclotron frequency ω_c) in order to set $E_3 = E_F$. Therefore conduction electrons exists also in the bulk.

Therefore we can see that the study of the Landau levels explains the existence of the edge-states where the electrons can be transported. After this discovery, a lot of prolific studies have been achieved. Among those, physicists began to think about the possibility to use such effect in order to perform quantum optics experiments with electrons. Indeed by considering the regime $\nu = 1$, the electrons are transported in a single edge state which can be assimilated to an optical fiber for electrons. Consequently it should be possible to perform quantum optics experiments with electrons in this regime, and in the next section we will describe the electronic equivalent of the Mach-Zehnder interferometer.

5.1.2 The electronic Mach-Zehnder interferometer.

The ability to guide the electrons through the edge-states opens the route to realization of interference experiments. Among those, the Mach-Zehnder interferometer can be easily understood by first dealing with photons (figure 5.3 (a)). Let us consider a photon beam arriving from a coherent light source to a first beam splitter BS1. It splits the light beam into two paths which are then recombined on a second beam splitter BS2 via two

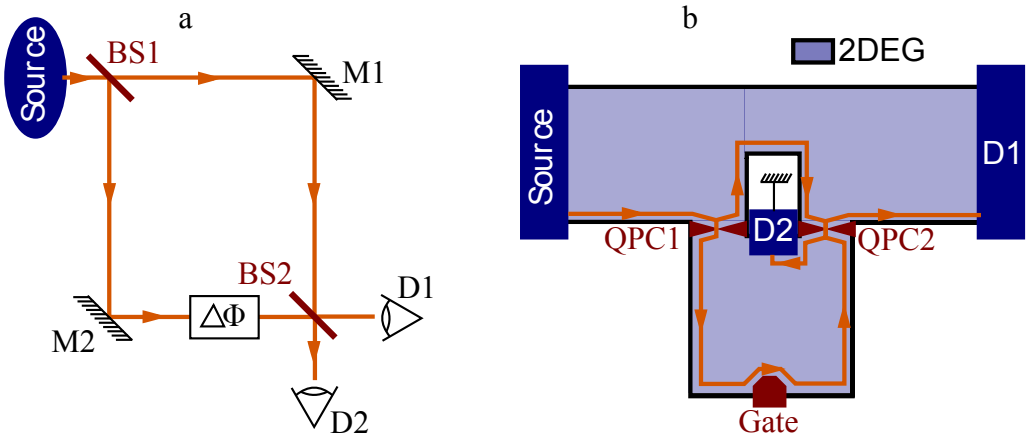

Figure 5.3: **Mach-Zehnder interferometer (a)** A photonic Mach-Zehnder interferometer. D1 and D2 are detectors, BS1 and BS2 are beam splitters, and M1 and M2 are mirrors. **(b)** The electronic equivalent of the photonic Mach-Zehnder interferometer. The electrons are transported in a single edge state. The beam splitters are made of QPC, and the electrons are collected in two ohmics contacts (detector) D1 and D2. In addition a gate located next to the lower path allows for changing the phase.

mirrors M1 and M2. With $0(\pi)$ phase difference between the two paths, the detector D1 measures maximum (zero) signal while D2 measures zero (maximum) signal. The sum of the output signals is constant and equal to the input signal. If a phase shift is added in one of the path, the signal in the two detectors should oscillates out of phase with respect to this added phase.

An electronic equivalent can be done by tuning a 2DEG in the $\nu = 1$ regime via the magnetic field. Therefore the electrons are transported along a single edge state (figure 5.3 (b)). The beam splitters can be easily replaced by two QPCs tuned in order to get a transmission and a reflection coefficients equal to 0.5. The current is collected in two ohmic contacts, and a gate located in the lower path allows for changing the area A defined by the two paths, and therefore the phase due to the magnetic field. This experiment has first been achieved by Ji and coworkers [8]. They experimentally observed a modulation of the current in the detector D1 with respect to the applied gate voltage.
In the photonic case, single photon detectors with large bandwidth (avalanche photodiode) exist and it is consequently possible to perform correlations between the signal measured in each detector. In the electronic case, only a few experiments have been performed, and the detection was done by means of the current generated by an ensemble of electrons, while the electrons correlations were encrypted in the current noise [8, 9, 10, 11, 12, 13]. Such an experiment on the single electron level, i.e with single electron detection has not yet been realized. In the following section we outline a way to

perform this single electron detection by using a double quantum dot system as described earlier (see chapter 4).

5.2 A double quantum dot as a single electron detector

In the previous chapter, we detailed the exchange oscillations in a double quantum dot with two electrons. Considering a double quantum dot occupied with a single electron in each quantum dot, the triplet $|T_0\rangle$ and the singlet $|S\rangle$ are split by the exchange energy J due to the tunnel coupling between the two quantum dots (figure 5.4 (a)). Therefore an initial superposition of singlet and triplet will evolve coherently with a frequency related to the exchange energy $J(\varepsilon)$. In figure 5.4 (b)(already seen in chapter 4), the singlet probability is plotted with respect to the exchange pulse detuning ε and duration τ. As we have already seen, the oscillation frequency depends on the detuning parameter ε which changes the exchange energy $J(\varepsilon)$. The tuning of the double quantum dot used in this chapter is exactly the same as the one detailed in the previous chapter. Consequently the expression for the exchange energy is the same:

$$J(\varepsilon) = 50.10^{-9} + 6.10^{-6} exp(-\frac{|\varepsilon|}{0.2\,10^{-3}})(eV) \tag{5.6}$$

For decreasing detuning ε, the exchange energy increases, and the oscillation frequency increases as observed in figure 5.4 (b). If the accumulated phase depends on the detuning parameter, which is nothing else than gate voltages, it means that this phase is sensitive to the electrostatic environment. Recently it has been demonstrated experimentally that this dependence of the accumulated phase on the electrostatic environment can be used in order to perform controlled operations between two capacitively coupled qubits [14, 15]. In this case they consider the qubit subspace as being $\{|S\rangle, |T_0\rangle\}$, and therefore a double quantum dot acts now as a single qubit. We will not describe in detail the difference related to the use of such qubit subspace, but we can notice that the SWAP gate detailed in the previous chapter is now a single qubit rotation around the $\hat{z}$ axis. The principle of the controlled operation first demonstrated by Van Weperen and coworkers [14] relies on the high sensitivity of the exchange oscillations with respect to the qubit's electrostatic environment. They demonstrated that the exchange oscillation frequency in a target qubit depends on the charge state in a control qubit (figure 5.4 (c)). Shulman and coworkers [15] demonstrated first the entanglement of two qubits by using controlled operation via capacitive coupling.

Here we propose to use the exchange oscillations as a quantum electrometer in order to detect the passage of a single electron in an edge-state (figure 5.4 (d)). The passage of this electron should change the electrostatic environment of the qubit (detector) and therefore the accumulated phase should change. Indeed, a Singlet-Triplet qubit is a quantum system where the two quantum levels can be tuned on fast timescale from a charge-like to spin-like qubit. Whereas the qubit is highly sensitive to the electrostatic

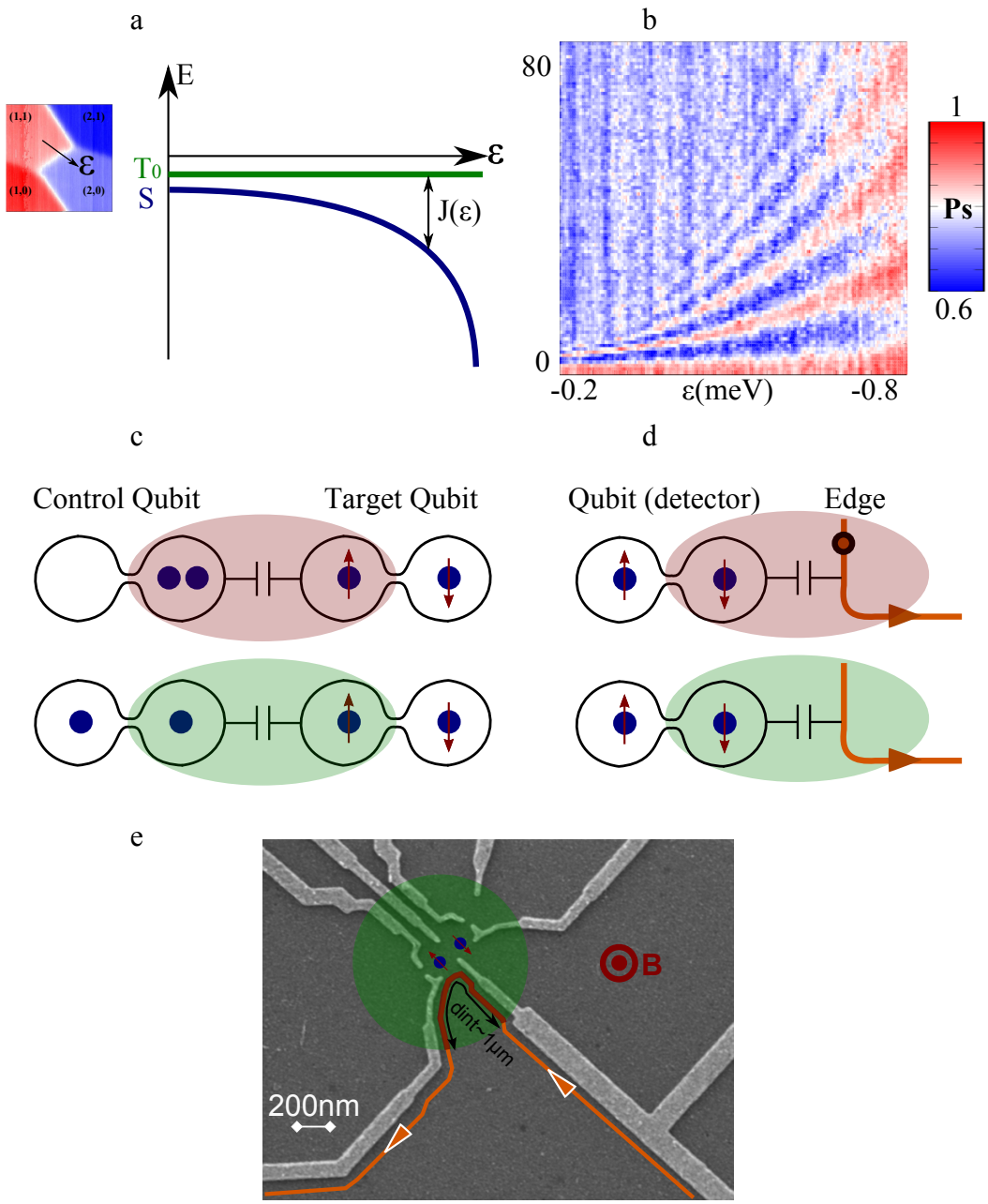

Figure 5.4: **Exchange coherent oscillations** **(a)** In a double quantum dot where a single electron lies in each quantum dot, the singlet and the triplets state ($|S\rangle$ and $|T_0\rangle$) are energy split by the exchange energy J which depends on the detuning parameter ε. **(b)** Exchange oscillations. The singlet probability is plotted with respect to the pulse duration τ and the pulse detuning ε. **(c)** Two qubits capacitively coupled. The frequency of the exchange oscillations in the target qubit depends on the charge state of the control qubit. **(d)** A double quantum dot is used as a "quantum detector" in order to detect the passage of a single electron in an edge next to the quantum dot. **(e)** SEM picture of the double quantum dot device. We assume roughly the capacitance coupling distance between the electrostatic environment and the double quantum dot as being equal to $\sim 500nm$ (green disk). It induces an interaction distance between the device and the closest edge state as being equal to $d_{int} \sim 1\mu m$.

environment and characterized by timescales as fast as few hundreds of picoseconds in the charge regime, the information stored in the qubit in the spin regime can be preserved for a time longer than few hundreds of microseconds [15]. This gives seven orders of magnitude between the two important quantities of a quantum detector: the interaction time and the time to preserve the information. It allows for interacting strongly for a very short time with a single electron [15], storing the resulting effect on the population of the two-level system for a time sufficient long [15] and reading-out single shot the state of the qubit with fast charge detection [16]. The question which arises is of course the sensitivity of such a device. This sensitivity to the electrostatic environment is obviously related to the derivative $\frac{dJ}{d\varepsilon}$. The bigger is $\frac{dJ}{d\varepsilon}$, the bigger will be the sensitivity. The first result of the increasing sensitivity at $\varepsilon \to 0$ (figure 5.4 (b)) is the increasing decoherence. Indeed as we can clearly observed in figure 5.4 (b), the decoherence is much faster for $\varepsilon \to 0$. In a recent paper, Dial and coworkers demonstrates that the charge sensitivity of such a device was of the order of $\sim 10^{-8} e/\sqrt{Hz}$ which is two orders of magnitude better than the sensitivity of a RF-SET [3].
In order to detect the passage of a single electron in an edge state, the first issue relies on the velocity of such a particle, and consequently the duration of the interaction between the electron and the detector. The edge-state velocity (the velocity of a particle transported in an edge-state) can be estimated to $v_e \sim 10^4 - 10^5 m.s^{-1}$ [17, 18, 19]. It is related to the derivative of the energy with respect to the space coordinates. Due to confinement, the energy of the Landau levels increase at the edge of the sample. The origin of this confinement can be diverse (gated sample, etched sample) and gives rise to different energy profiles at the edge of the sample. To get an order of magnitude of the duration of the interaction between an electron transported in the edge-state and the double quantum dot device, we assume the distance of the capacitive coupling between the system and the electrostatic environment as being roughly equal to $\sim 500nm$ (green disk in figure 5.4 (e)). This value is a rough estimation and to obtain it, we assume it was roughly the same than the one of a QPC and a quantum dot. This allows us to estimate the "edge length" with which the device is coupled, and which is roughly equal to $d_{int} \sim 1\mu m$. With this interaction distance we obtain an interaction duration $\tau_{int} \sim \frac{d_{int}}{v_e} \sim 5 - 50ps$.

5.3 Quantum hall regime

First of all, the system has to be tuned into the quantum Hall regime, meaning that the magnetic field has to be increased. We could have reproduced the measurement presented in figure 5.1 (d), but with the present sample, four-point measurements were not easy to achieve. On the other hand, a two-point measurement is sufficient to get the information that we need. We remind that the sample is the same (as well as the tuning) than the one

from the chapter 4. Figure 5.5 (a) shows a SEM picture of the whole sample. The double quantum dot previously studied is located in the top left of the picture. The only new feature compared to what we have seen in chapter 4 is the gate located in the bottom right part of the picture. For the moment we assume the gate voltage V_g^{qpc2} applied to this gate being equal to 0. In order to tune the system in the quantum hall regime we studied the behaviour of the conductance of the 2DEG with respect to the external magnetic field. To do so, we applied a voltage bias $V_{qpc2} = 50\mu eV$ to one ohmic contact (in the right part of the picture) and observed the current response I_{qpc2} in another contact (in the left part). The measurement of the current with respect to the external magnetic field is presented in figure 5.5 (b). Such a measurement refers to the Shubnikov de Haas effect, but this is nothing else than probing the Landau levels. When the external magnetic field $\mathbf{B}_{ext}$ increases we observe current oscillations which are the manifestation of the presence of the Landau levels :

- For maximum current, the conductance of the 2DEG is maximum, and this can be related to the nearly vanishing dissipation $R_{xx} = V_{xx}/I = 0$ (figure 5.1 (d)). In this case we can consider that the electron are mainly transported by the edge-states rather than by the bulk states.
- For a minimum of the current I_{qpc2}, we can consider one of the Landau level aligned with the Fermi energy. Therefore the conductance through the bulk is now possible.

The first idea should be to tune the 2DEG in the $\nu = 1$ regime. But a new issue arises concerning the spin measurements at high magnetic fields. Indeed in order to measure the spin states of a double quantum dot system, we have seen that we took advantage of the inaccessible triplet states in the region (2,0). When the external magnetic field increases, the energies of these triplets decrease, and the spin-blockade phenomenon is no more observed. This can be seen by studying the mixing of the $S - T_0$ (see chapter 4) at high magnetic field. Figure 5.5 (c) shows two stability diagrams where the pulse allowing for such spin manipulations is running. At $\mathbf{B}_{ext} = 700mT$, we still observe the triangular shape related to the spin blockade. But for $\mathbf{B}_{ext} = 900mT$, this triangle has disappeared, indicating that the spin-blockade has been lifted. Therefore the maximum external magnetic field $\mathbf{B}_{ext}$ that we can apply to the system is limited and we fixed it at $\mathbf{B}_{ext} = 700mT$ (corresponding to a maximum of current). At this position we are obviously not in the regime $\nu = 1$ (a single edge-state), and the number of edge-states is bigger than one. By looking at the peak current value at $\mathbf{B}_{ext} = 700mT$, we can see that $I_{qpc2}(B_{ext} = 700mT) \sim 20nA$. By taking into account of voltage bias $V_{qpc2} = 50\mu eV$, we obtain the 2DEG resistance at this magnetic field $R_{2DEG}(B_{ext} = 700mT) \sim 2500\Omega$. This resistance being $R_{2DEG} = \frac{1}{\nu}\frac{h}{e^2}$, it allows us to extract the number of edge-states $\nu = 10$ for $B_{ext} = 700mT$, which is consistent with the value expected from magnetic field and 2DEG electron density. Although $\nu \neq 1$, it should still be possible to test the sensitivity of the double quantum dot detector. In figure 5.5 (a) we depicted the edge-states by

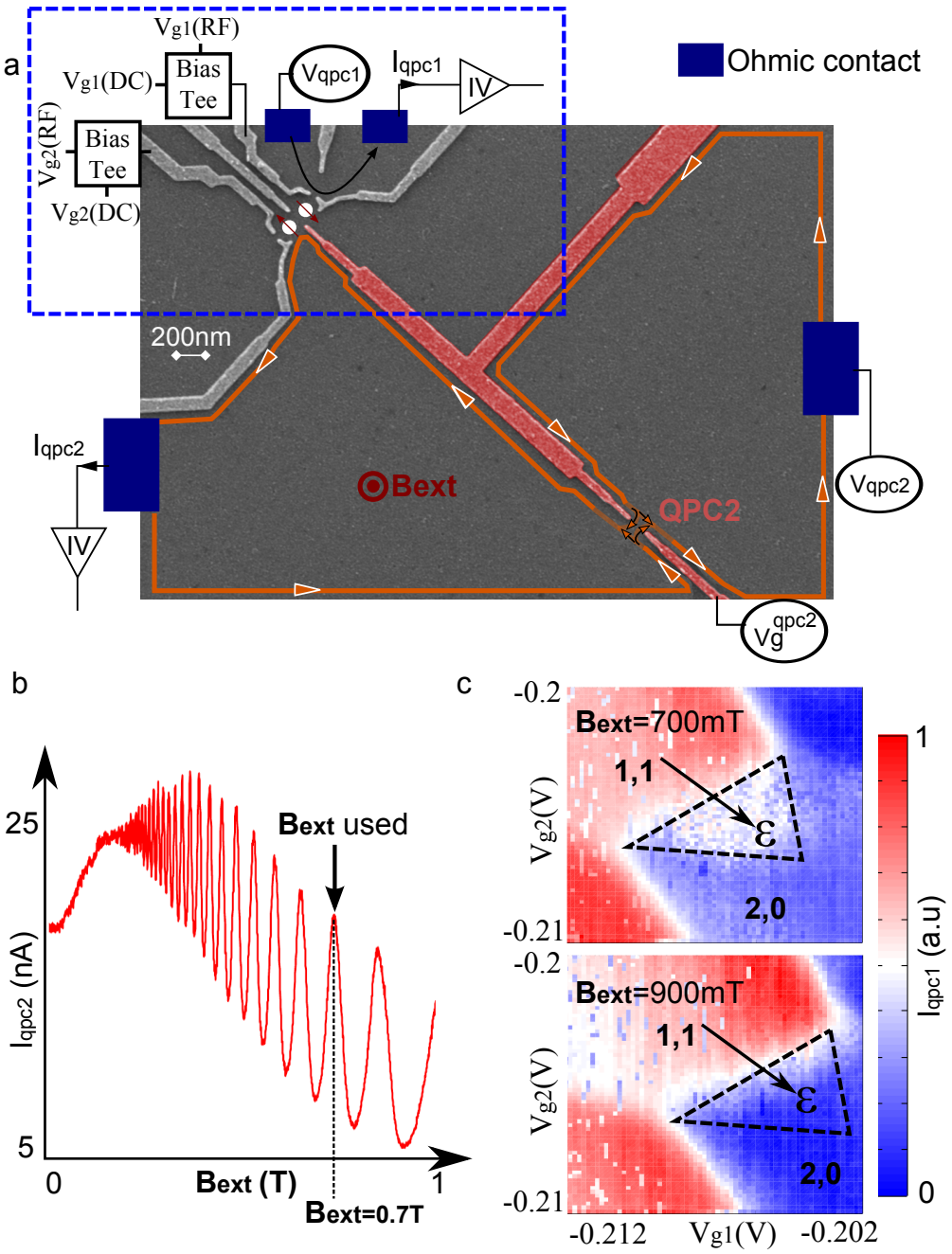

Figure 5.5: **(a)** SEM (scanning electron microscopy) picture of the studied device. The double quantum dot located in the top of the picture is the one already seen in the chapter 4. **(b)** Shubnikov de Haas oscillations. The voltage vias V_{qpc2} has been set to $100\mu eV$ and the current I_{qpc2} is plotted with respect to the external magnetic field applied perpendicularly **(c)**

the orange lines. For clarity we depicted a single edge-states. The electron movement (orange arrows) in these edges is related to the direction of the external magnetic field. In order to quantify the interaction between the electrons transported in an edge-state and the detector device, we first tried to detect a large number of electrons traveling in these edge-states.

5.4 Quantification of the detector device

In order to test our detector device we first used a simple system, where a large number of electrons can be injected into the edge-states through a QPC (QPC2 in figure 5.5 (a)), and be transported from the QPC2 to the detector via the edge-states. In this section we will test the following detector capacities :

- The first expected capacity of the detector is to be sensitive to the electrostatic environment. Therefore by changing the number of electrons transported in the edge-states, it should change the frequency of the exchange oscillations.
- In addition, the working principle of the detector relies on the coherent exchange oscillations. Therefore the fluctuations of the electrostatic environment induce decoherence. We have already observed this feature on the exchange oscillations where the decoherence was clearly observed. In order to emphasize this capacity, we can increase the electrostatic fluctuations by injecting electrons into the edge-states in a stochastic manner. Indeed by injecting the electrons through a QPC with partial transmission, the electrons will arrive next to the detector stochastically and it should increase the decoherence of the exchange oscillations.

The transmission of QPC2 can be tuned by changing the gate voltage V_g^{qpc2}. Figure 5.6 (a) shows the current flowing through QPC2 (in response to a bias voltage $V_{qpc2} = 100\mu eV$) with respect to the gate voltage V_g^{qpc2}. The current plateau corresponds to a QPC where a single channel with a transmission equal to 1 allows the electron flow. In addition we can change the number of injected electrons by changing the voltage bias V_{qpc2}. We tested the behaviour of QPC2 with respect to this voltage bias (V_{qpc2} from 0 to $1\mu eV$), and we did not see any change. Figure 5.6 (b) shows the same measurement than figure 5.6 (a), but here we used a bias voltage $V_{qpc2} = 1meV$. As clearly observed the two curves are identical.

5.4.1 Detection of the electron density of the edge-states

To test the main capacity of the detector, namely its dependence to the electrostatic environment, the density of electrons transported in the edge-states can be changed. Therefore we first consider that a single conducting channel is allowed in the QPC2 and its transmission is set equal to 1 (figure 5.6 (a)). In this case the electrons are transported

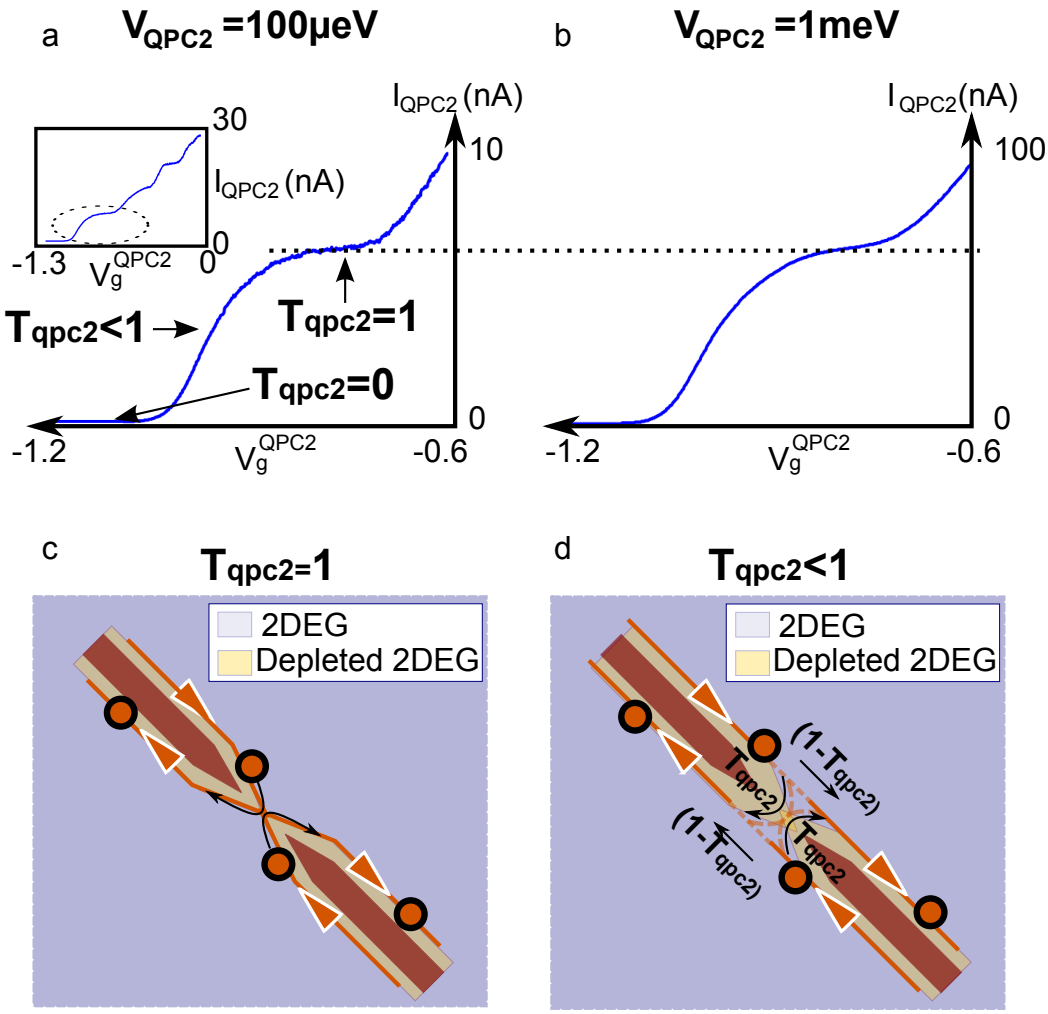

Figure 5.6: **(a) and (b)** QPC current I_{qpc2} with respect to the gate voltage V_g^{qpc2} for two different values of the bias voltage : $V_{qpc2} = 100\mu eV$ **(a)**, and $V_{qpc2} = 1meV$ **(b)**. **(c) and (d)** Scheme of the transport of the electrons in the edge-states across the QPC. **(c)** For the QPC2 transmission $T_{qpc2} = 1$. **(d)** For the QPC2 transmission $T_{qpc2} < 1$.

T	1	1	1	1	1
$V_{qpc2}(\mu eV)$	500	250	0	-250	-500
I_{qpc2}(nA)	36	18	0	-18	-36
amplitude	0.125	0.13	0.14	0.14	0.13
ε(meV)	-0.342	-0.332	-0.319	-0.308	-0.269
T_2^*(ns)	17	16	19	15	13

Table 5.1: Fit parameters of the exchange oscillations (amplitude, detuning ε and decoherence time T_2^*) for different values of the voltage bias V_{qpc2} with the QPC2 transmission equal to 1.

from one side of the QPC to the other side. Therefore all the electrons injected through the QPC2 via the bias voltage V_{qp2} will be transported into the edge-states (orange lines in figure 5.5 (a)) and pass next to the detector before being finally collected in the ohmic contact located in the left part of figure 5.5 (a). The measurement of the current I_{qpc2} gives the number of electrons transported in the edge-states. If the voltage bias V_{qpc2} is changed, it induces a change of the electron density in the edge-states (meaning a change of the number of electrons transported), and consequently a change of the electrostatic environment of the double quantum dot detector. In other words the electrons act as a gate voltage. In order to understand the expected effect we need to have look at the sample geometry (figure 5.6 (a)). Indeed, the geometry has been designed in order to make the edge-states being closer with quantum dot 2 than with quantum dot 1 . The capacitive coupling between quantum dot 2 and the edge-states is therefore expected to be stronger than the one with quantum dot 1 and hence :

- If the number of electrons flowing next to the detector increases, it is equivalent to decreasing (set more negative) the gate voltage V_{g2}, meaning to increase ε.
- On the other hand, if we decrease the flow of electrons, it is equivalent to increase V_{g2} leading to an increase of ε.

Therefore the increase (decrease) of the electron flow should increase (decrease) the exchange energy during the exchange pulse, leading to higher (lower) exchange oscillation frequencies. Figure 5.7 (a) shows exchange oscillations for different values of the voltage bias V_{qpc2} (giving rise to the QPC2 current I_{QPC2}). The experimental data have been superimposed with their fits. The fit procedure is exactly the same than the one described in the previous chapter, and here the fit parameters are the oscillation amplitude, the exchange pulse detuning and the decoherence time T_2^* (the nuclear magnetic field gradient is assumed to be equal to $4mT$). We regrouped these fit parameters in the table 5.1.

The first observation is the expected dependence of the exchange pulse detuning with respect to the number of electrons flowing in the edge-states (I_{QPC2}). This feature can be

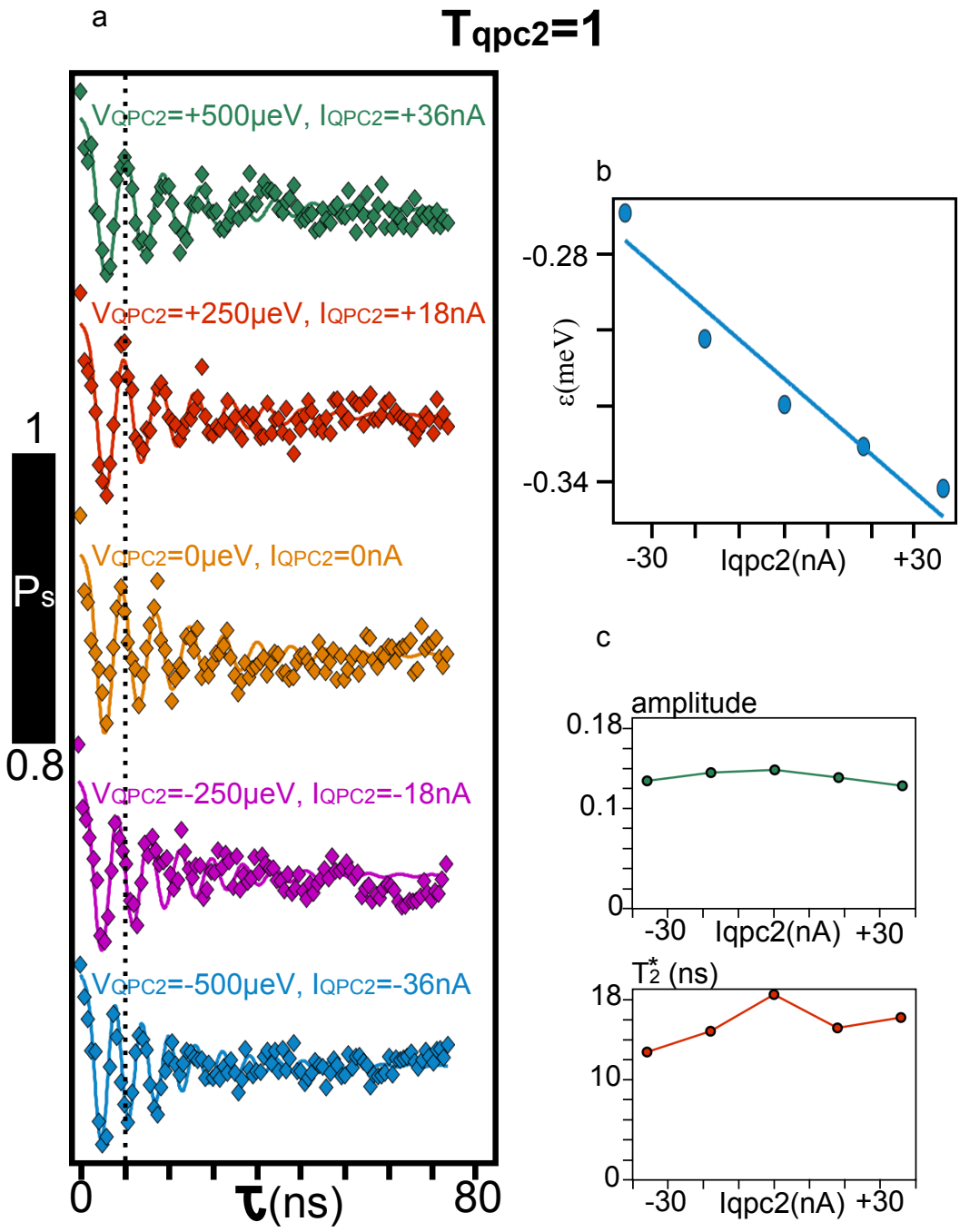

Figure 5.7: **(a)** Exchange oscillations for different number of electrons flowing through the QPC2 (I_{qpc2}) at fixed QPC2 transmission $T = 1$. **(b)** Fitted values of the detuning ε with respect to bias voltage V_{qp2}. The linear fit is relative to the linear dependence of the number of electrons flowing through the QPC with respect to V_{qpc2}. **(c)** Fitted values of the amplitude and the deocherence T_2^* with respect to to V_{qpc2}

easily seen in figure 5.7 (a) where the oscillations frequency exhibits a clear dependence with respect to I_{QPC2}. For instance between the curve at $I_{QPC2} = +36nA$ and the one at $I_{QPC2} = -36nA$, we observed a π-phase shift after 10ns (dotted line in figure 5.7). Figure 5.7 (b) shows the fitted value of ε with respect to the bias voltage V_{qpc2}. The number of electrons injected into the edge-states scales linearly with V_{qpc2}, therefore by assuming a linear dependence of the exchange pulse detuning with respect to the current I_{qpc2}, the detuning shift induced by the change of the electron density in the edge-states is $\Delta\varepsilon = 1\mu eV/nA$. Let us explain this value. The detuning shift is directly related to the capacitive coupling between the detector and the edge-states. Its value is intrinsic to the present sample measured. But this value is not a measure of the sensitivity of the detector. Indeed this sensitivity depends on the derivative of the exchange energy with respect to the detuning parameter. In other word the sensitivity of the detector is fixed by the amplitude of the exchange pulse.
Another feature can be observed in this measurement. Indeed, as we can see in table 5.1, the decoherence time T_2^* decreases when the number of electrons flowing in the edge-states next to the detector increases. In this case, we can relate this decrease to the change of the detuning parameter ε. Indeed when ε increases, the derivative of the exchange energy with respect to ε increases. The decoherence induced by the electrostatic fluctuations being proportional to this derivative, we observe a decrease of T_2^*. Figure 5.7 (c) shows the fitted value of the amplitude and the decoherence time T_2^* with respect to V_{qpc2}. Similarly to the decoherence, the decay of the amplitude can be explained by the detuning shift induced by the increasing number of electrons flowing into the edge-states. Concerning the maximum of amplitude and decoherence at zero bias V_{qpc2} (figure 5.7 (c)), we can make the assumption that the QPC2 transmission was not perfectly set to one. This feature leads, as we will see later, to stochastic events inducing decoherence.

5.4.2 Detection of stochastic events

In addition to the measurement of the exchange oscillations with respect to the number of electrons transported in the edge-states, we performed measurements at a fixed number of electrons $I_{QPC2} = -20nA$ ($\sim 200 electrons/ns$)for different values of the QPC2 transmission varying from T=1 to almost T=0. If the QPC2 is not fully transmitting ($T < 1$), it acts as a tunnel barrier for the electrons. Therefore the passage of the electrons through the QPC2 becomes a stochastic event. Figure 5.6 (b) illustrates this case. An electron arriving on the QPC2 has a probability to be transmitted to the other side of the QPC2 equal to T, while it has a probability to be reflected of $1 - T$. Because the electrons transported in the edge-states arrive close to the detector in a stochastic manner, they induce electrostatic fluctuations, and the signature of these fluctuations in the detector is a faster decoherence. Figure 5.8 shows exchange oscillations for different values of the QPC2 transmission at fixed QPC2 current $I_{qpc2} = -20nA$. In order to maintain this current at QPC2 transmission lower than one, the voltage bias V_{qp2} has to be

T	1	0.85	0.75	0.6	0.45	0.3	0.2
$V_{qpc2}(\mu eV)$	-280	-308	-362	-444	-600	-850	-1350
I_{qpc2}(nA)	-20	-20	-20	-20	-20	-20	-20
amplitude	0.21	0.21	0.21	0.21	0.21	0.21	N/A
ε(meV)	-0.267	-0.255	-0.260	-0.250	-0.243	-0.239	N/A
T_2^*(ns)	12.8	11.5	10.5	8.5	7.1	4.8	N/A

Table 5.2: Fit parameters of the exchange oscillations (amplitude, detuning ε and decoherence time T_2^*) for different values of the QPC2 transmission T_{qpc2} with the QPC2 current I_{qpc2} equal to 20 nA.

increased. One more time the experimental data and their fits have been superimposed and we regrouped the fit parameters in table 5.2.

Contrary to the previous case, here the number of electrons flowing through the QPC2 is constant, consequently we do not expect to observe a change in the exchange pulse detuning. Despite all, the fitted value of ε exhibits a small decrease when the transmission is decreased (figure 5.8 (c)). We suppose this feature is related to the change of the electrostatic environment induced by the gate voltage change in order to tune the QPC2 transmission. But the main feature of this measurement relies on the evolution of the decoherence time with respect to the transmission. We observe a net decrease of the decoherence time while the transmission T_{qpc2} decreases (figure 5.8 (b)). As explained below it is related to the stochasticity of the tunnel events. Indeed, since the number of electrons flowing through the QPC2 and transported along the edge-states next to the detector is constant, changing the transmission of the QCP2 does not modify the number of electrons seen by the detector. On the other hand, changing the QPC2 transmission modifies the time interval Δt between each passage of a single electron. Figure 5.9 (a) shows a scheme of the edge-states when the QPC2 transmission is set to 1. The time interval between each passage of as single electron is well defined and equal to $\Delta t = e/I_{qpc2}$. On the contrary, if the transmission is lower than 1, this time interval becomes a statistical distribution centered in $\Delta t = e/I_{qpc2}$ (figure 5.9 (b)). The smaller is the transmission, the more dispersive will be the time interval statistics. Such a feature explains the behaviour of the exchange oscillations of figure 5.8 (a).

5.4.3 Evolution of the detector visibility with respect to the QPC transmission

Finally we study the evolution of the exchange oscillations with respect to the QPC2 transmission at fixed bias voltage $V_{qpc2} = -1meV$. In this case when the QPC2 transmission decreases, the current also decreases, leading to a decrease of the number of electrons (seen by the detector) coming from the edge-states of the right side of QPC2. Therefore

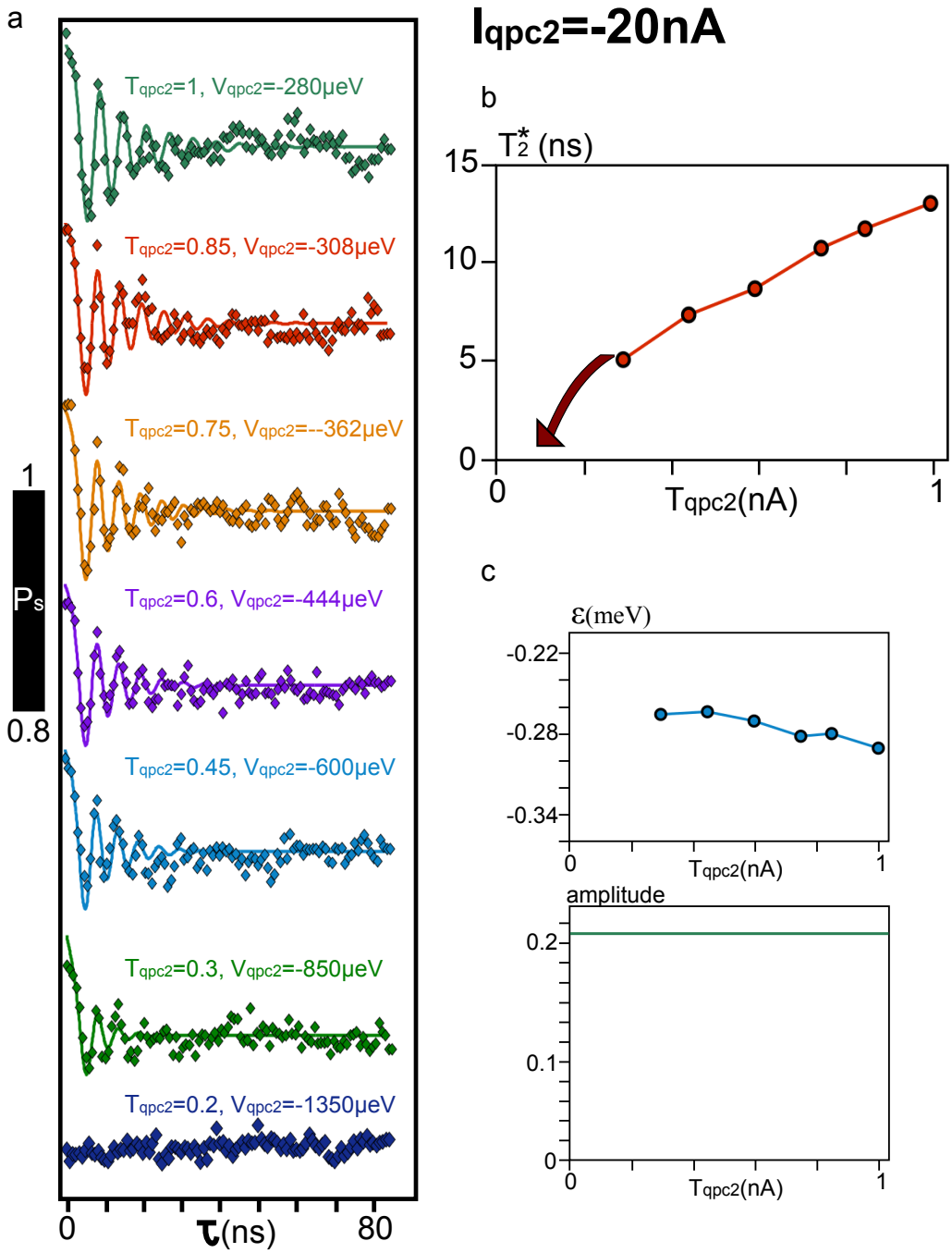

Figure 5.8: **(a)** Exchange oscillations for different QPC2 transmission at fixed current $I_{QPC2} = -20nA$. **(b)** Fitted values of the decoherence time T_2^* with respect to the QPC2 transmission T. **(c)** Fitted values of the amplitude and the detuning ε with respect to the QPC2 transmission T.

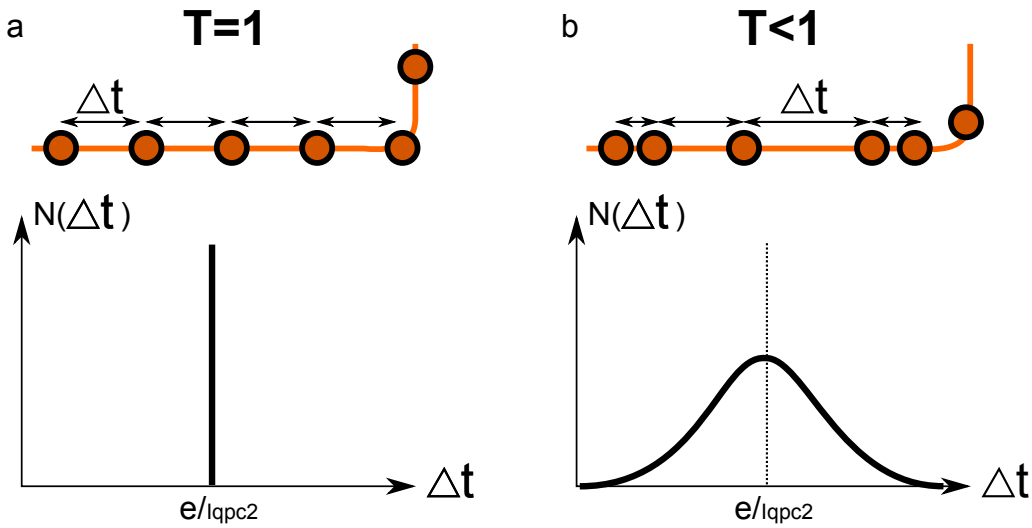

Figure 5.9: **(a)** Time intervals between each passage of a single electron for QPC2 transmission equal to 1. In this case each electron is separated in time from the previous one (and the next one) by the time interval $\Delta t = e/I_{qpc2}$ and the detector sees deterministic events. **(b)** Time intervals between each passage of a single electron for QPC2 transmission lower than 1. In this case the QPC2 acts as a tunnel barrier, and the passage of the electrons through it becomes a stochastic process. Therefore the time interval between the electrons is no more well defined, but becomes a statistical distribution centered around $\Delta t = e/I_{qpc2}$.

T	1	0.91	0.76	0.62	0.51	0.38	0.23	0.002	0
$V_{qpc2}(\mu eV)$	-1000	-1000	-1000	-1000	-1000	-1000	-1000	-1000	-1000
I_{qpc2}(nA)	-7.3	-6.67	-5.57	-4.55	-3.78	-2.78	-1.7	-0.02	0
amplitude	0.084	0.1	0.076	0.055	0.036	0.042	0.1	0.17	0.17
ε(meV)	-0.294	-0.317	-0.336	-0.345	-0.354	-0.368	-0.387	-0.437	-0.44
T_2^*(ns)	13.4	18.2	20.3	22.4	26.2	29	32	34	36

Table 5.3: Fit parameters of the exchange oscillations (amplitude, detuning ε and decoherence time T_2^*) for different values of the QPC2 transmission T_{qpc2} at fixed bias voltage $V_{QPC2} = 1meV$

the detector sees a mix between the electrons coming from the edge-states of the right and the left side of the QPC2. The electrons from the left side are at zero potential while the one from the right are at the potential V_{qpc2} and we can distinguish two borderline cases :

- If the QPC2 transmission is equal to 1, the detector sees only the electrons coming from the right side of QPC2 (at potential $V_{qpc2} = -1meV$). In this case the number of electrons flowing next to the detector is large. Therefore we expect to observe fast exchange oscillations. For the following we denote the detuning relative to this electrostatic environment $\varepsilon_{T=1}$

- If the QPC2 transmission is equal to 0, the detector sees only the electrons coming from the left side of QPC2 (at zero potential). In this case the number of electrons flowing next to the detector is weak and we expect to observe slower exchange oscillations. For the following we denote the detuning relative at this electrostatic environment $\varepsilon_{T=0}$.

Between these two borderline cases (for QPC2 transmission $0 < T < 1$), the detector should see a mix between these two borderline electrostatic environment characterize by a detuning $\varepsilon_T = T\varepsilon_{T=1} + (1-T)\varepsilon_{T=0}$. In addition due to the stochasticity described earlier and happening at QPC2 transmission $T < 1$, the visibility of the detector (meaning the amplitude of the exchange oscillations) should be minimum for $T = 0.5$ and maximum for $T = 1$ or $T = 0$.

Figure 5.10 (a) shows the exchange oscillations obtained at fixed bias voltage V_{qpc2} for different QPC2 transmissions T. One more time the experimental data and their fits have been superimposed and we regrouped the fit parameters in the table 5.3. We observe the expected behaviour of the amplitude (visibility) of the detector with respect to the QPC2 transmission T (figure 5.10 (b)) : the case $T = 1$ and $T = 0$ correspond to a maximum of visibility while the minimum is obtained around $T = 0.5$. The reason why the curve is not symmetric can be explained by the change of the detuning parameter induced by

the change of the QPC2 transmission. Indeed by lowering the detuning parameter (and this is what happens when T increases, figure 5.10 (b)), the decoherence increases (as it can be observed in figure 5.10 (b)).
To conclude these three sets of measurements allow us to confirm the working principle of our detector. But in the present configuration, we clearly see that it is not yet sensitive to a single electron. For instance in figure 5.7 (a), a π-phase shift is obtained after 10ns and for a variation of the QPC2 current equal to 72nA. It means that approximatively 7000 electrons are responsible of this phase shift, and we are far from the single electron sensitivity. We will now develop a method to increase the sensitivity of the detector.

5.5 Perspectives : Toward the single electron detection

In the previous section, we verified the working principle of the detector. But the present configuration does not allow for single electron detection. In order to do so, we have to to increase the sensitivity of the detector, that is to say, we have to increase the derivative of the exchange energy with respect to the detuning parameter $\frac{dJ}{d\varepsilon}$. But a major issue arises from this requirement. Indeed the decoherence due to electrostatic fluctuations scales also with this derivative, and for large value of $\frac{dJ}{d\varepsilon}$, the time ensemble average decoherence time T_2^* is roughly equal to $\sim 1ns$. The principle of our detector relying on the coherent evolution of our system, we should therefore have to be able to observe coherent oscillations on the sub-nanosecond time-scale. This is actually not possible with the present set-up which have been used :

- First the RF arbitrary waveform generator which has been used during this thesis has a sampling rate equal to 1.2 Gsamples/s. In other words, it means that it is able to generate a point every 0.83ns. Therefore if the exchange oscillations exhibit a period of $\sim 1ns$, we would be able to reconstruct them with only a single point per period, which is quite low.

- Secondly the bandwidth of our measurement set-up is also limited. This is mainly due to the bias tee, and it leads to a finite rise time of the pulses equal to $\sim 1ns$.

These two technical constraints did not allow us to use a "basic" exchange pulse as we always did until now. Therefore we have to engineer a more sophisticated pulse in order to detect a single electron. The data related to the detection of a single electron with this "new" kind of pulse are still under analysis. In the following we will just describe how we can inject a single electron in the edge-states.
Indeed before we used a voltage bias in order to change the edge-states density of electrons. We have seen that a $100\mu eV$ voltage bias across a QPC (whose transmission is equal to one) leads to few tens of electrons flowing in the edge-states per nanosecond. Here we want to be able to trigger at a nanosecond time-scale the injection of a single electron, and

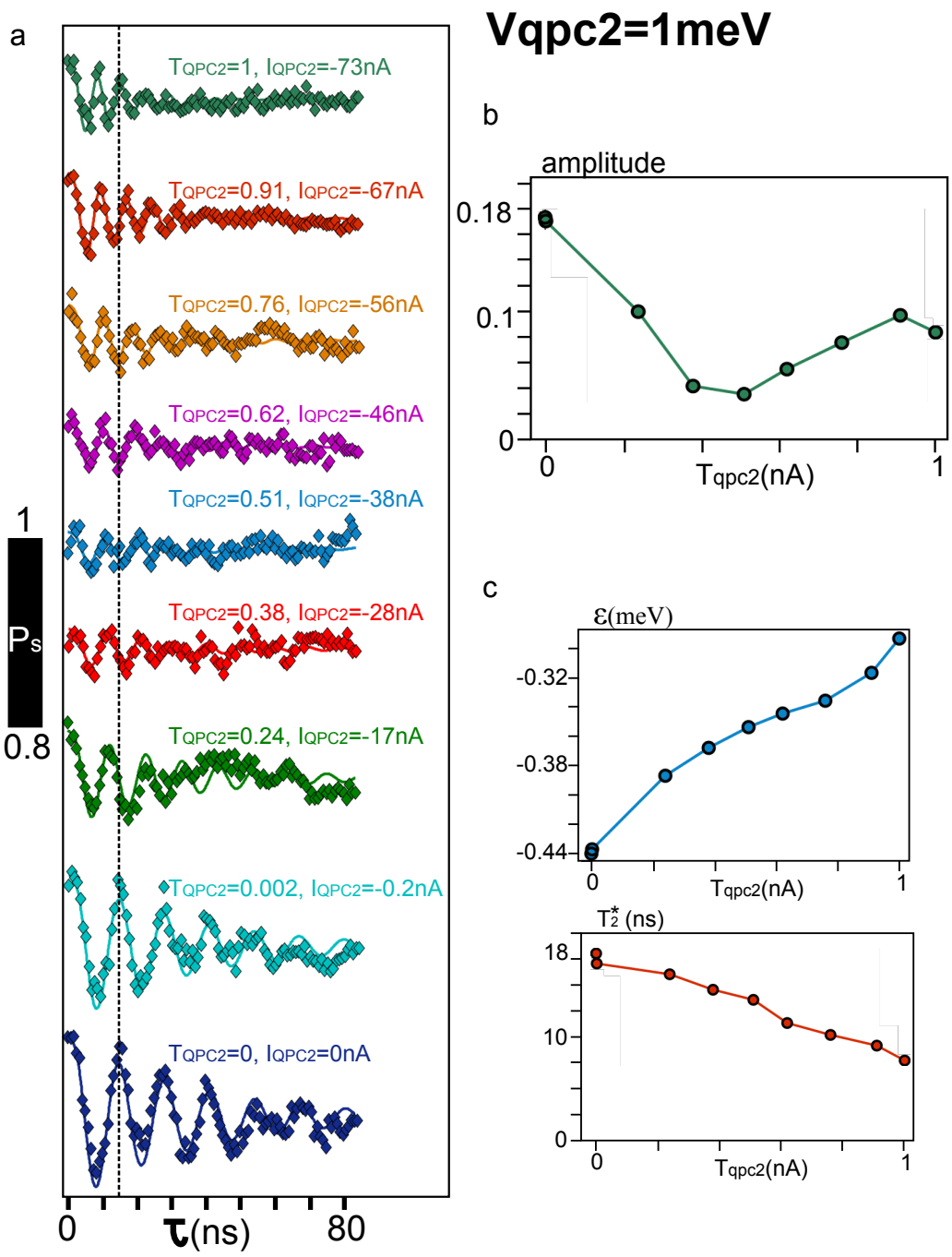

Figure 5.10: **(a)** Exchange oscillations for different QPC2 transmissions at fixed bias voltage $V_{QPC2} = 1meV$. **(b)** Fitted values of the exchange oscillation amplitude with respect to the QPC2 transmission T. **(c)** Fitted values of the decoherence time T_2^* and the detuning ε with respect to the QPC2 transmission T.

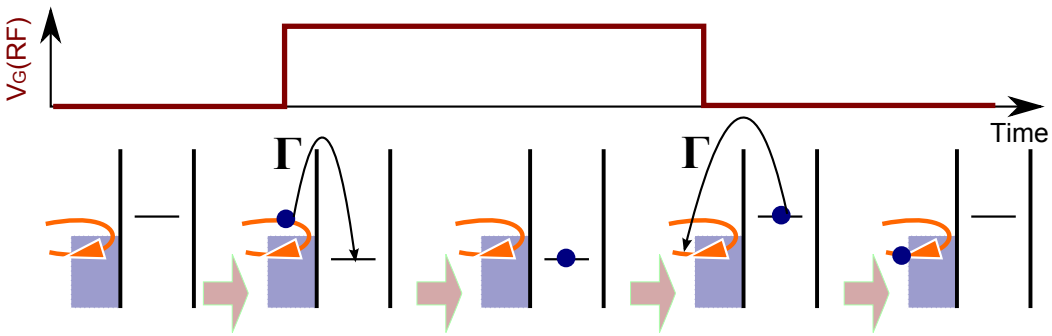

Figure 5.11: A quantum dot as an on demand single electron source.

the use of a quantum dot is of direct relevance. Feve and coworkers [20] first demonstrated the use of a quantum dot as a on demand single electron source. The principle is quite easy to understand (figure 5.11) :

- First the quantum dot can be set in such a configuration where an electrochemical potential level lays $1meV$ above the Fermi energy of the reservoir (the edge-states in this case).
- A positive RF gate voltage can be applied in order to lower this level below the Fermi energy of the reservoir. Consequently an electron from the edge-states enters in the quantum dot with a characteristic time $T = \Gamma^{-1}$, where Γ is the tunnel rate related to the tunnel barrier separating the quantum dot from the edge-states.
- When the pulse is set down, the electrochemical potential goes back above the Fermi energy of the reservoir, and the electron is injected into the edge-states. Again the characteristic time $T = \Gamma^{-1}$ of this event is related to the tunnel barrier between the quantum dot and the edge-states.

The tunnelling rate Γ can be tuned by changing the gate voltages configuration of the quantum dot, and it is possible to reach $\Gamma^{-1} \sim 1ns$. Finally we get a single electron source which can be triggered at the nanosecond.

Therefore we designed a sample with an additional quantum dot. Figure 5.12 (a) shows a SEM picture of the sample. This is exactly the same sample already seen in figure 5.5 (a) where we have hidden some gates for clarity. An additional quantum dot located in the bottom right part of the picture can be engineered by using the gates coloured in red. The particularity of the sample geometry relies on the 3 μm long gate separating the upper double quantum dot from the bottom single one. Consequently, in the Quantum Hall regime, edge-states are defined along this gate and we can use the bottom quantum dot to inject a single electron into these edge-states. The electron should

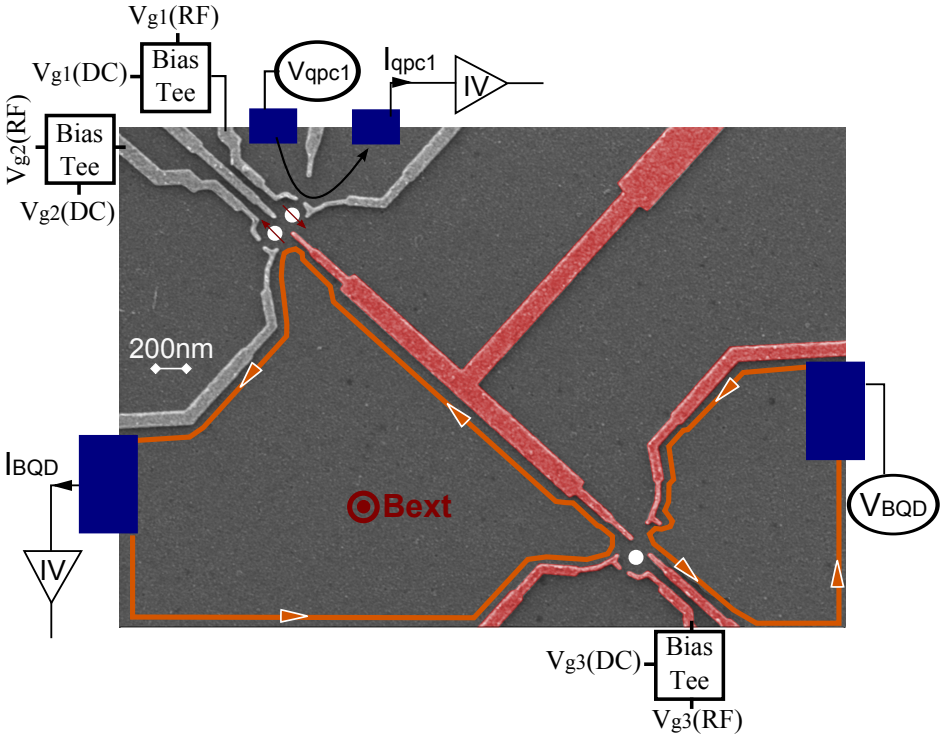

Figure 5.12: SEM picture of the studied device. The double quantum dot located in the top of the picture is the one already seen in the chapter 4. In addition a single quantum dot separated by a 3 μm long gate from the detector allows for injecting a single electron into the edge-states (orange line). The potential of this additional quantum dot is controlled via the gate voltage V_{g3} (DC+RF).

be transported along the gate and finally pass next to the double quantum dot device. If the sensitivity of our detector is sufficient we should be able to see this event.

Bibliography

[1] CleuziouJ.-P., WernsdorferW., BouchiatV., OndarcuhuT., and MonthiouxM. *Nat Nano* **1**(1), 53–59 October (2006). 124

[2] Maze, J. R., Stanwix, P. L., Hodges, J. S., Hong, S., Taylor, J. M., Cappellaro, P., Jiang, L., Dutt, M. V. G., Togan, E., Zibrov, A. S., Yacoby, A., Walsworth, R. L., and Lukin, M. D. *Nature* **455**(7213), 644–647 October (2008). 124

[3] O. E. Dial, M. D. Shulman, S. P. H. H. B. V. U. A. Y. **arXiv:1208.2023** (2012). 106, 113, 124, 131

[4] Klitzing, K. v., Dorda, G., and Pepper, M. *Phys. Rev. Lett.* **45**, 494–497 Aug (1980). 2, 124

[5] Girvin, S. **69**, 53–175 (1999). 124

[6] Yennie, D. R. *Rev. Mod. Phys.* **59**, 781–824 Jul (1987). 124

[7] Landau, L. D. and Lifshitz, E. M. *Quantum Mechanics: Non-relativistic theory*, volume 3 of *Course of Theoretical Physics*. Pergamon Press, Oxford; New York, third edition, (1989, c1977). 92, 125

[8] Ji, Y., Chung, Y., Sprinzak, D., Heiblum, M., Mahalu, D., and Shtrikman, H. *NATURE* **422**(6930), 415–418 MAR 27 (2003). 128

[9] Roulleau, P., Portier, F., Glattli, D. C., Roche, P., Cavanna, A., Faini, G., Gennser, U., and Mailly, D. *Phys. Rev. B* **76**, 161309 Oct (2007). 128

[10] Roulleau, P., Portier, F., Roche, P., Cavanna, A., Faini, G., Gennser, U., and Mailly, D. *Phys. Rev. Lett.* **101**, 186803 Oct (2008). 128

[11] Roulleau, P., Portier, F., Roche, P., Cavanna, A., Faini, G., Gennser, U., and Mailly, D. *Phys. Rev. Lett.* **100**, 126802 Mar (2008). 128

[12] Neder, I., Marquardt, F., Heiblum, M., Mahalu, D., and Umansky, V. *Nat Phys* **3**(8), 534–537 August (2007). 128

[13] Neder, I., Heiblum, M., Mahalu, D., and Umansky, V. *Phys. Rev. Lett.* **98**, 036803 Jan (2007). 128

[14] van Weperen, I., Armstrong, B. D., Laird, E. A., Medford, J., Marcus, C. M., Hanson, M. P., and Gossard, A. C. *PHYSICAL REVIEW LETTERS* **107**(3) JUL 15 (2011). 129

[15] Shulman, M. D., Dial, O. E., Harvey, S. P., Bluhm, H., Umansky, V., and Yacoby, A. *SCIENCE* **336**(6078), 202–205 APR 13 (2012). iii, 129, 131

[16] Barthel, C., Reilly, D. J., Marcus, C. M., Hanson, M. P., and Gossard, A. C. *Phys. Rev. Lett.* **103**, 160503 Oct (2009). iii, 131

[17] Kamata, H., Ota, T., Muraki, K., and Fujisawa, T. *Phys. Rev. B* **81**, 085329 Feb (2010). 131

[18] Kumada, N., Kamata, H., and Fujisawa, T. *Phys. Rev. B* **84**, 045314 Jul (2011). 131

[19] McClure, D. T., Zhang, Y., Rosenow, B., Levenson-Falk, E. M., Marcus, C. M., Pfeiffer, L. N., and West, K. W. *Phys. Rev. Lett.* **103**, 206806 Nov (2009). 131

[20] FÃ¨ve, G., MahÃ©, A., Berroir, J.-M., Kontos, T., PlaÃ§ais, B., Glattli, D. C., Cavanna, A., Etienne, B., and Jin, Y. *Science* **316**(5828), 1169–1172 (2007). 145

Conclusion and perspectives

During this thesis, we studied the use of a single electron spin as a quantum bit as well as a very sensitive electrometer :

- We demonstrated that a single electron spin can be transported along a closed path inside a quadruple quantum dot system. This opens the way toward topological spin manipulations using the spin-orbit interaction. In the following we will develop an experimental way to measure a geometric phase.

- In the context of quantum computing with single spin qubits, we studied the evolution of the natural two-qubit gate in two tunnel coupled quantum dots. In particular, as expected from the theoretical predictions, we demonstrated that the natural two-qubit gate evolves from the SWAP gate at weak magnetic field gradient ΔB_z to the C-phase gate for stronger gradient ΔB_z. Our study allows us to expect a controlled $\pi-$phase gate duration lower than 80ns. We have already seen in the chapter 4 the further experimental requirements in order to prove the entanglement efficiency of the C-phase gate and consequently we will not come back to it here.

- Finally we addressed the possibility to use the electron spin in order to engineer a very sensitive electrometer. We demonstrated that this detector is able to probe the passage of electrons in the edge-states. By taking into account the experimental constraints (limited bandwidth of our present set-up) we developed a sophisticated pulse in order to detect the passage of a single electron in the edge-states. The experimental data continue to be analysed. As a perspective, we will expose a possible sample geometry to perform the Hanbury Brown and Twiss experiment with electrons and with integrated Singlet-Triplet qubit detectors.

Geometric phase measurement proposal

In this paragraph, we will develop a way to measure experimentally a geometric phase in our quadruple quantum dot system. In the following, we assume that the system experiences an external magnetic field B_{ext}. Due to the spin-orbit interaction, the dynamics of an electron spin are related to its charge dynamics. San Jose and coworkers demonstrated via a semi-classical approach that due to the spin-orbit interaction, the spin of an electron moving along a closed path will experience a magnetic field perpendicular to the plane of this path (in our case, it means perpendicular to the 2DEG ($\hat{z}$ axis)). This magnetic field depends on the area enclosed by the path but does not depend on the time dependence of the path. Due to this feature, we assume in the following that the electron will acquire a geometric phase ϕ_g when the electron is driven along a closed

path. By comparing the typical distance between the quantum dots of our quadruple quantum dot device ($\sim 100nm$) and the spin orbit length in GaAs $l_{SO} \sim 1 - 10\mu m$ (the spin orbit length corresponds to the typical length required to flip the spin of an electron experiencing spin-orbit interaction), we expect that the accumulated geometric phase will be relatively small in comparison to the dynamical phase (due to the external magnetic field (B_{ext}). Therefore we have to design a pulse sequence allowing for cancelling the dynamical phase. This proposal follows the principle of the geometric phase measurement in superconducting qubits [1] :

- First we have to empty the quadruple quantum dot system. Then, by lowering one of the gate voltages, an electron with a spin state $|\uparrow\rangle$ can enter in a quantum dot. The state of the system at the beginning of the manipulation is therefore (figure 5.13 (a)).

- A single qubit $\frac{\pi}{2}$-rotation [2] around the $\hat{x}$ axis is therefore applied to the electron spin in order to prepare a superposition of state (figure 5.13 (b)) :

$$\Psi(\tau = 0)\rangle = \frac{|\uparrow\rangle + i|\downarrow\rangle}{\sqrt{2}} \tag{5.7}$$

- The electron is then driven along a closed path a first time, with a path duration equal to t_1. During it, the electron acquires both the dynamical and the geometric phase. At the end of this path (duration t_1), the spin state comes as (figure 5.13 (c)) :

$$\Psi(\tau = t_1)\rangle = \frac{|\uparrow\rangle e^{i(\phi_d(t_1)+\phi_g)} + i|\downarrow\rangle e^{-i(\phi_d(t_1)+\phi_g)}}{\sqrt{2}} \tag{5.8}$$

  where $\phi_d(t_1)$ is the dynamical phase acquired by the electron spin during the time t_1, and ϕ_g is the geometric phase acquired along the closed path.

- In order to cancel the dynamical phase, a spin-echo pulse inverting the two states ($\pi-$rotation around the $\hat{x}$ axis) is applied. The spin state after this spin echo operation (duration t_2) is (figure 5.13 (d)) :

$$\Psi(\tau = t_1 + t_2)\rangle = \frac{|\downarrow\rangle e^{i(\phi_d(t_1)+\phi_g)} + i|\uparrow\rangle e^{-i(\phi_d(t_1)+\phi_g)}}{\sqrt{2}} \tag{5.9}$$

- Afterwards the electron is driven along the same closed path but in the opposite direction with a path duration t_3 equal to the first one ($t_3 = t_1$). This should cancel the dynamical phase. Additionally it leads to the accumulation of the same

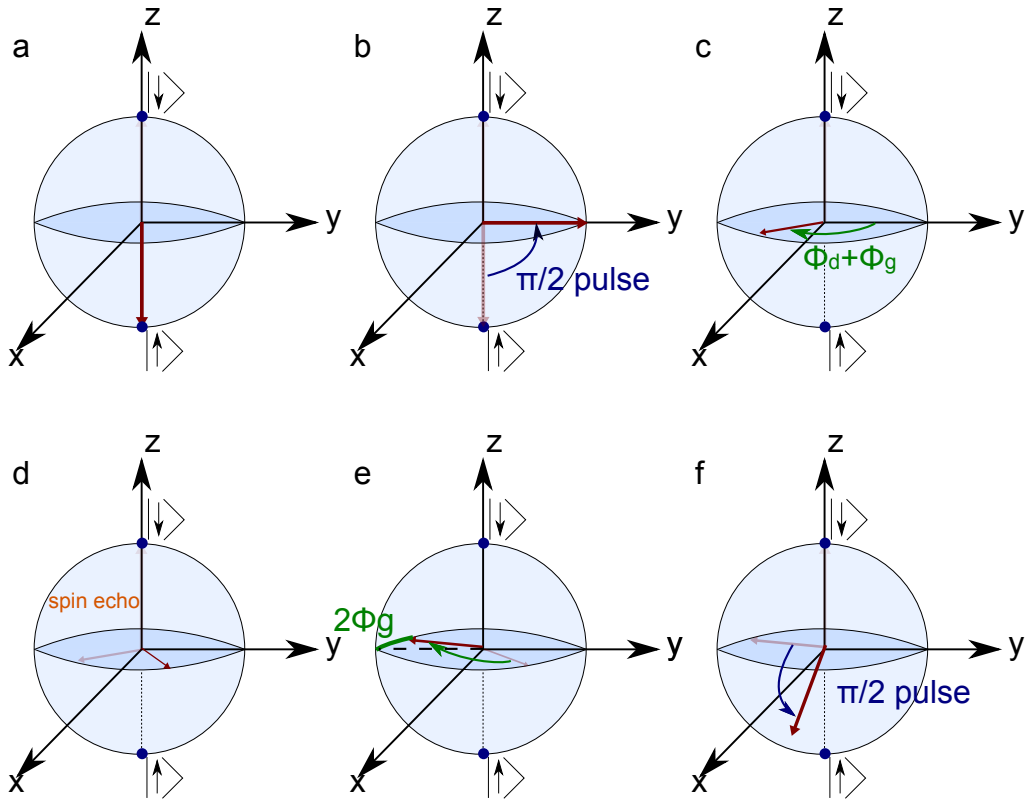

Figure 5.13: **Measurement of a geometric phase with semiconductor spin qubits.** **(a)** The initial state corresponds to the ground state $|\uparrow\rangle$. **(b)** A $\frac{\pi}{2}-$rotation around the $\hat{x}$ axis is applied in order to set the spin state into the equatorial plane, where it is described by the superposition of states 5.7. **(c)** The electron is driven along a closed path and accumulates both the dynamical and geometric phases. **(d)** A spin-echo pulse ($\pi-$rotation around the $\hat{x}$ axis) is applied in order to invert the two states $|\uparrow\rangle$ and $|\downarrow\rangle$. **(e)** The electron is driven back along the same path but in the opposite direction. This should cancel the dynamical phase, while the geometric phase is again accumulated. **f** Finally another $\frac{\pi}{2}-$rotation around the $\hat{x}$ axis is applied in order to measure the final state, which should differ from the initial one ($|\uparrow\rangle$) by a phase factor related to the accumulated geometric phase.

geometric phase ϕ_g. Indeed if the electron is transported in the opposite direction, the effective magnetic field induced by the spin-orbit interaction will point in the opposite direction. Consequently after a time $2t_1 + t_2$ the electron spin state should be (figure 5.13 (e)):

$$\Psi(\tau = 2t_1 + t_2)\rangle = \frac{|\downarrow\rangle e^{2i\phi_g)} + i|\uparrow\rangle e^{-2i\phi_g)}}{\sqrt{2}} \tag{5.10}$$

- Finally by applying another $\frac{\pi}{2}-$rotation around the $\hat{x}$ axis, and by measuring the spin state along the quantification axis ($\hat{z}$ axis) [3], it should differ from the initial one ($|\uparrow\rangle$) by a phase factor related to the accumulated geometric phase (figure 5.13 (f)).

The sample allowing for such topological manipulations has not yet been measured.

Hanbury Brown and Twiss experiment with electrons

The principle of the Hanbury Brown and Twiss effect with photons is the following. Two coherent photons arrive from two different paths (figure 5.14 (a)) at a beam splitter (BS). Two detectors (D1 and D2) allow for measuring the reflection or the transmission of these two photons. Due to the photon bosonic statistics, the amplitude of the detector D1 is maximal (minimal) while the one of D2 is minimal (maximal). By analyzing the two detectors signals, it is possible to extract the coincidences between the two detectors as a function of the delay between the two photon arrivals at the beam splitter (figure 5.14 (b)), the so-called photon bunching. The coincidences should be equal to 0 at zero delay, and increase when the delay increases (decreases).

In order to perform such an experiment with electrons, we propose the sample geometry depicted in figure 5.14 (c). Two single electron sources (single quantum dots) allow for injecting a single electron into an edge-state. The two injected electrons arrive on a beam splitter and are further detected by two singlet-triplet detectors.

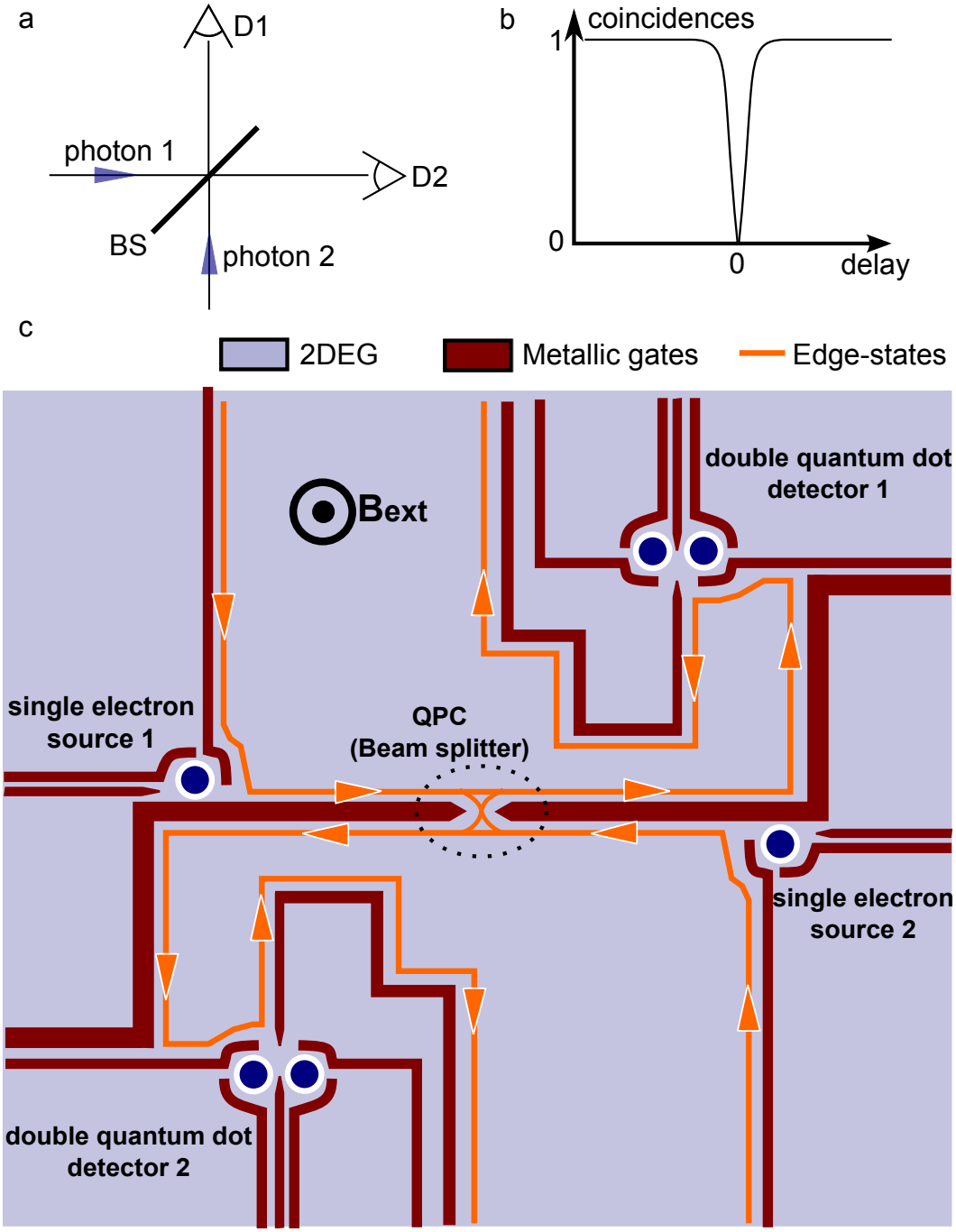

Figure 5.14: **Hanbury Brown and Twiss experiment.** **(a)** Hanbury Brown and Twiss experiment with photons. **(b)** Coincidences between the two detectors (experiment with photons) **(c)** Proposed sample geometry in order to perform an Hanbury Brown and Twiss experiment with electrons.

Bibliography

[1] Leek, P. J., Fink, J. M., Blais, A., Bianchetti, R., Goeppl, M., Gambetta, J. M., Schuster, D. I., Frunzio, L., Schoelkopf, R. J., and Wallraff, A. *SCIENCE* **318**(5858), 1889–1892 DEC 21 (2007). 152

[2] Koppens, F. H. L., Buizert, C., Tielrooij, K. J., Vink, I. T., Nowack, K. C., Meunier, T., Kouwenhoven, L. P., and Vandersypen, L. M. K. *Nature* **442**(7104), 766–771 August (2006). 77, 119, 152

[3] Elzerman, J. M., Hanson, R., van Beveren, L. H. W., Witkamp, B., Vandersypen, L. M. K., and Kouwenhoven, L. P. *Nature* **430**(6998), 431–435 July (2004). ii, 4, 17, 119, 154

Appendices

Nanofabrication recipes

We give here the recipes for the nanofabrication steps described in the chapter 2. We start by detailing the three resists used during the thesis, and finally we give the details for each fabrication steps.

.1 Optical lithography (thin plating)

The resist used is a bilayer of LOR3A (400nm) and UV3 (300nm). LOR3A is a general purpose layer to get undercut under other resists. Its use makes the lift-off step much easier and help to get cleaner edges for the deposited metal. This recipe allows for metal depositions up to 200nm.
Proceed as follows :

- Clean the sample
- Spin coat LOR3A, 2000rpm, 2000rpm/s, 30s
- Hotplate bake, 170°C, 30s
- Spin coat UV3, 4000rpm, 2000rpm/s, 30s
- Hotplate bake, 130°C, 1min
- Exposure, deep UV, 15 to 16s
- Post exposure bake, hotplate, 130°C, 1min
- Development, LDD26W for 55 to 60s
- Metal deposition
- Lift-off, acetone followed by PG remover at 70°C for 2 hours
- Dry, N_2 blow dry

.2 Optical lithography (thick plating)

The resist used is a mono-layer of S1818 (1.8 μm). This recipe allows for metal depositions up to 600nm.
Proceed as follows :

- Clean the sample
- Spin coat S1818, 4000rpm, 2000rpm/s, 60s
- Hotplate bake, 80°C, 60s
- Exposure, UV, 20s
- Development
- Metal deposition
- Lift-off, acetone
- Dry, N_2 blow dry

.3 Electronic lithography

Proceed as follows :

- Clean the sample
- Spin coat OEBR 1000:OFPR 800 3:2, 4000rpm, 50s
- Hotplate bake, 180°C, 3min
- Exposure, electron beam, 650 to 800 $\mu C.cm^{-2}$
- Development, MIBK:IPA (1:3), 60s, and then stop with IPA, 60s
- Extremely soft N_2 blow dry since it can push the resist edges in the defines patterns
- Deposition
- Lift-off, acetone
- Dry, N2 blow dry

.4 Alignment marks

- Clean the sample
- Resist : LOR3A/UV3
- Deposition : 20nm Ti, 100nm Au
- Lift off

.5 Mesa etching

- Clean the sample
- Resist : LOR3A/UV3
- Deposition : 50nm Al
- Lift off
- Ion beam etching (IBE) with argon : RF power (600W), Ar pressure (1.5×10^{-4}), incidence angle for the ions beam (35°). The depth etched could be quite fluctuating, so for each sample a run of the machine test has been done in order to verify the depth etched.
- Aluminium mask withdrawal : 1min in caustic soda ($> 1moll^{-1}$), DI water rinse

.6 Ohmic contacts

- Clean the sample
- Resist : S1818
- Deposition : 10nm Ni, 60nm Ge, 120nm Au, 20nm Ni, 200nm Au
- Lift off
- Rapid thermal annealing under H_2 atmosphere at 400 °C during 1min

.7 Thin gates

- Clean the sample
- Resist : OEBR 1000:OFPR 800 3:2
- Deposition : 5 to 10nm Ti, 20 to 25nm Au
- Lift off

.8 Large gates

- Clean the sample
- Resist : LOR3A/UV3
- Deposition : 20nm Ti, 100nm Au
- Lift off

CI model

In this appendix we will describe the electrostatic properties of quantum dot systems. In [1], they developed the case of a double quantum dot. Here we will develop the CI model up to a quadruple quantum dot system, but first we will discuss about the electrostatics of a system of N conductors.

.9 Electrostatics of a N conductors system

In this part we consider a system made of N conductors. A capacitance is defined between each conductors as well as between the N conductors and the ground. This results in N(N+1)/2 conductances. We want to get the electrostatic energy of such a system.
We write the capacitance between the node i and j as c_{ij}, and its charge is written as q_{ij}. Then the total charge Q_i on node i is equal to the sum of all the charges stored on all the capacitance connected to the node i.

$$Q_i = \sum_{j=0}^{N} q_{ij} = \sum_{j=0}^{N} c_{ij}(V_i - V_j) \tag{11}$$

where $V_{i(j)}$ is the i(j) node potential (where ground is assumed to be at zero potential). As we can see in equation 11, the charge on a node is linear with respect to the potential. It is therefore convenient to write it in a matrix form :

$$\vec{Q} = \mathbf{C}\vec{V} \tag{12}$$

where $\vec{Q}$ and $\vec{V}$ are respectively the charge and the potential vectors. $\mathbf{C}$ is called the capacitance matrix. Its diagonal elements are the total capacitance of node i :

$$C_{ii} = \sum_{j=0, j\neq i}^{N} c_{ij} \tag{13}$$

The off-diagonal elements are minus the capacitance between node i and j :

$$C_{ij} = C_{ji} = -c_{ij} \tag{14}$$

The electrostatic energy of such a system being the energy stored on the N(N+1)/2 capacitances, it can written as :

$$U = \frac{1}{2}\vec{V}.\mathbf{C}\vec{V} = \frac{1}{2}\vec{V}.\vec{Q} = \frac{1}{2}\vec{Q}\mathbf{C}^{-1}\vec{Q} \tag{15}$$

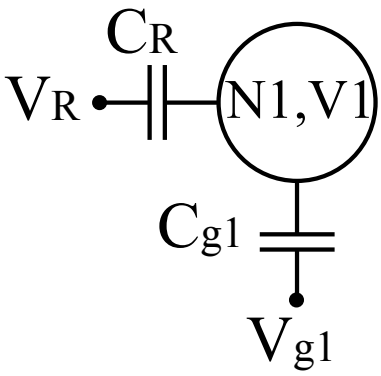

Figure 15: **Single quantum dot.** Capacitance network used to get the electrostatic energy of a single quantum dot.

We will used this formula in order to get the electrostatic energy of multiple quantum dot systems. First we will study the case of a single quantum dot.

.10 Single quantum dot

Considering the case of a single quantum dot (figure 15), the charge $Q_1 = -N_1|e|$ can be written as :

$$\begin{aligned} -N_1|e| &= C_{g1}(V_1 - V_{g1}) + C_R(V_1 - V_R) \\ -N_1|e| + C_{g1}V_{g1} + C_R V_R &= C_1 V_1 \end{aligned} \tag{16}$$

where $C_1 = C_{g1} + C_R$. In this case the capacitance matrix has only one element and the electrostatic energy can be written as :

$$U(N_1, V_{g1}) = \frac{[-N_1|e| + C_R V_R + C_{g1}V_{g1}]^2}{2C_1} \tag{17}$$

.11 Double quantum dot

We proceed by following the previous example. The system is made of a double quantum dot (figure 16 (a)), and we can calculate the charge on node 1 and 2. We notice that the capacitive coupling of the quantum dots with the reservoirs have been considered as equal, in order to simplify the calculation.

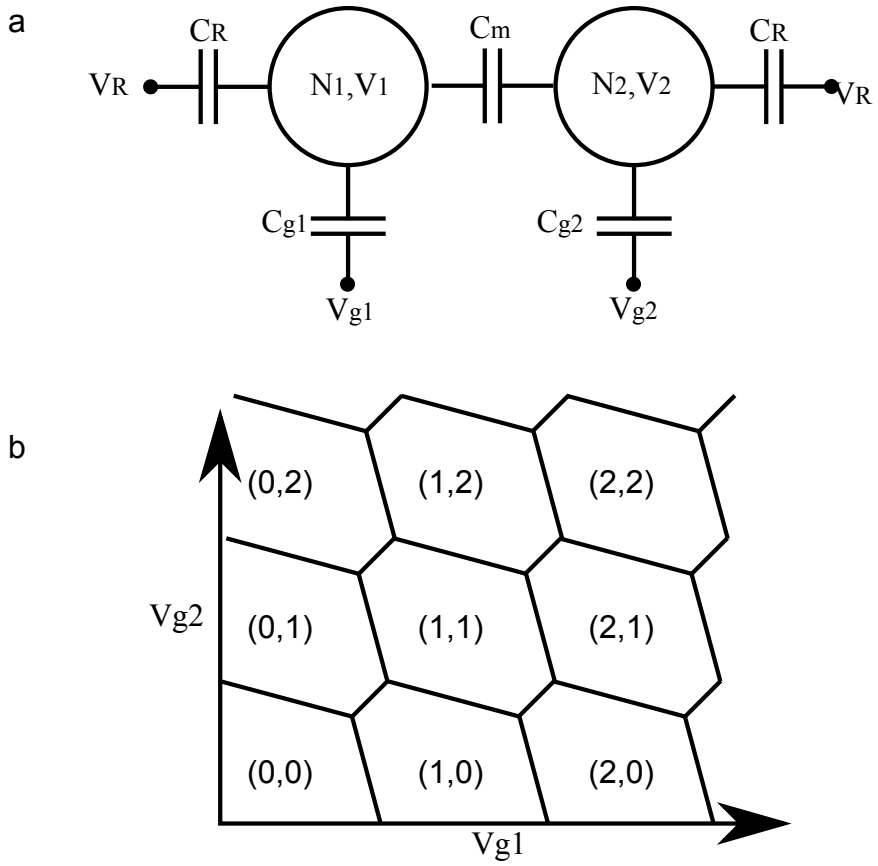

Figure 16: **Double quantum dot.** **(a)** Capacitance network used to get the electrostatic energy of a double quantum dot. **(b)** Stability diagram of a double quantum dot.

$$\begin{aligned} -N_1|e| &= C_{g1}(V_1 - V_{g1}) + C_R(V_1 - V_R) + C_m(V_1 - V_2) \\ -N_2|e| &= C_{g1}(V_2 - V_{g2}) + C_R(V_2 - V_R) + C_m(V_2 - V_1) \end{aligned} \tag{18}$$

This can be written as matrix form :

$$\begin{aligned} \begin{pmatrix} -N_1|e| + C_{g1}V_{g1} + C_RV_R \\ -N_2|e| + C_{g2}V_{g2} + C_RV_R \end{pmatrix} &= \begin{pmatrix} C_1 & -C_m \\ -C_m & C_2 \end{pmatrix} \begin{pmatrix} V_1 \\ V_2 \end{pmatrix} \\ \begin{pmatrix} V_1 \\ V_2 \end{pmatrix} &= \frac{1}{C_1C_2 - C_m^2} \begin{pmatrix} C_2 & C_m \\ C_m & C_1 \end{pmatrix} \begin{pmatrix} -N_1|e| + C_{g1}V_{g1} + C_RV_R \\ -N_2|e| + C_{g2}V_{g2} + C_RV_R \end{pmatrix} \end{aligned} \tag{19}$$

where $C1 = C_{g1} + C_R + C_m$ and $C2 = C_{g2} + C_R + C_m$. Then by following the formula 15 and assuming the reservoir potential equal to zero ($V_R = 0$), we get :

$$U(N_1, N_2, V_{g1}, V_{g2}) = \frac{1}{2}N_1^2E_{c1} + \frac{1}{2}N_2^2E_{c2} + f(N_1, N_2, V_{g1}, V_{g2}) \tag{20}$$

$$\begin{aligned} where \quad f(N_1, N_2, V_{g1}, V_{g2}) =& \frac{-1}{|e|}[C_{g1}V_{g1}(N_1E_{c1} + N_2E_{cm}) + C_{g2}V_{g2}(N_2E_{c2} + N_1E_{cm})] \\ & \frac{1}{e^2}[\frac{1}{2}C_{g1}^2V_{g1}^2E_{c1} + \frac{1}{2}C_{g2}^2V_{g2}^2E_{c2} + C_{g1}V_{g1}C_{g2}V_{g2}E_{cm}] \end{aligned} \tag{21}$$

with $E_{c1} = e^2\frac{C_2}{C_1C_2-C_m^2}$, $E_{c2} = e^2\frac{C_1}{C_1C_2-C_m^2}$ and $E_{cm} = e^2\frac{C_m}{C_1C_2-C_m^2}$ being respectively the charging energy of quantum dot 1 and 2, and the mutual charging energy.
In order to obtain the stability diagram of such a system, we can numerically find the minimum of $U(N_1, N_2, V_{g1}, V_{g2})$ for each values of V_{g1} and V_{g2} and $N_1, N_2 \in \mathbb{N}$. We obtained the so-called honeycomb diagram seen in figure 16 (b).

.12 Triple quantum dot

The case of a triple quantum dot follows the same principle, but in addition we take into account the cross-talk of the gates 1 and 2 on the quantum dot 3 (figure 17 (a)).

We can write the charge of the three quantum dots as (we omitted the capacitive coupling to the reservoir for simplicity) :

$$\begin{aligned} -N_1|e| &= C_{g1}(V_1 - V_{g1}) + C_{m12}(V_1 - V_2) + C_{m13}(V_1 - V_3) \\ -N_2|e| &= C_{g2}(V_2 - V_{g2}) + C_{m12}(V_2 - V_1) + C_{m23}(V_2 - V_3) \\ -N_3|e| &= C_{g3}(V_3 - V_{g3}) + C_{m13}(V_3 - V_1) + C_{m23}(V_3 - V_2) + C_{g13}(V_3 - V_{g1}) + C_{g23}(V_3 - V_{g2}) \end{aligned} \tag{22}$$

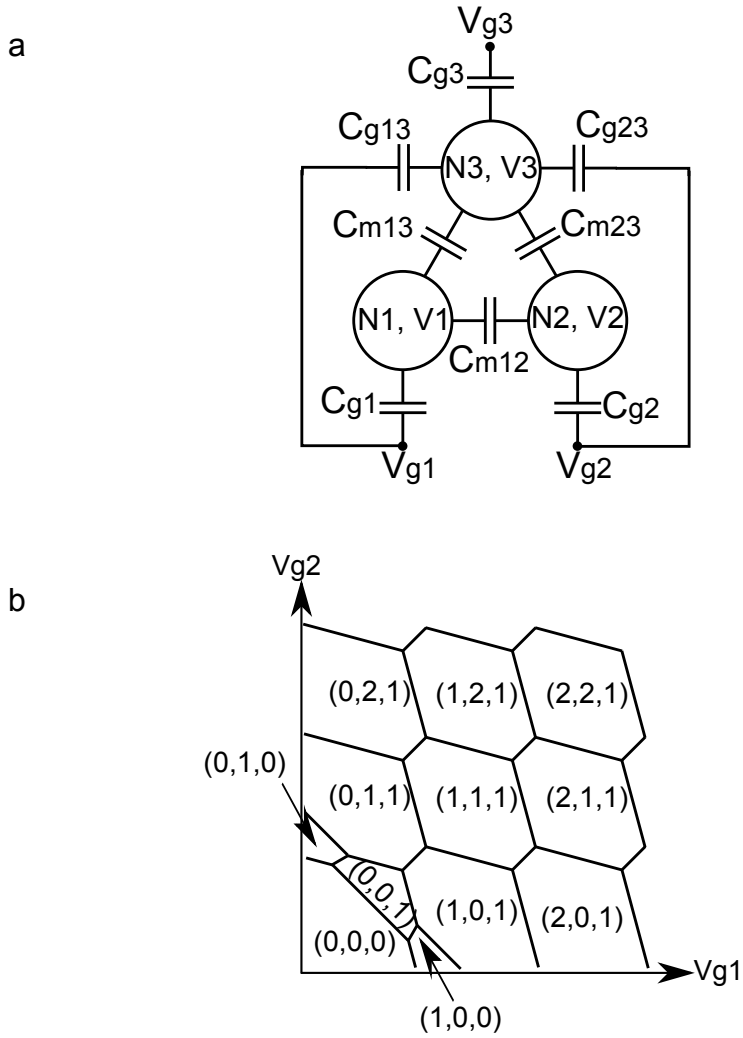

Figure 17: **Triple quantum dot.** **(a)** Capacitance network used to get the electrostatic energy of a triple quantum dot. **(b)** Stability diagram of a triple quantum dot where the gate voltage V_{g3} has been fixed.

Then in matrix form :

$$\begin{pmatrix} -N_1|e| + C_{g1}V_{g1} \\ -N_2|e| + C_{g2}V_{g2} \\ -N_3|e| + C_{g3}V_{g3} + C_{g13}V_{g1} + C_{g23}V_{g2} \end{pmatrix} = \begin{pmatrix} C_1 & -C_{m12} & -C_{m13} \\ -C_{m12} & C_2 & -C_{m23} \\ -C_{m13} & -C_{m23} & C_3 \end{pmatrix} \begin{pmatrix} V_1 \\ V_2 \\ V_3 \end{pmatrix} \tag{23}$$

with $C_1 = C_{g1} + C_{m12} + C_{m13}$, $C_2 = C_{g2} + C_{m12} + C_{m23}$ and $C_3 = C_{g3} + C_{m13} + C_{m23} + C_{g13} + C_{g23}$. We can then invert the previous equation in order to get the equation of the potential vector $\vec{V}$. Then as previously we can get the electrostatic energy of the system $U(N_1, N_2, N_3, V_{g1}, V_{g2}, V_{g3})$. We do not put the full result of $U(N_1, N_2, N_3, V_{g1}, V_{g2}, V_{g3})$ due to the expression size, but the reader got all the ingredients to verify by himself. Similarly to the double quantum dot case, we can minimize $U(N_1, N_2, N_3, V_{g1}, V_{g2}, V_{g3})$ for each value of the gate voltages in order to get the stability diagram. Here we decided to fix V_{g3} and we give one calculated stability diagram (figure 17 (b)).

.13 Quadruple quantum dot

We continue with the case of a quadruple quantum dot (figure 18 (a)) where the cross-talk between the gates 1 and 3 and the quantum dots 2 and 4 is taken into account.

One more time we can write the charge of the three quantum dots as (we omitted the capacitive coupling to the reservoir for simplicity) :

$$\begin{aligned} -N_1|e| &= C_{g1}(V_1 - V_{g1}) + C_{m12}(V_1 - V_2) + C_{m13}(V_1 - V_3) + C_{m14}(V_1 - V_4) \\ -N_2|e| &= C_{g2}(V_2 - V_{g2}) + C_{m12}(V_2 - V_1) + C_{m23}(V_2 - V_3) + C_{m24}(V_2 - V_4) \end{aligned} \tag{24}$$

$$\begin{aligned} -N_3|e| =& C_{g3}(V_3 - V_{g3}) + C_{m13}(V_3 - V_1) + C_{m23}(V_3 - V_2) + C_{m34}(V_3 - V_4) \\ &+ C_{g13}(V_3 - V_{g1}) + C_{g23}(V_3 - V_{g2}) \end{aligned} \tag{25}$$

$$\begin{aligned} -N_4|e| =& C_{g4}(V_4 - V_{g4}) + C_{m14}(V_4 - V_1) + C_{m24}(V_4 - V_2) + C_{m34}(V_4 - V_3) \\ &+ C_{g14}(V_4 - V_{g1}) + C_{g24}(V_4 - V_{g2}) \end{aligned} \tag{26}$$

Then in matrix form :

$$\begin{pmatrix} -N_1|e| + C_{g1}V_{g1} \\ -N_2|e| + C_{g2}V_{g2} \\ -N_3|e| + C_{g3}V_{g3} + C_{g13}V_{g1} + C_{g23}V_{g2} \\ -N_4|e| + C_{g4}V_{g4} + C_{g14}V_{g1} + C_{g24}V_{g2} \end{pmatrix} = \begin{pmatrix} C_1 & -C_{m12} & -C_{m13} & -C_{m14} \\ -C_{m12} & C_2 & -C_{m23} & C_{m24} \\ -C_{m13} & -C_{m23} & C_3 & -C_{m34} \\ -C_{m14} & -C_{m24} & -C_{m34} & C_3 \end{pmatrix} \begin{pmatrix} V_1 \\ V_2 \\ V_3 \\ V_4 \end{pmatrix} \tag{27}$$

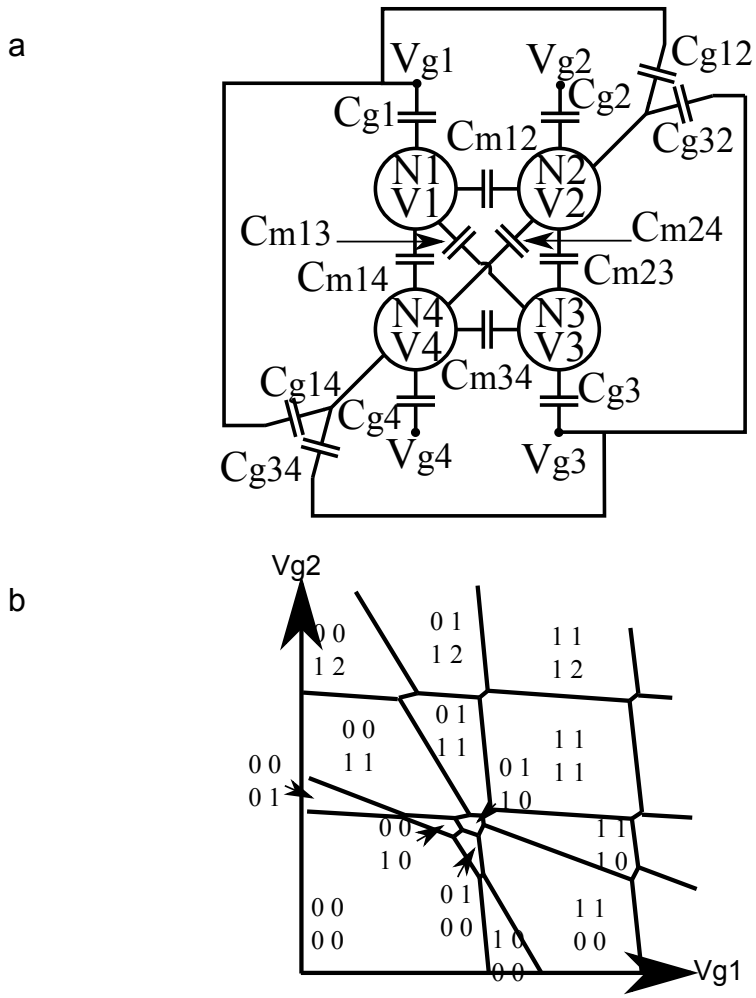

Figure 18: **Quadruple quantum dot.** **(a)** Capacitance network used to get the electrostatic energy of a quadruple quantum dot. **(b)** Stability diagram of a quadruple quantum dot where the gate voltage V_{g2} and V_{g4} have been fixed.

with $C_1 = C_{g1}+C_{m12}+C_{m13}+C_{m14}$, $C_2 = C_{g2}+C_{m12}+C_{m23}+C_{m24}$, $C_3 = C_{g3}+C_{m13}+C_{m23}+C_{m34}C_{g13}+C_{g23}$, $C_4 = C_{g4}+C_{m14}+C_{m24}+C_{m34}C_{g14}+C_{g24}$. One more time we will not give the full expression of the electrostatic energy $U(N_1, N_2, N_3, N_4, V_{g1}, V_{g2}, V_{g3}, V_{g4})$ due to the expression size, but the reader got all the ingredients to verify by himself. Similarly to the previous cases, we can minimize $U(N_1, N_2, N_3, N_4, V_{g1}, V_{g2}, V_{g3}, V_{g4})$ for each value of the gate voltages in order to get the stability diagram. Here we decided to fix V_{g2} and V_{g4}, and we give one calculated stability diagram (figure 18 (b)).

Bibliography

[1] van der Wiel, W. G., De Franceschi, S., Elzerman, J. M., Fujisawa, T., Tarucha, S., and Kouwenhoven, L. P. *Rev. Mod. Phys.* **75**, 1–22 Dec (2002). 57, 67, 165